ECOLE DES MINES
DE PARIS

Collège doctoral

THESIS

Presented to obtain the titles of
Docteur de l'Ecole Nationale Supérieure des Mines de Paris
Docteur Communitatis Europae
Speciality: Material Sciences and Engineering

by

Pascal BOUBIDI

Experimental characterization and numerical modelling of Low Cycle Fatigue in a Nickel base single crystal superalloy under multiaxial loading

18th December 2000

Jury

M. H.-D. BUI	Ecole Polytechnique
M. E. BUSSO	Imperial College
M. G. CAILLETAUD	Ecole des Mines de Paris
M. S. FOREST	Ecole des Mines de Paris
M. J.-Y. GUEDOU	SNECMA
M. S. KRUCH	ONERA
M. J. OLSCHEWSKI	BAM
M. L. REMY	Ecole des Mines de Paris
M R. SIEVERT	BAM

Centre des Matériaux P.M. FOURT de l'Ecole des Mines de Paris,
B.P. 87, 91003 EVRY Cedex

Abstract

The life prediction of single crystal components was studied in this work through an experimental approach and numerical modelling. It has been observed that a good evaluation of the life must include both a crack initiation model and a prediction of the crack propagation.
The main contribution of the thesis deals with crack initiation: a huge experimental data base on SC16 has been made, and two original approaches have been proposed for the simulation of the tests. Most of the tests performed in the study are unique in the literature, specially the section concerning the notched specimens with $\langle 001 \rangle$, $\langle 011 \rangle$ and $\langle 111 \rangle$ crystallographic orientations. Several notched radii and orientations of the material have been used. Metallurgical observations have been made to characterize crack location and the rupture mode.
The simulation section includes first the identification of the material parameters for a crystallographic model valid for non isothermal cyclic loadings, in the complete temperature range, a special attention being payed to $950°C$. The same set of coefficients is valid for monotonic loadings, including creep, and cyclic loadings with or without hold periods, for all the crystallographic orientations tested, with either single or multiple slip. This model was used to simulate isothermal low cycle fatigue tests on circumferentially notched specimen using a FE technique. Crack initiation models can then be applied in a post-processor to achieve the life prediction. A new definition of the critical variable, based on the resolved shear stress, has been validated. On the other hand, it was observed from micrographs of the surface ruptures that the cracks initiate from casting pores present near the surface. An second approach, a statistical failure model taking account of the defects distribution in the life prediction, has been successfuly applied too.
The methodology derived from the specimen observation is then tested on a "technological specimen" by the industrial partner, Siemens (KWU), simulating the most critical zone of a turbine blade. The classical procedures used in industry for life prediction are more and more questionable, due to the increasing complexity of the thermal and mechanical loading history. The FE model was taken from KWU, and the two previously defined assessment rules were successfully applied. Both lifetime and crack location given by the model were found in good agreement with experiment.
The last section of this work is a numerical study concerning the strain localisation patterns at the crack tip in f.c.c. single crystals under plane strain conditions at low temperature. This has to be seen as a first step for a better understanding of the crack propagation process, having in view the competition between strain localisation models and fracture mechanics approach. Our contribution concerns the modification of the theoretical classical continuum mechanics results produced by the introduction of the generalized continuum theory. A Cosserat model for single crystal has then been used, for several orientations of a CT specimen, and was shown to predict a qualitatively different answer to the problem of strain localisation at a crack tip and to give pertinent explanations for crack branching after stable crack growth.

Résumé

La durée de vie de structures monocristallines a été abordée selon une approche expérimentale et une modélisation numérique. Suite à des observations il s'avére qu'une satisfaisante détermination de la durée de vie doit inclure un modèle d'amorçage et une prévision de la propagation de fissure.
La principale contribution de cette thèse concerne l'amorçage de fissure: une importante campagne d'essais a été accomplie pour le SC16 et deux approches originales ont été mises en oeuvre pour leur simulation numérique. La plupart des essais effectués pendant cette étude, en particulier la partie traitant des essais sur éprouvettes entaillées avec les orientations cristallographiques $\langle 001 \rangle$, $\langle 011 \rangle$ et $\langle 111 \rangle$, constituent des resultats inédits. Plusieur rayons d'entaille et orientations du matériau ont été testés. Des observations métallographiques ont permis de caractériser la localisation de fissure et le mode de rupture.
La partie simulation traite d'abord de l'identification des paramètres du modèle cristallographique valables pour des chargements cycliques anisothermes, couvrant un large intervalle de température, une attention particulière étant prêter à $950^{\circ}\mathrm{C}$. Le même jeu de coefficients satisfait les chargements monotones (tension et fluage) et cycliques avec ou sans temps de maintien, pour differentes orientations crystallographiques, avec glissement simple ou bien multiple. Ce modèle a été utilisé pour simuler des essais isothermes LCF sur éprouvettes entaillées utilisant la méthode des Elements-Finis. Des modèles d'amorçage peuvent alors être appliqués par des post-processeurs pour aboutir à la durée de vie. Une nouvelle définition de la variable critique, issue de la cission resolue, a été validée. Par ailleurs, il a été observé sur des micrographies de surfaces de rupture que les fissures s'initient à partir de pores présents au voisinage de la surface. Une seconde approche, un modèle de rupture statistique tenant compte de la distribution de défauts dans l'estimation de la durée de vie, a également été appliqué avec succès.
La méthodologie obtenue à partir de l'éprouvette de laboratoire a été testée sur une "éprouvette technologique" par le partenaire industriel, Siemens (KWU), simulant les zones les plus critiques d'une aube de turbine. Les méthodes classiques utilisées dans l'industrie pour la détermination de la durée de vie sont de plus en plus discutables, dû à la compléxité croissante de l'histoire du chargement thermomécanique. A partir du modèle Element-Finis de KWU, on a montré que les deux méthodes précédemment définies présentent un bon caractère prédictif. La localisation de fissure et la prévision de la durée de vie obtenues à l'aide de ces modèles sont en bon accord avec les résultats expérimentaux.
La dernière partie concerne l'étude numérique des bandes de localisation de la déformation en pointe de fissure d'un monocristal en déformation plane et à basse température. Il s'agit d'une première étape pour une meilleure compréhension de la propagation de fissures, ayant en vue la compétition entre les modèles de localisation de la déformation et l'approche de la mécanique de la rupture. Notre contribution concerne la modification des résultats obtenus par la mécanique classique des milieux continus, produite par l'introduction de la théorie des milieux continus généralisés. Un modèle de Cosserat pour le monocristal a été utilisé, pour différentes orientations d'une éprouvette CT, et on a montré qu'il prévoit une solution qualitative différente au problème de localisation de la déformation en pointe de fissure et qu'il donne des explications pertinentes

pour les bifurcations de fissure après propagation stable.

Remerciements, Danksagung

J’adresse ma profonde gratitude à Monsieur H. D. Bui pour m’avoir fait l’honneur de présider cette thèse.

Merci à Messieurs Busso, Kruch et Sievert d’avoir accepté d’être rapporteur.
J’exprime ma vive reconnaissance à Messieurs Guédou, Rémy et Olschewski d’avoir porté un jugement sur mon travail.

Je remercie G. Cailletaud pour tous ses conseils et sa grande patience.

J’ai également une sincère admiration à l’egard de S. Forest qui, avec beaucoup d’enthousiasme et de compréhension, m’a transmis une partie de sa foi et a assumé son rôle d’éveilleur.

Deux ans et neuf mois passés au BAM de Berlin n’occultent en rien les quelques années de mon séjour au Centre des Matériaux de l’Ecole des Mines de Paris qui a débuté avec mon stage de DEA au sein du groupe *Simulation Numerique*.
Je tiens à remercier P. Pilvin qui m’a remis le pied à l’étrier dans un contexte très difficile et qui a certainement influencé ma façon d’aborder les problèmes scientifiques et techniques.
Ma sympathie d’adresse également aux numéricien(ne)s Fabrice, Farida, Françoise, Grégory, Jean-Marc, Olivier, Rodrigue, Sylvain, Stéphane, Toufik, Valérie, Vincent et Yann auquels doivent être associés Hélène, Laurent, Liliane L, Liliane M, Lucien, Michel, Sarojinee, Véronique D et Véronique M.
Enfin j’ai une grande estime envers A. Pineau et A. F. Gourgues qui ont aimablement été disponibles pour me donner leur avis sur cette thèse dans un délai très court.

Sehr herzlich möchte ich mich bei Jürgen Olschewski für den freundlichen Empfang innerhalb des Labors *Rechnerische Werkstoff und Baueteilanalyse* bedanken, der mir erst ermöglichte, meine Doktorarbeit unter diesen guten Bedingungen durchzuführen.
Gegenüber Joseph Ziebs möchte ich meine Dankbarkeit darüber ausdrücken, da”s er mir während meines Aufenthalts so viel Enthusiasmus entgegen gebracht hat.
Ebenso danke ich Rainer für seine theoretischen Gesichstpunkten und seine geistige Aufgeschlo”senheit.
Au”serdem bin ich Bernard gegenüber dankbar dafür, da”s er mir gezeigt hat, wie man rigoros durchhalten kann.
Danke Bodo, gro”ser Meister der Experimente der gekerbten Proben, da”s du mir so liebenswürdig zur Seite gestanden hast.
Anja, Arno, Bob, Cetin, Dietmar, Frederik, Georgia, Ilse, Max, Mirjana, Renate, Yusuf waren ebenso immer sehr verständnisvoll und sehr freundlich und erleichterten mir damit die Arbeit.
Dank an Hellmuth Klingelhöffer, Verantwortlicher für das Labor der *Werkstoffemechanik der Metall und Metallmatrix-Verbundwerkstoffe*. Durch ihn habe ich Nutzen aus technischen Mitteln von hohem Niveau gezogen und mit einem sympathischen Team von

Experimentatoren arbeiten können: Joachim, Felix, Katherin, Matthias, Sigmar, Suzanne und Wolfgang.
Und schlie”slich gebührt mein Dank Werner Österle, der uns wirkungsvolle Beobachtungsmittel zur Verfügung stellte, mit denen Monika Engelhardt so schöne Bilder in die Tat umgesetzt hat.

Contents

I Introduction **13**

II Constitutive model for single crystals at small deformation **15**

1 Introduction **15**

2 Presentation of a crystallographic model **17**

3 Identification of the model for SC16 at different temperatures **19**
3.1 Presentation of the material 19
3.2 Methodology and results 20
3.2.1 Elasticity constants 20
3.2.2 Calibration of the viscoplastic constants at low and high temperature 20

4 Conclusion **22**

III Analysis of Low-Cycle Fatigue at notches in a single crystal superalloy at high temperature **33**

1 Introduction **33**

2 Low-Cycle Fatigue tests on SC16 notched specimens **34**
2.1 Material and experimental procedure 34
2.2 Experimental results 35
2.2.1 Metallographic observations 35
2.2.2 Fatigue life results 36

3 Model predictions and comparison with the experimental results **55**
3.1 Viscoplastic strain-stress behaviour at notches 55
3.1.1 Conditions of the FE analysis 55
3.1.2 Results 55
3.2 A deterministic approach for LCF at notches 69
3.2.1 Definition of a critical variable 69
3.2.2 A τ-N fatigue diagram 69
3.3 A multiscale probabilistic failure model 72
3.3.1 Introduction 72
3.3.2 General scheme of the method 72
3.3.3 Calibration of the material parameters 74
3.3.4 Application to the notched specimen 79
3.4 Discussion 85

4 Conclusion **86**

IV Application of the rules to a component 89

1 Introduction 89

2 Experimental results 89

3 Application of the assessment rules 90
3.1 Conditions of the FE analysis 90
3.2 Crack location assessment and comparison with experimental evidence . . 90
3.3 Application of the deterministic method for lifetime 91
3.4 Application of the probabilistic failure model 91

4 Conclusion 92

V Strain localization phenomena at a crack tip in single crystals 109

1 Introduction 109

2 Large cracks in single crystals 109

3 Cosserat single crystal plasticity 113
3.1 Motivations 113
3.2 Kinematics of the Cosserat continuum 113
3.3 Forces and stresses 115
3.4 Isotropic elasticity 115
3.5 Elastoplastic Cosserat single crystal 116
3.6 Explicit integration of the constitutive equations 117
3.6.1 Kinematic of plastic deformation and curvature 117
3.6.2 Generalized Schmid law 117

4 Numerical analysis of near tip fields for different orientations of the crystal 119
4.1 Conditions of the finite element calculations 119
4.1.1 General conditions 119
4.1.2 Conditions of the analysis with classical crystal plasticity 120
4.1.3 Conditions of the analysis with the Cosserat model 120
4.2 Results and interpretation of the localization bands 120
4.2.1 Results obtained with the classical model and the Cosserat model with vanishing H' 120
4.2.2 Characteristic of the inelastic strain localization bands 121
4.2.3 Consequences of the introduction of hardening due to lattice curvature 121
4.3 Discussion 122

5 Application to tridimensional notched specimens 132
5.1 Analysis of the 2D equivalent problem 132
5.2 Comparison with experimental results 132
5.3 Analysis of the whole component 134

6 Conclusion **134**

VI Conclusion 139

A Orientation of the SC16 bulk smooth specimens used in the calibration of the crystallographic model **149**

B Orientation of the SC16 notched specimens used in the LCF tests **151**

Part I
Introduction

This thesis has been performed at the BAM, Federal Institute for Materials Research and Testing from Berlin (FRG), during more than two years and at the Centre des Matériaux de l' Ecole des Mines de Paris during several months.
The work was performed in the laboratory "Computational Analysis of Material and Components", in the framework of the Brite-Euram Project "Advanced Analysis Tools to Predict Failure Mechanisms in TBC Coated and Uncoated Single Crystal Superalloy" [Boubidi et al., 1998, Boubidi et al., 1999].

The growing demand for energy saving has led to the development of combined cycle plants for base power generation. The demand for high efficiency in industrial gas turbines, as well as than in aircraft engines, can be satisfied by raising the turbine inlet temperature or by reducing the cooling of the hot section of the components. Three different ways can be followed to improve the performance of the components:

(1) *use of better materials* (materials science domain), In the past, significant advances have been made concerning material development: the materials used in the hot parts of the engines are Nickel-base superalloys. They present a good resistance against high temperature and environmental effects,
(2) *have a better design of the blade*, to lower the temperature of the metal for a given temperature of the gas (fluid mechanics, study of the temperature fields, structural calculations). The geometries are now very elaborate, with hollow blades, and a complex system of cavities and holes, in order to eject cool gas at the surface of the blade, to make a protective film,
(3) *improve the knowledge of the material behaviour* and its failure properties(field of design, mechanics of materials). Our contribution concerns this last point. The aim of the project concerning the BAM was to build numerical tools to assess the lifetime of turbine blades, especially gas turbine blades used in power generation.

A thorough review of high temperature durability methods for calculating time to crack initiation on engineering components working at high temperature can be found in [Lemaitre and Chaboche, 1985, Halford, 1991]. Recent investigations have shown that high temperature fatigue behavior of polycrystalline superalloys is well known, with many lifetime prediction methods available for that class of material [Danzer, 1988, Rémy, 1993]. Nevertheless, the knowledge concerning the fatigue life behavior of anisotropic structural materials like directionally solidified or single crystalline superalloys is rather poor [Nissley et al., 1992]. Progress is needed on this point, having in view the fact that severe and complex multiaxial thermomechanical loading conditions are found in the components, and that the rough surface and the micro-cracks of the film cooling holes produced by manufacturing, lead to fatigue cracks. Depending on the loading conditions, these cracks will develop or might be stopped. A reliable prediction method should then include three steps, the first one concerning the evaluation of the stress and

strain fields, the second one the crack initiation models, the third one the crack propagation models. One can reasonably consider that step one is solved now. So, the topic of the thesis work was first to contribute to steps (2) and (3). The crack initiation problem was treated with BAM, and preliminary elements concerning step (3) were investigated at Centre des Matériaux during the last year.

In the first part, we present a constitutive model for single crystals at small deformations already developed at Centre des Matériaux in the framework of a previous thesis [Méric, 1991]. The good predictive capabilities of this model and its simplicity for Finite Element analyses is confirmed in this study.
The material parameters are calibrated for a large experimental date base on single crystal superalloy SC16 at low and high temperatures. A thorough numerical identification is performed at 950°C since we investigate the Low-Cycle Fatigue behavior of the material at this temperature and under isothermal loading.

The second part deals with the influence of notches on LCF behavior of the alloy at high temperature, from a numerical and experimental point of view.
Several LCF notched specimens have been tested at 950°C. Three different notch radii and three characteristic orientations of the crystal have been investigated. Metallographic observations show the effect of anisotropic behavior of the material on the crack location in the notch area. A "good" life prediction model must be able to predict these tests with material parameters identified on the smooth specimens. Numerical simulations are then performed to model the stress/strain state in the notch area. They will allow us to test several approaches for crack initiation, involving new critical variables, taken from the crystallographic model (model 1), or adding the probabilistic aspect and taking into account the population of defects (model 2).

In the third part, we apply the crack location and the lifetime assessment rules to a "technological specimen", which is a plate with several holes, used to simulate the cooling holes of turbine blades. Several LCF tests have been carried out by KWU with representative loading conditions for the blades. Micrographs of the surface of the specimens during the test allow to analyse precisely the crack mechanism at the holes. On the other hand Finite Element calculations of these tests are performed. The lifetime and the crack location assessment rules are applied from the numerical analyses. A comparison between experimental and numerical results is made.

The fourth part is the preliminary study of the large crack growth in single crystal superalloy. The high strain gradients at the crack tip lead us to use a generalized continuum theory on the localized deformation patterns in this anisotropic material. After a review of recent publications about large cracks in monocrystalline materials, the constitutive equations of the generalized continuum model is briefly recalled. Then calculations of some representative crack configurations with this model are presented. The results characterize the modification of the strain localisation bands distribution. Moreover some explanations of crack branching after stable crack growth are given. Finally some encouraging experimental results are given in the last section.

Part II
Constitutive model for single crystals at small deformation

1 Introduction

The high cost of mechanical testing on structures needs to promote the development of efficient numerical techniques and methods. Indeed nowadays a lot of efforts are made to have high performance numerical tools. In particularly it is essential to design an accurate and predictive model for the materials used in turbine blades under severe conditions of thermomechanical loadings. Nickel-base single crystal superalloys present the required properties to resist creep at high temperature and therefore to increase the lifetime of the components. Unfortunately their specific microstructure leads to a complex behaviour. For that reason, a lot of models have been developed for single crystals during the last twenty years. In this section we give a review of the most representative and we will present the model used in our work. The main properties that we seek, for a model which has to be used to perform structural calculations, can be summarized as follows:

- The model must have predictive capabilities for a volume element and for a component which has a non homogeneous state of stress and strain under uniaxial and multiaxial loading conditions.
- The time of computation must be relatively low in order to stay in the framework of industrial applications.
- A reduced number of material parameters must define the model for a given temperature and must be easy to calibrate.

Viscoplastic models for cubic single crystals based on Hill's criterion can be used for onedimensional cyclic loadings [Nouailhas and Freed, 1992]. The reduced number of state variable is an advantage for F.E. computations. But this type of model is a little simplistic: for instance, it does not take into account the experimental observations made on tubular specimens under torsional loading, which present inhomogeneous deformation along the circumference [Nouailhas et al., 1995]. Moreover the application of the Schmid law shows that the strain and stress distribution cannot be homogeneous [Nouailhas and Cailletaud, 1995].
On the other hand, a similar class of models based on a tensorial generalization of a uniaxial non-linear rheological model allows to determine the creep behavior of structural elements in single crystals [Bertram and Olschewski, 1991], [Bertram and Olschewski, 1996].

At the scale of the precipitates other authors performed finite element calculations of two-phase periodic cells in order to give a description of the internal stresses and strains

in the microstructure [Espié, 1996], [Nouailhas and Lhuillier, 1997], [Busso et al., 1998]. For each phase a phenomenological constitutive behavior has been calibrated.
From a representative two-phase cell one can also obtain the constitutive equations of the homogeneous equivalent medium with the self-consistent scheme [Forest and Pilvin, 1996].

At a lower scale the micromechanical approaches model the elementary mechanisms. [Feng et al., 1996] has taken into account residual stresses, direction-dependent lattice parameters and lattice misfits in the γ' phase in a finite element-modelling of a tensile creep-deformed monocrystalline nickel-base superalloy SRR99.
From an analysis of the main deformation mechanisms with the explicit introduction of the dislocation networks [Fedelich, 1999] has designed a constitutive model for the mechanical behavior at high temperatures of superalloys with a high volume fraction of γ' phase. This analysis allows to give clear physical interpretations of the internal variables used by the model. Nevertheless the large number of internal variables could be an obstacle for finite element structural analyses.

An intermediate way between micromechanical approaches and the macroscopic phenomenological ones is crystallographic slip theory. This approach is known for a long time [Taylor, 1938, Bui, 1969, Mandel, 1971]. On the other hand, it is now more and more efficient, due to the development of the computers (starting with [J. Asaro, 1983]). Our approach is based on a version of these models developed at Ecole des Mines de Paris [Cailletaud, 1987, Forest, 1996].

Many papers can be found on the modeling of Nickel Base single crystals, for instance PWA 1480 at high temperature [Walker and Jordan, 1989], [Nissley et al., 1992]. A good agreement s generally found between model and experiment for the uniaxial hysteresis loops, if one introduces both octahedral and cubic slip in the modelling.

The model we use in this work was developed in a previous thesis, using constitutive equations which involve both kinematic and isotropic hardening [Méric et al., 1991a]. The equations are written at the scale of the crystallographic structure. The simplicity of this approach and the relatively small number of variables to integrate allow the model to be implemented in a finite element code [Méric et al., 1991b]. Moreover due to its physical basis it can be also successfully applied for biaxial loadings. Good agreements were found in the case of tension and torsion loadings for the nickel base single crystal superalloy CMSX2 at high and low temperature [Nouailhas et al., 1995], [Nouailhas and Cailletaud, 1995], for AM1 [Hanriot, 1993, Espié, 1996] and more recently for SC16 [Forest et al., 1996].

In the next section we give the principal constitutive equations of this model written at small deformations. Then we propose a parameter set for the single crystal SC16 at low and high temperatures after an identification from a large experimental data base of uniaxial tests on bulk smooth specimens.

2 Presentation of a crystallographic model

Due to the cubic symmetry of the FCC material the relation between the stress tensor, $\underset{\sim}{\sigma}$, and the elastic strain tensor, $\underset{\sim}{\varepsilon}^e$, is determined by three independent constants C_{1111}, C_{1122} and C_{1212} of the elasticity tensor $\underset{\approx}{\mathbf{C}}$

$$\underset{\sim}{\sigma} = \underset{\approx}{\mathbf{C}}.\underset{\sim}{\varepsilon}^e \tag{1}$$

with the partition of the mechanical strain into an elastic and a plastic part

$$\underset{\sim}{\varepsilon} = \underset{\sim}{\varepsilon}^e + \underset{\sim}{\varepsilon}^p. \tag{2}$$

For single crystals the viscoplastic deformation results from the effects of dislocation motion on crystallographic planes by slip processes:

$$\dot{\underset{\sim}{\varepsilon}}^p = \sum_{g=1}^{18} \dot{\gamma}^g \frac{1}{2} \left(\underline{\mathbf{l}}^g \otimes \underline{\mathbf{n}}^g + \underline{\mathbf{n}}^g \otimes \underline{\mathbf{l}}^g \right) \tag{3}$$

where $\underline{\mathbf{l}}^g$ and $\underline{\mathbf{n}}^g$ respectively are the slip direction and the normal to the slip plane of slip system g which define the symmetric second order tensor. As at room temperature [Hanriot et al., 1991], [Forest et al., 1996], we consider both octahedral (12 $\{111\}(110)$) and cubic (6 $\{100\}(011)$) slip systems at high temperature [Walker and Jordan, 1989].
The flow rule is

$$\dot{\gamma}^g = \left\langle \frac{|\tau^g - x^g| - r^g}{k} \right\rangle^n \operatorname{sign}\left(\tau^g - x^g\right), \tag{4}$$

the isotropic hardening rule is given by

$$r^g = r_o + q \sum_r H^{gr} \left(1 - e^{-bv^r}\right) \text{ with } \dot{v}^r = |\dot{\gamma}^r|, \tag{5}$$

and the kinematic hardening is governed by the equation, valid with the isothermal assumption:

$$\dot{x}^g = |\dot{\gamma}^g| \left(c \operatorname{sign}(\dot{\gamma}^g) - d\, x^g\right) - \left(\frac{|x^g|}{M}\right)^m \operatorname{sign}(x^g). \tag{6}$$

We call total cumulated slip in a slip family G the quantity $\sum_{g \in G} v^g$, where v^g is the cumulated slip of the slip system g.
The resolved shear stress is obtained for each system g by the classical Schmid law

$$\tau^g = \frac{1}{2} \left(\underline{\mathbf{l}}^g \otimes \underline{\mathbf{n}}^g + \underline{\mathbf{n}}^g \otimes \underline{\mathbf{l}}^g \right) : \underset{\sim}{\sigma}. \tag{7}$$

The material has an elastic behaviour with cubic symmetry until the difference between the resolved shear stress τ^g and the kinematic hardening variable x^g reaches the critical shear stress r^g of the slip system g. The interaction matrix H^{gr} allows to take into account the self hardening and the cross hardening between the different systems. An additional term has been introduced in the kinematic hardening law in order to account for the effect

of the static recovery present at high temperature. This term depends on two material parameters M and n.
The model is implemented in the finite element program ZéBuLoN [Méric et al., 1991b], [Besson et al., 1998], [Besson and Foerch, 1998].

3 Identification of the model for SC16 at different temperatures

3.1 Presentation of the material

The efficiency of gas turbines for power generation relies in part on temperature resistance of turbine blade and vane materials. The composite structure and the absence of grain boundaries allow the single crystal to have better creep-fatigue resistance than its conventionally cast polycrystalline counterparts.
Fig. 1 shows a typical morphology of SC16 γ' precipitates. The non homogeneous microstructure is obtained after heat treatment, see table 6, and consists of 35 % cuboidal γ' particles with a mean edge length of 450 nm and about 5 % spherical particles with a mean diameter of 80 nm [Jiao et al., 1996].
The chemical composition of the alloy is given in table 7. The single crystal develops a simple unidirectional dendritic structure and also exhibits significant interdendritic porosity. The initial orientation of each specimen was checked by the Laue back-reflection X-ray technique and are given in the standard triangle of the stereographical projection in the appendix A (Figs. 98, 99 and 100) in the standard triangle of the stereographical projection.

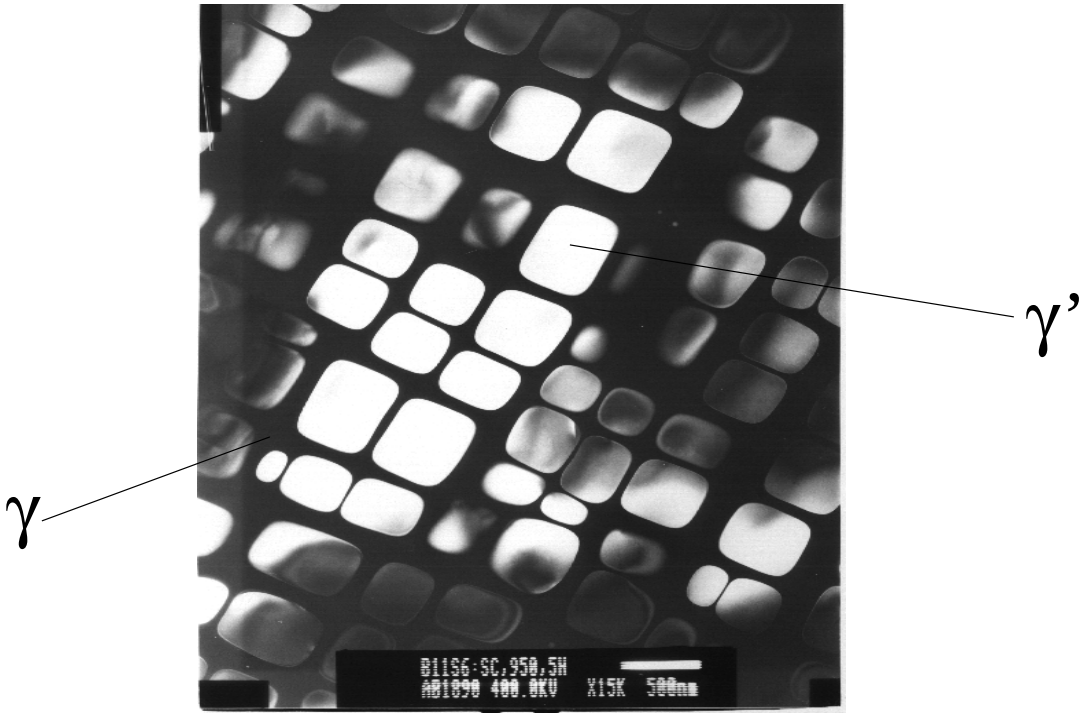

Figure 1: Microstructure of SC16 after heat treatment at 950°C.

3.2 Methodology and results

3.2.1 Elasticity constants

Two techniques can be used to determine the elastic constants of single crystalline superalloys [Olschewski, 1997]. A method based on resonance measurements allows to identify dynamic or adiabatic elasticities [Han, 1995]. The alternative method is to obtain with tensile and torsion tests the static or isothermal elastic parameters. However it has been assessed that the differences between both set of constants are negligible if one stays in the framework of engineering applications. [Olschewski, 1998] has shown how experimental errors and the specimen orientation used in the tensile and torsion tests influence the accuracy of the cubic elastic constants.

For a given temperature two monotonic tension tests in different directions and one torsion test are required to obtain three linear independent equations in which the elastic constants are the unknowns. At 650 and 950°C we followed the static method because one torsion test on tubular specimen was available. Unfortunately it was not the case for 850°C and an approximate solution has been found at this temperature from an initial set of constants given in the literature [Han, 1995] for another nickel base single crystal superalloy SRR99. At room temperature we have taken the parameters already given by [Forest, 1996] for the same material. Table 1 summarizes the values of elastic constants at various temperatures used in this work.

3.2.2 Calibration of the viscoplastic constants at low and high temperature

From a large experimental data base (tests performed at the BAM for different orientations, strain rates and strain ranges) we calibrated the viscosity (k,n), the hardening parameters (c,d,r_o,q,b) and the constants of the static recovery (M,n) for each slip system family with a classical technique of numerical optimization process [Cailletaud and Pilvin, 1993] applied to a volume element of the crystalline material.
The identification is first performed on one hand on [001] specimens, on the other hand on [111] specimens, since they respectively produce pure octahedral and predominant cubic slip. The material parameters can be determined independently for each family. The other tests are then introduced, and finally the whole data base is included for polishing the identification procedure.

Previous studies [Poubanne, 1989] have shown that the most pertinent interaction matrix is a diagonal. Anyway, only a low cyclic softening is generally present in the material, so that the corresponding terms generally remains negligible. The comparison between experimental results and the corresponding numerical simulations is given Figs. 2 to 10. For the Low-Cycle Fatigue tests we have plotted the experimental and simulated values for the initial and the stabilized loops.

For 20°C , only monotonic tension tests were available. At these low temperatures the influence of strain rate is negligible, see for example the tests for $10^{-2}\ s^{-1}$ and $10^{-3}\ s^{-1}$

of a $\langle 001 \rangle$ specimen in Fig. 2. Thus the parameter set of each slip system family can be identified independently from the tests performed with a strain rate of $10^{-3}\ s^{-1}$ and with specimens which are $\langle 001 \rangle$ and $\langle 111 \rangle$ oriented. At 20°C the identification is satisfying, see Fig. 2, whereas at 650°C the initial isotropic hardening of the cubic slip system family is a little too low to describe accurately the experimental values, see Fig. 3 (right). Indeed we cannot increase this radius if we want a good description of the global curve shear stress-shear strain of a monotonic torsion test on a $\langle 001 \rangle$ tubular specimen, see Fig. 4. The axis of the specimen coincides approximately with the crystallographic axis [001] of the crystal. Only cubic slip systems are activated according to the model and four zones of concentration of the equivalent inelastic strain are expected along the circumference and opposite to the secondary crystallographic directions [100] and [010]. The contour plot of the total cumulated slip of the cubic slip system in the cross section of the tubular specimen shows that the soft zones, the black ones on the Fig. 4, are a little rotated from the ideal position since the deviation of the single crystal has been taken into account. Local measurements of similar tests at room temperature have confirmed such inhomogeneous strain and stress distribution along the circumference of the tube for single crystal superalloy [Forest et al., 1996].

An analysis of the monotonic and cyclic behaviour of SC16 smooth specimens at high temperature, such as 850 and 950°C , shows the necessity to take into account the local kinematic hardening and the viscosity. These observations confirm the ones already done for other single crystal nickel base superalloys [Méric et al., 1991a], [Hanriot, 1993].
At 850°C two cyclic tests for the orientation $\langle 001 \rangle$, the same strain rate $10^{-3}\ s^{-1}$ but a different strain range, allow us to determine the kinematic hardening for the octahedral slip system, see Fig. 6. The calibration is good for the small strain range (1.2%) and acceptable for a larger strain range (2%). The agreement between the simulation and the experiment of the tension tests is not as good as for 20°C due to the larger number of tests, see Fig. 5. Note the important viscosity of the material at this temperature.
At 950°C we have extended the experimental data base to creep tests. Therefore we have the largest experimental data base with 18 tests. Five tension tests for different strain rates have allowed to propose an acceptable parameters set for the viscosity of the octahedral slip system family, see Fig. 7. In addition to the isotropic and kinematic hardening parameters of the cubic one, the parameters characterizing viscosity are obtained from three LCF tests, given Fig. 8, with specimens which are $\langle 011 \rangle$ and $\langle 111 \rangle$ oriented. The agreement is good for the orientation $\langle 001 \rangle$ and the simulation is not far from the experimental values for $\langle 011 \rangle$ and $\langle 111 \rangle$. From the creep tests tests given Fig. 9, 10 the constants of the static recovery have been calibrated for both slip system family. Only one creep test (R1604113 from Fig. 10) for the orientation $\langle 111 \rangle$ is not correctly simulated.
The viscoplastic constants of SC16 at different temperatures are given in tables 2, 3, 4 and 5. Due to the negligible viscosity at low temperature the constant k (respect. n) is relatively low (respect. high) for 20 and 650°C whereas in contrary a high (respect. low) value of k (respect. n) characterize the important viscosity of the material above 850°C.

4 Conclusion

From a large experimental data base of nickel base superalloy SC16 we have calibrated a crystallographic viscoplastic model at four characteristic temperatures. Unfortunately because of the lack of cyclic tests at low temperature we do not have the parameters set of the material to simulate cyclic loading at room temperature. On the other hand the great number of tension, cyclic and creep tests identified at 950°C provide a realistic set of constants for typical loading conditions, such as a full power operation mode for instance, in an industrial gas turbine.

As far as we are concerned we only consider in the following the cyclic operating mode of the turbine at this temperature. Moreover we will investigate in the next section how stress raisers could affect the life of blades under isothermal loading.

T °C	C_{1111} GPa	C_{1212} GPa	C_{1122} GPa	$E_{[001]}$ GPa	$G_{[001]}$ GPa
20	272	184	118	124	118
650	253	185	95	97	95
850	222	160	91	88	91
950	208	153	86	78	86

Table 1: Elasticity constants of SC16.

Slip system Family	k $\mathrm{MPa}^{1/n}$	n	r_o MPa
Octahedral	90	20	280
Cubic	50	15	400

Table 2: Material constants of SC16 at 20°C.

Slip system Family	k $\mathrm{MPa}^{1/n}$	n	r_o MPa
Octahedral	90	5.0	300
Cubic	70	18	225

Table 3: Material constants of SC16 at 650°C.

Slip system Family	k $\mathrm{MPa}^{1/n}$	n	r_o MPa	c MPa	d
Octahedral	889	5.0	8.8	200000	1536
Cubic	541	2.7	160	96660	4553

Table 4: Viscoplastic constants of SC16 at 850°C.

Slip system Family	k $\mathrm{MPa}^{1/n}$	n	r_o MPa	q MPa	b	c MPa	d	M $\left(\mathrm{MPa}^{m-1}s\right)^{1/m}$	m
Octahedral	700	4.7	4.6	3.9	3.7	96536	1050	$3.0\ 10^7$	4.9
Cubic	1172	2.4	17.3	-4.4	2.7	77081	1056	$1.2\ 10^7$	9.9

Table 5: Viscoplastic constants of SC16 at 950°C.

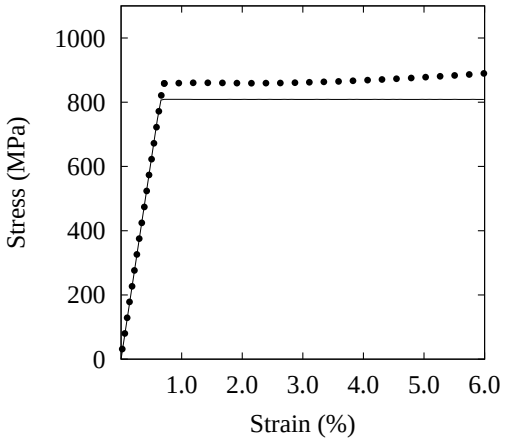

L16018E5, $\langle 001 \rangle$, $\dot{\varepsilon} = 10^{-2}\, s^{-1}$.

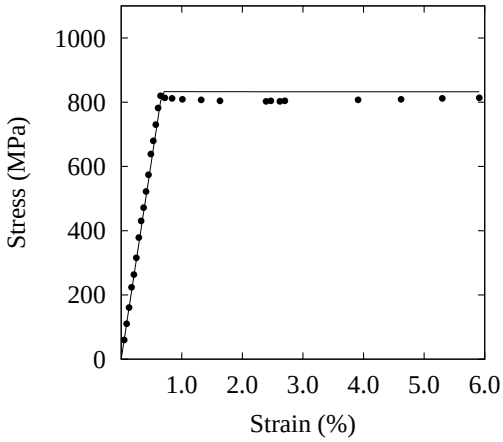

L1602741, $\langle 001 \rangle$, $\dot{\varepsilon} = 10^{-3}\, s^{-1}$.

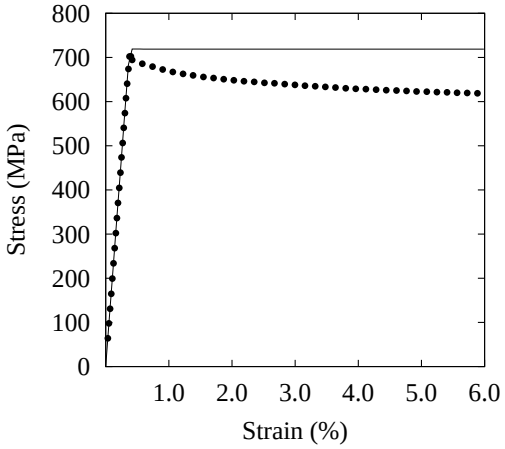

R1606005, $\langle 011 \rangle$, $\dot{\varepsilon} = 10^{-3}\, s^{-1}$.

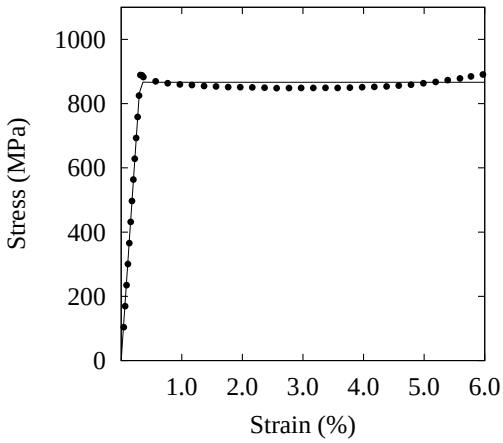

R1606104, $\langle 111 \rangle$, $\dot{\varepsilon} = 10^{-3}\, s^{-1}$.

Figure 2: Simulated and experimental tension tests on SC16 smooth bulk specimens at 20°C (• exp, − sim).

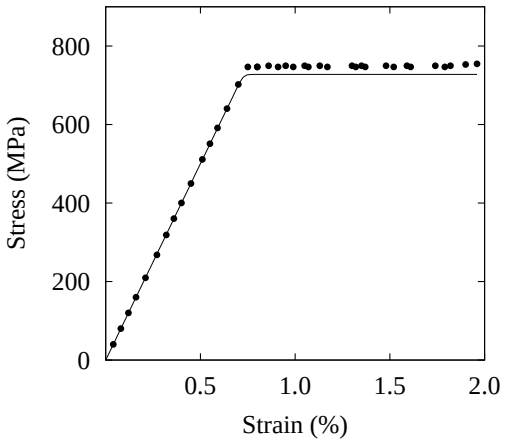

L1602732, $\langle 001 \rangle$, $\dot{\varepsilon} = 10^{-3}\, s^{-1}$.

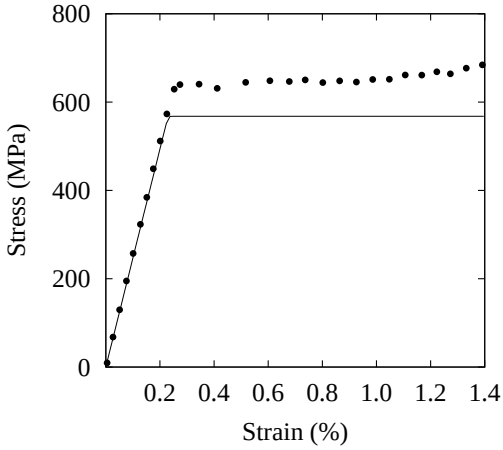

L1609212, $\langle 111 \rangle$, $\dot{\varepsilon} = 10^{-3}\, s^{-1}$.

Figure 3: Simulated and experimental tension tests on SC16 smooth bulk specimens at 650°C (• exp, − sim).

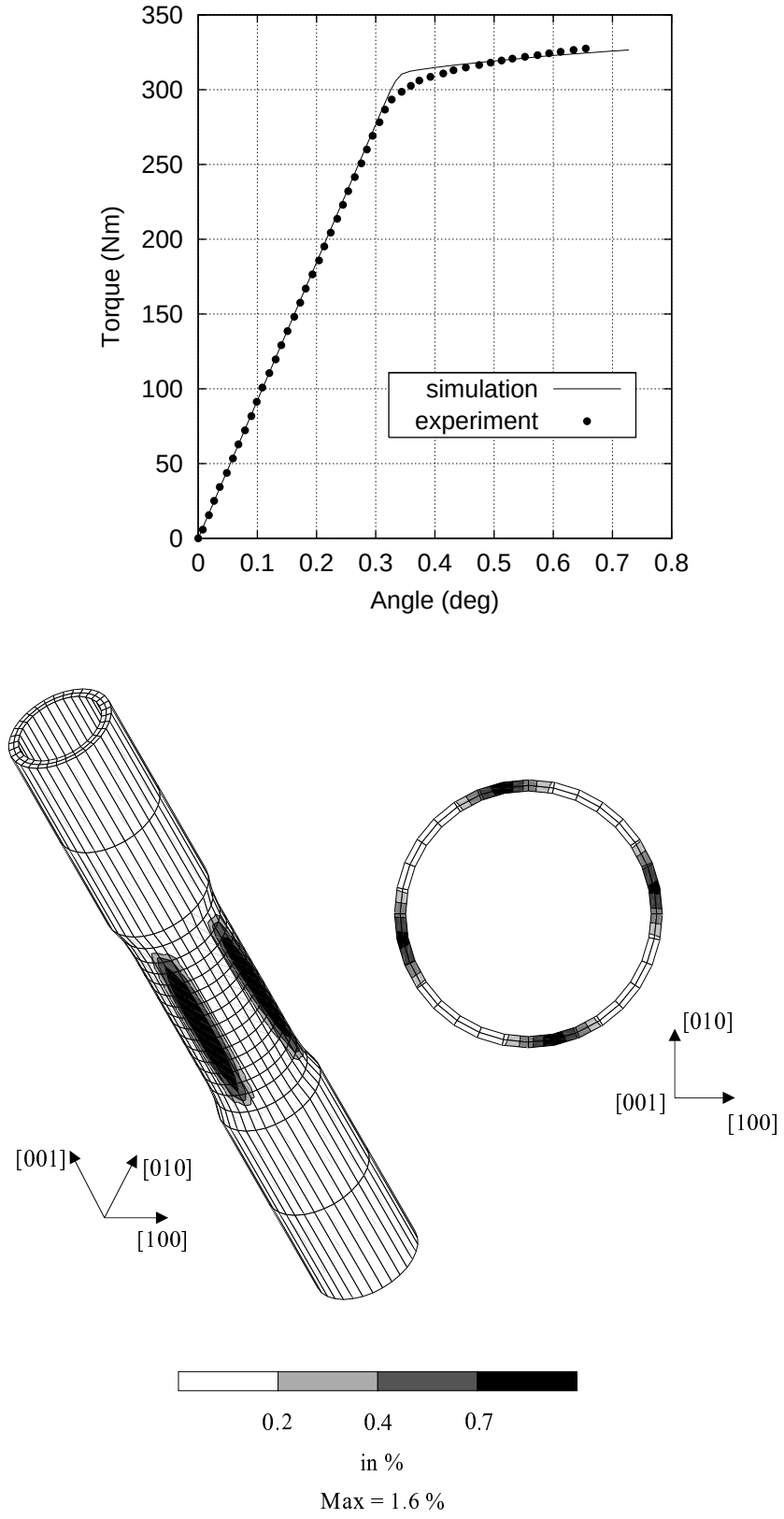

Figure 4: Global curve torque versus angle (above) and contour plot of the total cumulated cubic slip on a SC16 tubular specimen (below) of a monotonic torsion test at 650°C (● exp, − sim).

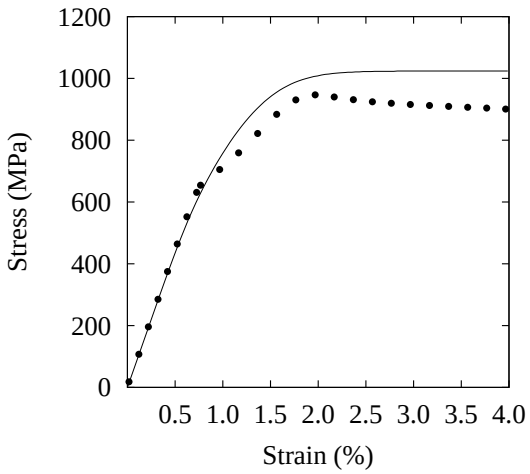

L1601853, $\langle 001 \rangle$, $\dot{\varepsilon} = 10^{-2}\ s^{-1}$.

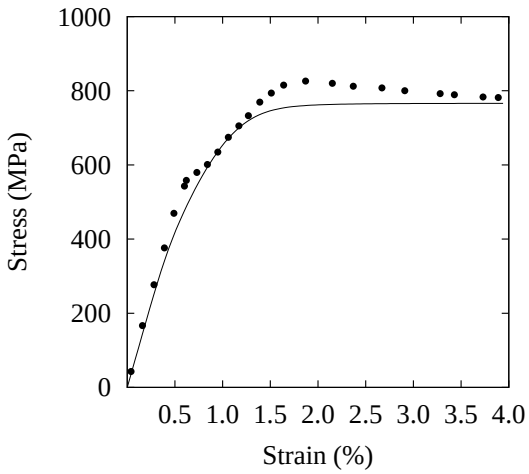

L1602722, $\langle 001 \rangle$, $\dot{\varepsilon} = 10^{-3}\ s^{-1}$.

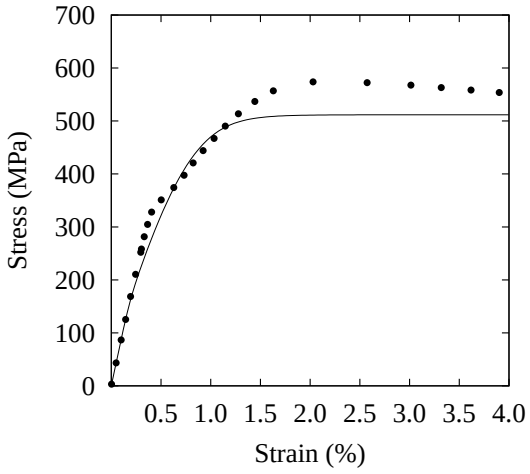

L16018J1, $\langle 001 \rangle$, $\dot{\varepsilon} = 10^{-5}\ s^{-1}$.

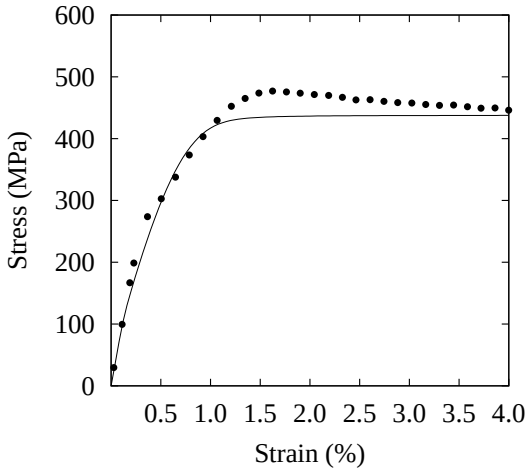

L16018D6, $\langle 001 \rangle$, $\dot{\varepsilon} = 10^{-6}\ s^{-1}$.

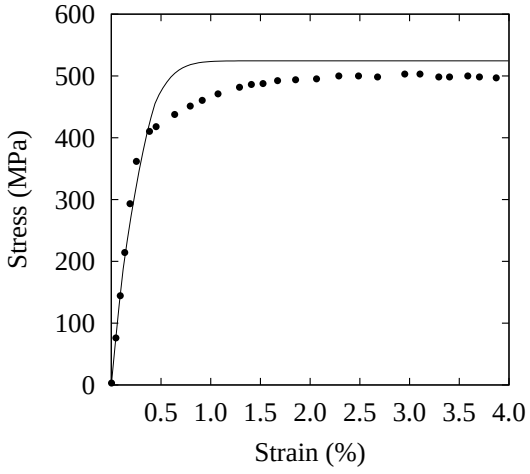

L1609248, $\langle 011 \rangle$, $\dot{\varepsilon} = 10^{-5}\ s^{-1}$.

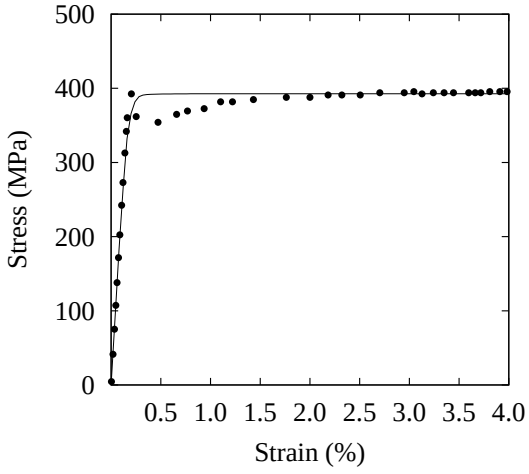

L1609241, $\langle 111 \rangle$, $\dot{\varepsilon} = 10^{-5}\ s^{-1}$.

Figure 5: Simulated and experimental tension tests on SC16 smooth bulk specimens at 850°C (● exp, – sim).

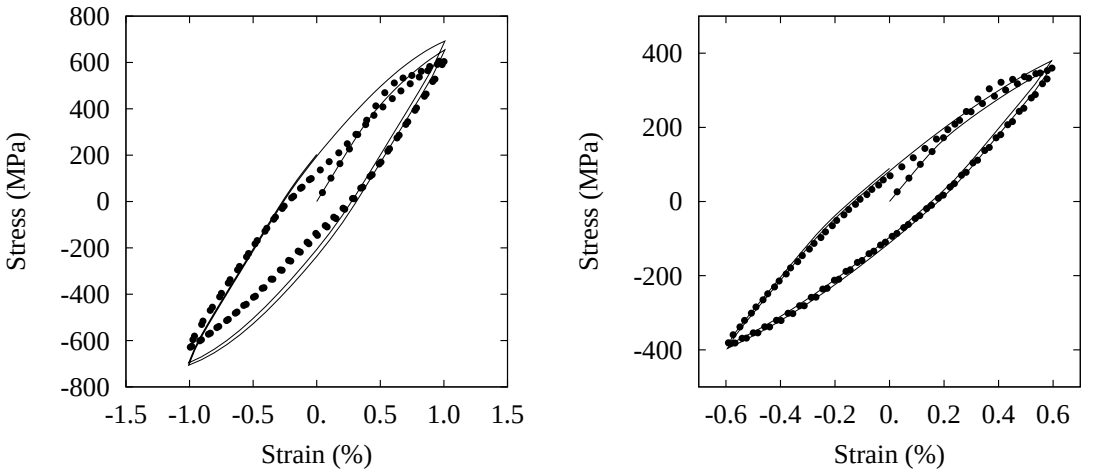

L16018N6, $\langle 001 \rangle$, $\dot{\varepsilon} = 10^{-3}\, s^{-1}$. L16018B2, $\langle 001 \rangle$, $\dot{\varepsilon} = 10^{-3}\, s^{-1}$.

Figure 6: Simulated and experimental Low-Cycle Fatigue tests on SC16 smooth bulk specimens at 850°C (● exp, – sim).

Time (h)	T (°C)	Environment
3	1260	vacuum
4	1100	vacuum
24	850	air

Table 6: Heat treatment of SC16.

	Cr	Al	Ti	Ta	Mo	Fe	C	Ni
Mass Fraction (%)	15.4	3.5	3.5	3.6	2.8	0.3	< 0.005	balance

Table 7: Chemical composition of SC16.

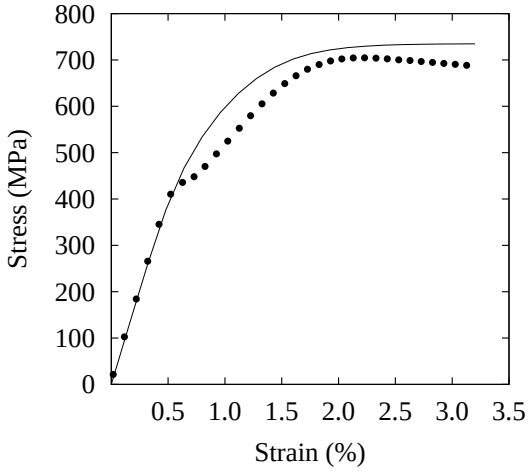

L16018C6, $\langle 001 \rangle$, $\dot{\varepsilon} = 10^{-2}\ s^{-1}$.

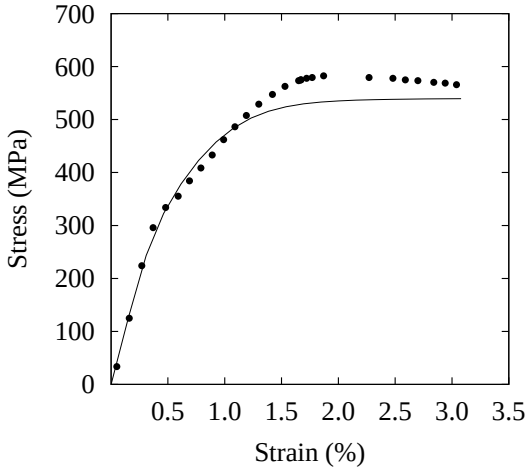

L1602721, $\langle 001 \rangle$, $\dot{\varepsilon} = 10^{-3}\ s^{-1}$.

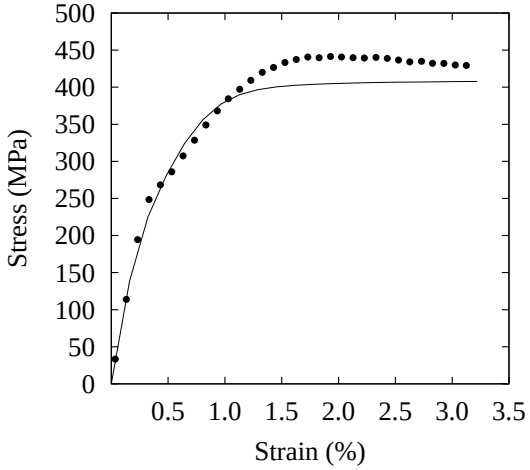

L16018F1, $\langle 001 \rangle$, $\dot{\varepsilon} = 10^{-4}\ s^{-1}$.

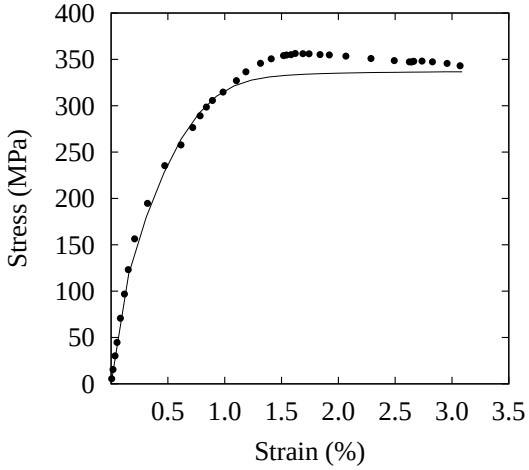

L16018F5, $\langle 001 \rangle$, $\dot{\varepsilon} = 10^{-5}\ s^{-1}$.

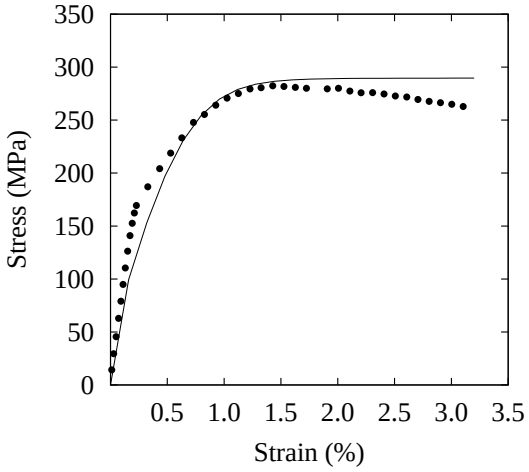

L16018N4, $\langle 001 \rangle$, $\dot{\varepsilon} = 10^{-6}\ s^{-1}$.

Figure 7: Simulated and experimental tension tests on SC16 smooth bulk specimens at 950°C (● exp, – sim).

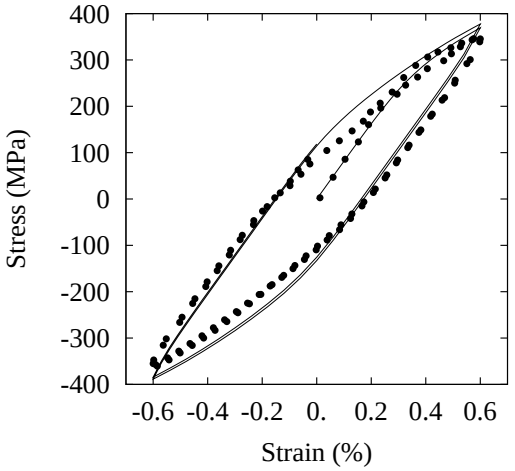

L1602783, $\langle 001 \rangle$, $\dot{\varepsilon} = 10^{-3}\ s^{-1}$.

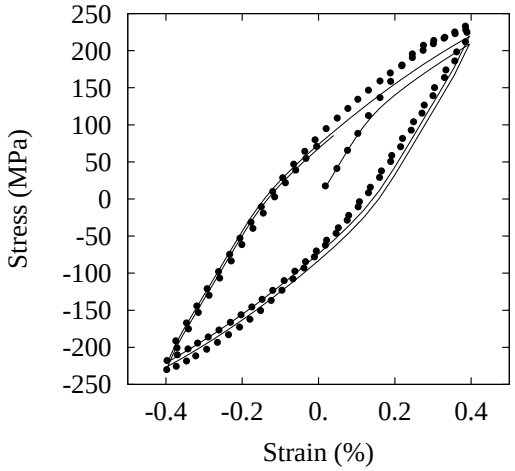

L1601831, $\langle 001 \rangle$, $\dot{\varepsilon} = 10^{-5}\ s^{-1}$.

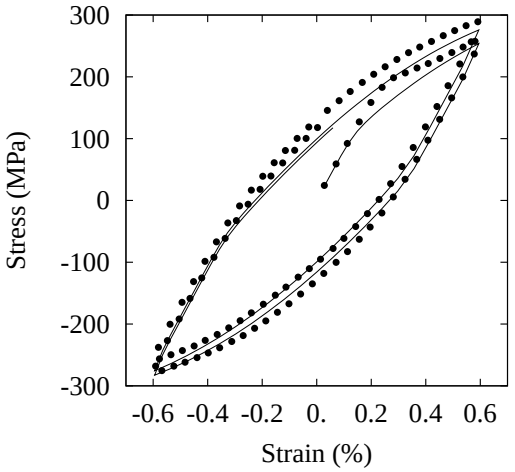

L16018l6, $\langle 001 \rangle$, $\dot{\varepsilon} = 10^{-5}\ s^{-1}$.

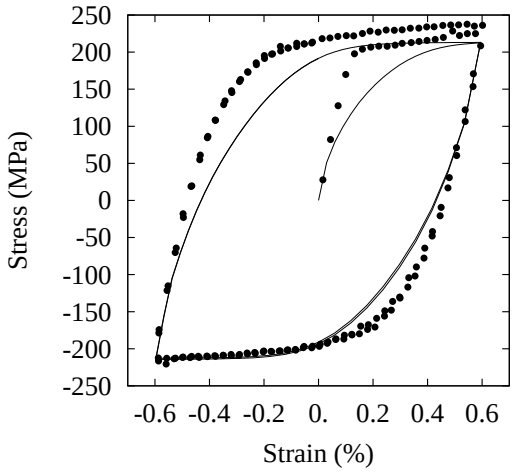

R1606105, $\langle 111 \rangle$, $\dot{\varepsilon} = 10^{-5}\ s^{-1}$.

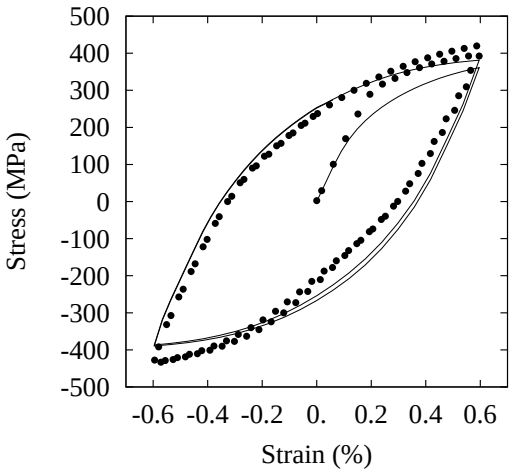

R1604013, $\langle 011 \rangle$, $\dot{\varepsilon} = 10^{-3}\ s^{-1}$.

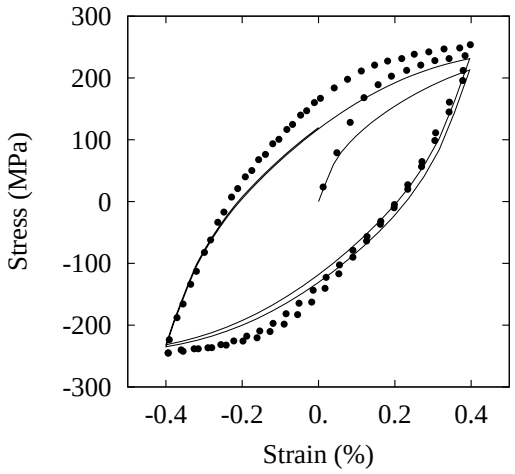

R1604902, $\langle 011 \rangle$, $\dot{\varepsilon} = 10^{-5}\ s^{-1}$.

Figure 8: Simulated and experimental Low-Cycle Fatigue tests on SC16 smooth bulk specimens at 950°C (● exp, – sim).

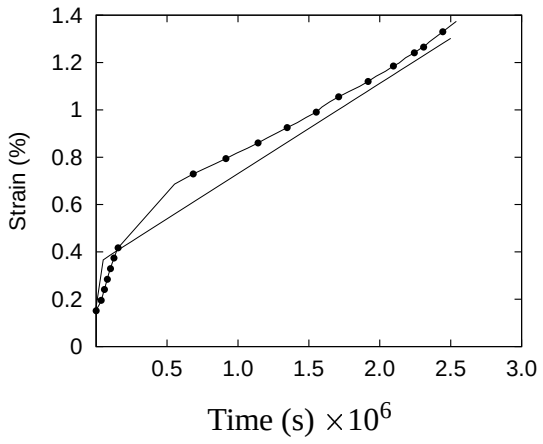

K1602662, $\langle 001 \rangle$, loading: 135 MPa.

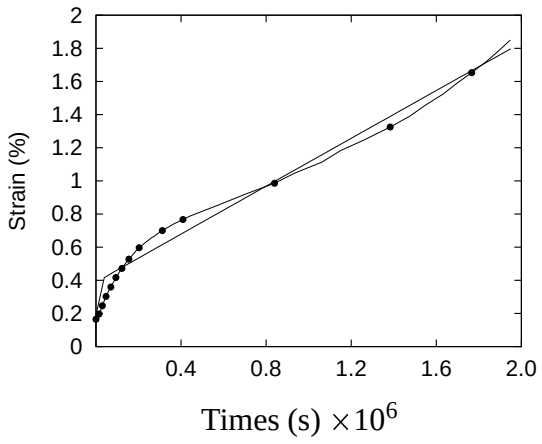

K1602668, $\langle 001 \rangle$, loading: 150 MPa.

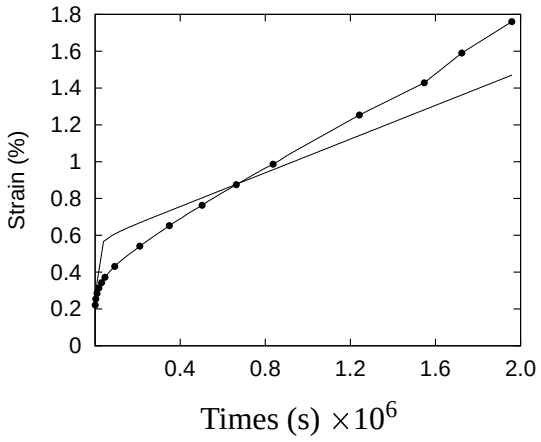

K1602675, $\langle 001 \rangle$, loading: 200 MPa.

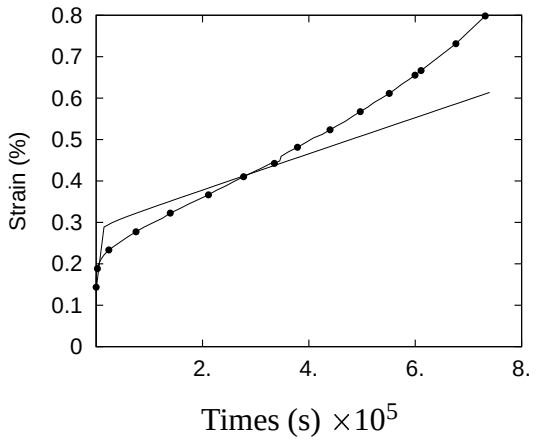

R1604608, $\langle 011 \rangle$, loading: 150 MPa.

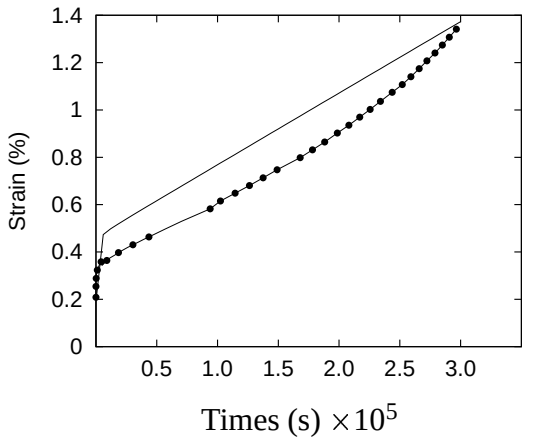

R1604020, $\langle 011 \rangle$, loading: 200 MPa.

Figure 9: Simulated and experimental creep tests on SC16 smooth bulk specimens at 950°C (● exp, – sim).

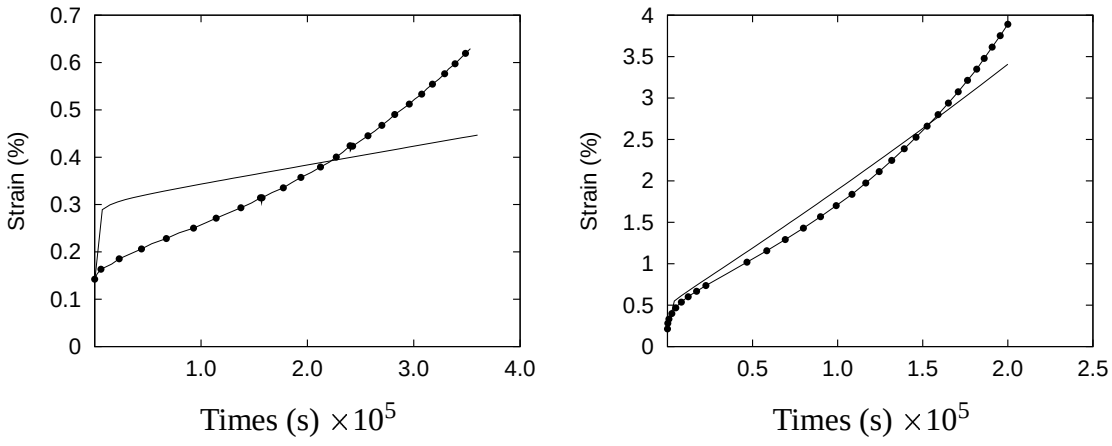

R1604113, $\langle 111 \rangle$, loading: 150 MPa. R1604125, $\langle 111 \rangle$, loading: 200 MPa.

Figure 10: Simulated and experimental creep tests on SC16 smooth bulk specimens at 950°C.

Part III
Analysis of Low-Cycle Fatigue at notches in a single crystal superalloy at high temperature

1 Introduction

The aim of the work covered by this chapter is to develop assessments tools for the life prediction of uncoated single crystal superalloy structural components such as gas turbine blades operating under fatigue loading conditions.

In particular gas turbine blades are subjected to severe and complex thermal loading conditions which have been increased these last years in order to raise the turbine inlet temperature. Thus it was necessary on one hand to introduce advanced material with high temperature capability and in the other hand to design efficient cooling air channels to reduce the effects of thermal gradient toward the wall of the blade, see Fig. 11. Unfortunately these channels create stress raisers and especially their intersection with the outer or inner surfaces of the component. Indeed such regions lead often to fatigue crack initiating due to high localization of cyclic plasticity. Moreover the presence of notches in the component leads to three principal effects:

- A high stress concentration.
- A stress gradient behind the notch.
- A tridimensional state of stress.

From engineering design practice point of view lifetime prediction of gas turbine hot section components are still based on thermo-elastic finite element analysis [Sato et al., 1985], [Guédou and Honnorat, 1993]. Inelastic calculations of high temperature components are very exceptional because of high computational costs and difficulties related to the identification of viscoelastic constitutive models. A life prediction procedure based on the Neuber's rule has been successfully used for isotropic high-temperature alloys [Chaudonneret and Chaboche, 1986]. The local inelastic behaviour of the most critical part of the structure is assessed from the elastic stress-strain state by using Neuber's hyperbola [Neuber, 1961]. Then thermal fatigue is predicted by using the assessed local inelastic strain and corresponding thermal fatigue data. Finally the prediction is confirmed through a comparison with experimental data.
For multiaxial state of stress the results are still acceptable if one uses the second invariant of the stress and strain tensor deviator [Chaudonneret, 1994]. A similar method based on an energetic approach gives an acceptable approximate solution for cyclic as well as for

creep loading [Moftakhar and Glinka, 1992].

The same lifetime assessment rule based on the classical Neuber's law has been applied for low cycle fatigue on nickel base SC16 single crystal superalloy at high temperature [Bischoff-Beiermann, 2000]. Unfortunately the crack initiation life of such a structural engineering material is very conservative.
As far as we are concerned we only try to assess the crack initiation life in the framework of low cycles fatigue loading at a relatively high strain rate and high temperature for the same alloy [Boubidi and Sievert, 2000]. Thus oxidation, corrosion and erosion phenomena have been neglected in this work, but they have to be taken into account at lower strain rates [Gallerneau, 1995, Fleury, 1991].
I will propose in the next sections two methods for the lifetime modelling. The first one is based on the anisotropic behavior of single crystal which should influence the crack initiation mechanism. The second one introduces a statistical approach depending on the defects distribution responsible for the failure.

This analysis of low cycle fatigue at notches in single crystals is experimental and numerical. In addition to a considerable data base available in a previous gas turbine project at the BAM [Wedell et al., 1996] for the single crystalline model material SC16 especially at $950°C$, several tests on notched specimens have been carried out.
The results, presented in the next section, confirm the physical bases assumed in our lifetime assessment rules and allow to valid these numerical tools.

2 Low-Cycle Fatigue tests on SC16 notched specimens

2.1 Material and experimental procedure

Three cast rods samples in SC16 (see the Section 3.1 in the previous part for the characteristics of the alloy) were provided by Thyssen Guss AG (tests 1, 2 and 3, see in table 8), whereas the others were cast by Howmet Ltd. In order to check if the two alloys have the same behavior, at least in Low-cycle Fatigue, we have performed several uniaxial LCF tests with zero mean strain on SC16 (provided by Howmet) bulk smooth specimens for the orientations $\langle 001 \rangle$, $\langle 011 \rangle$ and $\langle 111 \rangle$. Then we have put the experimental values in the fatigue diagram obtained from the material of Thyssen in the same conditions of testing, see Fig. 12. Finally we have observed no difference between the LCF behavior of the single crystal SC16 of each supplier.

The exact orientation of the rods given by the manufacturers was checked by standard X-ray diffraction technique after machining and electropolishing the specimens. Figure in Appendix B shows that the real orientation of each specimens is not far from the ideal one, except for one "$\langle 011 \rangle$" oriented specimen. The deviation is never higher than $5°$ for the specimens oriented near $\langle 001 \rangle$.

In order to study the effect of the stress concentration on low cycle fatigue for single crystals, we chose the geometry of the notched specimen given Fig. 13 in accordance with the ASTM norm.
The root of the V-shaped notch had three different radii, 0.2 mm, 0.5 mm and 1 mm, see Fig. 13. They allow us to estimate the influence of multiaxial proportional loading on fatigue behaviour. Moreover the last one is of the order of magnitude of the notched radius of the turbine blade air cooling channels [Bischoff-Beiermann B., 1999]. This geometry allows us to have a stress-concentration factor between 2.1 and 2.6.

A prior measure at room temperature of the negligible bending torque allows to ensure that the axis of loading coincides with the center line of the specimen. A picture of the testing equipment is given in Fig. 14. A three zone AC furnace has been used to control the homogeneous temperature along the axis of the specimen. At 950°C, in air, constant strain amplitude fatigue tests with zero mean strain were performed. The displacement measured by the extensometer with a 21.5 mm gauge length over the notches was ± 0.3225 mm, which corresponds to a "global strain amplitude" of $\pm 0.15\%$. The strain rate was $10^{-3}\ s^{-1}$ for all the tests.

Usually we define the fatigue life N_f as the number of cycles showing a 5% stress drop in load with respect to decreasing regression straight-lines including points behind saturation (see table 8).
Except for the test 2, which was performed until rupture and an interrupted one, test 5, we stopped the tests after 10% stress drop in tension. Some photomicrographs of the surface of these specimens were taken. Then the specimens tested again to failure at room temperature.
Some micrographs of their rupture surface were taken in order to characterize the crack initiation and crack growth mechanisms. The test 5 was interrupted after successively 54, 236 and 406 cycles. We examined the surface of the notch with scanning electron microscope after each interruption to detect a crack. This test is particularly interesting to quantify the crack length and depth at the notch which produces the stress drop.

2.2 Experimental results

2.2.1 Metallographic observations

The fractographic observations of near $\langle 001 \rangle$ notched specimens (Figs. 15, 16, 17) with a scanning electron microscope (SEM) show two main cracks, perpendicular to the external load, but indeed they arose not directly at the notch root, instead they are shifted a little away from there. Figure 16 shows that each main crack on the surface grows not perfectly straight. Thus it is reasonable to assume that cracks initiate or growth in a scatter band of about $400\,\mu$m according to Fig. 24 which is the larger value after the investigation of the whole circumference.
For near $\langle 011 \rangle$ oriented specimen the main crack seems to be concentrated at the notch root, see Fig. 19. On one face of the $\langle 111 \rangle$ oriented specimen, see Fig. 20 above, the main crack is perfectly at the notch root. On the other hand a crack occurs a little above

this one, see Fig. 20 below. One can observe, especially in the case of the tests 3 and 4 an oxidised layer which is commonly met for single crystals at high temperature on air [Defresne and Rémy, 1990], [Mück, 1997].
The "square shape" of the crack front (Figs. 21, 22) allows us to assume that the cracks do not grow isotropically in the depth. Moreover the maximum crack depth seems to be close to the secondary crystallographic axis [010].

The interrupted test 5 gives more information about the cracking mechanism and the crack depth which corresponds to the number of cycles to failure of our criterion of the $\langle 001 \rangle$ notched specimens. Fig. 25 shows that the interruptions do not influence too much the evolution of the maximum axial force in comparison with the reference.
One can clearly see in Fig. 26 the dark zones near the surface rupture which are the crack depths after each interruption. Moreover we have drawn the secondary crystallographic axis on the micrograph of the surface rupture. Unfortunately no precise conclusion could be drawn about the correlation between the position of the crack initiation along the circumference of the specimen and the orientation of the crystal.
According to Figs. 23, 27, 18, 28 and 29 and as already observed for such single crystal nickel base superalloys which contains a low quantity of carbon and for this relatively low strain rate, the cracks start from the casting pores localised near the surface ([Defresne and Rémy, 1990], [Defresne, 1989], [Fleury, 1991]).
In Fig. 29 we observe a hole near the surface but it is not possible to know if it is really an initiation site. Note the small pore with approximately a mean diameter equal to $10\,\mu$m left to this hole and near the surface. The situation is clearer with the local observation of the vicinity of the surface in the case of the interrupted test, see Fig. 27. We have in this zone three crack initiation sites near the surface. Moreover we can measure from this picture a crack depth of about 0.4 mm which is our characteristic crack depth for the lifetime because the test has been stopped not far from the number of cycles to failure assessed with the test L1610609, see table 8. If we observe more precisely each crack initiation site, see Figs. 18, 28 and 29, it is reasonable to assume that the hole near the surface was initially a pore since its mean size is about $20\,\mu$m.

2.2.2 Fatigue life results

A lot of axial strain controlled LCF tests at high temperatures were already carried out at the BAM on SC16 smooth specimens [Wedell et al., 1996]. Despite the relatively large scatter, the fatigue diagram at 950 °C and $10^{-3}\ s^{-1}$ strain rate, Fig. 46, shows essentially no dependence of the lifetime on the orientation of the single crystal at the same total stress range. Between the doted lines the number of cycles to failure are under a factor 3 in comparison with the corresponding value of the line obtained after fitting. Of course, the stresses itself arise in dependence on the crystal orientation. The same observations have been made for AM1 single crystal superalloy by [Fleury, 1991]. For example, at the same total strain range, the lifetime is lower for near $\langle 011 \rangle$ orientation than for near $\langle 001 \rangle$ orientation, but the stress range is higher at $\langle 011 \rangle$, see Fig. 8. Thus, we obtain within a scatter band a very simple assessment rule, see Fig. 46. It is noteworthy that the inelastic strain range increases too, at $\langle 011 \rangle$ orientation due to the higher elastic stiffness (Young's modulus) in this direction.

The number of cycles to failure of the notched specimens are given in table 8. The maximum equivalent Mises stress range at the notch is calculated by FE method for the stabilized cycle.

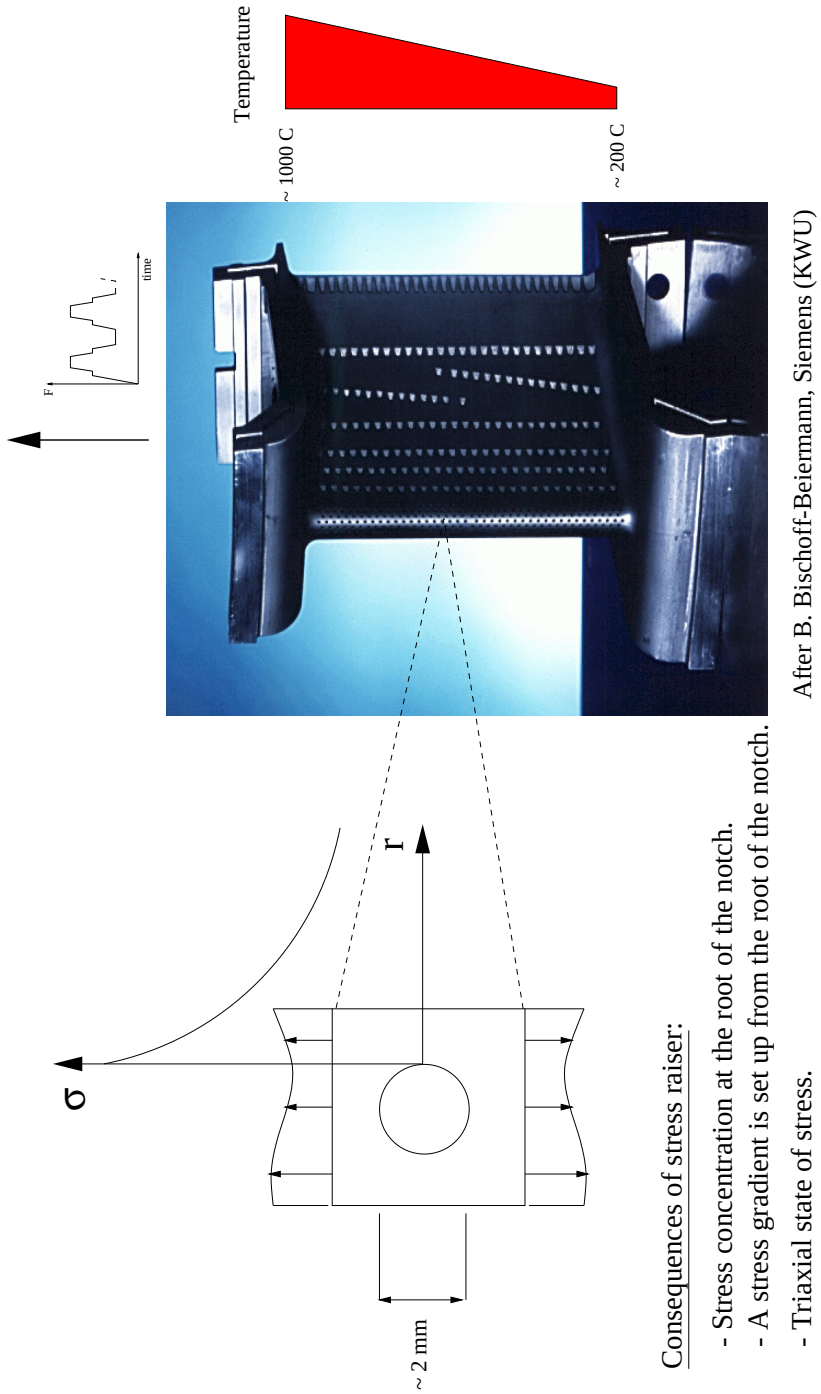

Figure 11: Notch effects due to the presence of the cooling air channels in turbine blades.

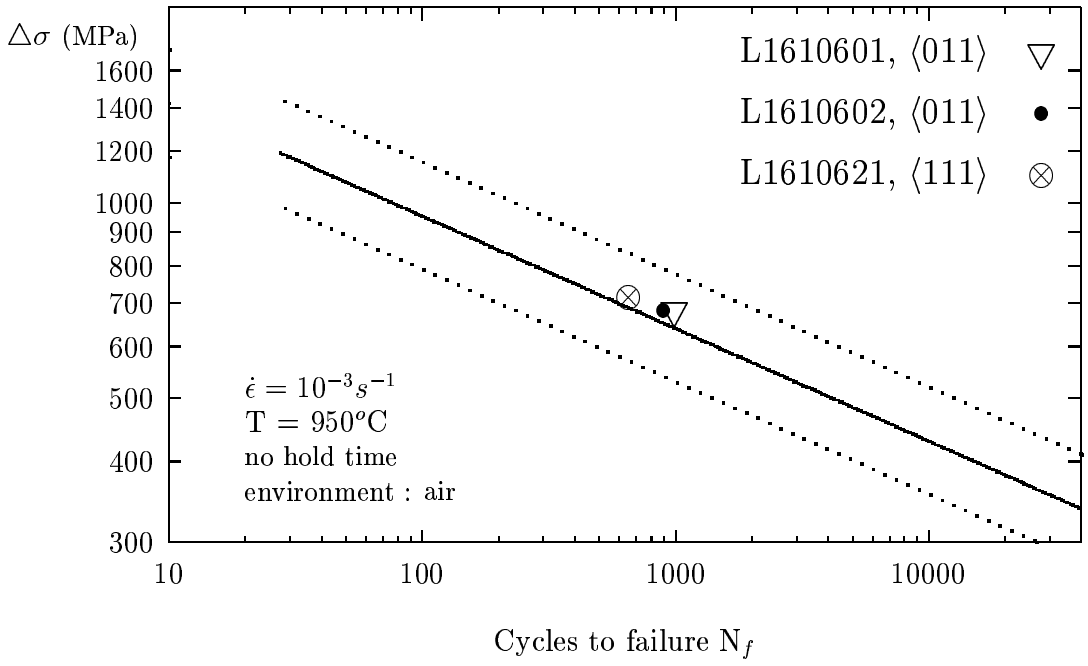

Figure 12: Fatigue diagram of SC16 on bulk smooth specimens for different orientations at 950°C. The line is fitted to the data of the material provided by Thyssen, whereas the symbols are the values obtained from the single crystal cast by Howmet.

Spec.	Test	Notched radius (mm)	Orientation	$\triangle\sigma_{\text{Mises}}$ (MPa)	N_f
1	L1604424	0.2	⟨001⟩	1508	120
2	L1604423	0.2	⟨001⟩	1508	127
3	L16018L5	0.2	⟨001⟩	1508	131
4	L1610609	1.0	⟨001⟩	966	583
5	L1610617	1.0	⟨001⟩	966	$\oplus$
6	L1610603	1.0	⟨011⟩	1286	120
7	L1610604	1.0	⟨011⟩	1286	120
8	L1610623	1.0	⟨111⟩	1154	80
9	L1610624	1.0	⟨111⟩	1154	75

Table 8: LCF tests on SC16 circumferentially notched round specimens at 950°C. $\triangle\sigma_{\text{Mises}}$ denotes the maximum Mises stress range in the notch for the stabilized cycle. $\oplus$ interrupted test.

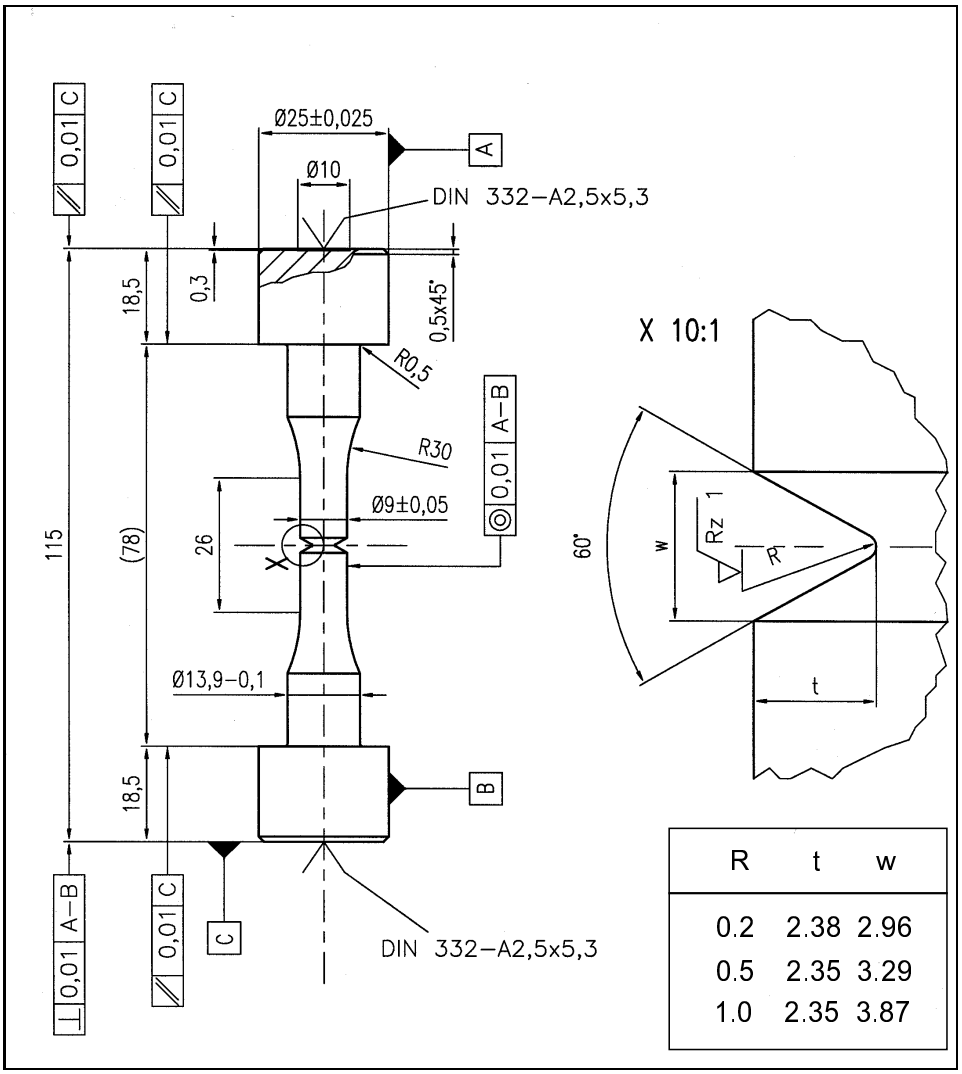

Figure 13: Geometry of the notched specimens.

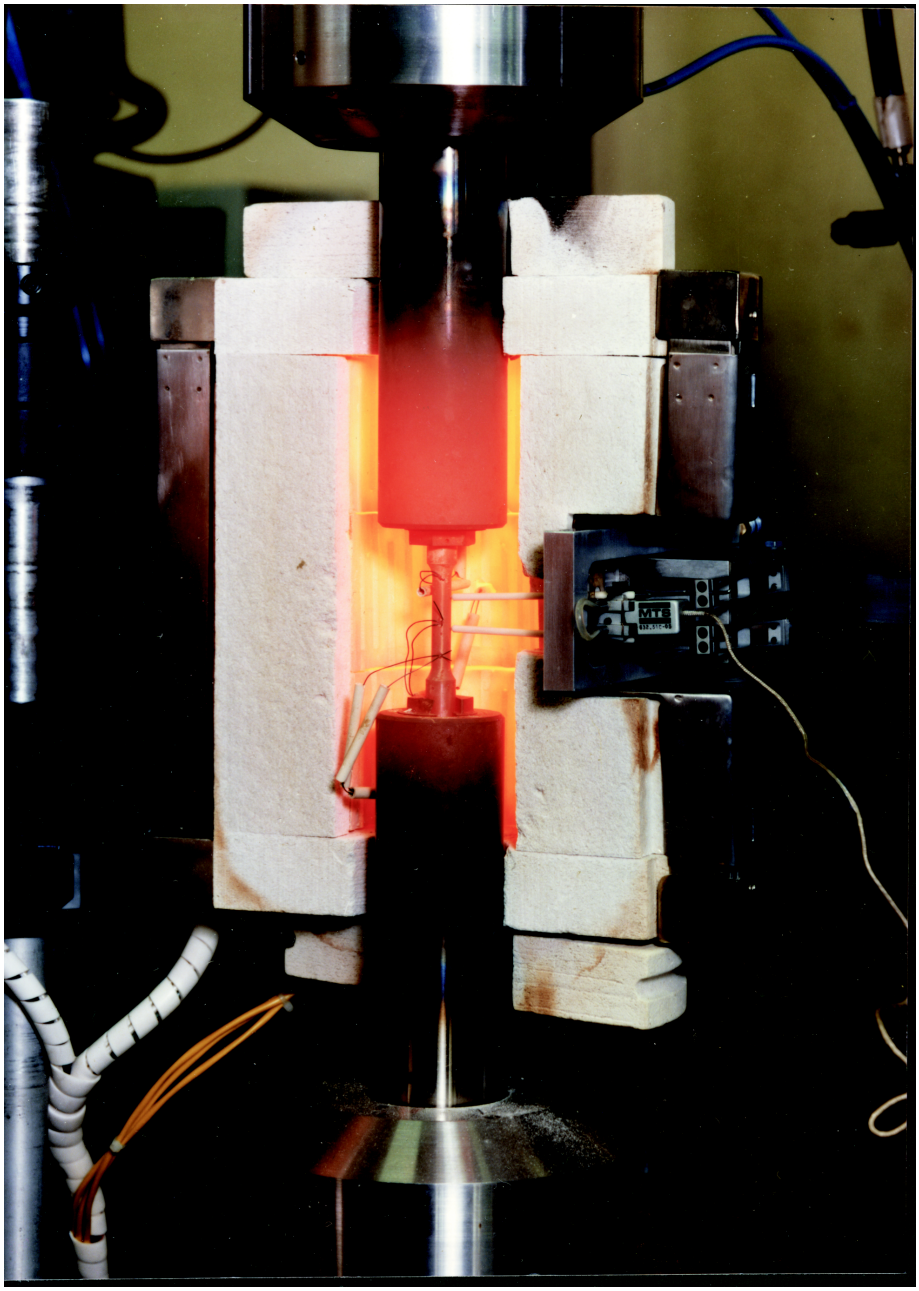

Figure 14: Testing equipment of the LCF tests at high temperature.

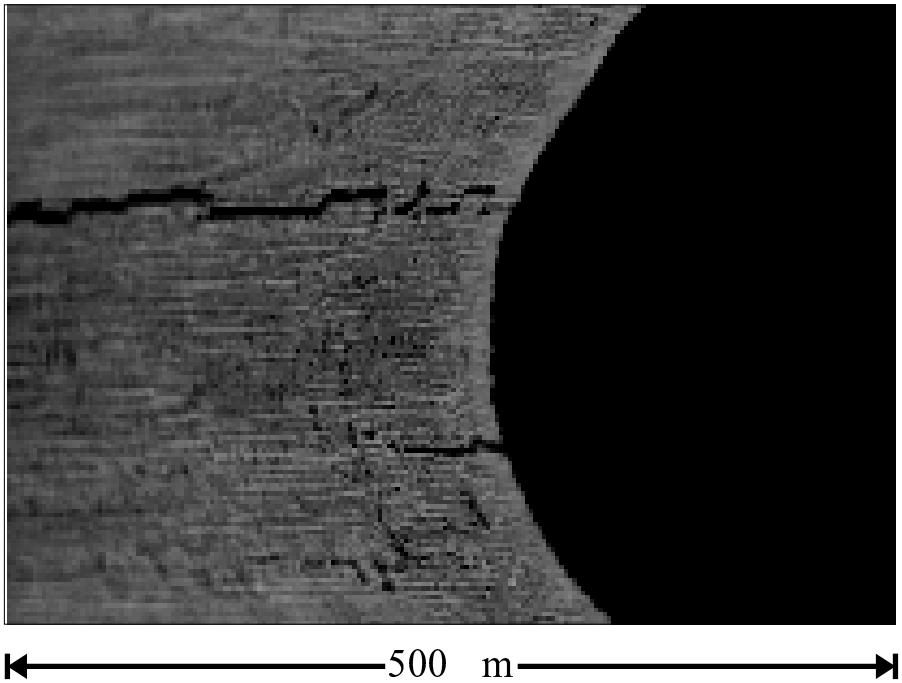

Figure 15: Notch of the ⟨001⟩ SC16 specimen 3 with 0.2 mm notch radius after N = 250 cycles at 950°C.

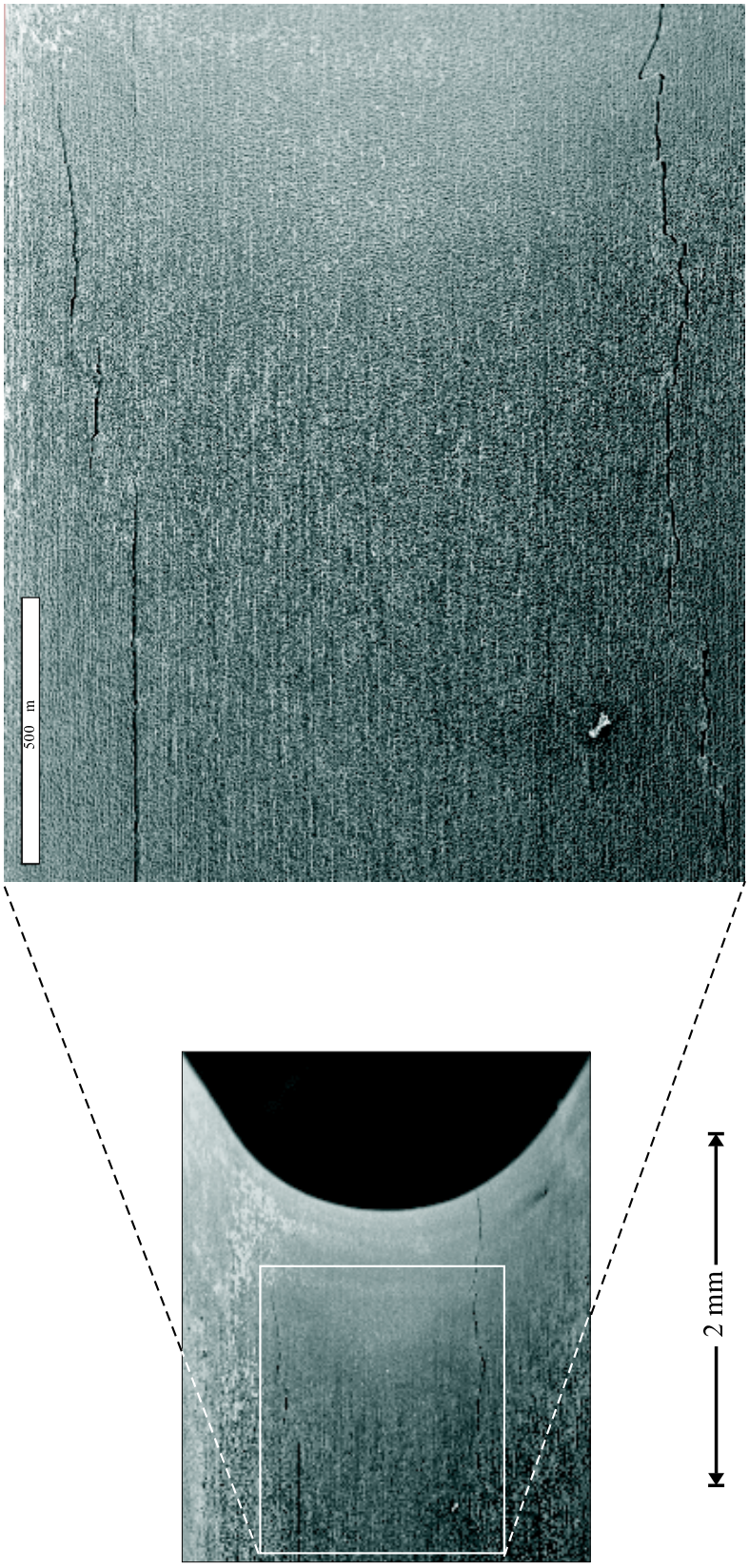

Figure 16: Notch of the ⟨001⟩ SC16 specimen 4 with 1 mm notch radius after N = 810 cycles at 950°C.

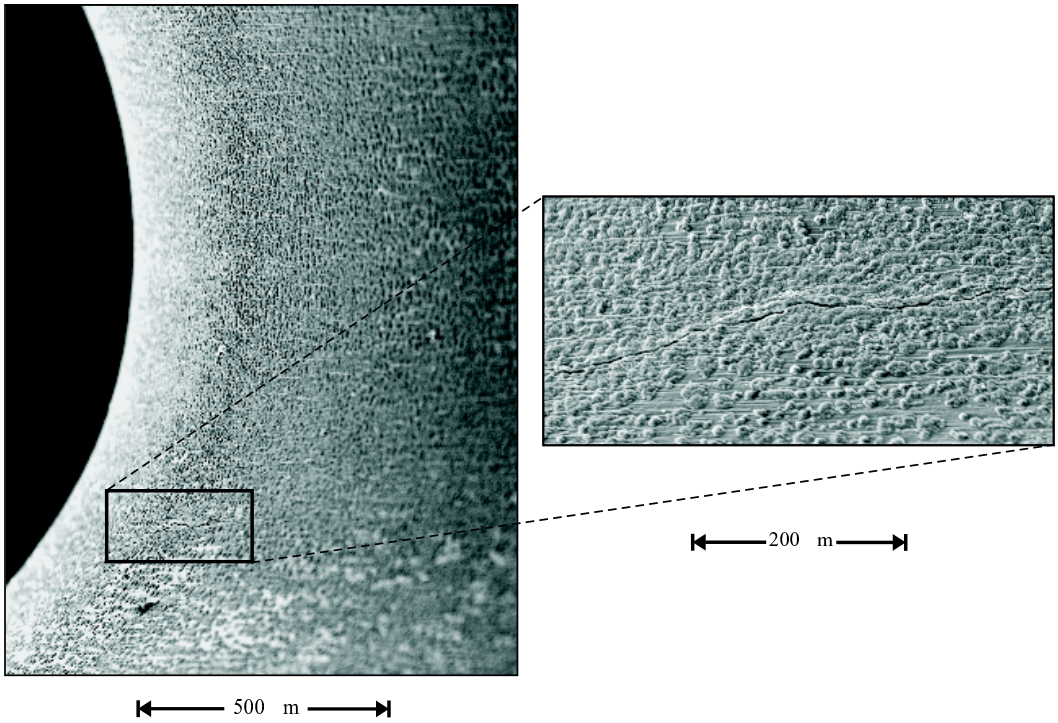

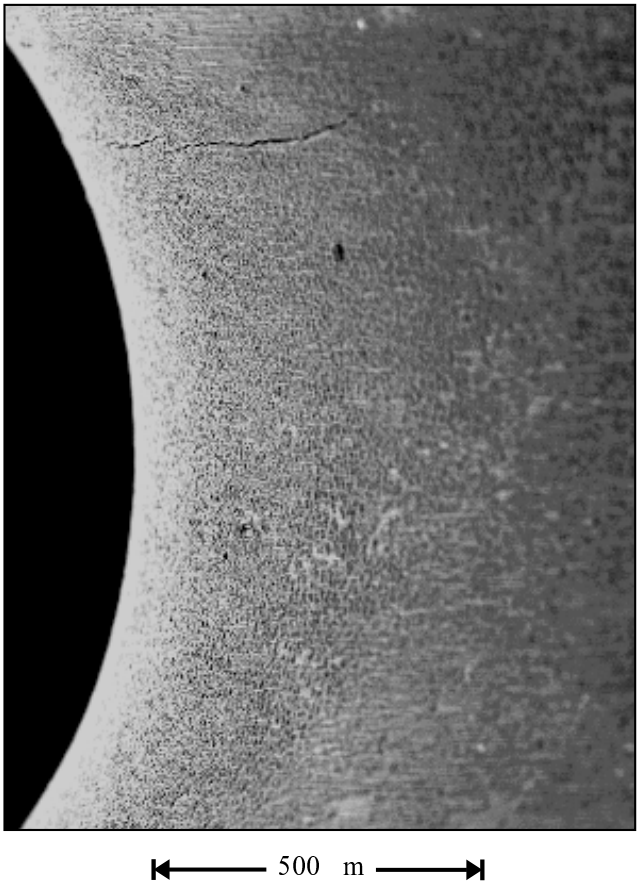

Figure 17: Notch of the ⟨001⟩ SC16 specimen 5 with 1 mm notch radius after N = 560 cycles at 950°C.

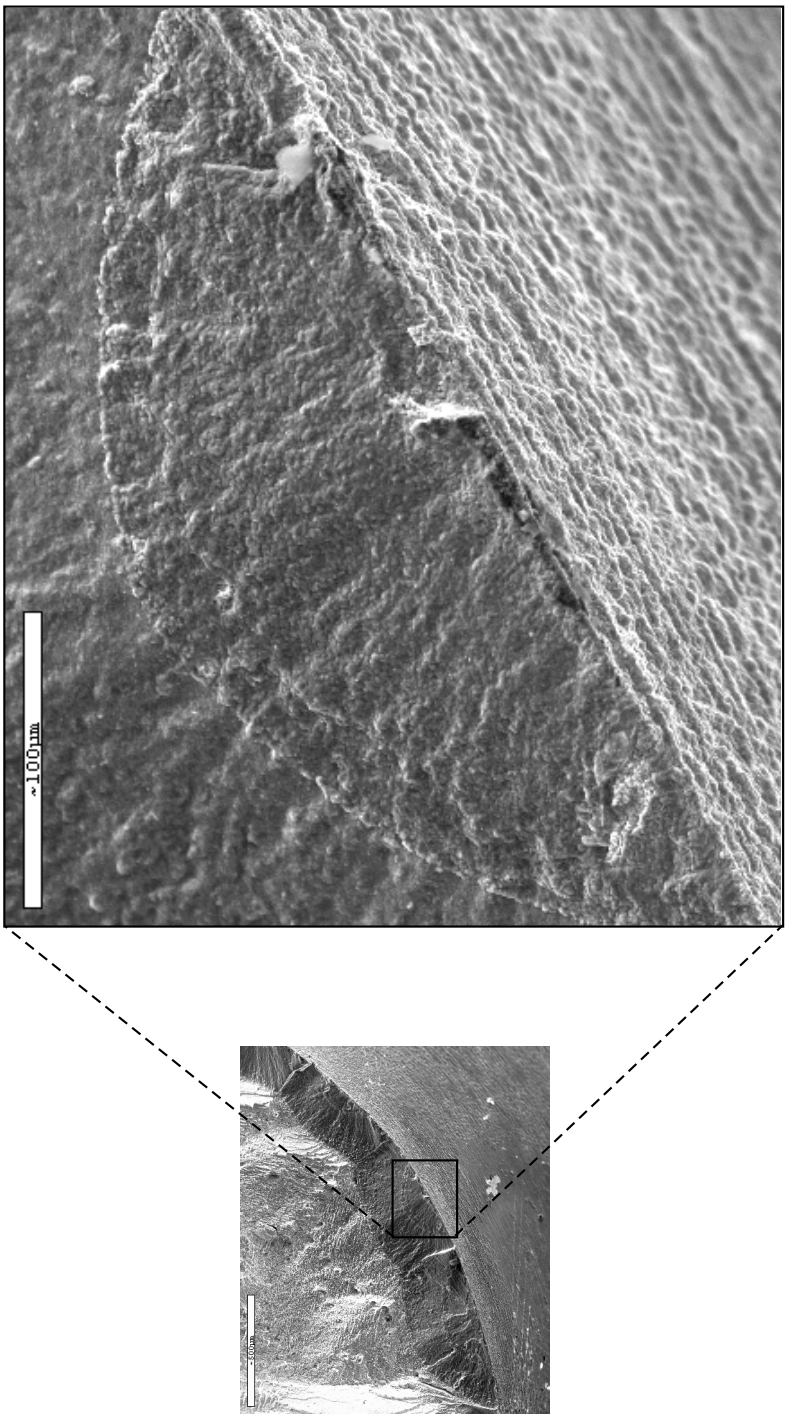

Figure 18: Notch of the ⟨001⟩ SC16 specimen 5 with 1 mm notch radius after N = 560 cycles at 950°C.

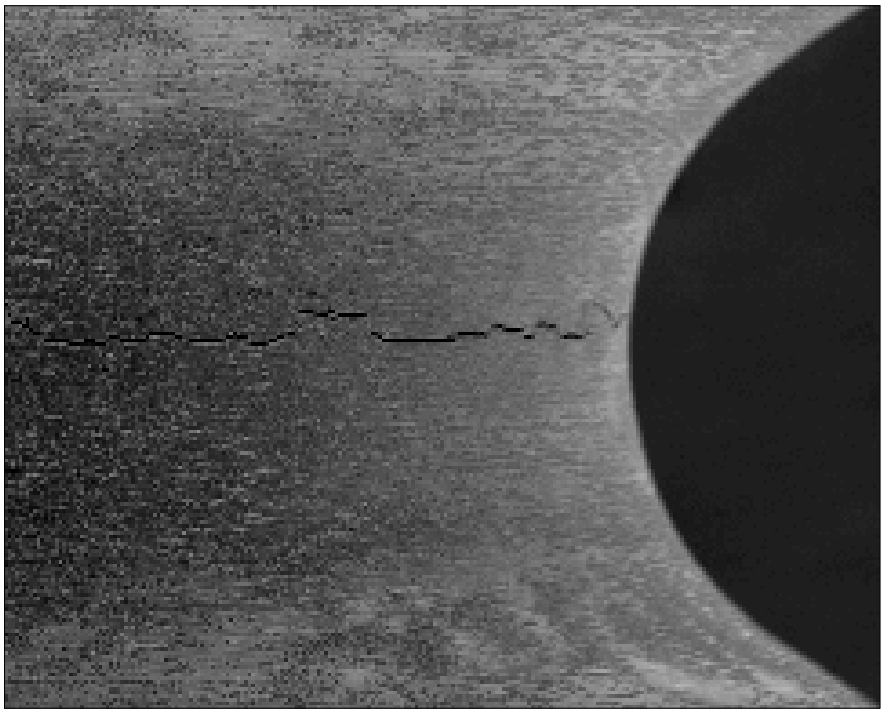

2 mm

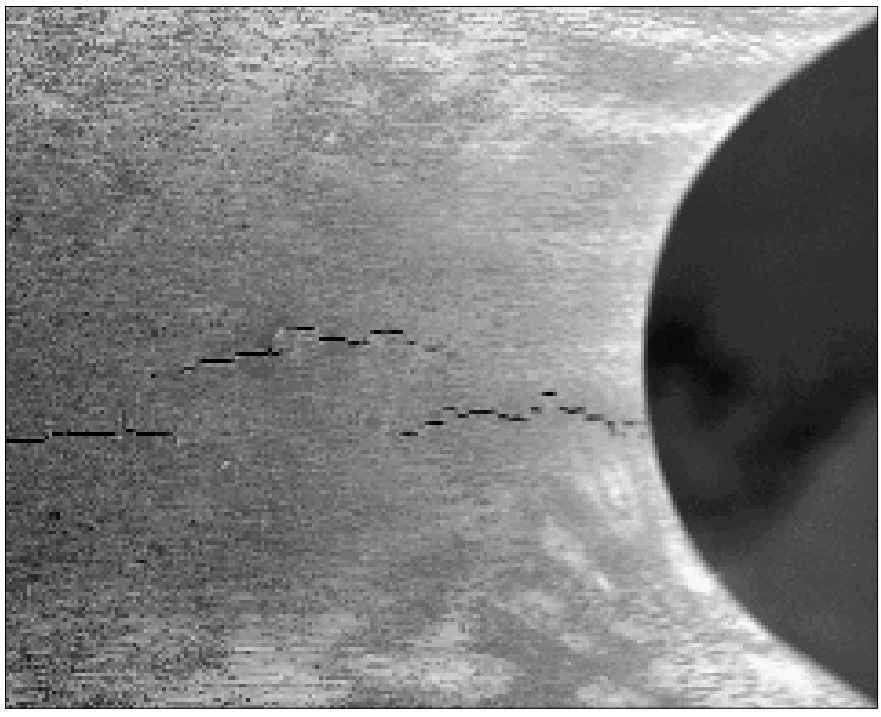

2 mm

Figure 19: Notch of the ⟨011⟩ SC16 specimen 6 with 1 mm notch radius after N = 165 cycles at 950°C . The views correspond to two different positions.

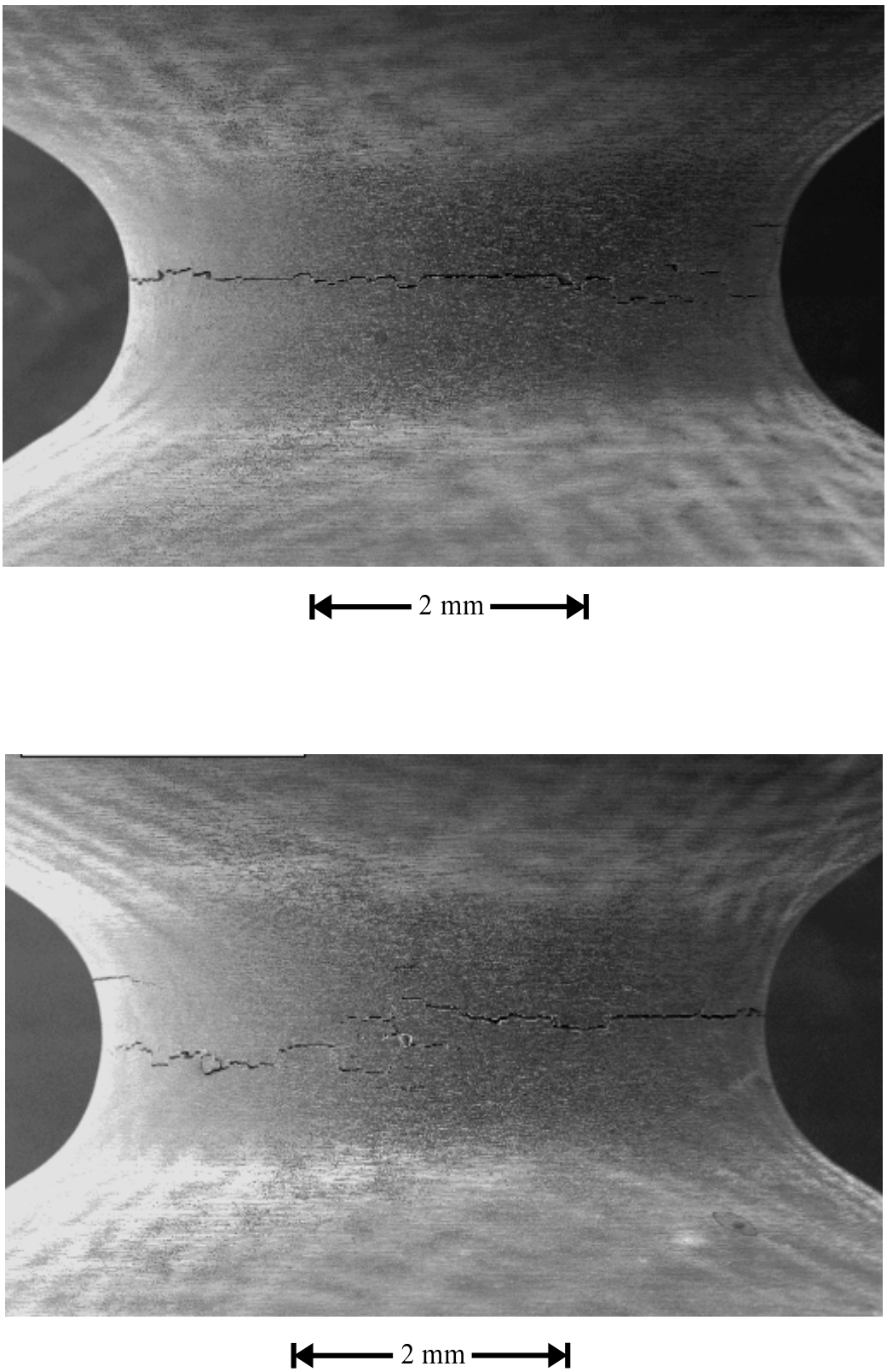

Figure 20: Two opposite faces of the ⟨111⟩ SC16 notched specimen 8 with 1 mm notch radius after N = 128 cycles at 950°C.

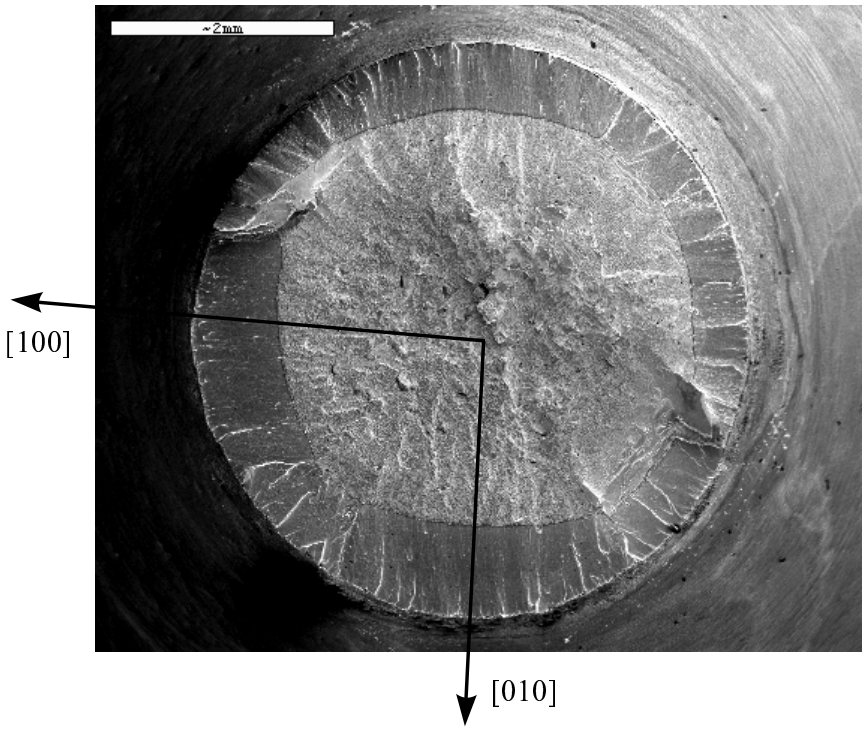

Figure 21: Fracture surface of the ⟨001⟩ SC16 specimen 1 with 0.2 mm notch radius after N = 275 cycles at 950°C

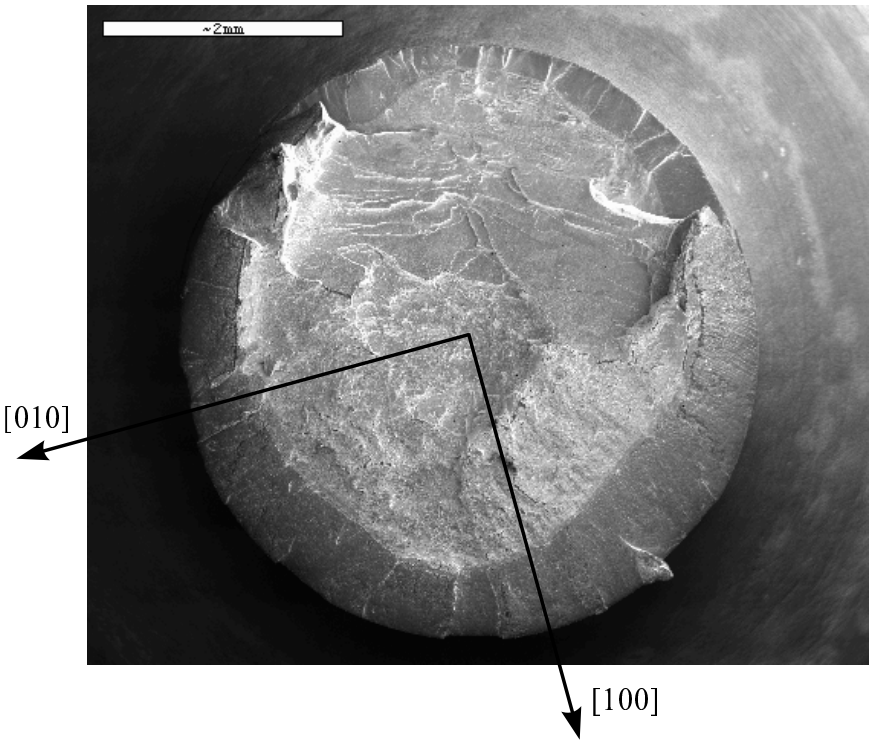

Figure 22: Fracture surface of the ⟨001⟩ SC16 specimen 4 with 1 mm notch radius after N = 810 cycles at 950°C.

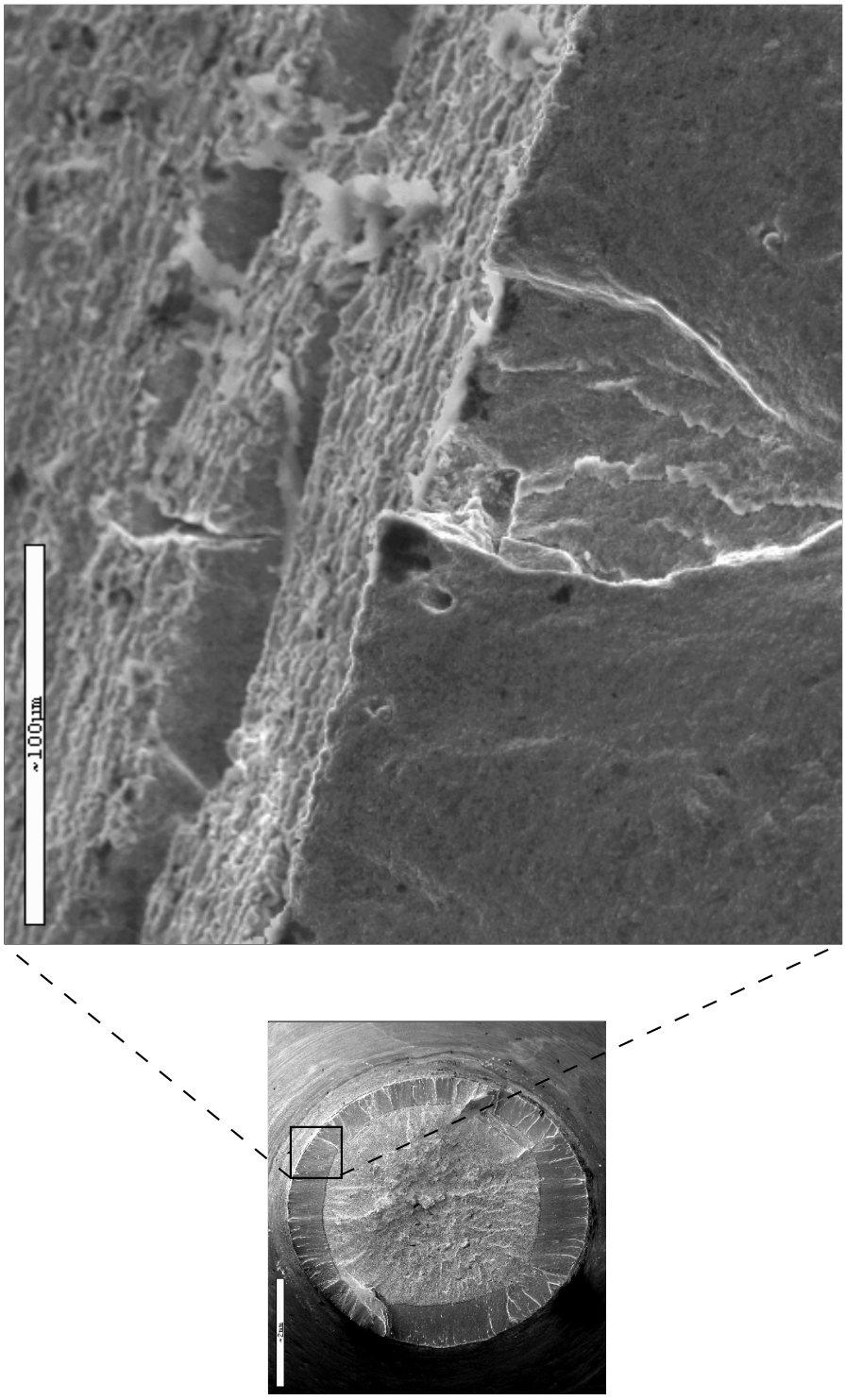

Figure 23: Fracture surface of the ⟨001⟩ SC16 specimen 1 with 0.2 mm notch radius after N = 275 cycles at 950°C.

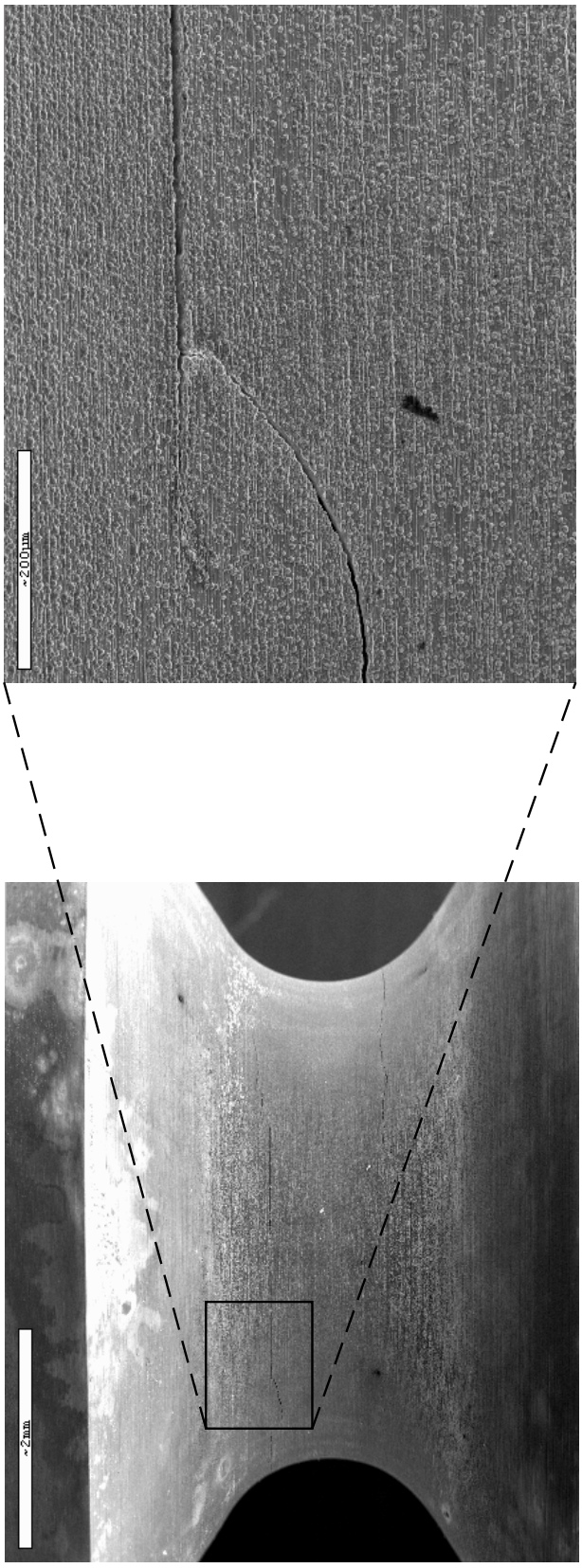

Figure 24: Notch of the ⟨001⟩ SC16 specimen 4 with 1 mm notch radius after N = 810 cycles at 950°C.

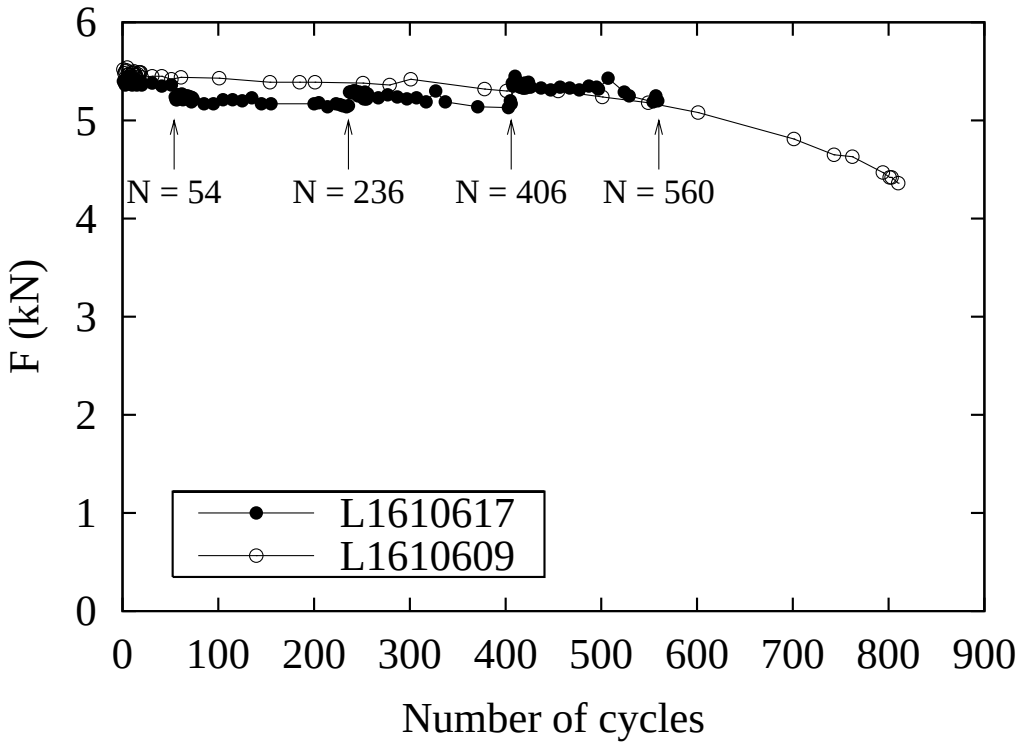

Figure 25: Maximum axial force versus the number of cycles of LCF tests on notched ⟨001⟩ oriented specimens.

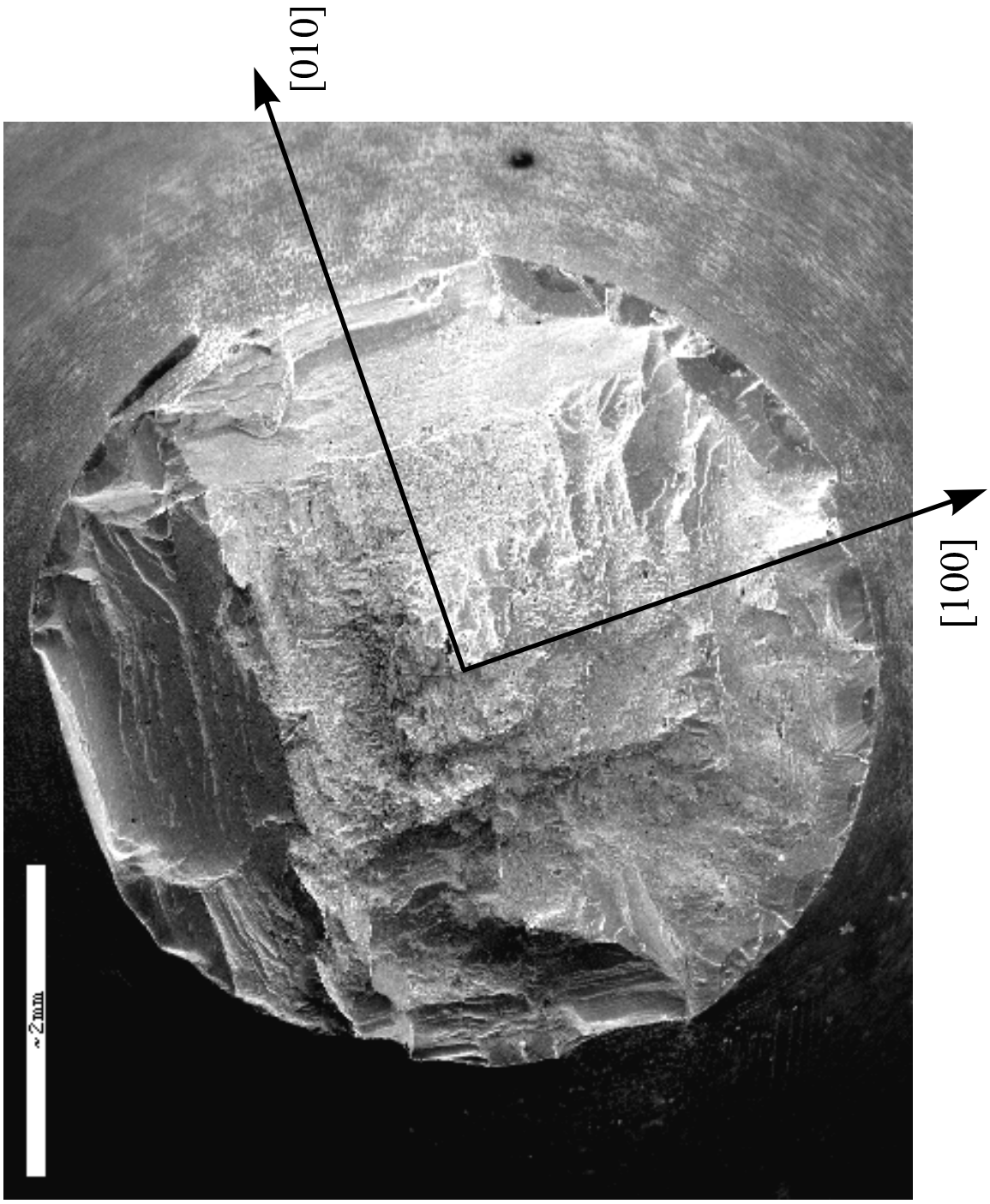

Figure 26: Fracture surface of the ⟨001⟩ SC16 specimen 5 with 1 mm notch radius after N = 560 cycles at 950°C.

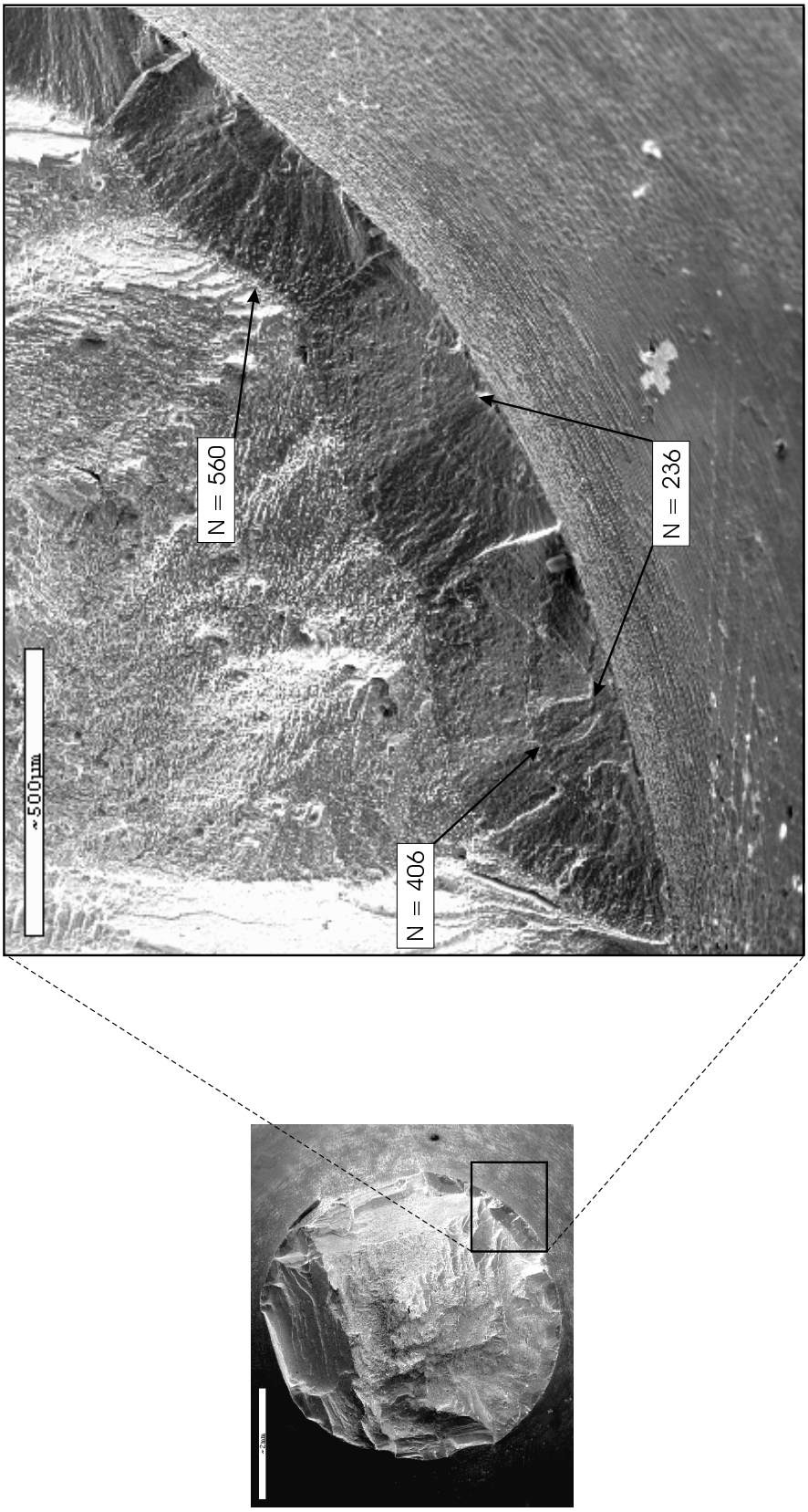

Figure 27: Fracture surface of the ⟨001⟩ SC16 specimen 5 with 1 mm notch radius after N = 560 cycles at 950°C.

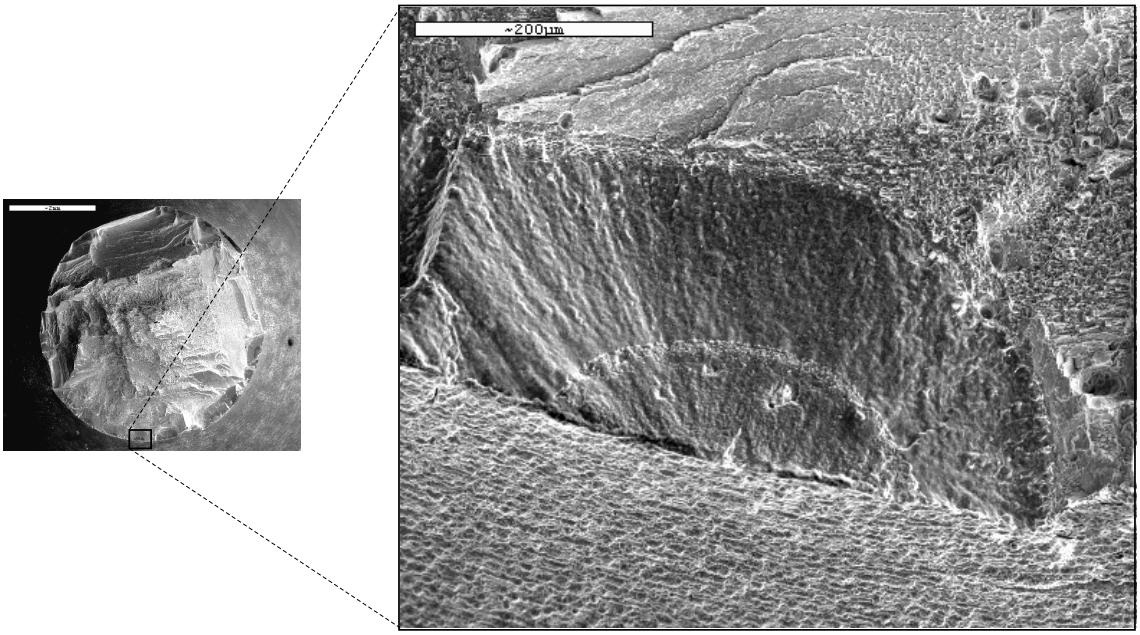

Figure 28: Fracture surface of the ⟨001⟩ SC16 specimen 5 with 1 mm notch radius after N = 560 cycles at 950°C.

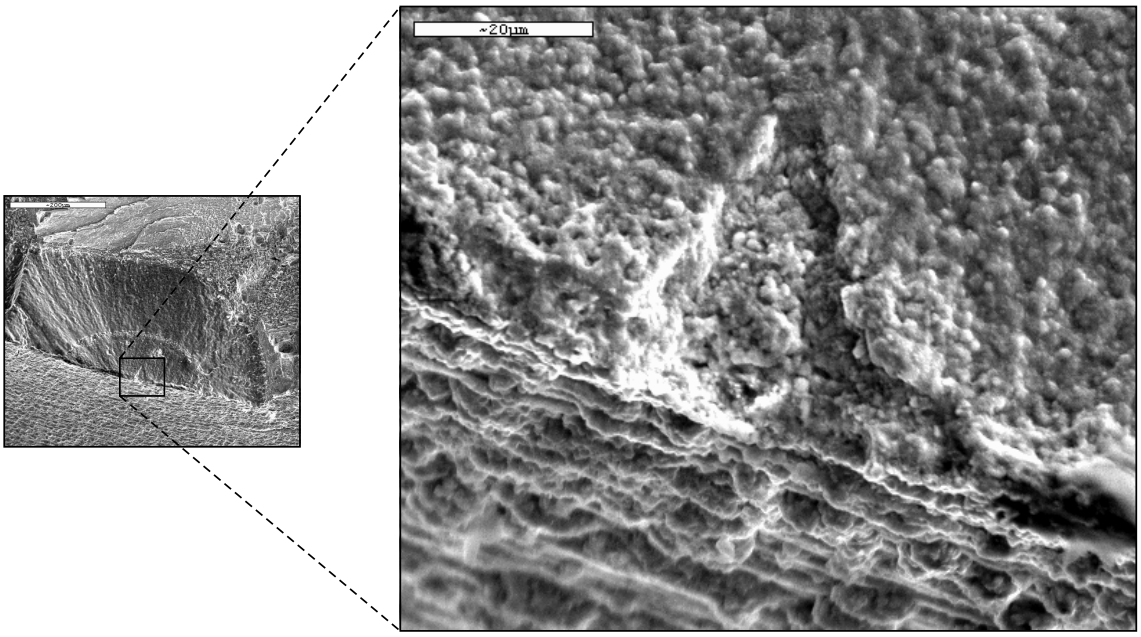

Figure 29: Fracture surface of the ⟨001⟩ SC16 specimen 5 with 1 mm notch radius after N = 560 cycles at 950°C.

3 Model predictions and comparison with the experimental results

In this section we will propose a physically relevant variable for the damage of our anisotropic material under low-cycle fatigue at high temperatures. The previous experimental observations concerning the crack location at the notch lead to choose a local approach for the crack initiation. Moreover it is absolutely necessary to take into account the anisotropic behavior of the single crystal too.

Thus numerical simulations with the crystalline model of these LCF tests on notched specimens will be presented first in order to confirm such expected inhomogeneous strain and stress distribution at the notch. Then we will propose a simple lifetime assessment rule for nickel base single crystal superalloy based on a deterministic approach. Finally an alternative method based on a statistical approach will be explained in the third part.

3.1 Viscoplastic strain-stress behaviour at notches

3.1.1 Conditions of the FE analysis

We give in this section the results of the calculations for two geometries and three orientations of the specimen: $\langle 001 \rangle$, $\langle 011 \rangle$ and $\langle 111 \rangle$. In order to investigate the influence of such a geometry on the stress-strain state and on the fatigue life of the single crystal we have computed a notched specimen with two radii: 0.2 mm and 1 mm.
Finite element calculations have been performed for the single crystal ideally oriented to reduce the size of the problem. It is particularly the case for our LCF tests specimens which deviates from the [001] crystallographic axis of about 5°, see appendix B. Moreover, due to the cubic symmetry, we only need to mesh one eighth of the structure, which is the length of the extensometer, see Fig. 30. The mesh of the 0.2 mm notched radius specimen has 642 isoparametric and quadratic elements. The number of degrees of freedom is 9384 with the appropriate boundary conditions. The mesh of the 1 mm notched radius specimen has 690 quadratic elements and the number of degrees of freedom is 9816.
The LCF tests have been carried out with displacement control and we prescribed in the calculations the displacement at the end of the structure in order to account for the experimental value at the location of the extensometer: a displacement amplitude of ± 0.016125 mm for the gauge length, and a loading rate of $10^{-3}\ s^{-1}$.
The material constants of SC16 at 950°C previously calibrated in the first part (section 3.2.2) has been used in this finite element analysis, see table 5.

3.1.2 Results

Calculations of torsionally loaded tubular specimens have shown the inhomogeneity of the viscoplastic strain along the circumference [Méric et al., 1991b]. More recently at the

BAM it was confirmed with experimental results and even for tension-torsion tests the good agreement between the FE model and the local measurements at room temperature [Forest et al., 1996].
Due to the complex state of stress in the notch a similar inhomogeneity of the strain field is expected at the notch according to the model.

Unfortunately it is impossible to use the same local measurement due to the high temperature and the geometry. However we have compared the position of the crack location in the notch with the one of the total cumulated slip distribution.
From that point of view the $\langle 001 \rangle$ oriented notched specimen is distinguished from the others.

Specimen $\langle 001 \rangle$ oriented:

Contrary to the results of a tension test of a $\langle 001 \rangle$ single crystal smooth specimen, the presence of the notch activates both slip system families, see Figs. 31 and 32. The total cumulated slip computed from cubic slip is higher than the one coming from the octahedral slip.
Moreover cubic slip is not located exactly at the notch root instead it is shifted a little away from there. The total cumulated cubic slip is maximum in the plane $\{010\}$ but a precise evaluation of its variation along the circumference is not possible from this contour plot. I have plotted the cumulated slip along two different lines on the surface, see Fig. 35. Thus we deduce from these curves the weak variation of the total cumulated slip for the cubic slip systems along the circumference.

From the analysis of the micrographs at the notches a scatter band for each main cracks on the surface can be defined for two geometries, see Figs. 38 and 39, except for the specimen of the interrupted test. We have assessed an average of the distance between the main cracks despite the relative precision of such a measurement. Moreover the distance between the maximum cubic cumulated slip located at the notch has been calculated. The agreement between the main cracks location and the position of the maximum total slip is acceptable if we take into account the inaccuracy of the measurements.

Specimen $\langle 011 \rangle$ oriented:

Fig. 33 shows that both slip system families are activated in the notch.
The higher value is reached by the cubic slip system family. In order to know where its maximum along the circumference is, which is not clear from the contour plots, we have plotted the total cumulated cubic slip along three characteristic lines, see Fig. 36. The maximum is reached at the notched root in the crystallographic plane $\{100\}$. Note however that the cubic slip is high (1 %) in the $\{01\bar{1}\}$ plane too.

Figs. 41 and 42 show that the locations of the cracks is consistent with the zone of high total cumulated cubic slip at the notched root.

Specimen $\langle 111 \rangle$ oriented:

The octahedral slip is negligible in comparison with the cubic one in the notch, see Fig. 34. Moreover the cubic slip is more concentrated at the notch root than for the $\langle 011 \rangle$ notched specimen. The curves plotted in Fig. 34 confirm this situation.

Figs. 43 and 44 illustrate that the total maximum cumulated slip and the main crack are located at the same area.

Summary:

If we consider the maximum total slip as a relevant variable for the crack initiation at the surface in the notch and if we take into account the scatter attached to the experimental definition of the location of the crack, the experimental results are in good agreement with the FE analyses.
For the $\langle 001 \rangle$ notched specimen, two symmetric main cracks can be observed. They are not located at the notch root, whereas cracks initiate at the notch root for the orientation $\langle 011 \rangle$ and $\langle 111 \rangle$.
For the $\langle 001 \rangle$ oriented specimen, the total cumulated slip of the cubic slip systems is quasi-homogeneous along the circumference. Thus the crack initiation should be determined by the statistical distribution of the pores along the circumference in the area of maximum total cumulated slip.

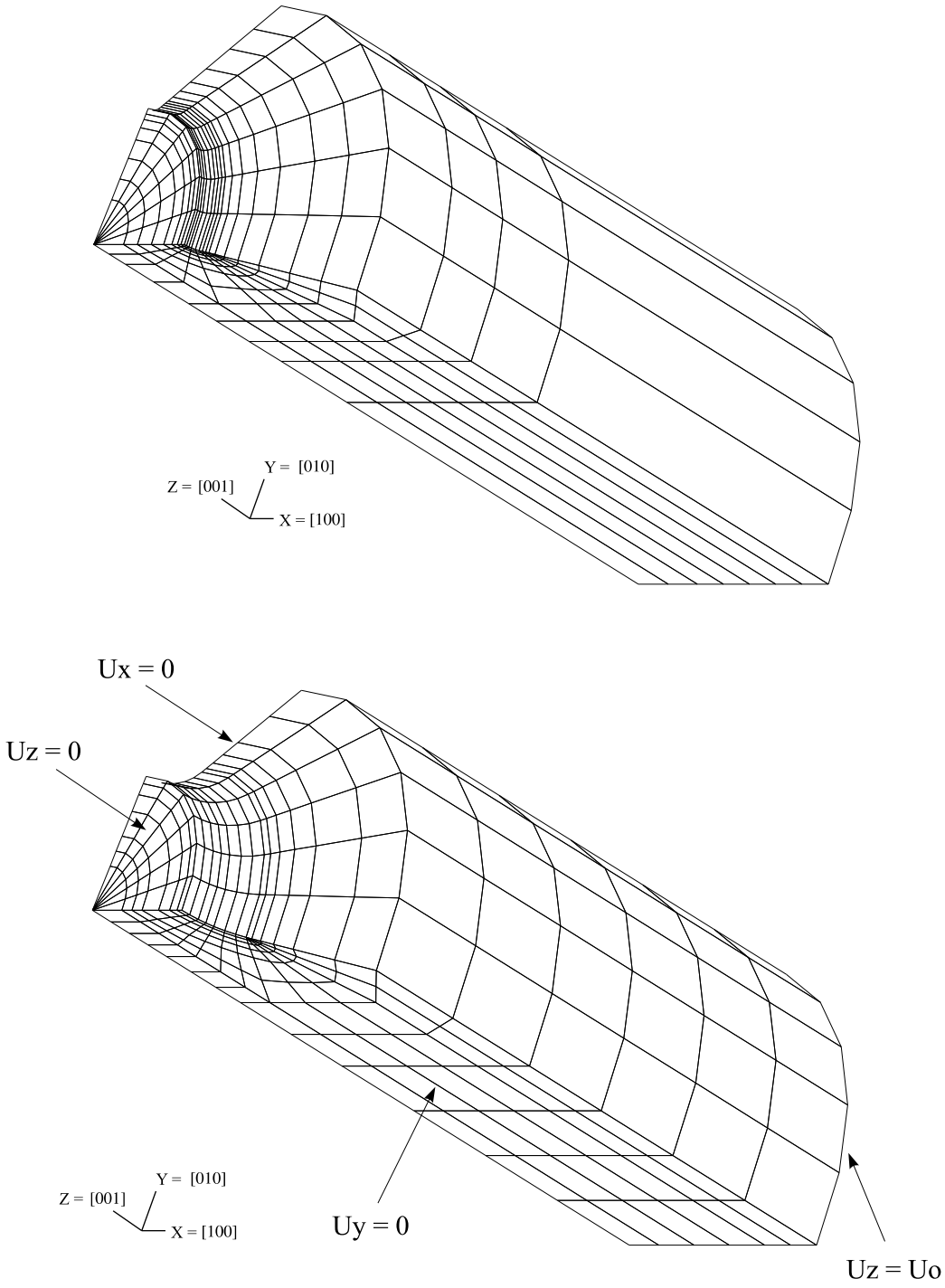

Figure 30: Meshes of one eighth of the notched specimens for 0.2 mm (above) and 1 mm (below) notch radius. The axes (X;Y;Z) correspond to a ⟨001⟩ oriented specimen.

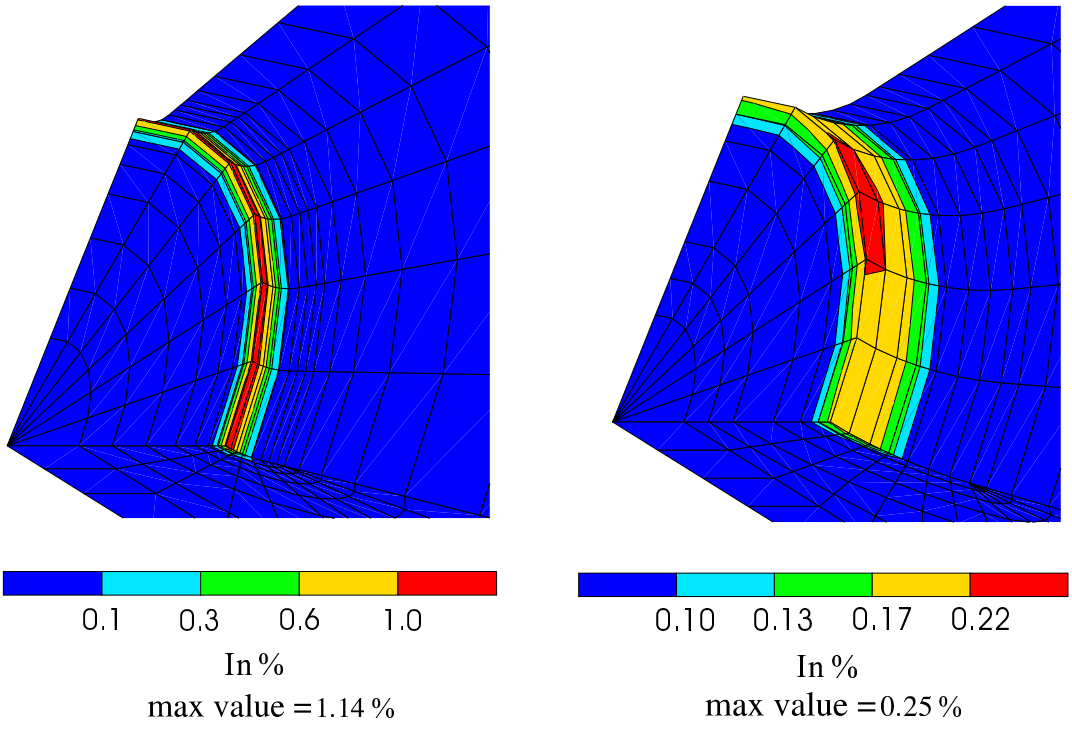

Figure 31: Total cumulated slip for the octahedral slip systems for two notch radii (0.2 mm (left) and 1 mm (right)) of a ⟨001⟩ specimen.

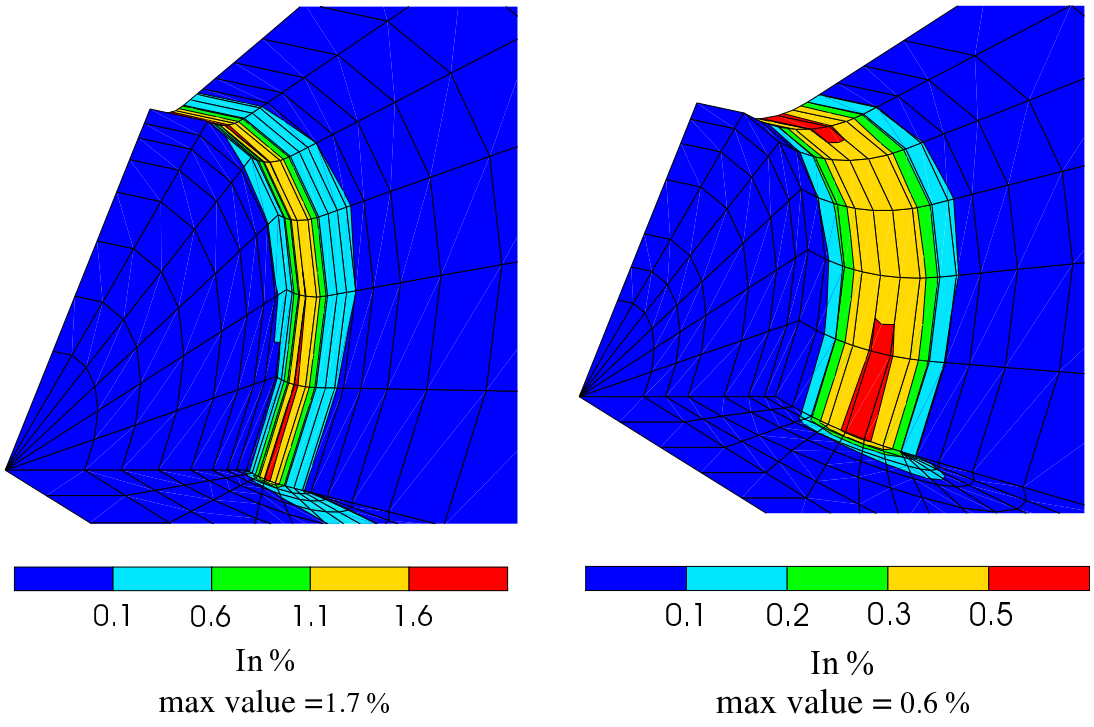

Figure 32: Total cumulated slip for the cubic slip systems for two notch radii (0.2 mm (left) and 1 mm (right)) of a ⟨001⟩ specimen.

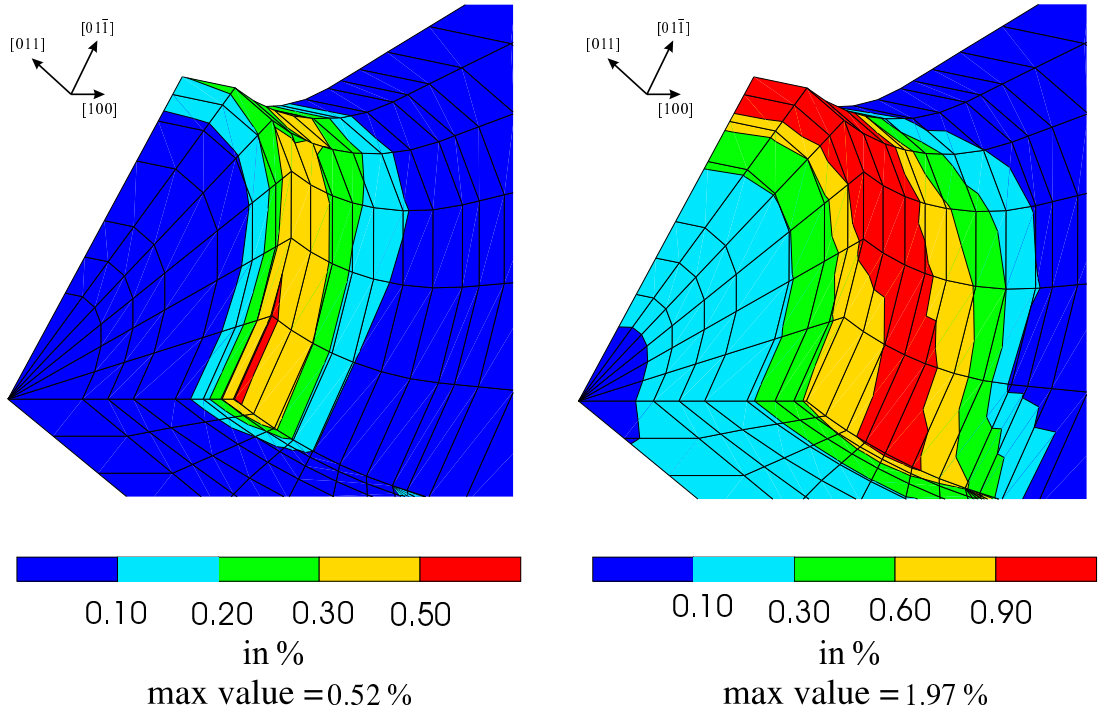

Figure 33: Total cumulated slips of a ⟨011⟩ oriented specimen and for 1 mm notch radius (octahedral (left) and cubic (right)).

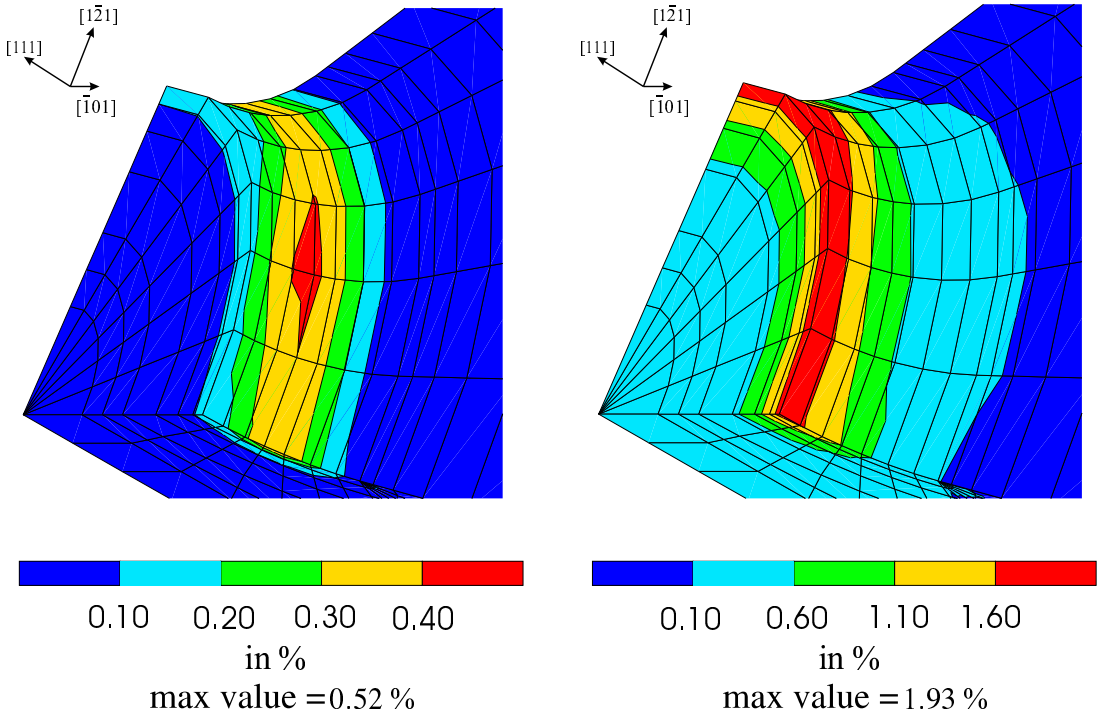

Figure 34: Total cumulated slips of a ⟨111⟩ oriented specimen and for 1mm notch radius (octahedral (left) and cubic (right)).

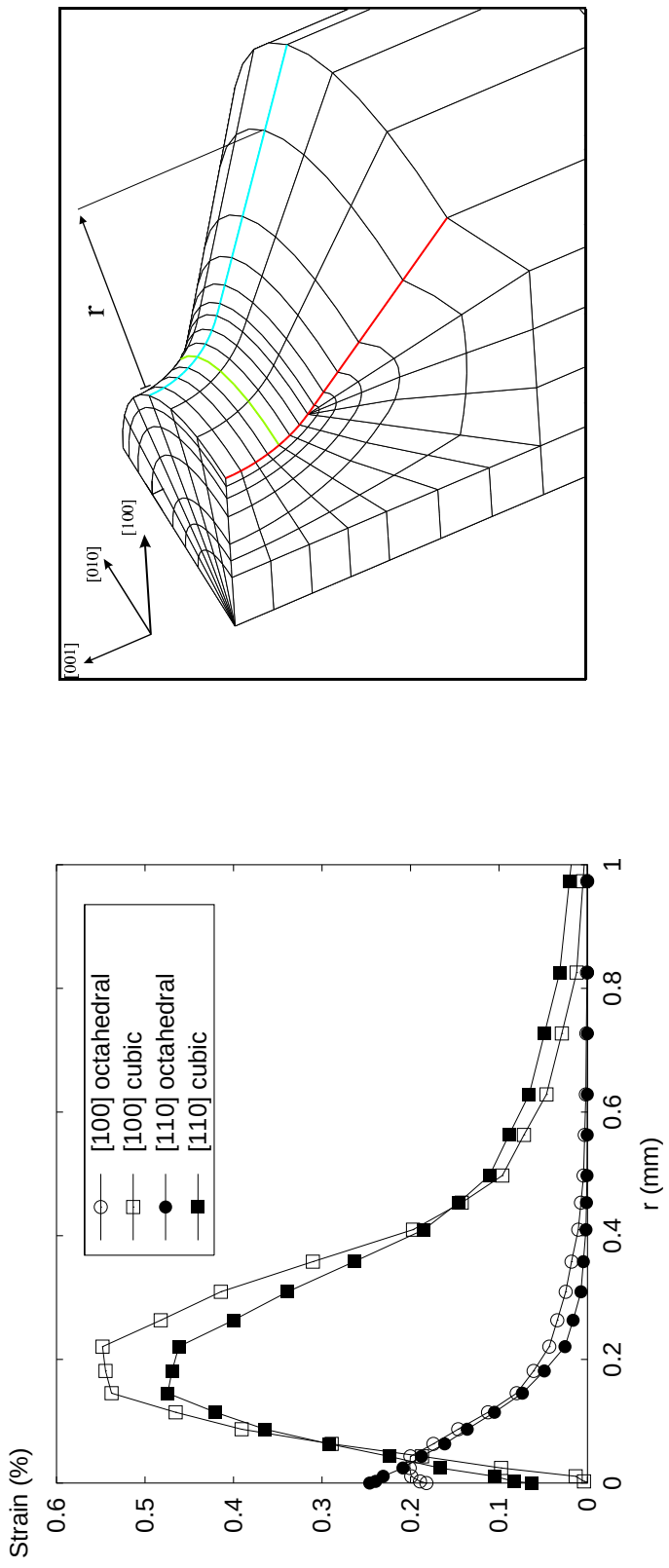

Figure 35: Total cumulated slip for each slip system family of the $\langle 001 \rangle$ oriented specimen on two lines on the surface of the notch (radius 1 mm). "[100] cubic" denotes the total cumulated slip of the cubic slip systems on the the line, the red one, in the plane $\{010\}$.

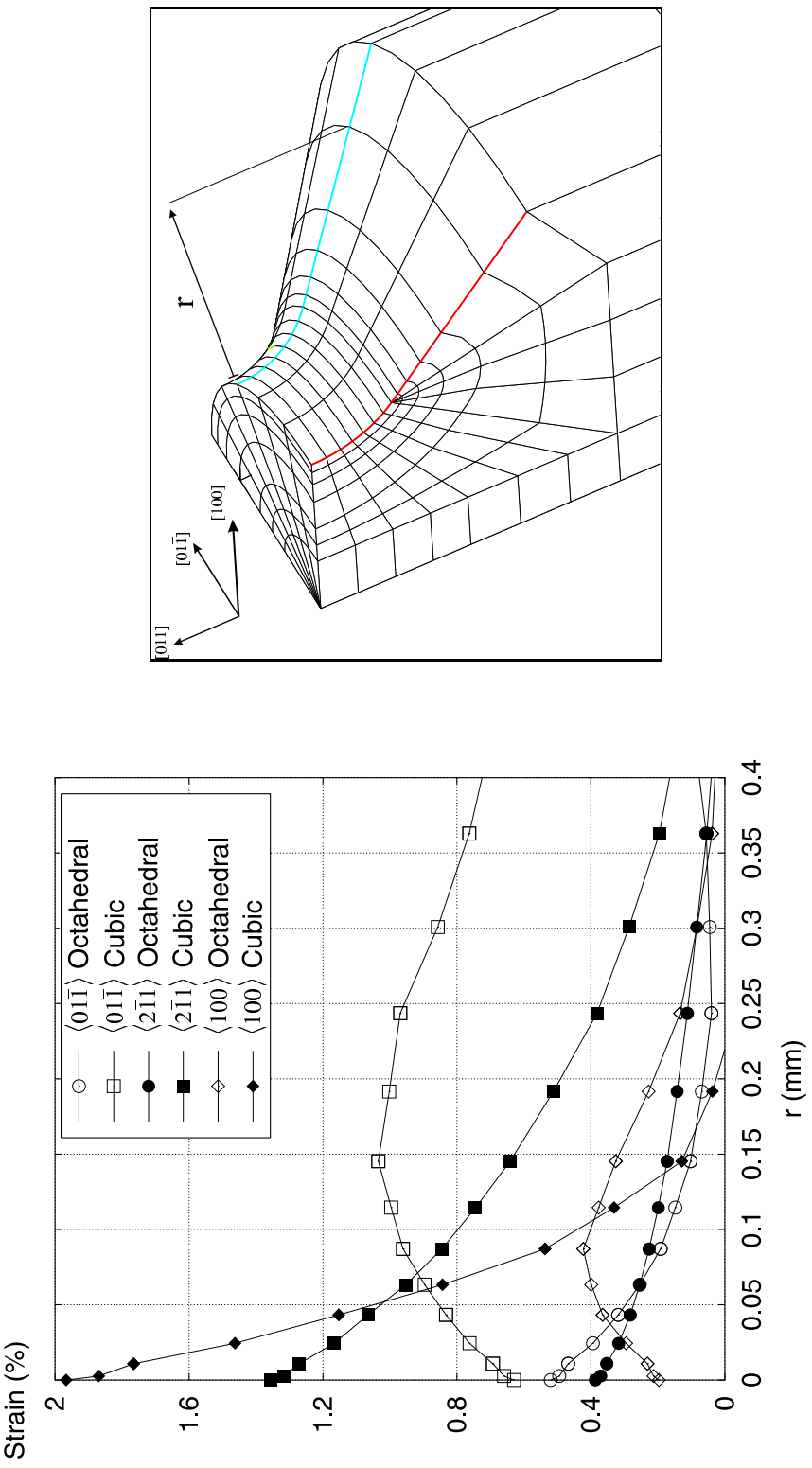

Figure 36: Total cumulated slip for each slip system family for the $\langle 011\rangle$ specimen for the lines on the surface of the notch (radius 1 mm) in three crystallographic planes, $\{0\bar{1}1\}$, $\{2\bar{1}1\}$ and $\{100\}$. For example, the curve "$\langle 0\bar{1}1\rangle$ Cubic" corresponds to the cubic slip on the red line in the plane $\{0\bar{1}1\}$. The blue line is on the crystallographic plane $\{2\bar{1}1\}$.

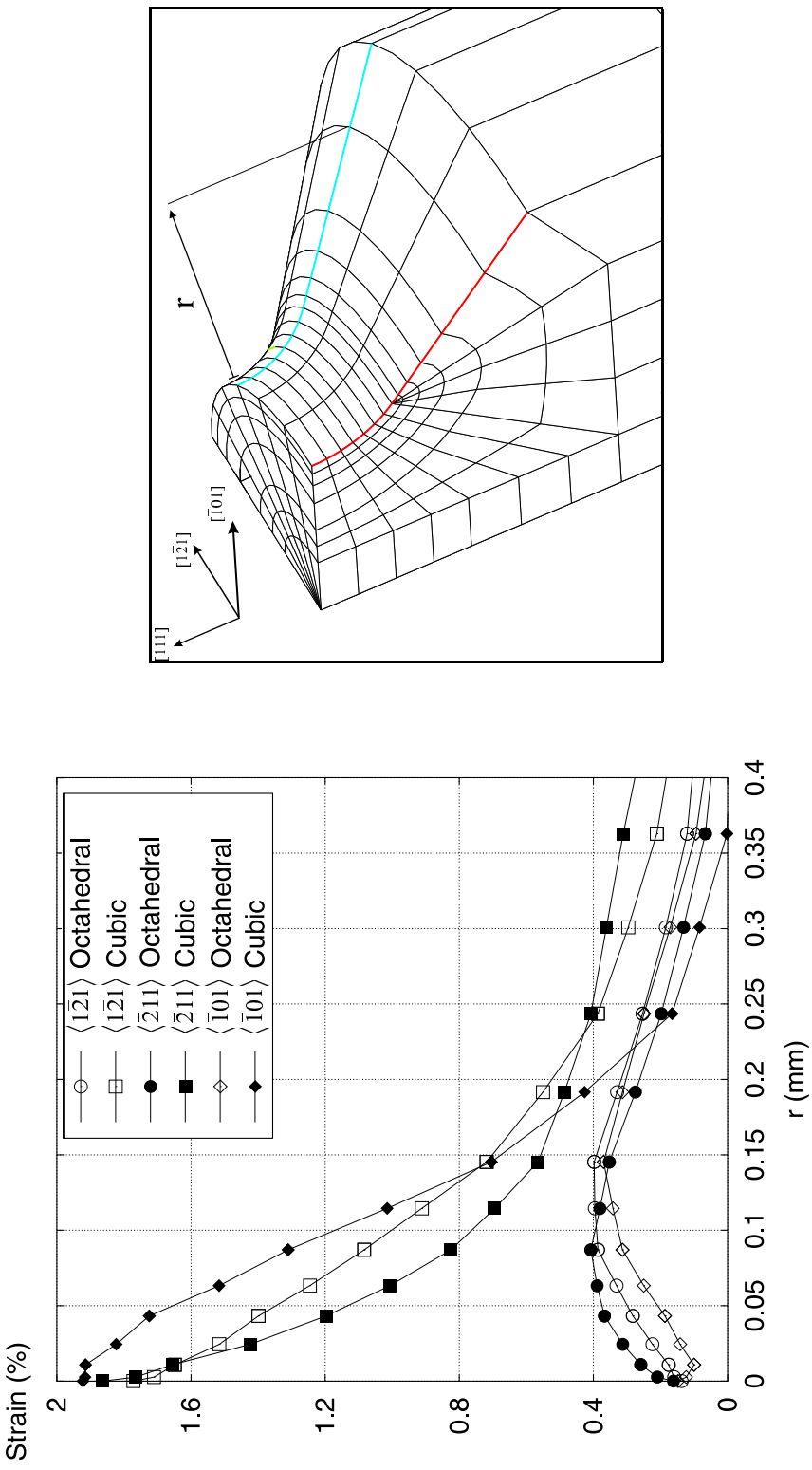

Figure 37: Total cumulated slip for each slip system family for the $\langle 111 \rangle$ specimen for the lines on the surface of the notch (radius 1 mm) in three crystallographic planes, $\{1\bar{2}1\}$, $\{\bar{2}11\}$ and $\{\bar{1}01\}$. For example, the curve "$\langle 1\bar{2}1 \rangle$ Cubic" corresponds to the cubic slip on the red line in the plane $\{1\bar{2}1\}$. The blue line is on the crystallographic plane $\{\bar{2}11\}$.

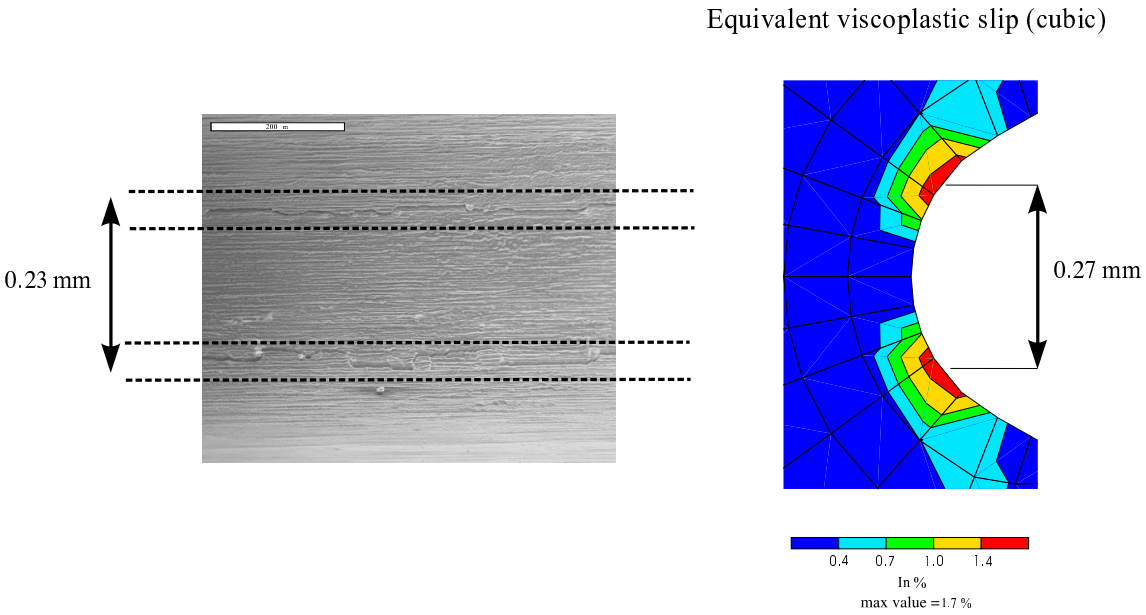

Figure 38: Correlation between the location of the maximum cumulated slip and notch cracking. ⟨001⟩ oriented specimen 1 with 0.2 mm notch radius.

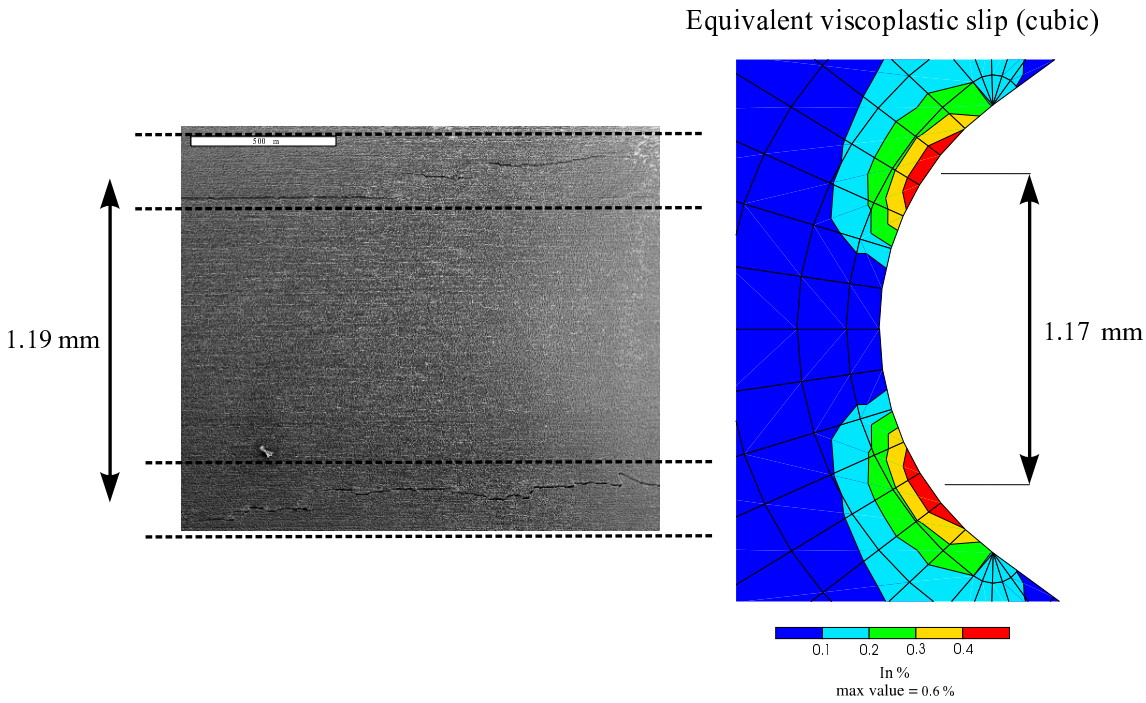

Figure 39: Correlation between the location of the maximum cumulated slip and notch cracking. ⟨001⟩ oriented specimen 4 with 1 mm notch radius.

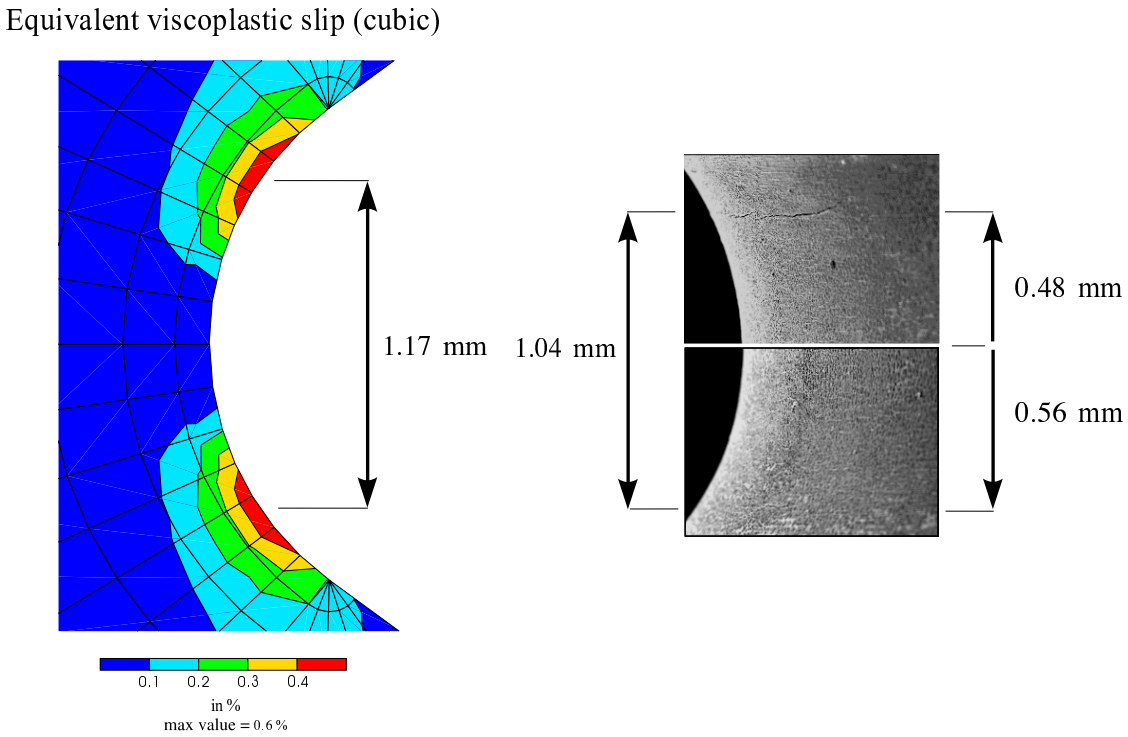

Figure 40: Correlation between the location of the maximum cumulated slip and notch cracking. ⟨001⟩ oriented specimen 5 with 1 mm notch radius.

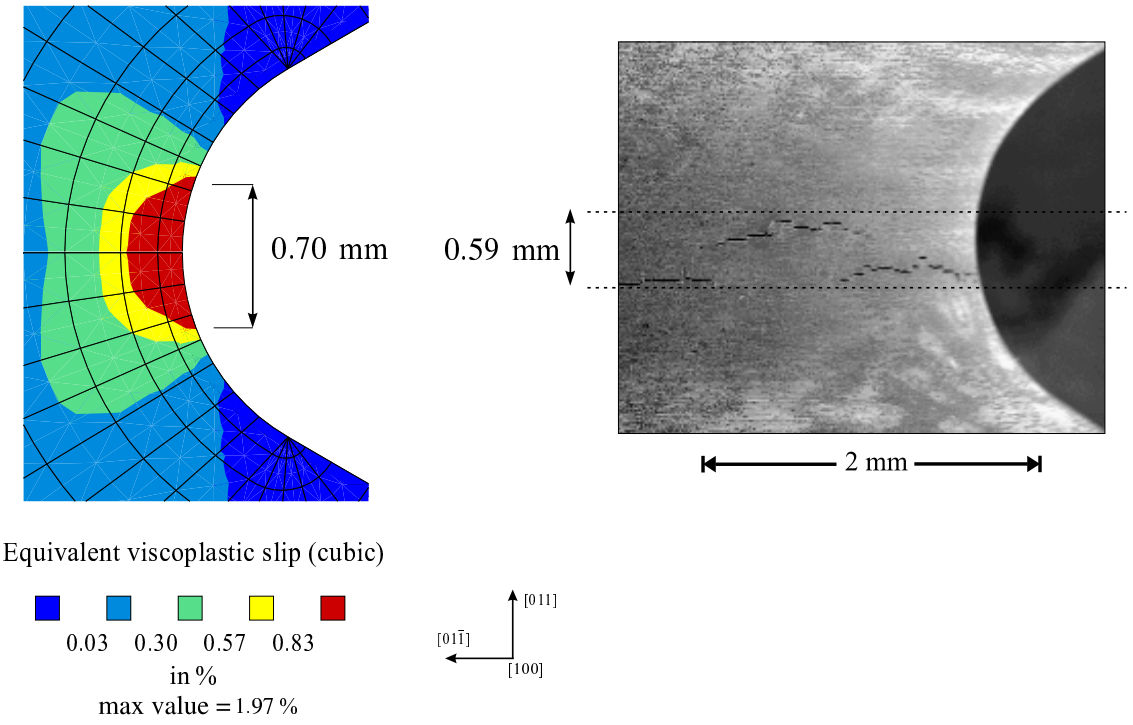

Figure 41: Correlation between the location of the maximum cumulated slip and notch cracking. ⟨011⟩ oriented specimen 6 with 1 mm notch radius.

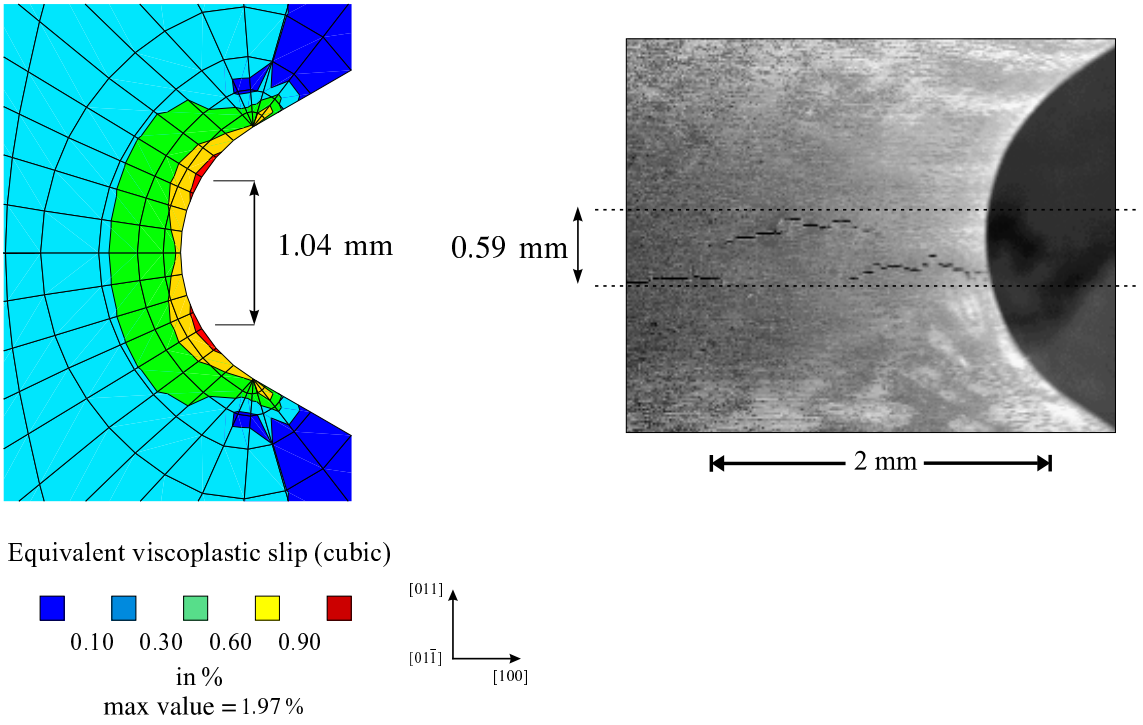

Figure 42: Correlation between the location of the maximum cumulated slip and notch cracking. ⟨011⟩ oriented specimen 6 with 1 mm notch radius.

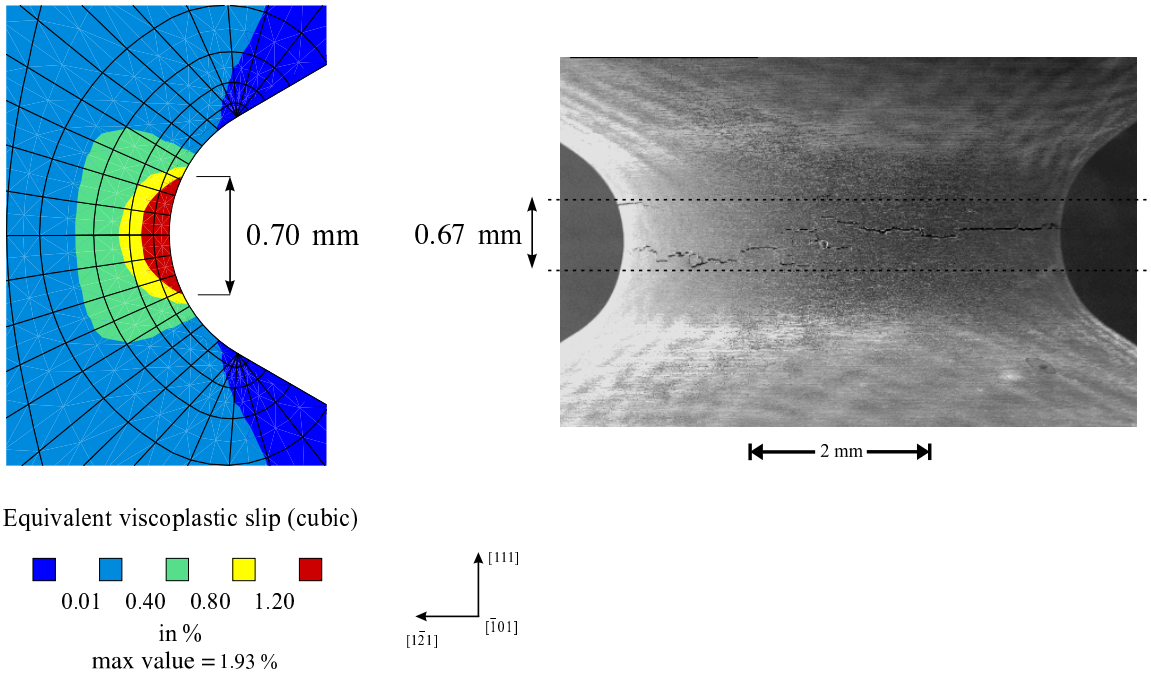

Figure 43: Correlation between the location of the maximum cumulated slip and notch cracking. ⟨111⟩ oriented specimen 8 with 1 mm notch radius.

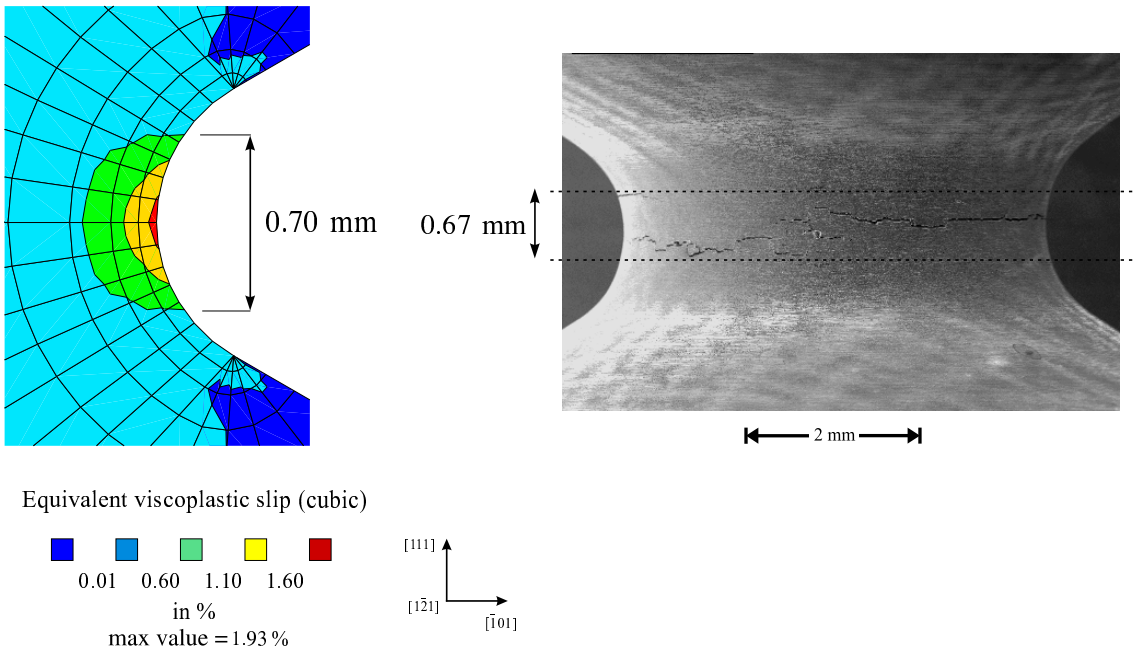

Figure 44: Correlation between the location of the maximum cumulated slip and notch cracking. $\langle 111 \rangle$ oriented specimen 8 with 1 mm notch radius.

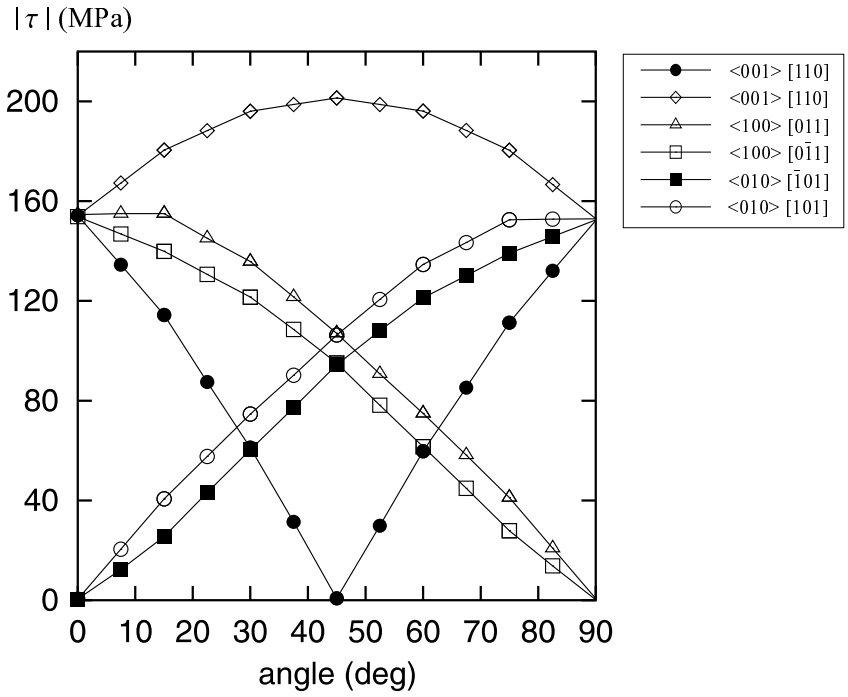

Figure 45: Resolved shear stresses along the circumference of the 1 mm notch radius and $\langle 001 \rangle$ oriented specimen at the axial height of maximum inelastic strain of one slip family, i.e. of cubic slip. The angle of 0° corresponds to the [100] secondary crystallographic axis.

3.2 A deterministic approach for LCF at notches

3.2.1 Definition of a critical variable

The damage of crystalline materials is influenced by intersecting slip systems at the surface (Cottrell-Hull mechanism [Cottrell and Hull, 1957]). The *resolved shear stresses* on such slip systems, which represent not the full stress state but are *physical components* of it, are the more adequate loading quantities for a single crystal.
Thus, a possible choice of critical variable for damage is to take *at the point of maximum total cumulated slip on the surface, the value of the maximum resolved shear stress for this slip family*.

3.2.2 A τ-N fatigue diagram

In order to design a fatigue diagram for the resolved shear stress we have simulated all the LCF tests given in Fig. 46 for a homogeneous volume element. The calculations give their maximum resolved shear stress ranges, taken from the 18 values of the two slip families (cubic and octahedral), versus the number of cycles to failure, see Fig. 47. Thus it is possible to draw a straigth line in this log-log representation. If we assume that the scatter, included in the "factor 3" scatter band limited by the dotted lines, is acceptable, this diagram is suitable to assess the lifetime of the point on the surface which has the highest total cumulated slip.

For example, Fig. 45 shows that the distribution of the resolved shear stress for cubic slip along the circumference of the 1 mm notch radius $\langle 001 \rangle$ oriented specimen at the loading amplitude of the first cycle where SC16 at 950^oC is already cyclic saturated essentially. The origin of the angle corresponds to the point of the plane $\langle 100 \rangle$ and which presents the maximum total cumulated slip for cubic slip systems (Fig. 35). The maximum resolved shear stress range is 320 MPa in this area. It is not the highest resolved shear stress in the vicinity of the notch. It is strongly determined by the anisotropy of the material. If we insert this value of the critical variable and the value of the lifetime (id est 583 cycles for the test 4, see table 8) in this fatigue diagram, the point is within the scatter band (see the symbol $\ominus$ in Fig. 47).
The assessed lifetime at 0.2 mm notch radius is lower than the experimental one within a factor of 3 too, see the symbol $\oslash$ in Fig. 47.
Note that the simple method based on the Mises stress does not work for these tests: the symbols are out of the scatter band in Fig. 46.

As a result, the number of cycles to failure of the performed LCF tests on notched specimens are comparable to the lifetimes of smooth specimens at the same maximum resolved shear stress value at maximum total cumulated slip.

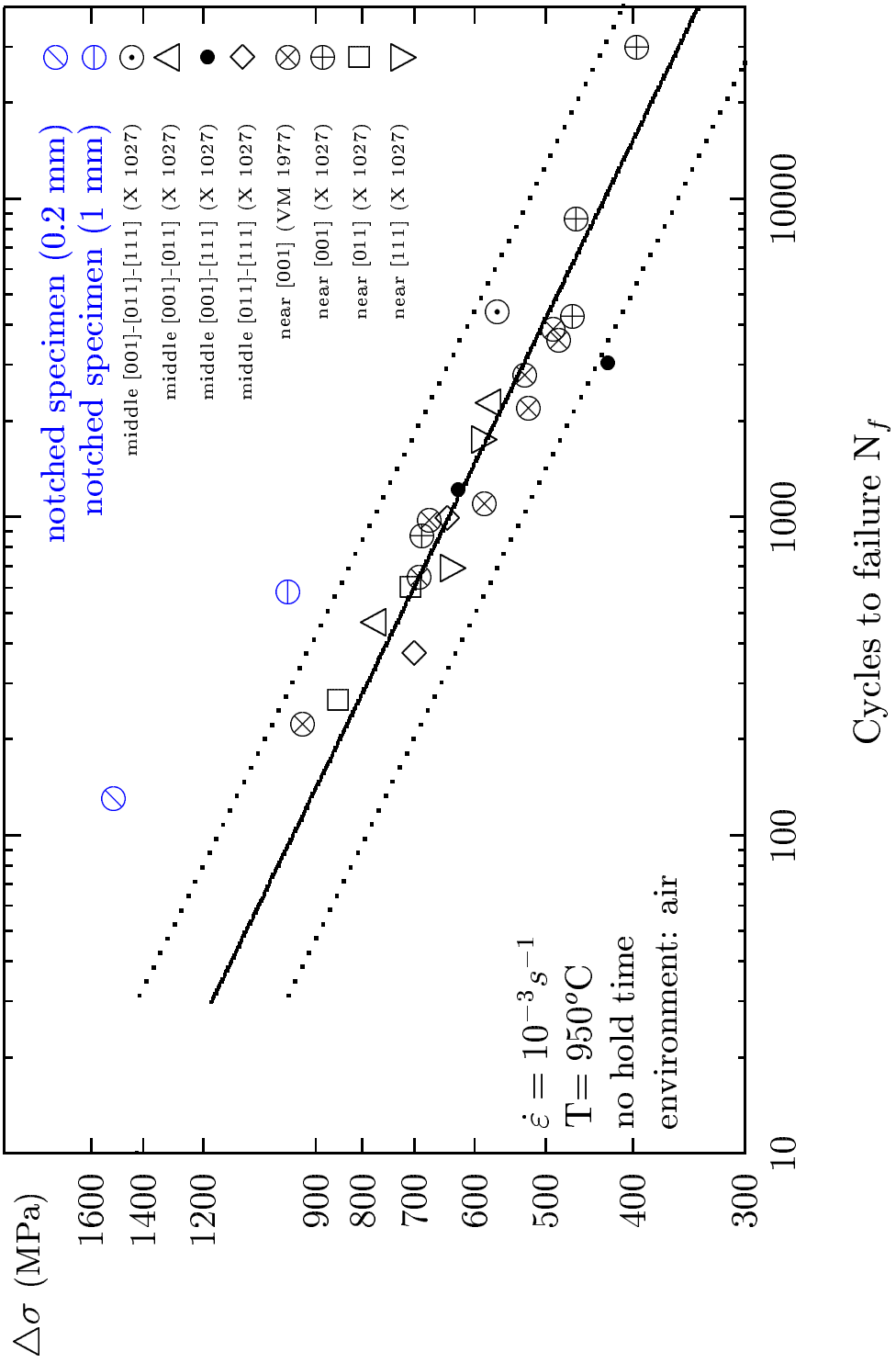

Figure 46: Experimental fatigue life for different orientations depending on the axial stress range for the single crystal superalloy SC16 at uniaxial loading for different charges (X,VM). The maximum Mises stress range in the ⟨001⟩ specimen with 0.2 and 1 mm notch radius are inserted.

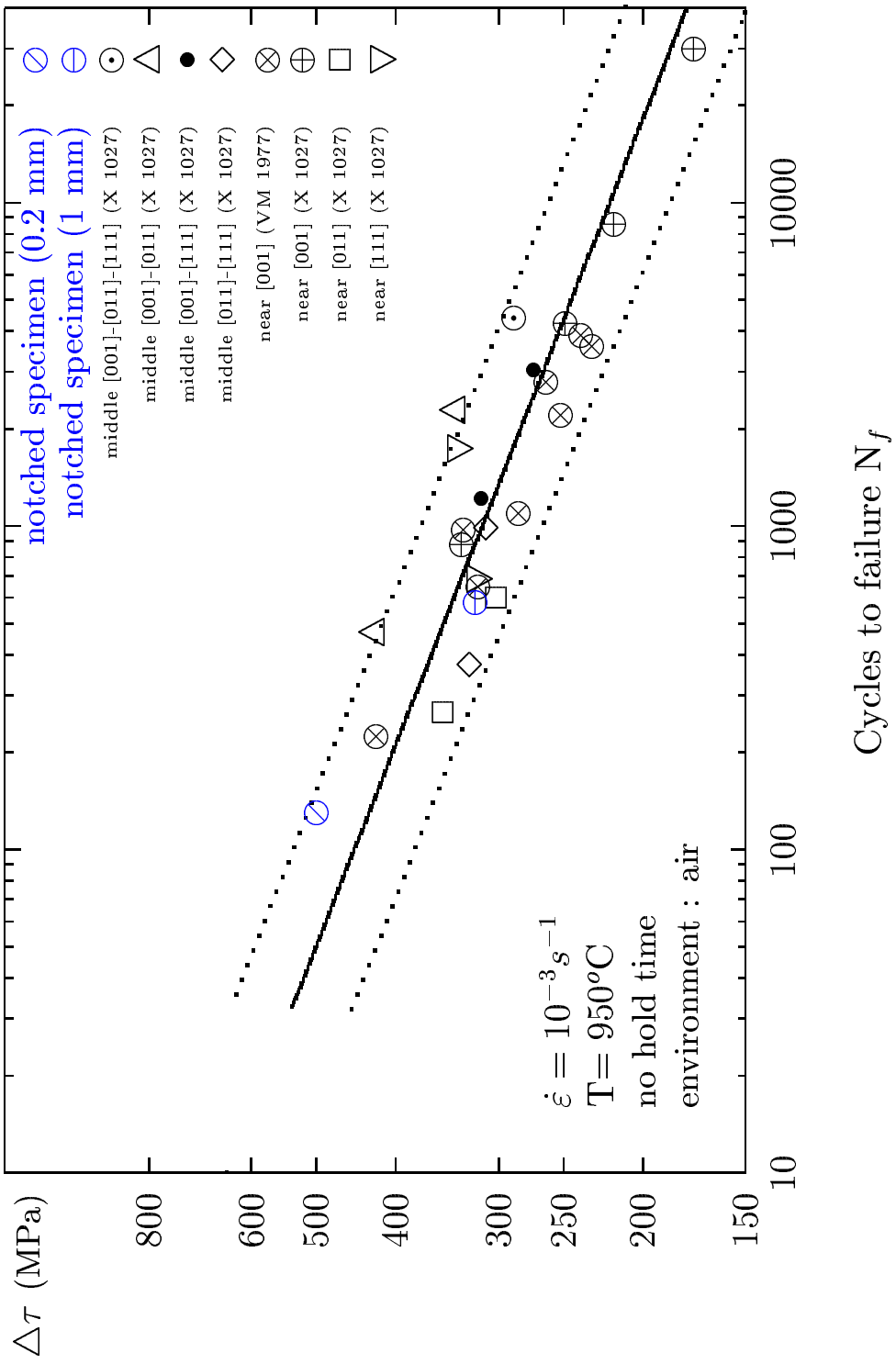

Figure 47: Experimental fatigue life for different orientations depending on the maximum resolved shear stress range simulated for the single crystal superalloy SC16 at uniaxial loading for different charges (X,VM). The maximum resolved shear stress range at maximum total cumulated slip in the $\langle 001 \rangle$ specimen with 0.2 and 1 mm notch radius are inserted.

3.3 A multiscale probabilistic failure model

3.3.1 Introduction

For many materials, the failure process starts due to local defects introducing perturbations in the stress/strain fields, and giving rise to stress levels unexpected at the macroscopic scale. This is the case when defects or pores are created by the material processing (ceramic, cast materials) [Dennis, 2000]. On the other hand, the effect of these defects differs according to their relative position with respect to the free surface of the material. The present model is designed to account for both the real distribution and location of the defects in the specimen, and for the resulting statistical aspect. The method proposed can be applied to various types of transformation from the macroscopic stress state and the stress used for deriving the criterion and with various initiation criteria.

3.3.2 General scheme of the method

The model can be applied in a post-processing, after a structural computation, if we neglect the coupling between stress-strain behaviour and damage. For the versions shown in the following, the input data is the macroscopic stress history. Macroscopic strain or any kind of macroscopic variable might also be used, depending on the critical variables of the local model.

(1) The first step is the evaluation of the transformed stress tensor $\underset{\sim}{\sigma}$, trying to approach a variable being more representative for the real physical phenomenon, knowing the history of the macroscopic stress $\underset{\sim}{\blacksquare}$ and a function describing the defect distribution.

Defects act as stress concentrators, especially in the vicinity of the surface, and the relation between the microscopic stress $\underset{\sim}{\sigma}$ around a casting defect or pore and the macroscopic $\underset{\sim}{\blacksquare}$ obtained by a classical structural calculation on an assumed flawless component can be written:

$$\underset{\sim}{\sigma} = \underset{\approx}{\mathbf{A}}\left(\frac{r}{d}\right) : \underset{\sim}{\blacksquare} \tag{8}$$

In the case of classical continuum mechanics, the operator $\underset{\approx}{\mathbf{A}}$ depends on the ratio r/d (r=defect radius, d=distance of the centre of the defect to the free surface). Characterization of such an operator by Finite Element computations was the objective of a study of Pore-Surface Interactions [Cailletaud and Quilici, 2000].

(2) the stress $\underset{\sim}{\sigma}$ is then used in a local criterion, predicting either abrupt failure or initiation.

In the following, a simple initiation model of the form given will be considered:

$$N_i = \left(\frac{\Delta\sigma}{M}\right)^{-m} \tag{9}$$

(3) It is now possible to evaluate the time to failure (or initiation), allowing the user to estimate either the failure probability of the component, or the probability to reach a given number of cycles to initiation during a fatigue loading (respectively P_f or $P_f(N_i)$). The function used for that purpose involves an integral on the volume V of the component, and an integral on the defect radius r, measuring the probability of having a critical size ($r > r_c$) at the current point, the volume fraction $f_v(r)$ of defect of size r being known from experiment:

$$P_f(N) = 1 - exp\left[-\int_V \left(\int_{r_c(N,\mathbf{x})}^{\infty} f_v(r)dr\right) dV(\mathbf{x})\right] \tag{10}$$

Using this equation is fully justified when the weakest link assumption is verified. This is true for brittle failure, and it will be supposed that it remains acceptable in the case of fatigue starting from preexisting defects, when the defect volume fraction is low, so that there is no significant interaction between the various defects.

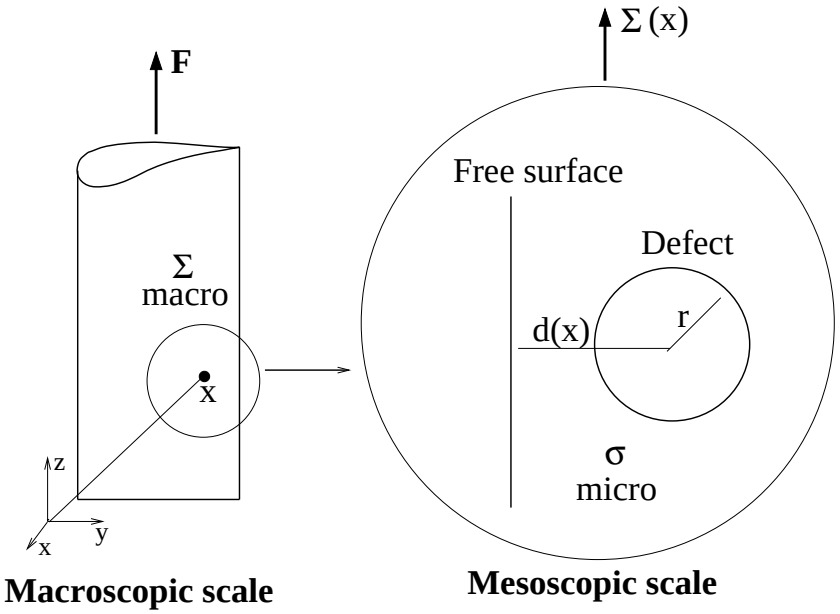

Figure 48: Application of the multiscale model on a structural component.

The initiation model, Eq. (9), defining the microscopic stress level $\underset{\sim}{\sigma}_c$ giving initiation in N_i cycles, the defect critical size $r_c(N_i, \mathbf{x})$ at a point with coordinate $\mathbf{x}$ needed to perform the integration in (10) can be derived from equation (8):

$$\underset{\sim}{\sigma}_c = \underset{\approx}{\mathbf{A}}\left(\frac{r_c}{d(\mathbf{x})}\right) : \underset{\sim}{\blacksquare}(\mathbf{x}) \tag{11}$$

where $d(\mathbf{x})$ is the distance to the surface at coordinate $\mathbf{x}$ (see Fig. 48).

3.3.3 Calibration of the material parameters

The defect volume fraction:

The defect volume fraction $f_v(r)$ integrated in equation (10) can be obtained from experimental data of densities of defects with a given size (Fig. 49).

A Gaussian distribution has been chosen to fit those microstructural observations (equation 12, where V_0 is a reference volume, typically chosen equal to 1 mm^3, B, μ and δ three fitting parameters).

$$f_v(r) = \frac{B}{V_0} exp\left[-\left(\frac{r-\mu}{\delta}\right)^2\right] \tag{12}$$

Results of the parameter identification are summarized on Fig. 50.

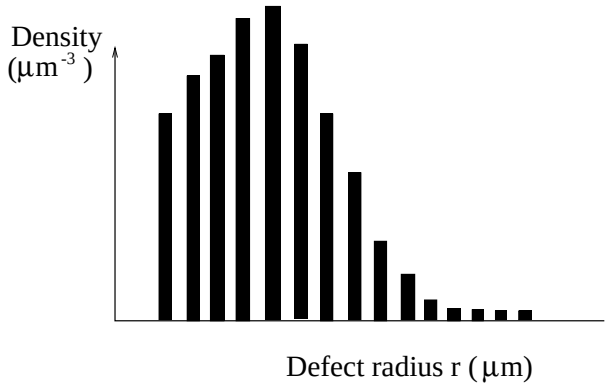

Figure 49: Density of defects experimental data.

The macro-micro relationship:

The Finite Element calculations performed in [Cailletaud and Quilici, 2000] to study porosity-surface interactions are summarized in table 9.

The results are given for traction/compression loadings (loading factor (R=-1) applied on defect geometries with several d/r ratios, at the point situated close to the defect at the free surface side where maximum stress levels are obtained.

The calculations performed under repeated loadings (loading factor R=0) have shown that after an adequate number of cycles, mean stress disappears in the most critical regions under the effect of plastic flow, and that the same local stress amplitude is finally obtained under (0,+2ε) and (-ε,+ε) loadings.

Therefore the macro-micro calibration relationship can be expressed in terms of stress amplitude:

$$\Delta\sigma = A\left(\frac{r}{d}\right)\Delta\Sigma \tag{13}$$

In the case of multiaxial loadings, $\Delta\Sigma$ can be replaced by a *stress range* calculated as the diameter of the smallest sphere including the loading path, a von Mises type invariant being used to calculate a distance in the 6-dimension stress space. Such a method is

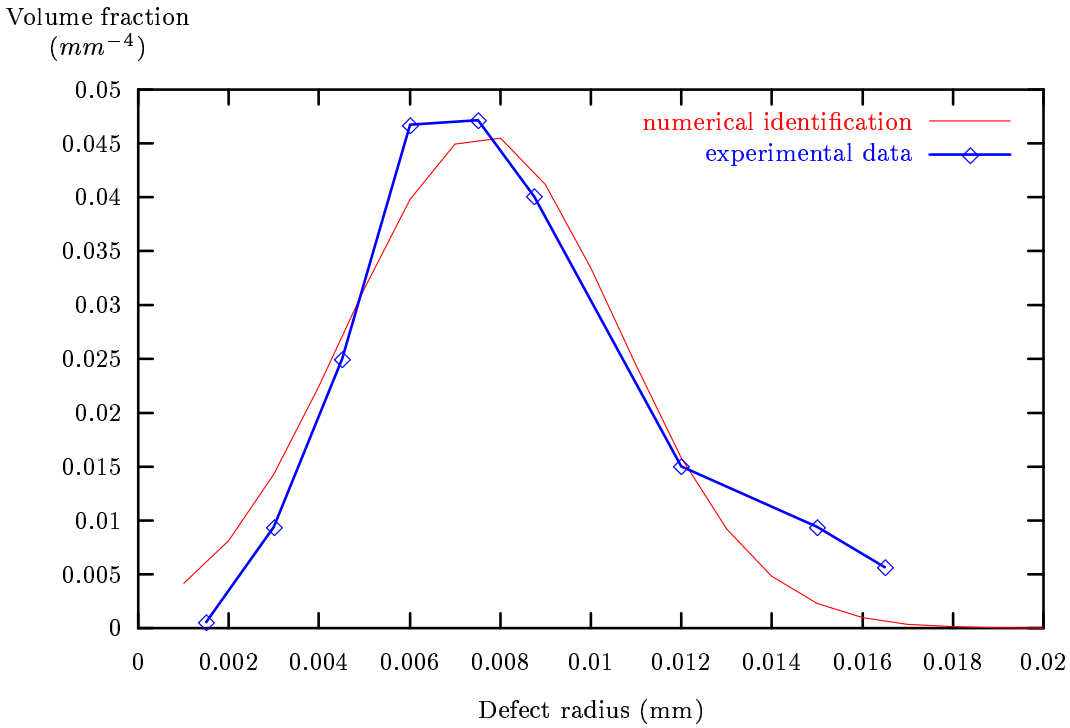

$$B = 4.59\ 10^{-2} mm^{-4}, \delta = 4.26 \mu m, \mu = 7.6 \mu m, V_0 = 1 mm$$

Figure 50: Defect volume fraction identification.

already implemented in the FE code ZéBuLoN to evaluate fatigue life under multiaxial loadings.

Maxima situated at the free surface side						
	$\frac{d}{r} = 0.$	$\frac{d}{r} = 1.1$	$\frac{d}{r} = 1.4$	$\frac{d}{r} = 2.$	$\frac{d}{r} = 4.$	$\frac{d}{r} = \infty$ (macro)
sig_{33} (MPa)	543.	638.	578.	551.	528.	345.
ein_{33} (%)	0.29	2.08	0.64	0.42	0.32	0.077
eto_{33} (%)	1.12	2.99	1.44	1.19	1.07	0.64

Table 9: Maximum stress in the tensile loading direction for different defect geometries of single crystal superalloy CMSX2.

Table 9 also shows that significant overstress is mainly obtained for defects close to the surface $(d/r < 1.4)$ and that around open defects $(d/r = 0)$ stress levels are the same as for defects situated far from the surface. This allows us to neglect the influence of open defects, and to replace the integration in (10) by an integration from r_c to d:

$$P_f(N_f) = 1 - exp\left[-\int_V \left(\int_{r_c(N_f,\mathbf{x})}^{d(\mathbf{x})} f_v(r)dr\right) dV(\mathbf{x})\right] \tag{14}$$

In order to get a closed form analytical solution, a macro-micro calibration relationship

of the form given by equation (15) is assumed. However, such a simple relationship is unable to predict correctly the results, and a direct numeric interpolation should be preferred for the implementation of a FE post-processor.

$$\Delta\sigma = A(\Delta\Sigma)^b \, exp\left(a\frac{r}{d}\right) \tag{15}$$

The values of the parameters *A*, *b* and *a* identified to fit the FE results are summarized on Fig. 51.

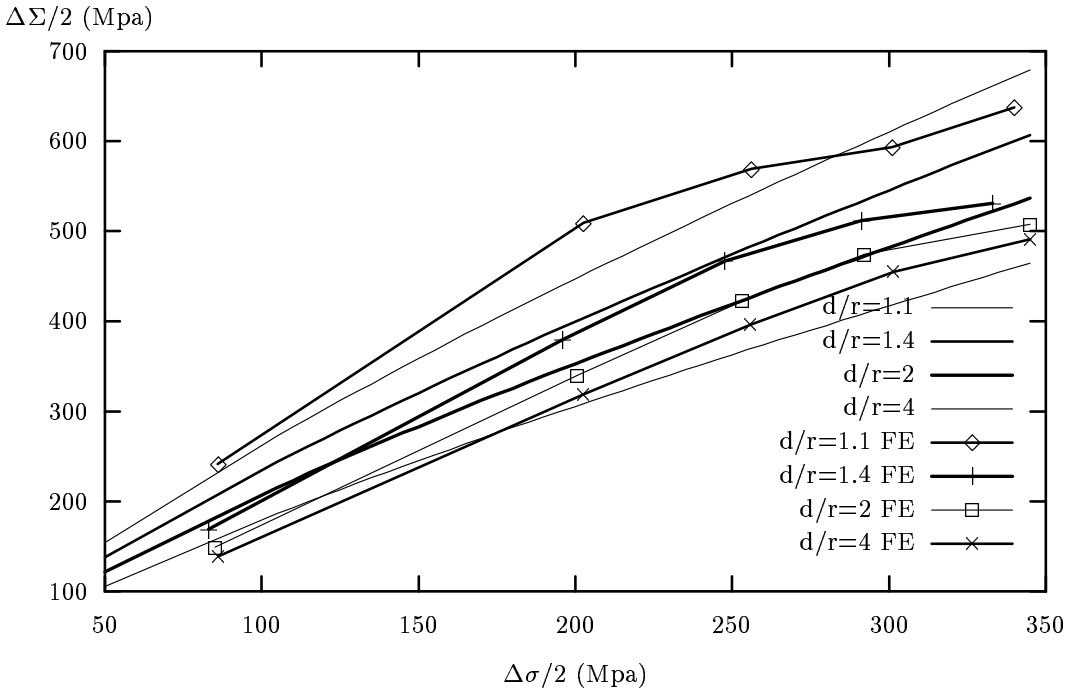

$$A = 4.55, b = 7.6710^{-1}, a = 5.7710^{-1}$$

Figure 51: Identification of the macro-micro relationship.

The initiation model by inverse problem:

An analytical application:

In order to illustrate the capabilities of the model, a simple analytical example concerning a cylindric bar (see Fig. 52) is presented in the following.

On this simple geometry the expression of the probability of failure can be written:

$$P_f(N_f, \Delta\Sigma) = 1 - exp\left[-\int_V \left(\int_{r_c}^{d} f_v(r)dr\right) dV\right] \tag{16}$$

$$P_f(N_f, \Delta\Sigma) = 1 - exp\left[-2\pi h \int_0^R \rho \left(\int_{r_c(\rho)}^{d(\rho)} f_v(r)dr\right) d\rho\right] \tag{17}$$

$$\text{with } d(\rho) = R - \rho \quad \text{and} \quad r_c(\rho) = C_2 d(\rho)$$

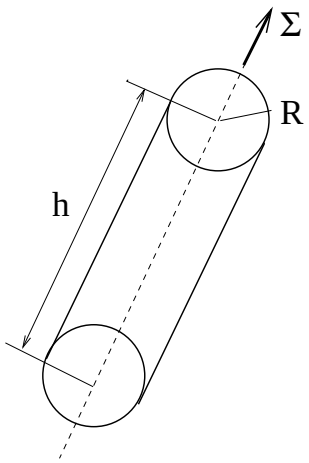

Figure 52: Application of the multiscale model on a cylindric bar of length h and radius R.

Coefficient C_2 is derived from the initiation model (equation (9)) and the macro-micro relationship (equation (15)):

$$C_2 = \frac{1}{a} log \left[\frac{M N_f^{-\frac{1}{m}}}{A (\Delta\Sigma)^b} \right]$$

Using the analytical expression identified for the defect volume fraction (equation (12)), the integration over radius ρ can be explicitly calculated as:

$$\int_{r_c(\rho)}^{d(\rho)} f_v(\rho) d\rho = \frac{B\sqrt{\pi}\delta}{2} \left[erf\left(\frac{R-\rho-\mu}{\delta} \right) - erf\left(\frac{C_2(R-\rho)-\mu}{\delta} \right) \right]$$

Identification for SC16:

The Zébulon Optimizer is used to find a value of parameters M and m that best fit the BAM fatigue results on smooth specimen. The previous analytical expressions have been used to identify a set of these initiation parameters for SC16 at 950°C.
For each set of trial M and m values calculated by the Optimizer, the analytical application presented previously is used to derive number of cycles to failure (probability of 0.5) for a cylinder whose dimensions correspond to BAM fatigue test smooth specimen:

- radius R=4.5mm
- length h=26mm

Results of the identification are summarized on Fig. 53.

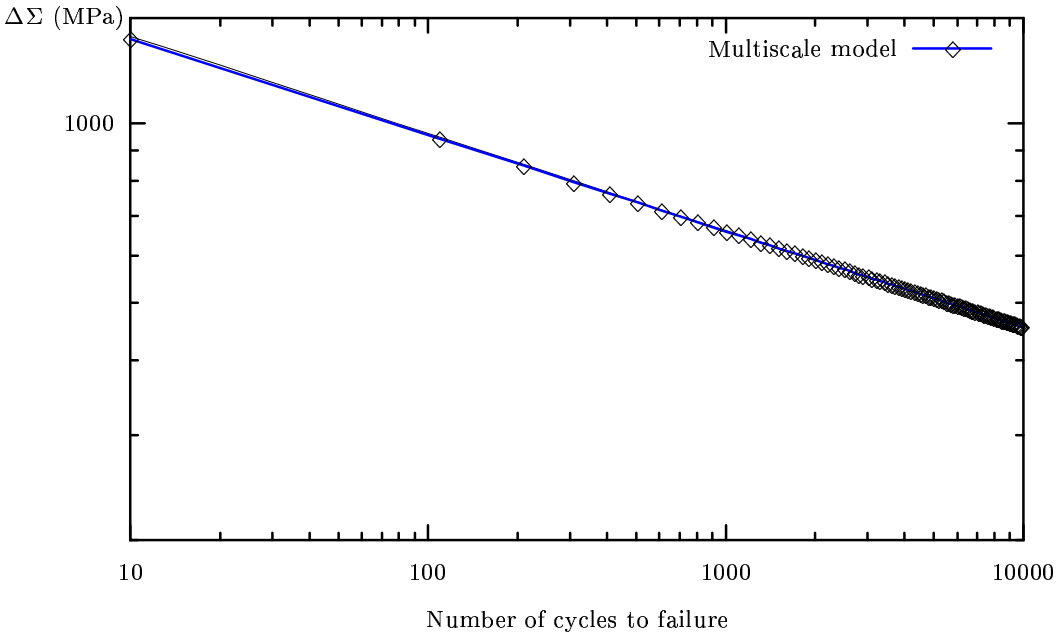

Figure 53: Identification of micro initiation parameters for SC16 at 950°C: M=1550 MPa, m=8.1

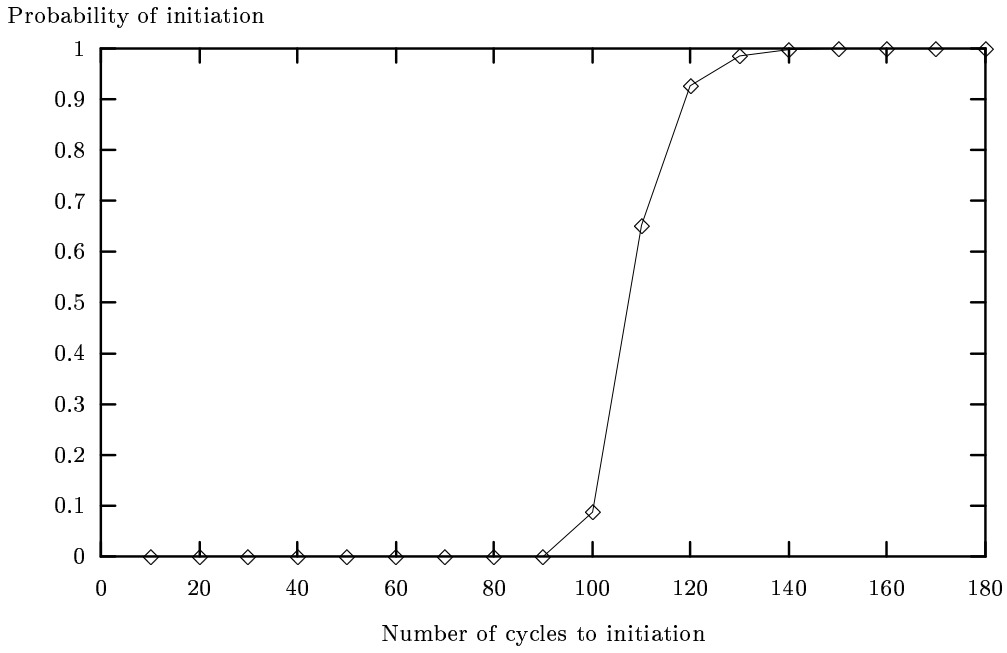

Figure 54: Failure probability versus number of cycles

Summarize:

Equations and material coefficients are summarized in table 10.

Defect volume fraction
$$f_v(r) = \frac{B}{V_0} exp\left[-\left(\frac{r-\mu}{\delta}\right)^2\right] \quad (18)$$
Parameters B, μ, δ identified by microstructural observations
Macro-micro relationship
$$\Delta\sigma = A\,(\Delta\Sigma)^b\, exp\left(a\frac{r}{d}\right) \quad (19)$$
Parameters A, b, a identified by FE calibration on representative defect geometries
Microscopic initiation model:
$$N_f = \left(\frac{\Delta\sigma}{M}\right)^{-m} \quad (20)$$
Parameters M, m identified by inverse problem when applying the multiscale model on fatigue test results

Table 10: Summary of the multiscale model equations.

Material coefficients such as volume fraction of defects and macro-micro transition rule are assumed to be the same as those calibrated for CMSX2. The whole material coefficients set is given in table 11.

B (mm^{-4})	μ (μm)	δ (μm)	A	b	a	M (MPa)	m
$4.59\ 10^{-2}$	7.26	4.26	4.55	$7.671\ 10^{-1}$	$5.771\ 10^{-1}$	1550	8.1

Table 11: Parameters for SC16 at 950°C.

3.3.4 Application to the notched specimen

The different steps needed to obtain probabilities of failure (or more exactly initiation) with the multiscale model presented above are summarized hereafter.

- Step 1: FE element calculation of several loading cycles up to a stabilized response,
- Step 2: Post-processing to evaluate the multi-axial stress range $\Delta\Sigma$ of the stabilized cycle,

- Step 3: Generation of a 2D surface mesh and transfer of results from the 3D analysis,
- Step 4: Application of the multiscale post-processor on the surface mesh.

This methodology has been applied to the notched fatigue specimen (notch radius 1mm, see Fig. 13 for the geometry) and for the single crystal SC16 which is oriented near $\langle 001 \rangle$.

Step 1: FE calculation up to the stabilized cycle.

The finite element results come from section 3. The analysis of two cycles (loading factor R=-1) was performed with Zébulon and the single crystal constitutive model identified in the first part section 3. Isocontours of von Mises stress equivalent at the point of maximum tensile load during the second (stabilized) cycle are plotted on Fig. 55. Note that the maximum value is not located at the notched root.

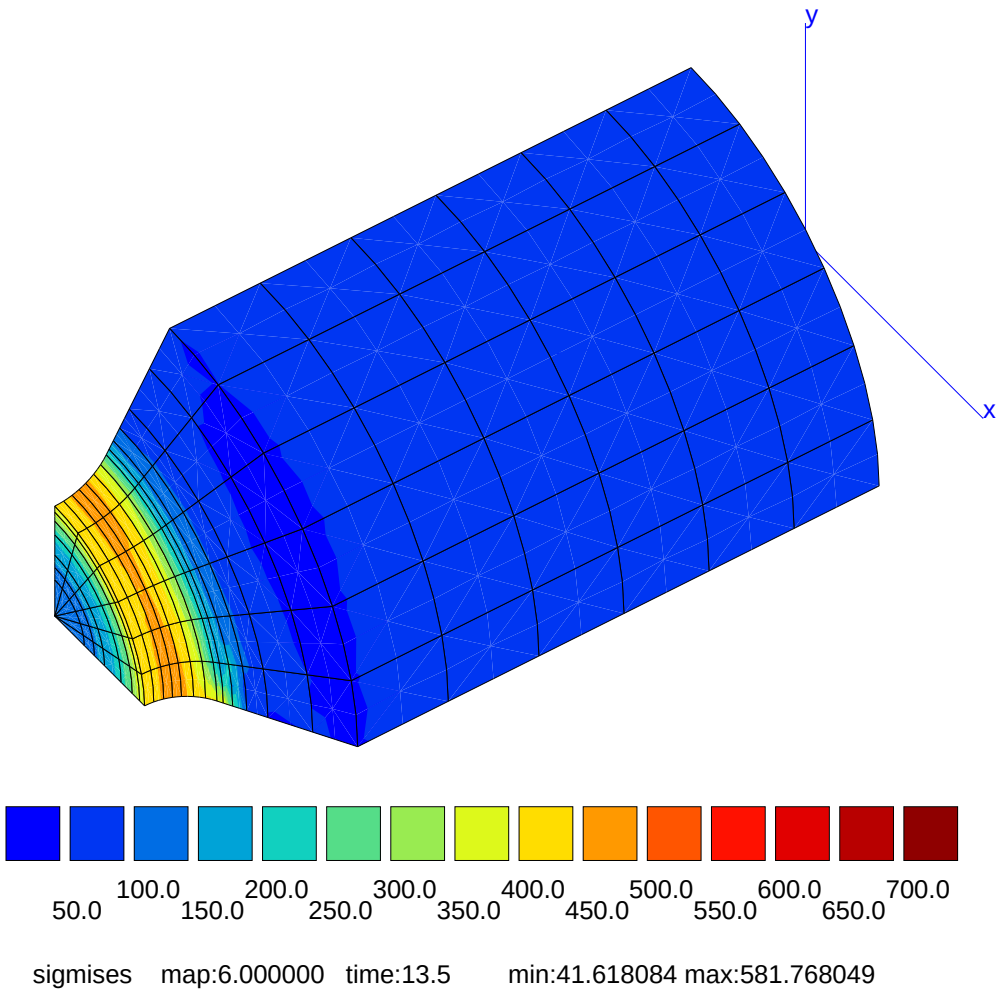

Figure 55: Isocontours of Mises stress equivalent.

Step 2-3: Multiaxial ΔΣ calculation and transfer of results on the surface mesh.

The multiaxial stress amplitude during the second cycle is calculated using the **range** post-processor available in Zpost. Results are then transferred to the surface mesh as shown on Fig. 56.

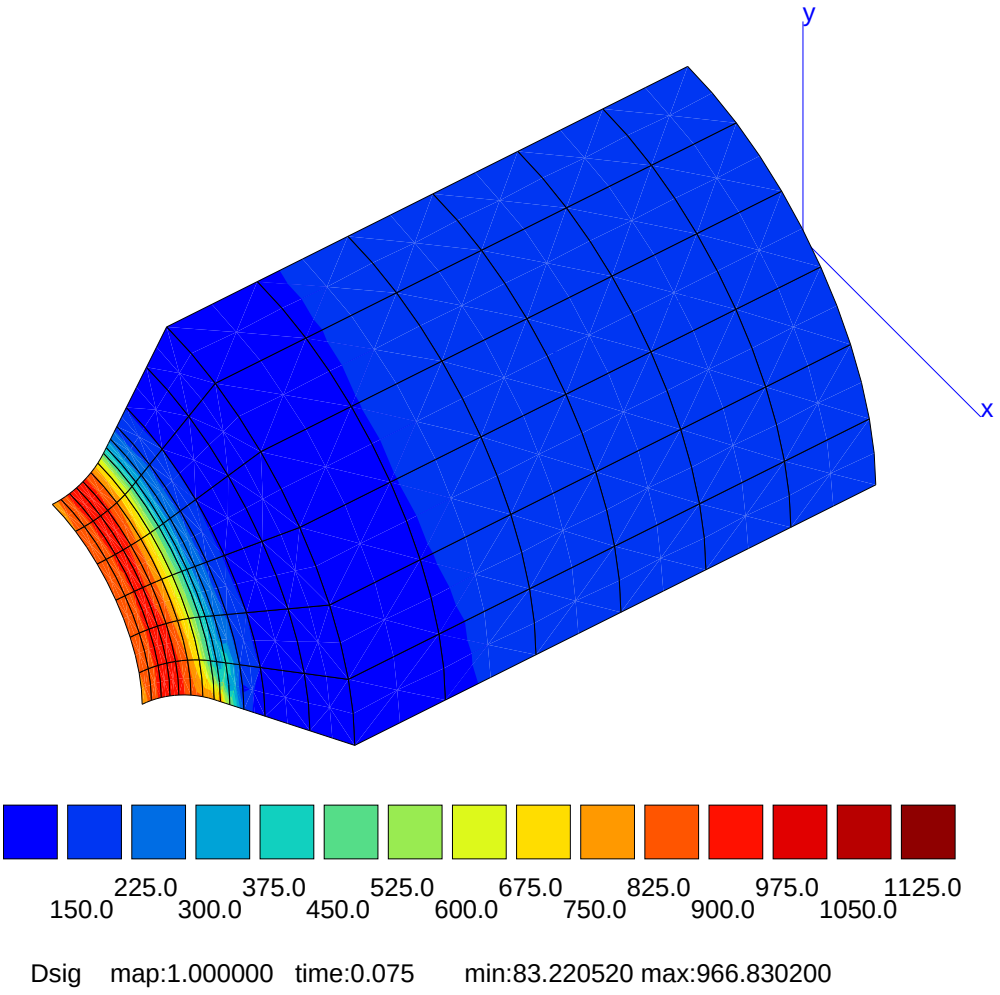

Figure 56: Isocontours of multiaxial ΔΣ on the surface mesh

Step 4: Application of the multiscale model on the surface mesh.

Because of the axial symmetry only one eigth of the structure has been modelled, and a corresponding multiplicative factor must be applied when calculating the probability of failure by integration over the surface of the specimen. The model gives curves of probability of failure versus number of cycles. Such a curve is drawn on Fig. 54, where it can be seen that the probability of failure only becomes significant after about 100 cycles. The experimental number of cycles to failure is 583, see table 8. Thus the multiscale model is too conservative for this component.
Isocontours of failure probabilities in a given number ofcycles can also be obtained. Such plots for number of cycles N equal respectively to 90, 100 and 110 and 120 are repre-

sented on Figs. 57 to 60.

This result reveals the limit of the conventional criterion. The analysis of the surface rupture of a bulk smooth SC16 specimen after LCF test at 950°C shows that the crack depth corresponding to 7.6% stress drop in tension is equal to 3 mm. On the other hand Figs. 21 and 22 show that only 1 mm crack depth leads to a stress drop of 10% for the notched specimen. In consequence one has to compare the number of cycles corresponding to the same crack depth or length. Unfortunately the maximum crack depth in the bulk smooth specimen corresponding to 5% stress drop is not available for SC16.

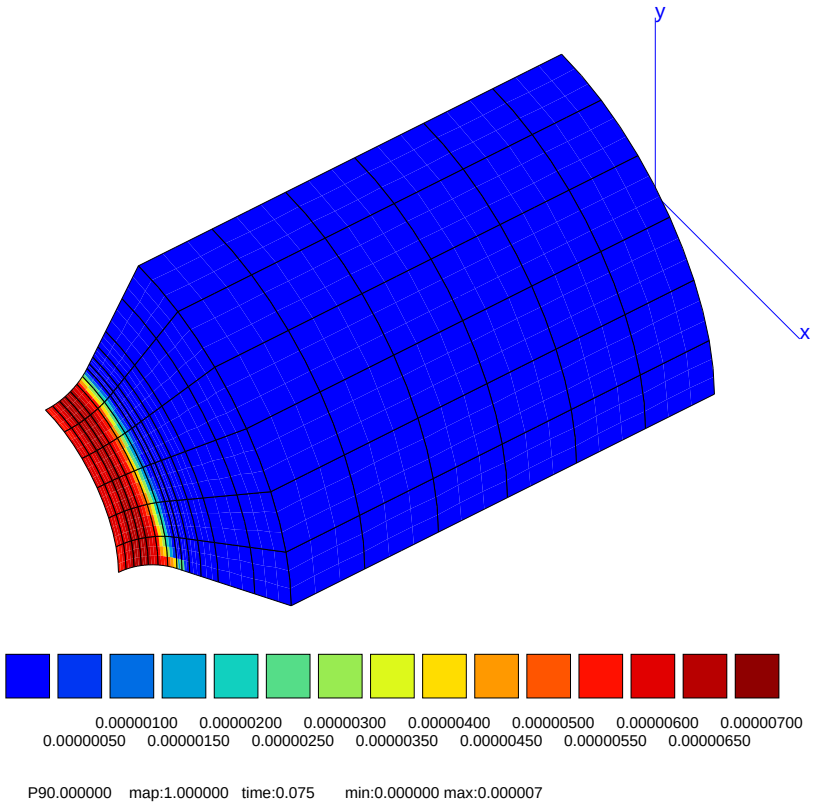

Figure 57: Isocontours of failure probability in 90 cycles

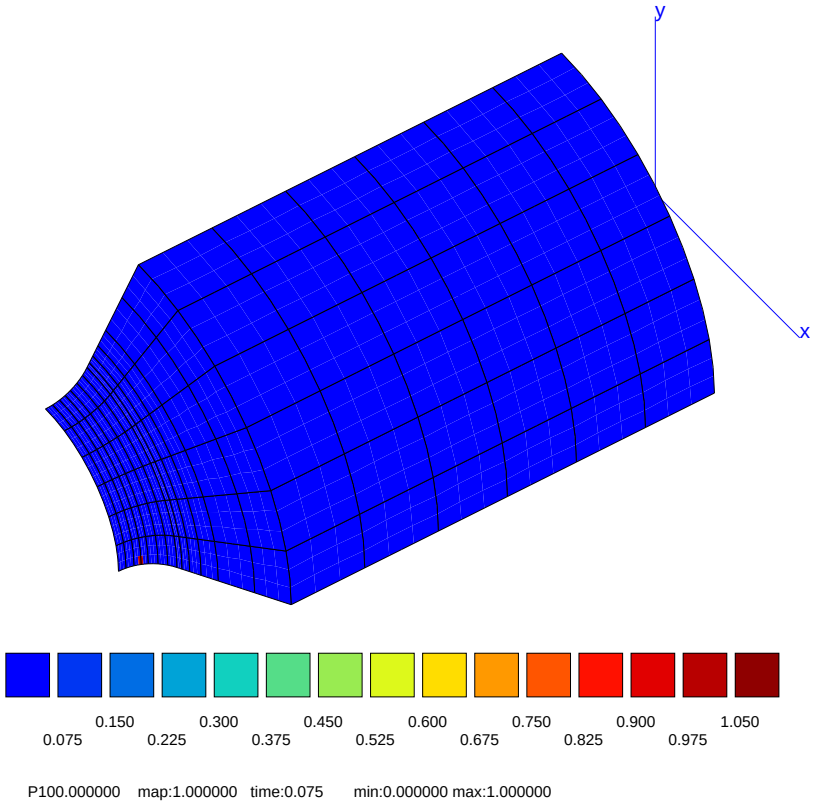

Figure 58: Isocontours of failure probability in 100 cycles

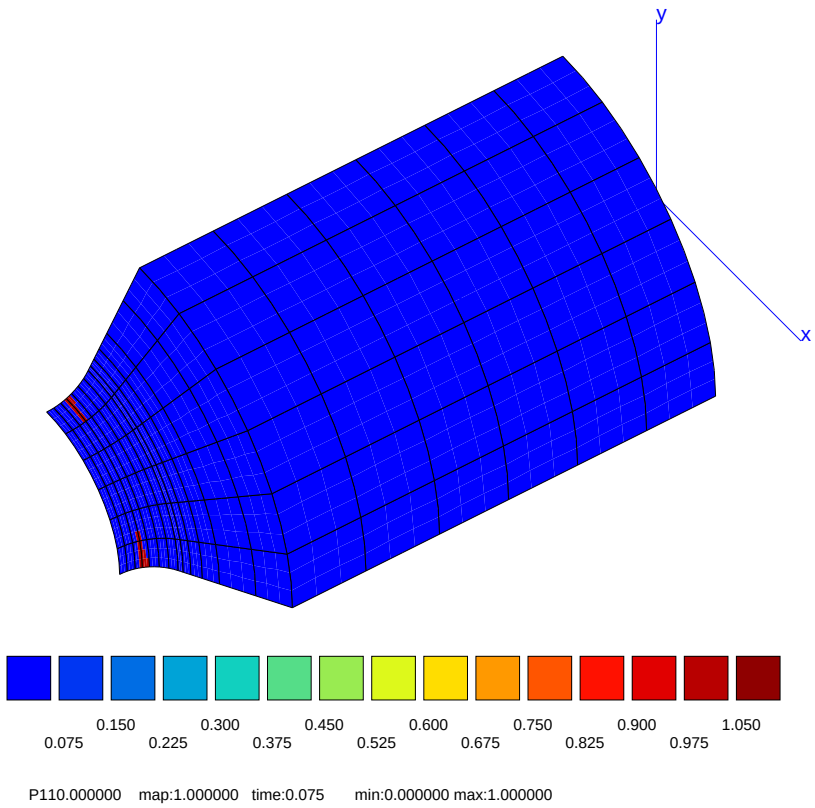

Figure 59: Isocontours of failure probability in 110 cycles

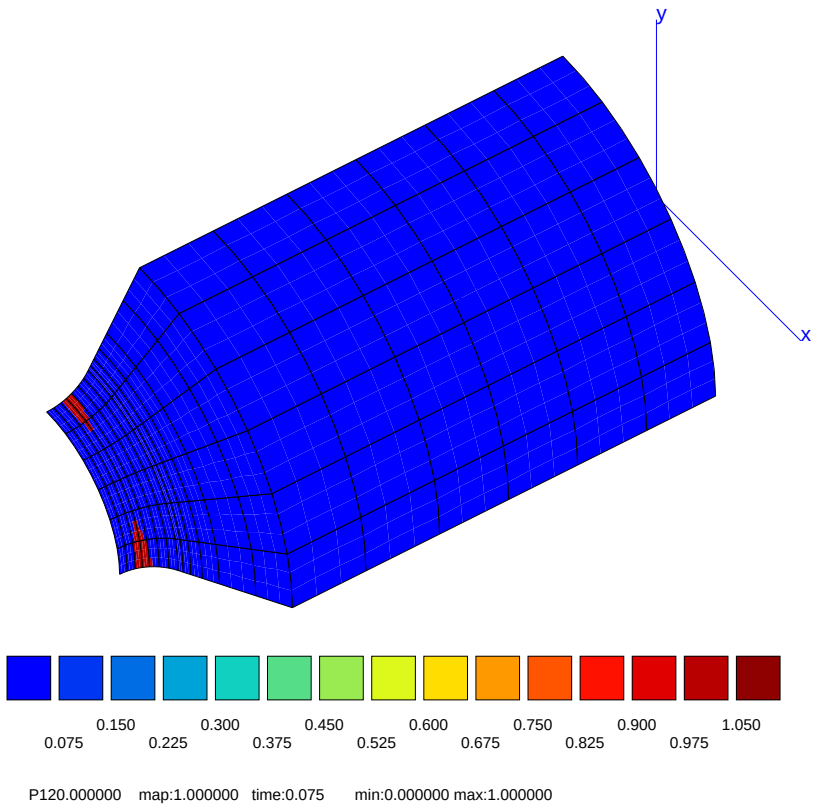

Figure 60: Isocontours of failure probability in 120 cycles

3.4 Discussion

Two steps should be considered to predict the lifetime of notched components, first the computation of the viscoplastic strain-stress state at the notch, then the failure criterion. The procedure must also save CPU time in order to stay in the framework of industrial applications. Chaudonneret [Chaudonneret and Chaboche, 1986] used such a method for isotropic materials. An adapted Neuber's rule and a non linear cumulative fatigue damage led to accurate results for different loadings (pure fatigue, hold time and creep). For axisymmetrical structures such as a cylindrical notched specimen the loading is strongly multiaxial. Thus the crucial point, to apply the same approach, would be the choice of an equivalent stress for our anisotropic material.

Thanks to the development of the numerical algorithms and of the power of computers, it is now reasonable to compute real components in 3D with the realistic constitutive equations identified in this work. The two successive steps are the finite element computation (no simplification to be made at this level), then a damage post-processing. We have built a lifetime assessment rule for pure fatigue based on the maximum resolved shear stress, a possible critical variable for the damage.

Another difficulty is a pertinent definition of the initiation criterion. The problem remains the characteristic size of the macro crack associated with the conventional lifetime. Traditionally one defines the macro-crack initiation at the "engineering level" which corresponds to a surface crack 0.5 or 1 mm in depth [Chaudonneret and Chaboche, 1986], [Defresne and Rémy, 1990]. [Defresne and Rémy, 1990] have checked this initiation criterion (i.e. a surface crack 0.12 mm in depth) with observations of fracture surfaces of interrupted test specimens. They found that the period of crack growth between initiation and the formation of a macro crack is no more negligible for a life duration less than 10^4 cycles.

Our interrupted test of a $\langle 001 \rangle$ oriented specimen provides such an information for our criterion. Some cracks were observed between 236 and 560 cycles. Our lifetime criterion corresponds to the crack depth at 5% load drop. This load drop is reached for the notched specimen with 1 mm notch radius at 583 cycles, Figs. 27, 28 and 29 show 0.32 mm maximum crack depth at that load drop. The diameter of the smallest cross-section of this specimen is approximately half of the diameter of the smooth specimens. Thus, maybe the crack depth of the smooth specimens at 5% stress drop could be twice of 0.32 mm: this gives an assessment of 0.7 mm or more roughly 1 mm for the crack depth of the smooth specimens at the number of cycles to failure, i.e. at 5% stress drop. According to Figs. 22 and 27, the maximum crack depth can grow from 5% to 10% stress drop, 0.32 mm to 1 mm, respectively, by a factor 3.
Concerning the site of the crack front relative to the crystal axes, the analysis of the fracture surfaces, Figs. 21, 22, is a difficult task. The crack initiation depends also on the defect (e.g. casting pore) location on the circumference. Nevertheles, the fracture surfaces illustrate the strong anisotropy of plasticity, the crack front seems to be well defined, but we cannot identify the fracture plane with a sufficient accuracy.

[Neumann, 1974] has already suggested that such circumferentially notched crystal is not pertinent to produce macroscopically plane fracture surfaces. He showed how some well defined fatigue tests with bending specimens of oriented copper single crystals could verify a model based on slip processes at propagating fatigue cracks. At the BAM other experiments on SC16 oriented notched specimens revealed macroscopically plane fracture surfaces [Ziebs and Frenz, 1997]. Nevertheless the problem of the definition of a pertinent crack driving forces remains. [Telesman and Ghosn, 1995] proposed to relate them with the resolved shear stresses which control the octahedral crack growth in single crystal alloys at high temperature. They invoked the important role of the frequency in the types failure process. Indeed at high temperature oxidation should influence the crack growth mechanism at low frequencies [Defresne and Rémy, 1990]. We assume in this study that such environmental effects are negligible for a global strain rate of $10^{-3}\,s^{-1}$.

Besides the inhomogeneity of resolved shear stresses and slip on the surface, decreasing stresses behind the notch root are present within a critical volume for crack initiation. [Chaudonneret and Chaboche, 1986] has already suggested that such stress gradient should be taken into account. A gradient dependent criterion for high-cycle fatigue was developed in [Papadopoulos and Panoskaltsis, 1996]. So, one can put forward the same idea to low-cycle fatigue and single crystals in order to include in lifetime assessment the influence of the small size of the highly loaded volume at sharp notches on the lifetime.

As classically observed for polycrystalline materials the tested notched specimens live significantly longer than the smooth ones at the same maximum Mises stress at the notch. Compare, for example, the lifetime at maximum Mises stress range in the $\langle 001 \rangle$ specimen with 1 mm notch radius, Fig. 46, with the experimentally obtained lifetime for that specimen (test 4) given in table 8. That means at least that the fatigue life at notches is not determined by the maximum value of this equivalent stress alone.
The physical mechanism of the crack initiation in SC16 at this strain rate leads us to take into account the size of the material to compare the lifetime between the bulk and the notched specimens. Indeed for the same state of stress, the volume in the notched specimen is smaller than the one in the bulk specimen. Thus the probability of failure in the notch is the lowest. Finally the argument of the size effect gives a good explanation for the too conservative approaches.

4 Conclusion

Fractographic observations on $\langle 001 \rangle$ oriented notched specimens showed that the main cracks are located not directly at the notch root, instead they are shifted a little away from these symmetry planes. This corresponds to the similarly shifted maximum total cumulated slip that is cumulated on cubic slip systems according to the numerical analysis.
For the other orientations $\langle 011 \rangle$ and $\langle 111 \rangle$ the main crack is more concentrated at the notched root.

In strain-controlled LCF tests on SC16 smooth specimens at different orientations, 950 °C and $10^{-3}\ s^{-1}$ strain rate, essentially no dependence of the fatigue lifetime on the orientation was found at the same axial stress range.

The lifetimes of the performed LCF tests on notched single crystal specimens can be assessed from the cycles to failure of the smooth specimens taking as lifetime parameter the maximum resolved shear stress present at the location of maximum total cumulated slip in the notch. This deterministic approach can be used in the framework of industrial applications due to its simplicity.

The size effect phenomenon should play an important role for SC16 single crystal superalloy since the cracks initiate from casting pores at high strain rates. Thus we have designed a probabilistic failure modelling, complementary to the previous one, taking into account the statistical distribution of the defects [Cailletaud and Quilici, 2000].

Both models will be applied in the following on a component representative of the turbine blade air cooling channels.

Part IV
Application of the rules to a component

1 Introduction

The aim of this chapter is to simulate the influence of film cooling holes on low cycle fatigue of gas turbine blades. Siemens (KWU) has proposed to check our lifetime assessment rules with another component which was especially designed to model such stress raisers and stress states at the leading edge of a blade with shower head cooling. This specimen with holes is really suited to observe the initiation and the propagation of the damage under representative loading conditions.
In the next section, experimental details of two LCF tests carried out by the manufacturer on SC16 at 950°C will be presented. Then, in comparison with these results, we will show how the lifetime and the crack location assessment tools introduced in the previous part could improve the classical one.

2 Experimental results

The geometry of the LCF sample is given in Fig. 61. Holes have been drilled by a laser drilling machine using the operating parameters taken for blade manufacturing. The thickness of the sample is similar to the wall thickness of the blade. The holes have a pattern with hole density, diameter and angle to surface as found in the leading edge, where a shower head cooling is applied, giving the highest cooling hole density, see Fig. 61.
The LCF tests were performed on a servohydraulic test machine with inductive heating under total strain control in air. The overall strain on the 11 mm gauge length was taken as the control signal.
The experimental tests has been investigated at 950°C . The maximum strain in the loading cycles was planed to be zero and the minimum strain equal to -0.52%, with $10^{-3}\,s^{-1}$ as strain rate.
The surface of the samples was continuously observed during the tests by a system composed of two CCD-cameras with a specially developed control program, so that crack initiation and growth is recorded automatically by computer.

The definition of the lifetime, N_f, is conventionnaly defined in LCF tests as the number of cycles corresponding to a load amplitude drop of 5%. Moreover the number of cycles corresponding to a crack length of 0.15 mm defines the crack initiation cycle N_i. Table 13 show the lifetime and the strain range for all the tests. The total number of cycles is denoted by N. Note the difference between the number of cycles of initiation for both tests.

Fig. 64 shows the maximum stress during a loading cycle as a function of the number of cycles. We define the stress as the force divided by the effective cross sectional area.

One can observe a relatively fast mean stress relaxation. Moreover the stress amplitude decreases at the end of the test when larger crack could be observed on the specimen.

The crack pattern on the front and rear surface of the specimen at the end of the test is given in Fig. 65. After cooling down the specimen at the end of the test the load of the test machine was increased until final fracture. On can observe (in dark grey on Figs. 66, 68) the surfaces of the crack created by the cyclic loading. Black lines within these areas are steps in the crack surface where single cracks, which are initiated at different positions along the hole, are linked together, see Fig. 62. The cracks are nearly perpendicular to the loading direction. There is a small tilt towards the axis of the cooling hole. Note that such a result has already been observed by [Pan et al., 1999] with an isotropic cobalt base alloy.
The locations of the cracks have been determined for the specimen of the test 3651-001. The crack starting positions are given in table 12 as the relative height a/a_o measured from the center of the cooling hole, see Fig. 63. We only consider seven crack initiation areas of one half of the specimen and indicated in Fig. 63 since, due to the symmetry, the others are found on the right side and the rear surface of the sample too. For the test 3651-002, the distribution of the crack initiation locations for the right and left row of holes does not respect the symmetry of the specimen, see Fig. 67. Actually, due to manufacturing error, the pattern of the holes is not properly aligned with the center to the specimen and could be an explanation of this phenomenon.

3 Application of the assessment rules

3.1 Conditions of the FE analysis

In order to check our crack location assessment for this component several cycles have been calculated by finite element with the crystallographic model for SC16 at 950°C.
Only the part of the test specimen between the extensometer has been modelled. Despite the small deviation of the orientation of the crystal, see Fig. 61, we assume that the axis of the holes coincides with the secondary crystallographic axis [010]. Therefore, due to the cubic symmetry of the single crystal and to the geometrical symmetries of the specimen, only one quarter of component has been modelled. The mesh of the component and the boundary conditions are given in Fig. 69. The applied displacement is calibrated to get the nominal strain and strain rate over the gauge length of the experiment, see Fig. 70.
The simulated relaxation of the force is in good agreement with the measured value, see Fig. 71.

3.2 Crack location assessment and comparison with experimental evidence

The total cumulated inelastic strain for each slip system family at the maximum loading of the first cycle has been plotted in Figs. 73, 74 and give an idea of the viscoplastic strain

at the holes. These results show that the total cumulated slip is not located at the notch roots as in the case of the notched specimens and in accordance with the position of the cracks around the notches obtained on the specimen after the LCF test, see Fig. 65.
The crack location assessment introduced for the round bulk LCF notched specimens in the second part (Section 3) is based on the determination of the position of the maximum total cumulated slip at the notch for the stabilized cycle. But the global curve plotted in Fig. 71 and the experimental one point out the necessity to take into account the stress/strain redistribution. Thus we have to determine the slip location at the notches till a stabilized one is obtained.

Moreover to simplify the application of our method the hole 6 of the rear surface of the sample represented in Fig. 63 has been chosen. The contour of the inelastic cumulated strain of each slip family which are concentrated in this hole have been plotted in Fig. 72 for an assumed representative cycle. The ratio $a/a_{\circ}$, which is characterized by the position of the crack at the intersection curve cooling hole - outer surface, has been calculated for the maximum slip at the hole according to the definition given in Fig. 72. We have obtained for that particular case a location ratio equal to 0.61. According to the table 12 the associated crack location ratio is between 0.5 and 0.65.
Finally the agreement between the position of the crack around that hole and the maximum total cumulated inelastic strain location is satisfying.

3.3 Application of the deterministic method for lifetime

We apply in this section the method explained in the previous part (Section 3.2) for the same hole 6 on the rear surface. In order to assess the lifetime of this part of the component we have to calculate the maximum resolved shear stress range over the stabilized cycle at the point where the equivalent inelastic strain is maximum. Over the first cycle the maximum resolved shear stress range at this point and of the same slip family is equal to 307 MPa. From the diagram of Fig. 47 we obtain 1300 as number of cycles to failure for this value of the critical variable. Our lifetime criterion is based on 5% stress drop on smooth specimens, corresponding to a crack depth of about 0.7-1 mm (compare the discussion in Section 3.4 of Part 3). According to the experimental results, such crack lengths are reached between 910 cycles at the evaluated hole in the middle and 3528 cycles at latest, see Fig. 65. Therefore this approach allows us to assess a realistic lifetime, at least within a factor of 3.

3.4 Application of the probabilistic failure model

The first step of this method described in Part two, Section (3.3) is a finite element calculation of the cycled specimen until the stabilized cycle is reached at $950^{\circ}\mathrm{C}$. Contour plots of Mises stress equivalent at the point of maximal load are plotted on Fig. 75.

Then the multiaxial stress amplitude, $\Delta\Sigma$, calculation has been performed and extrapolated to the surface mesh as shown on Fig. 76. Rigorously, only the surface around the cooling holes should be retained in the surface mesh. For demonstration purposes some of

the outside surfaces of the specimen have been kept however. The probability of failure, being considerably lower on those regions should not change the results dramatically.

Finally the multiscale model has been applied to the surface. The probabilities of failure calculated with this model for different numbers of cycles are plotted on Fig. 77, where it can be seen that the number of cycles to failure is of about 1000 cycles. Contour plots of failure probability for N equal respectively to 500, 1500 and 2500 cycles are represented on Figs. 78 to 80. These results are in a good agreement with the experimental values of the number of cycles to initiation given in Fig. 65.

4 Conclusion

The experimental results of low-cycle fatigue at 950°C on SC16 specimen with holes confirm the good capabilities of the crystalline model concerning the crack initiation. Indeed the maximun equivalent inelastic strain is a pertinent variable for the initiation of the damage at such stress raisers.

Two different lifetime assessment rules have been applied and give comparable results as the experimental one which have been obtained with sophisticated measures of the crack length during the tests at high temperature.
The first approach, based on the calculation of the resolved shear stress at the point of the component where the equivalent viscoelastic strain is higher over both octahedral and cubic slip system families, constitutes a simple method for SC16 under repeated symmetric tension compression loading. The second one takes into account the statistical distribution of the casting pores in the component and thus the real physical mechanism of the crack initiation. However these methods are still conservative even if the assessed lifetime is by a factor of 3 smaller than the experimental one.

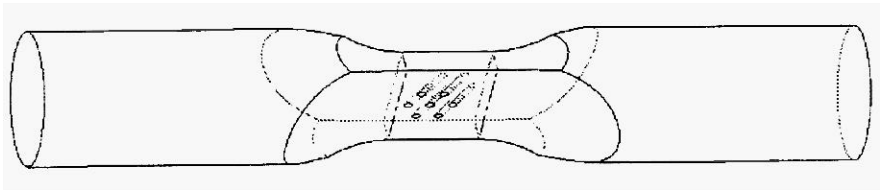

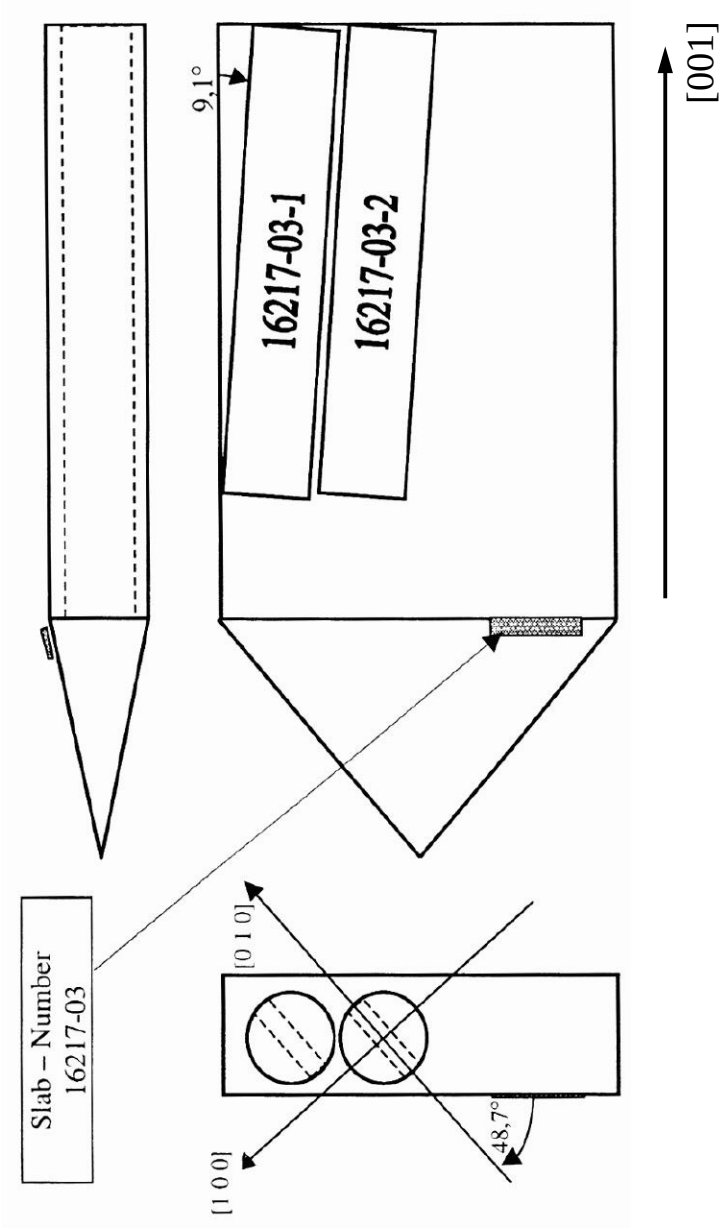

Figure 61: Geometry of the LCF specimen with holes; orientation of the rods within the SC16 slab (after Siemens (KWU)).

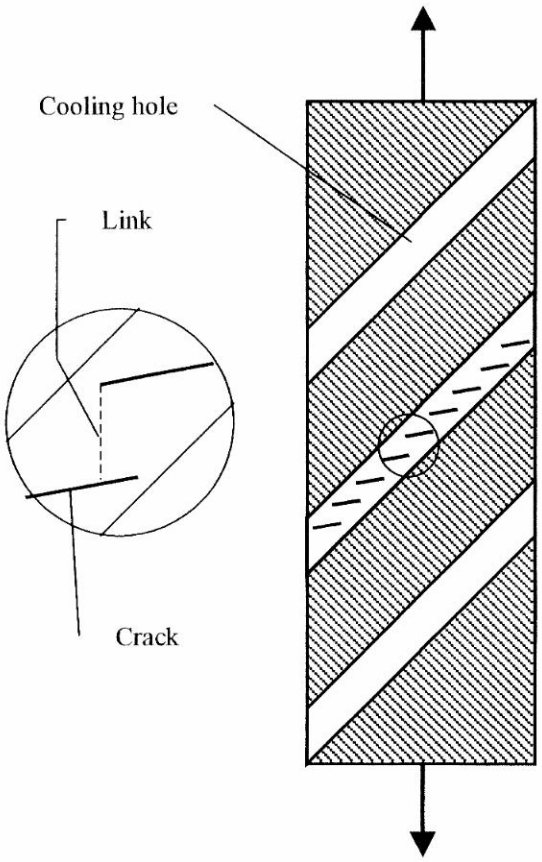

Figure 62: Crack pattern along the cooling hole (after Siemens (KWU)).

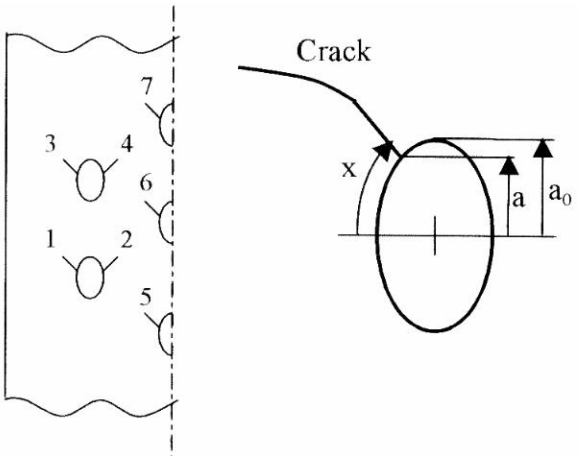

Figure 63: Crack positions at the intersection curve cooling hole-outer surface (after Siemens (KWU)).

relative height a/a_0 of crack start		Crack initiation areas (fig.1b)						
		1	2	3	4	5	6	7
Front surface	Left	0.55	0.75	0.35	0.6	-	0.5	-
	Right	0.3	0	0.5	0.25	-	0.6	-
Rear surface	Left	0.8	0.5	0.7	0.6	-	0.65	-
	Right	0.3	0.45	0.45	0.45	-	0.5	0.2

Table 12: Crack starting positions at each hole given Fig. 63 for the test 3651-001 (after Siemens (KWU)).

Test number	$\triangle\varepsilon\,(\%)$	N_i	N_f	N
3651-001	0.494	920	3100	3528
3651-002	0.506	1600	3500	6380

Table 13: Results of LCF tests at 950°C on specimens with holes (after Siemens (KWU)).

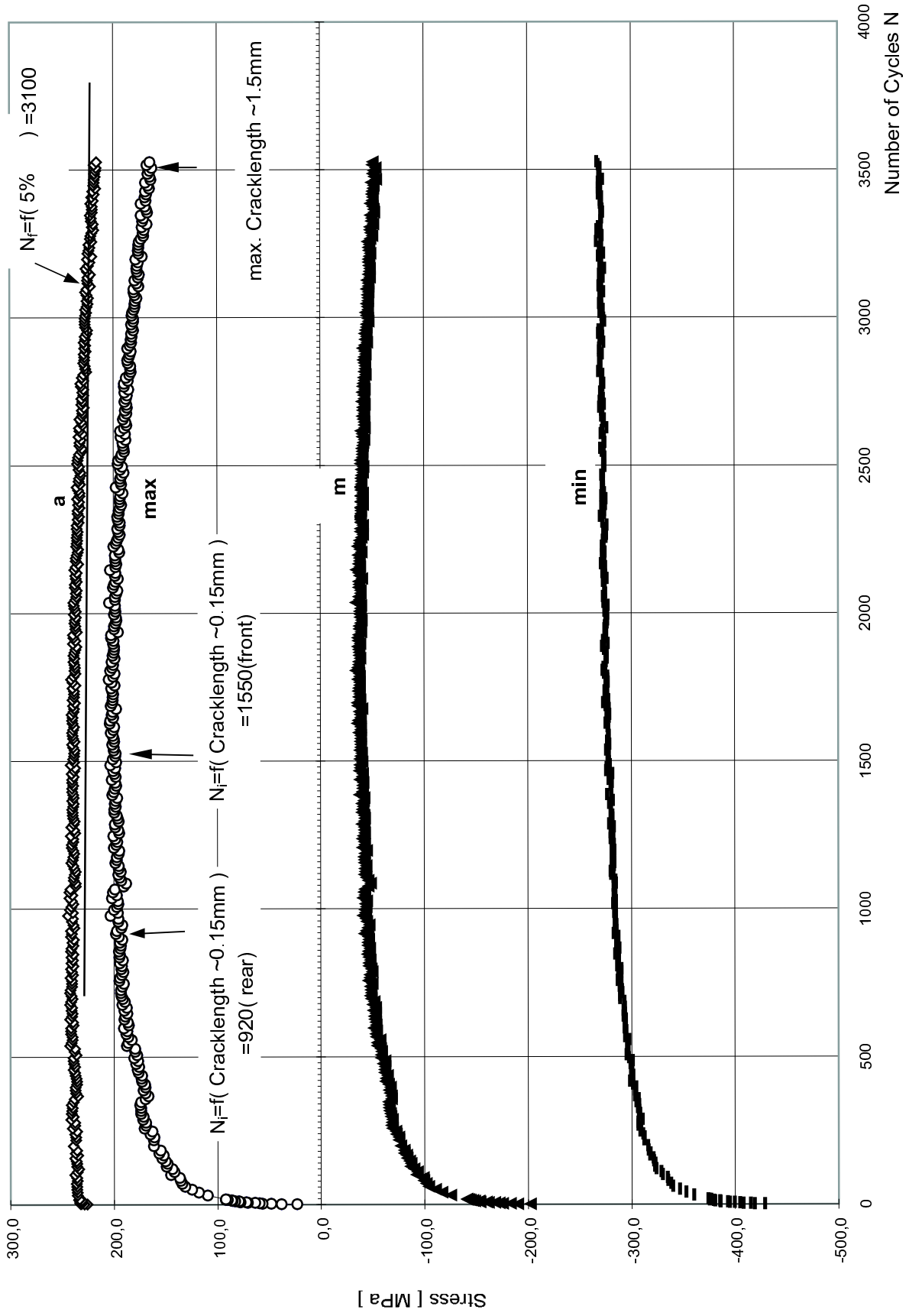

Figure 64: Global stress versus the number of cycles of the test 3651-001 at 950°C on SC16 ⟨001⟩ oriented specimen with cooling holes (after Siemens (KWU)).

Rear surface after the test, N=3528 cycles

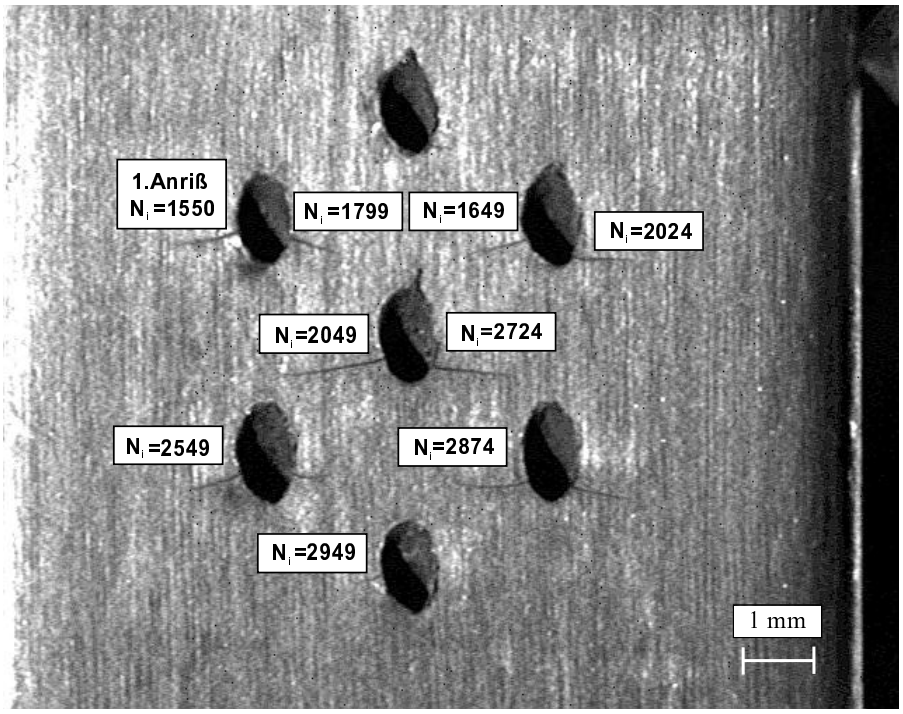

Front surface after the test, N=3528 cycles

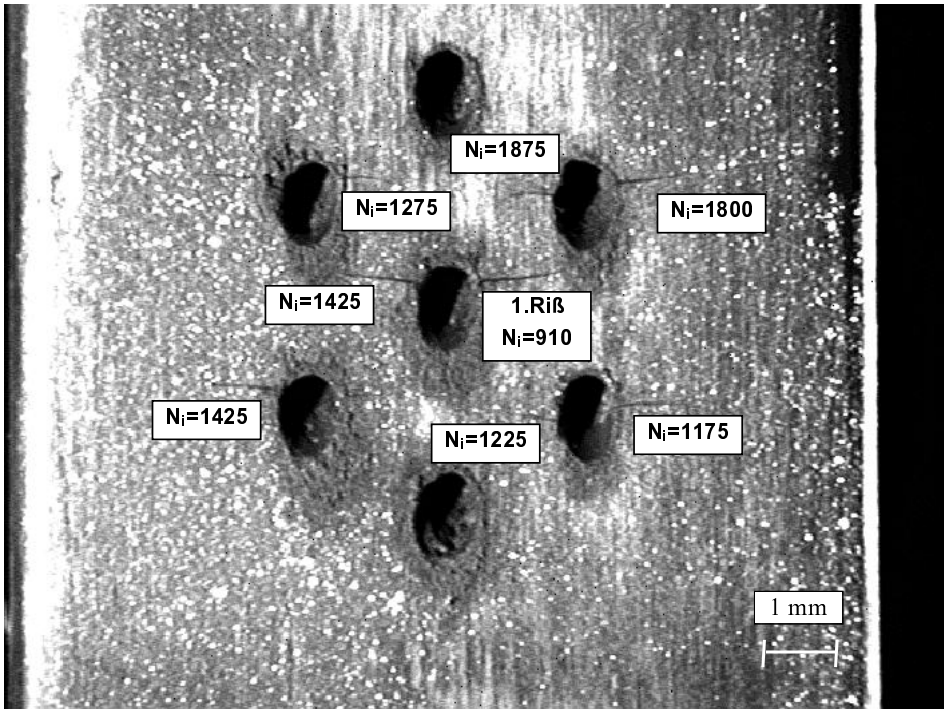

Figure 65: Surfaces of the SC16 specimens with cooling holes after N = 3528 cycles at 950°C . Test 3651-001 (after Siemens (KWU)).

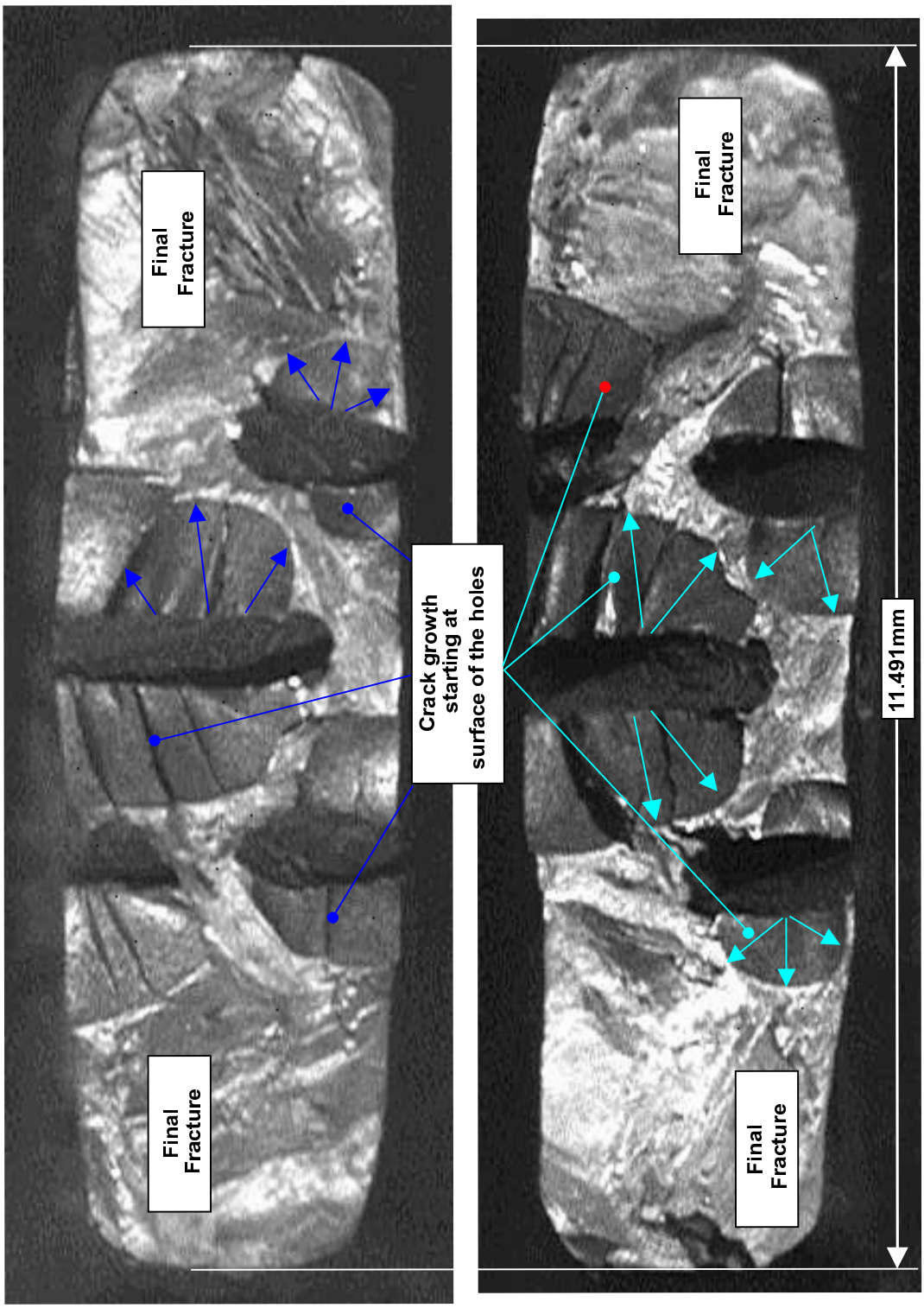

Figure 66: Surface rupture of the SC16 specimens with cooling holes after N = 3528 cycles at 950°C . Test 3651-001 (after Siemens (KWU)).

Front surface after the test, N=6380 cycles

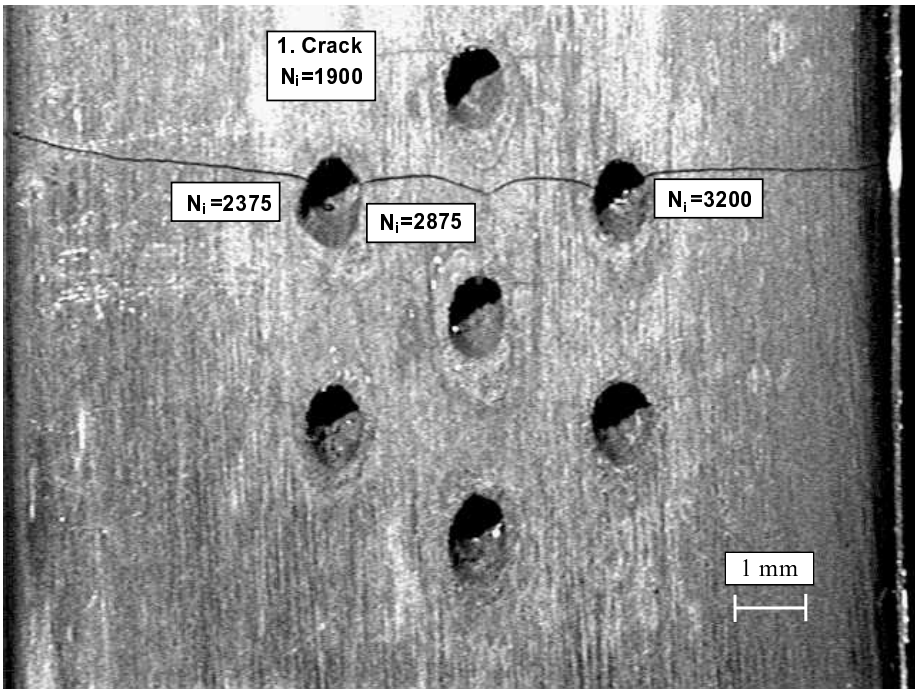

Rear surface after the test, N=6380 cycles

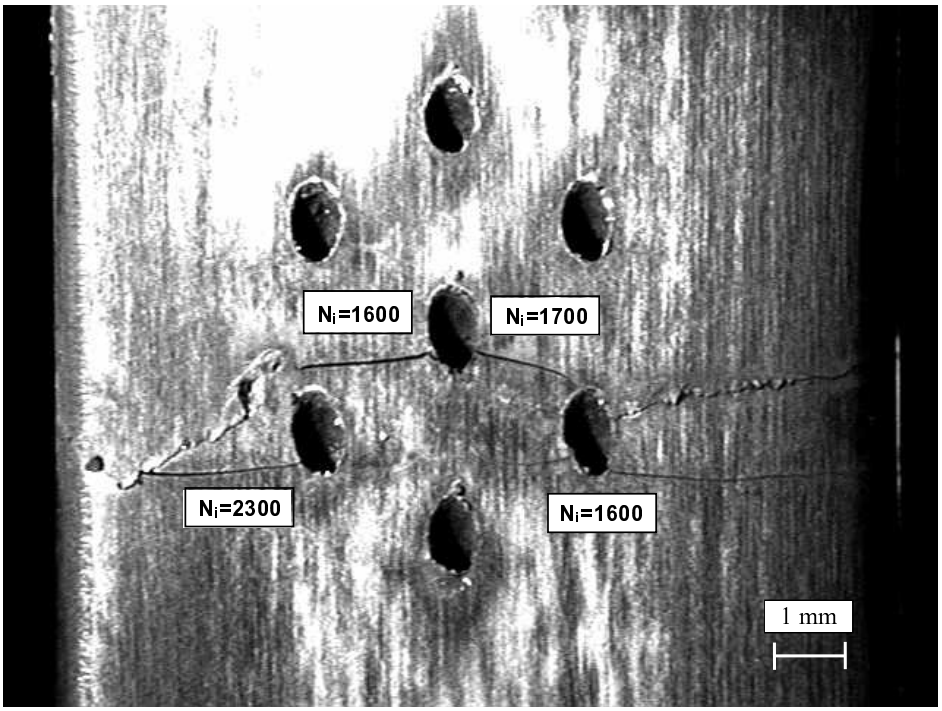

Figure 67: Surfaces of the SC16 specimens with cooling holes after N = 6380 cycles at 950°C . Test 3651-002 (after Siemens (KWU)).

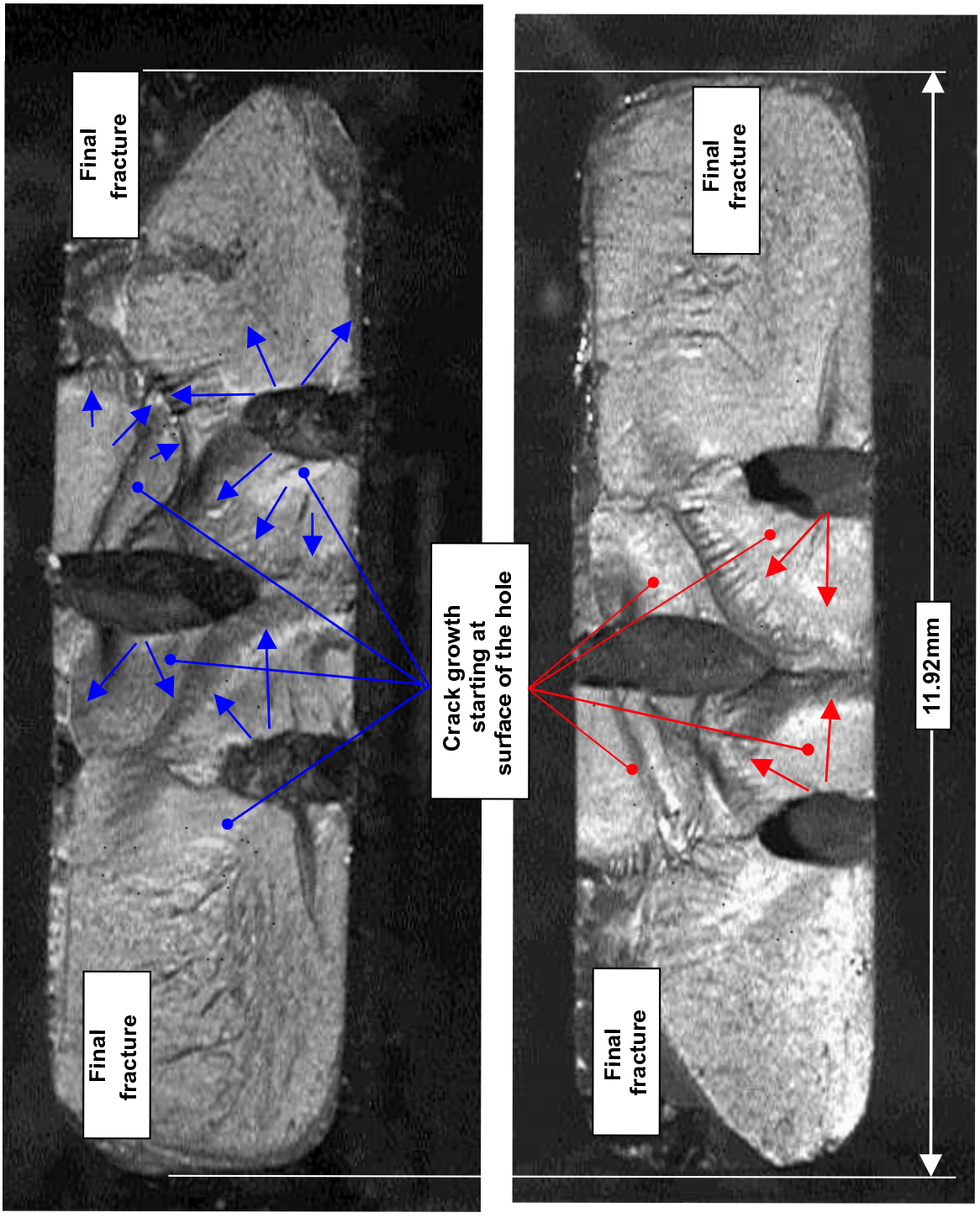

Figure 68: Surface rupture of the SC16 specimens with cooling holes after N = 6380 cycles at 950°C . Test 3651-002 (after Siemens (KWU)).

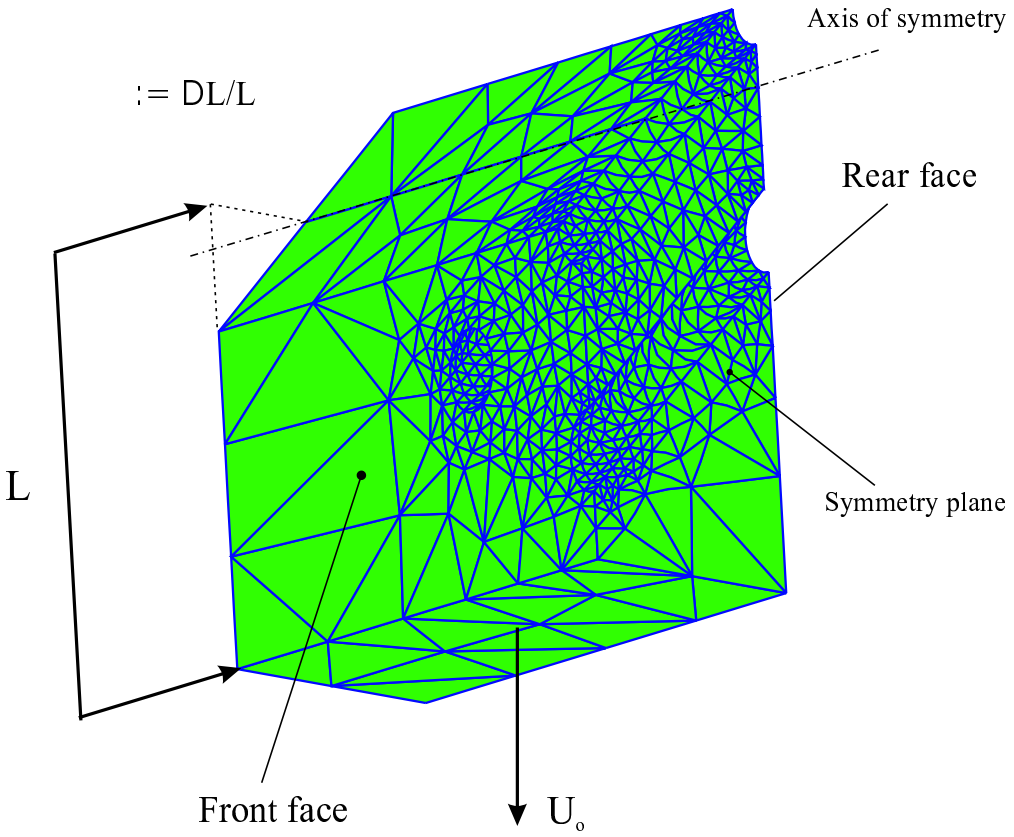

Figure 69: Boundary conditions of the specimen with holes of Siemens (KWU).

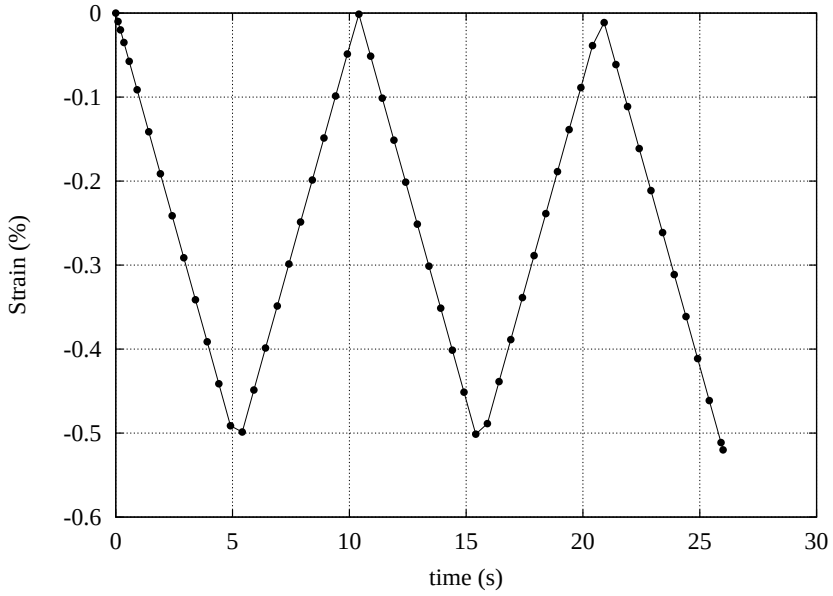

Figure 70: Loading applied on the specimen with holes.

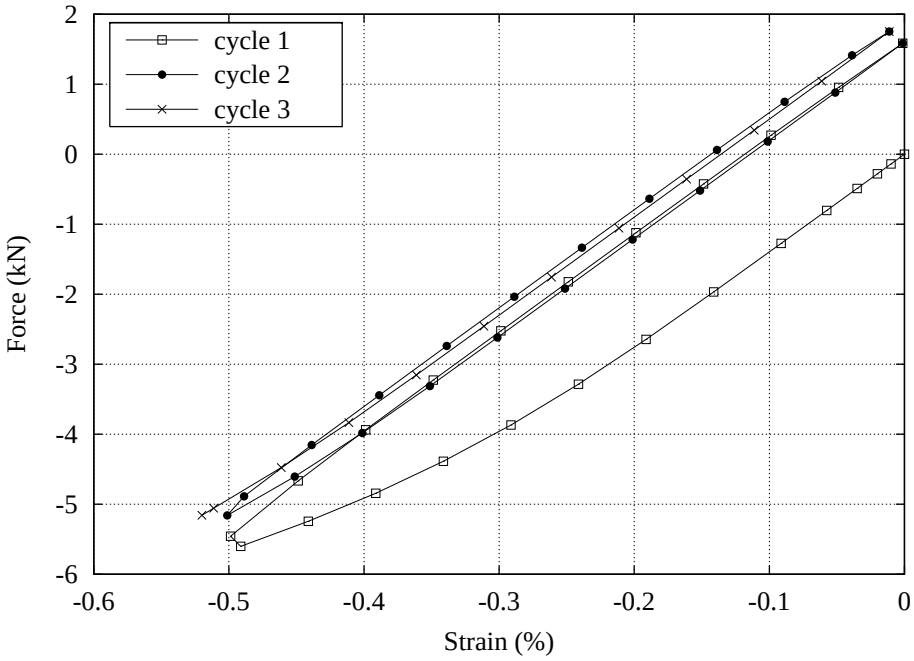

Figure 71: Global curve Force versus the nominal Strain.

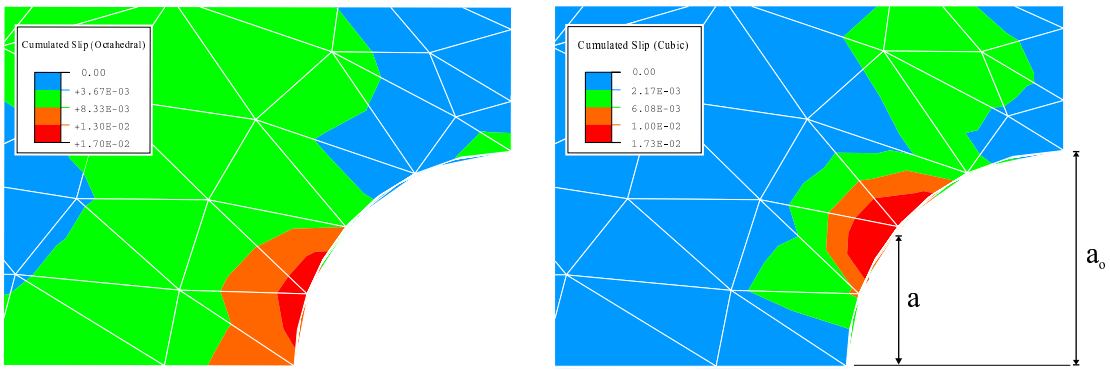

Figure 72: Total cumulated slip on the rear surface of the hole 6 at the end of the first cycle (octahedral (left) and cubic (right)).

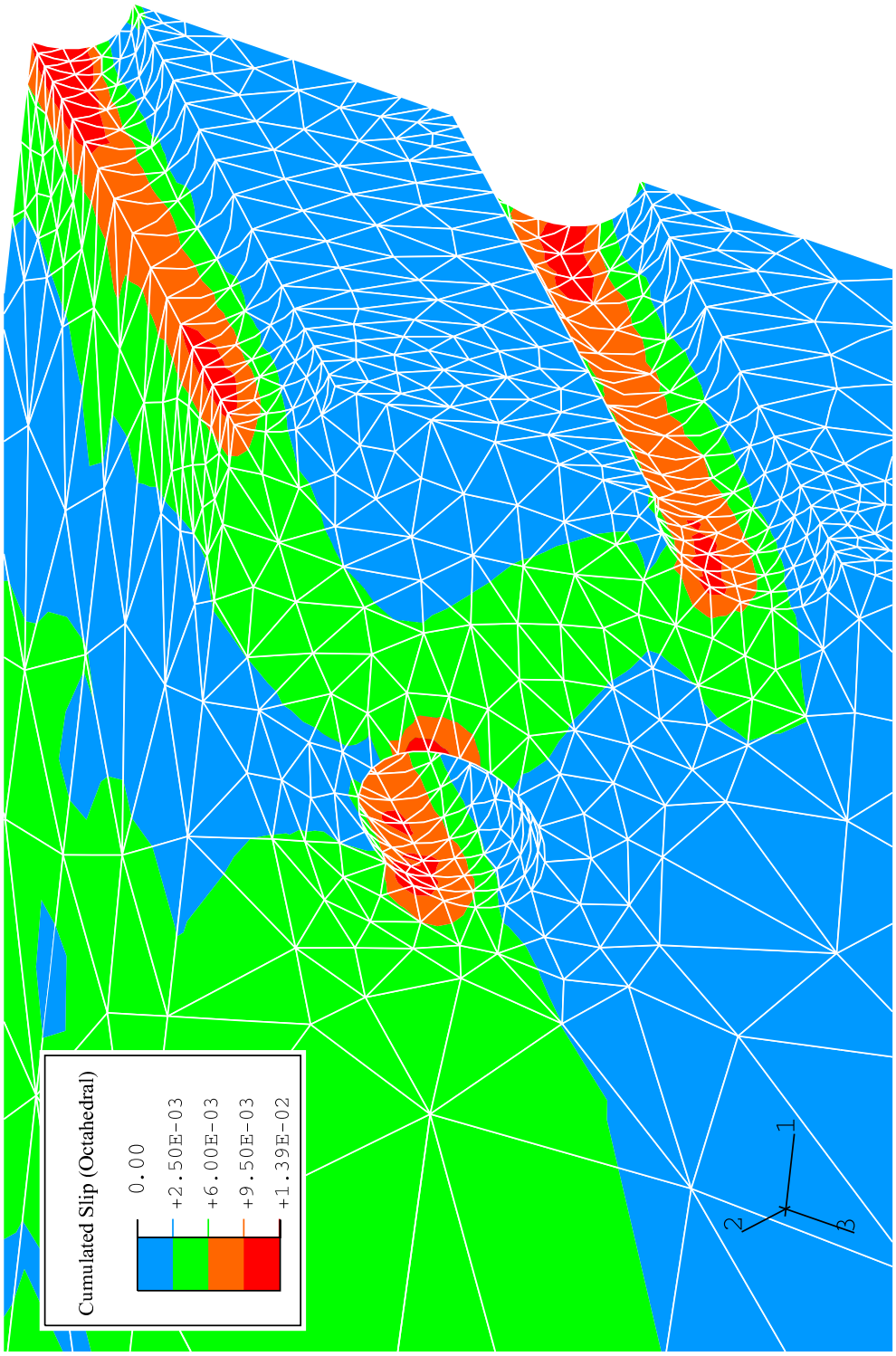

Figure 73: Total cumulated octahedral slip of the specimen with holes at the maximun loading of the first cycle.

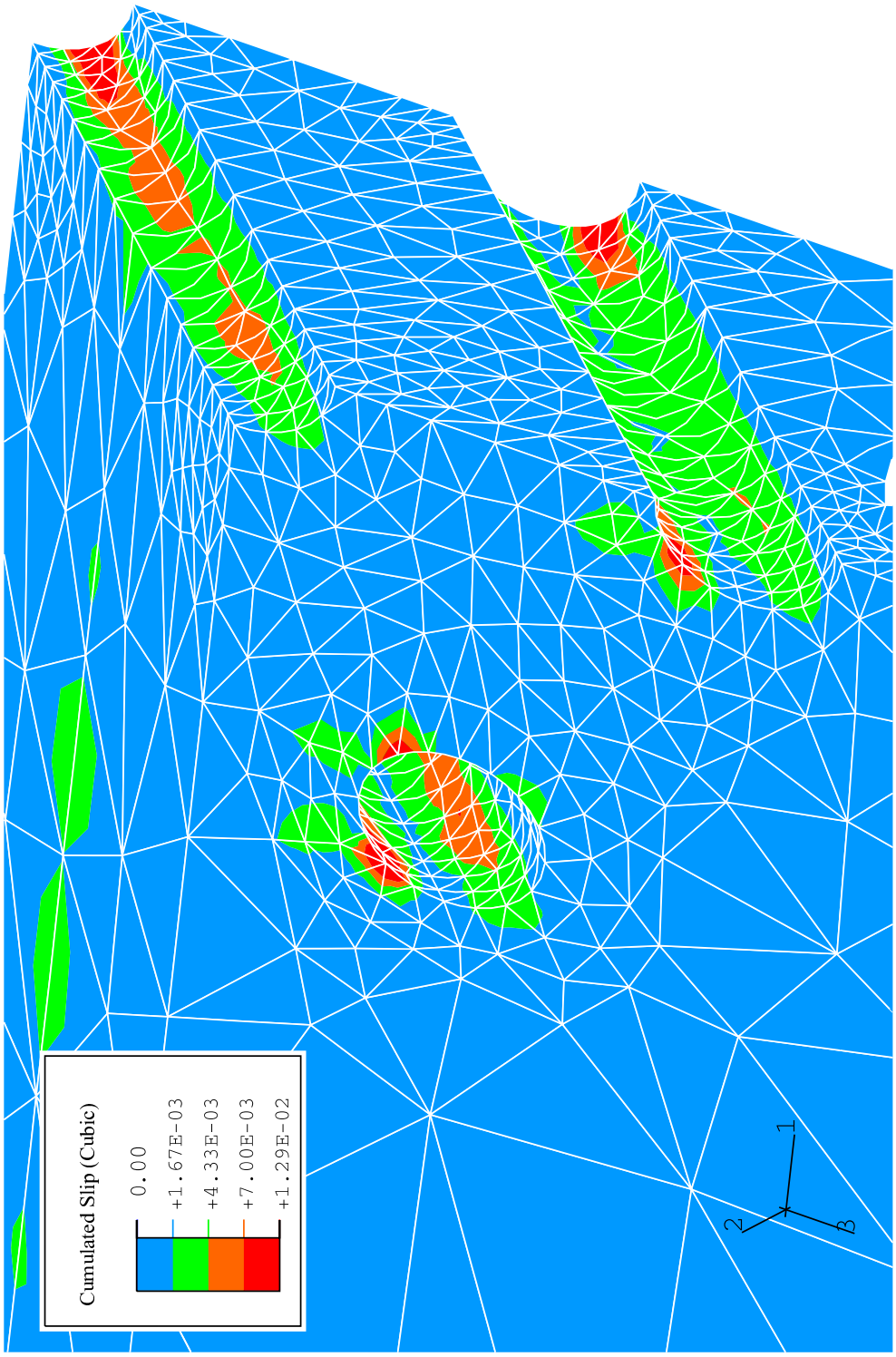

Figure 74: Total cumulated cubic slip of the specimen with holes at the maximun loading of the first cycle (cubic).

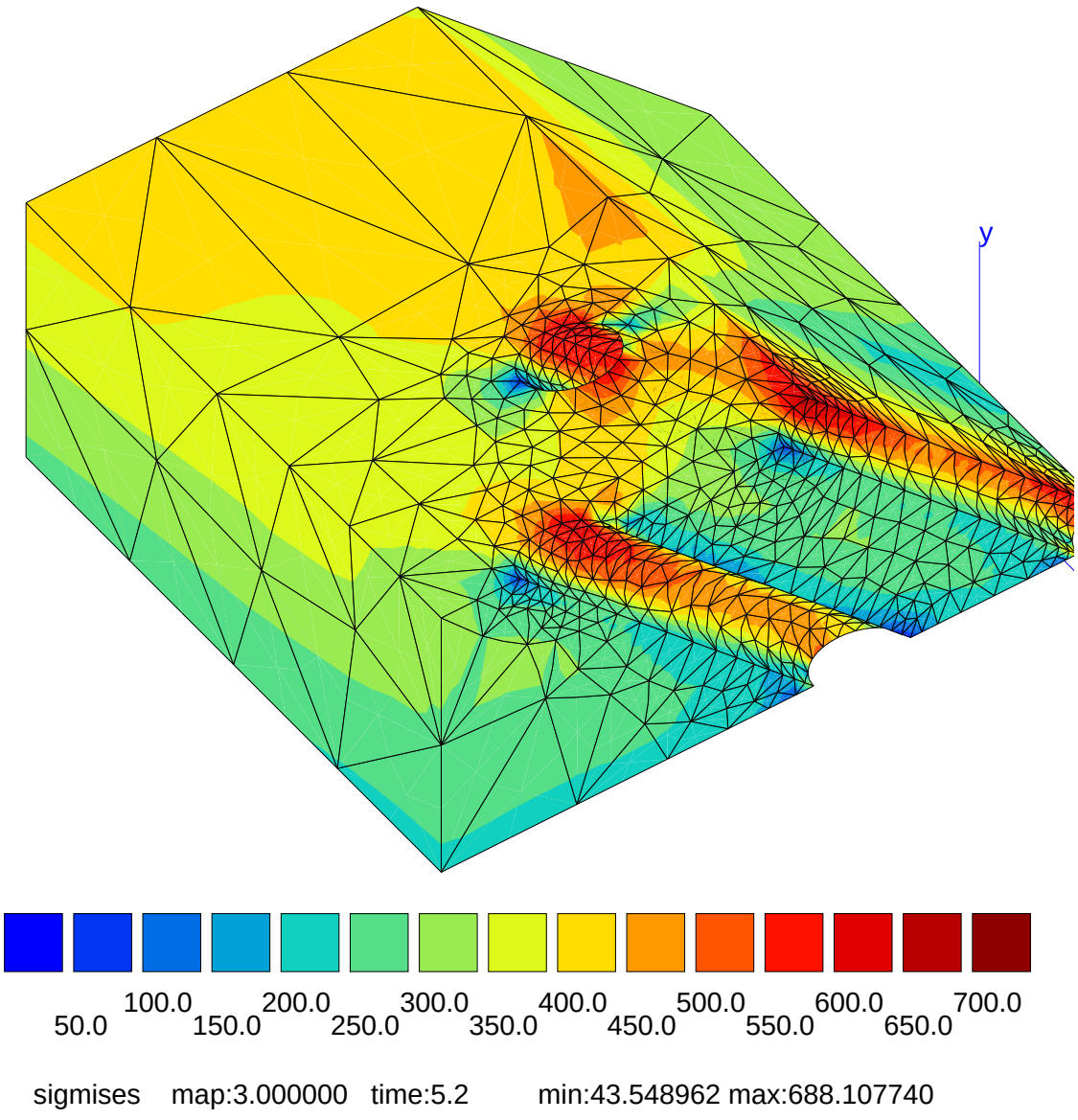

Figure 75: Isocontours of Mises stress equivalent.

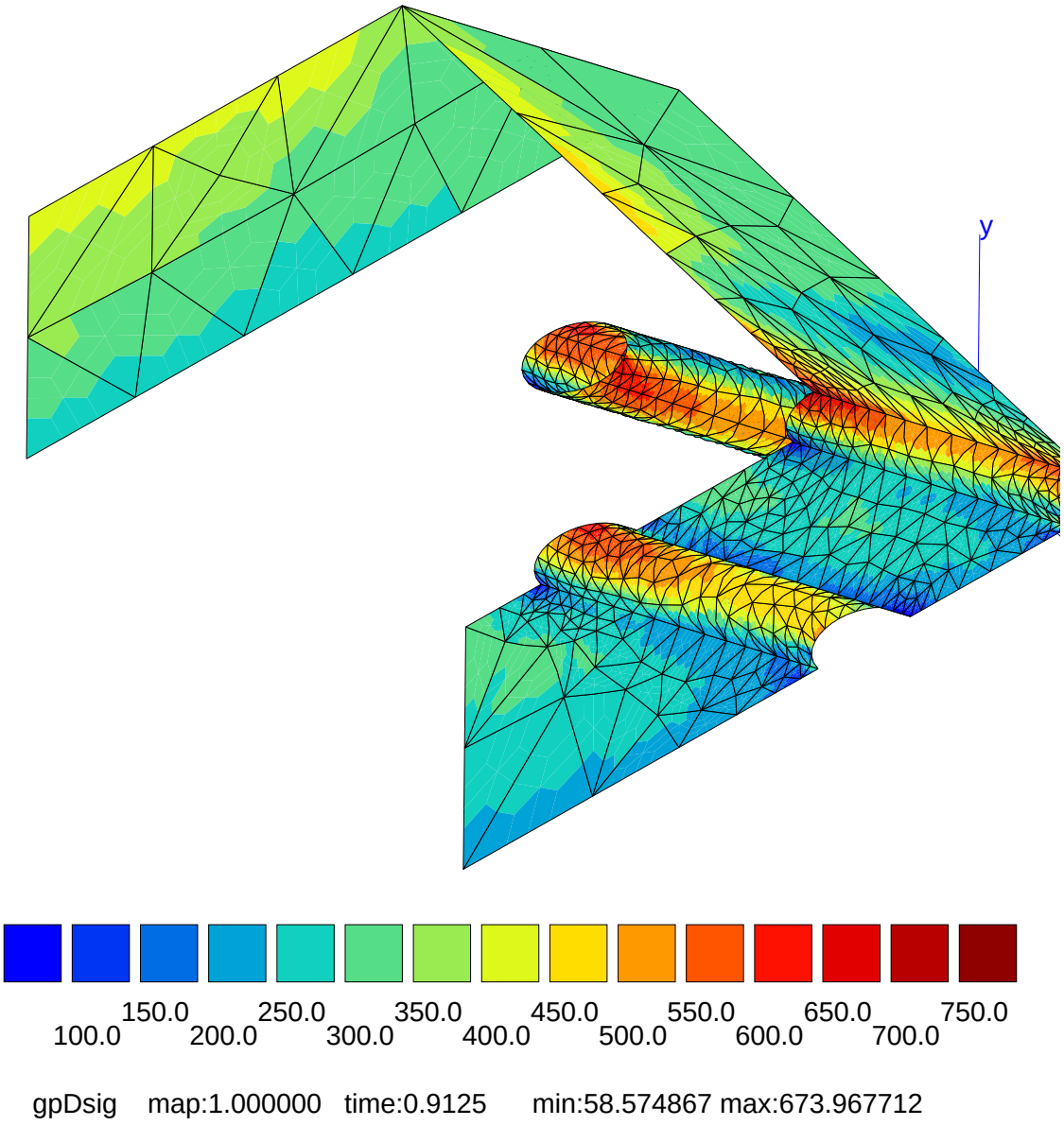

Figure 76: Isocontours of multiaxial $\Delta\Sigma$ on the surface mesh of the specimen with holes.

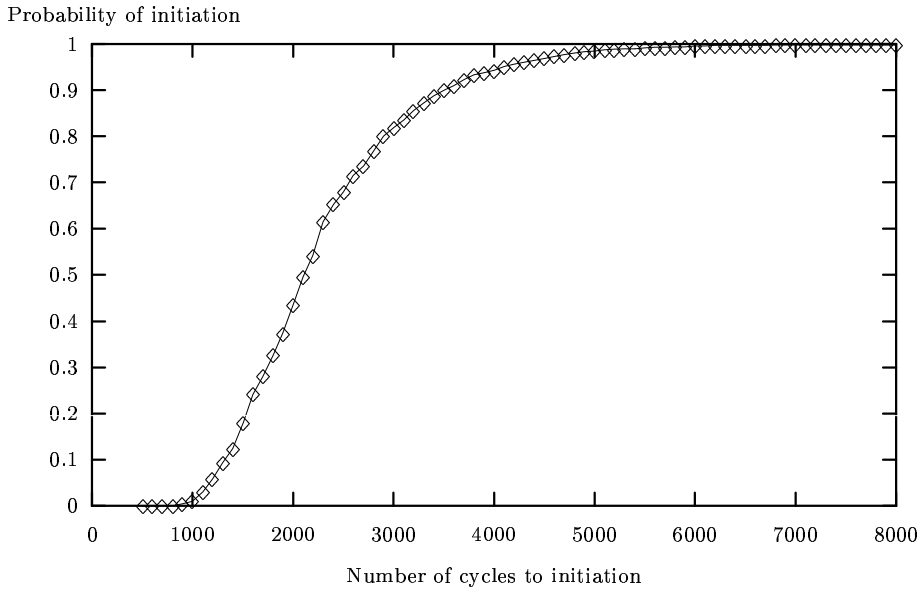

Figure 77: Failure probability versus number of cycles for the specimen with holes.

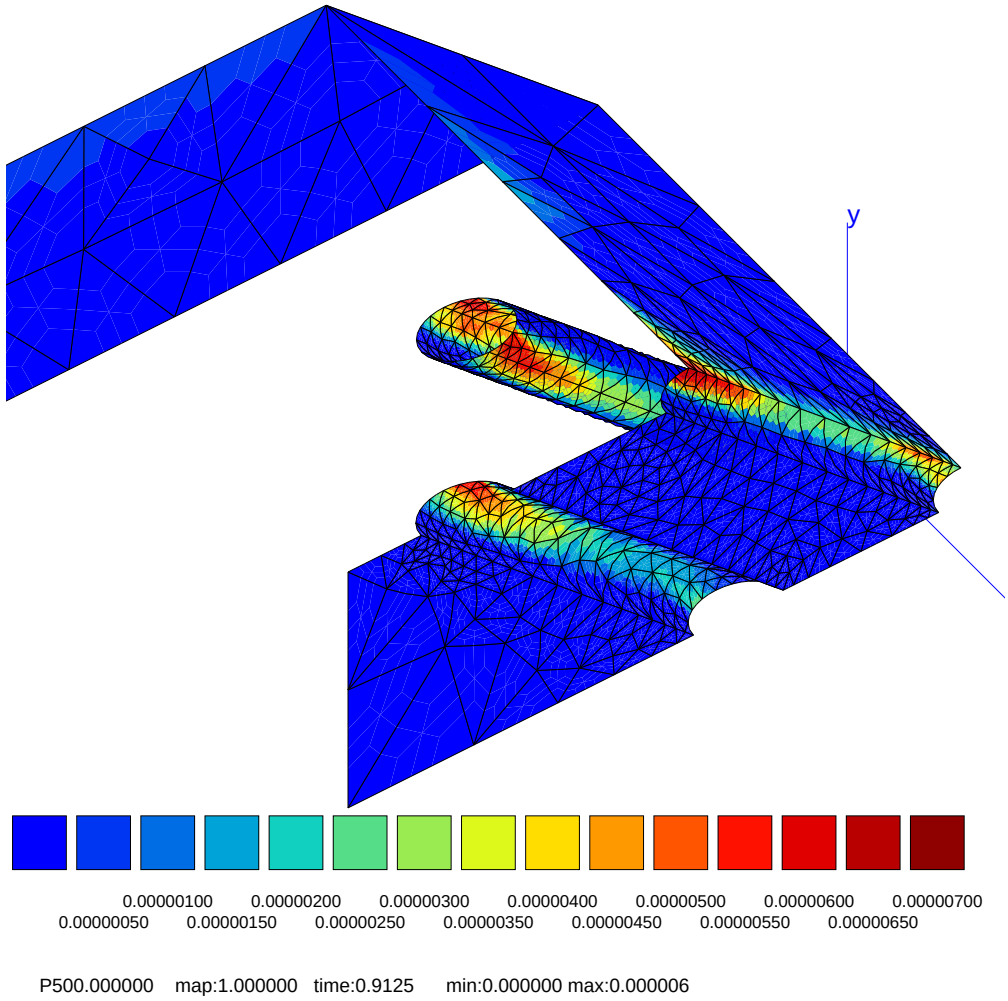

Figure 78: Isocontours of failure probability in 500 cycles.

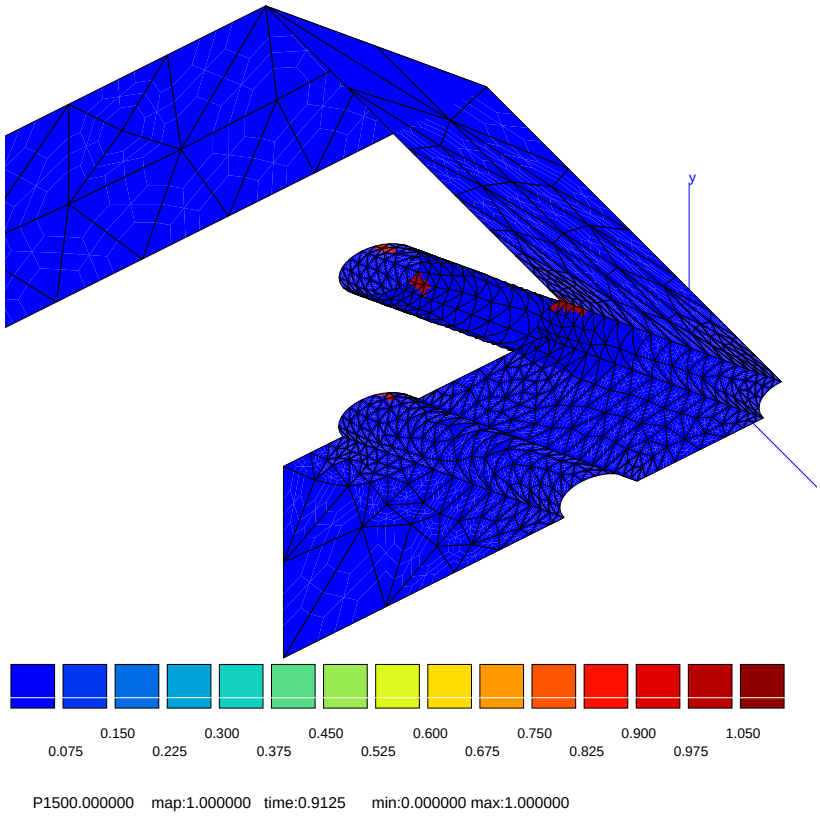

Figure 79: Isocontours of failure probability in 1500 cycles.

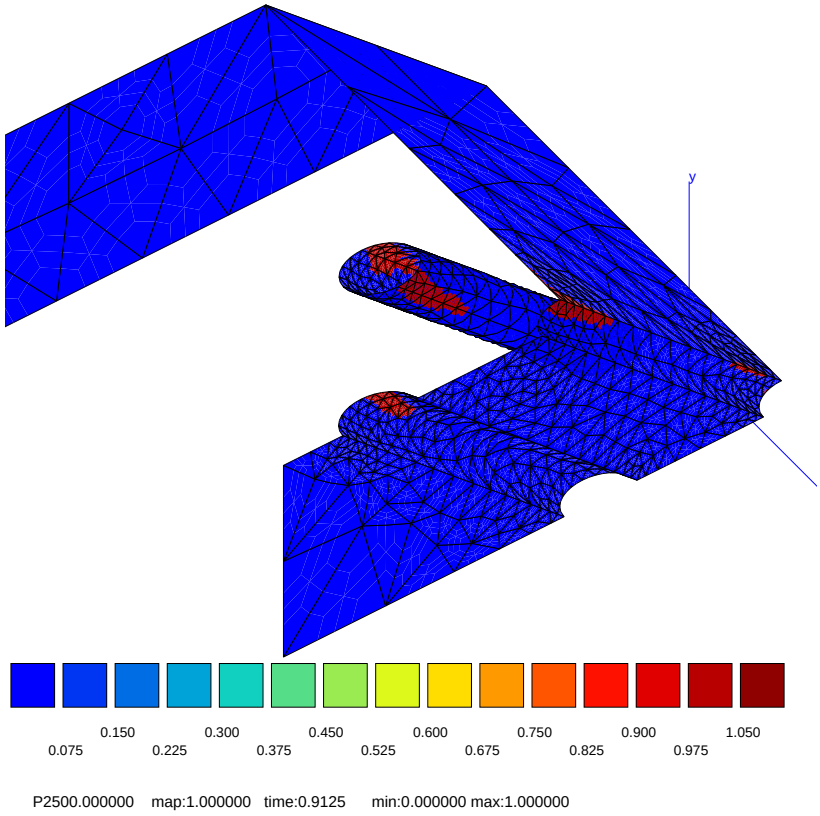

Figure 80: Isocontours of failure probability in 2500 cycles.

Part V
Strain localization phenomena at a crack tip in single crystals

1 Introduction

In the previous section crack initiation and macroscopic modelling of the lifetime for single crystal superalloy at high temperature have been studied.
The next step is then the investigation of large cracks growth in such an anisotropic material. The high strain gradients at the crack tip lead us to use a generalized continuum theory on the localized deformation patterns in f.c.c. single crystals [Forest et al., 2000].

I investigate in this part the stress-strain field at a given crack tip in a single crystal. First we will give a review of recent publications about large cracks in monocrystalline materials. Then we will recall briefly the main constitutive equations of the extended model. From numerical analyses of some representative crack configurations we will characterize the modification of the strain localization bands distribution with the generalized continuum model. Important consequences are expected regarding crack branching after stable crack growth. Finally in the last section we report some encouraging experimental evidence.

2 Large cracks in single crystals

The asymptotic stress-strain field at a stationary crack tip in elastic-ideally plastic f.c.c. and b.c.c. single crystals, as determined by Rice [Rice, 1973], [Rice, 1984], [Rice and Nicolic, 1985], [Rice, 1987], [Rice et al., 1990], turns out to be locally constant within angular sectors. It involves shear displacement discontinuities at sector boundaries, that can be interpreted as strain localization bands. When the crack orientations have high symmetry relative to the crystal, at least two kinds of bands can occur at the crack tip: slip bands lying in the slip plane of the locally activated slip system, or kinking mode of shear which corresponds to the discontinuity surfaces perpendicular to active slip plane, see Figs. 81, 82.
The numerical analysis of the same problem using finite strain crystal plasticity in [Cuitino and Ortiz, 1993], [Mohan et al., 1992] reveals that the condition of constant stress state in each sector must be relieved due to possible local elastic unloading, but also that the strain localization patterns pertain. These authors found in the outer section of the plastic zone the same solution as Rice in the case of a perfectly plastic behavior and for small strains and lattice rotation. Using an adaptative meshing technique, [Ortiz and Quigley, 1991] obtained a trace of the radial lines of displacement and stress discontinuity (Fig. 83).
Discrete models based on dislocation dynamics also lead to strongly localized dislocation

distributions near the crack tip and to the progressive formation of the predicted sectors [Cleveringa et al., 1999], as one can see on Fig. 84.
Experimental observations in a b.c.c. single crystal in [Shield and Kim, 1994] confirm the existence of such intense deformation bands radiating from the crack tip. Moreover, according to these authors, the rotation of the crystal lattice should play a significant role in the formation of strain field structure observed.
[Mesarovic and Kysar, 1996] have studied the experimentally observed directionally dependent cracking along the interface between a copper and alumina crystals. They tried to give some explanations about the effect of continuum deformation on the competition between dislocations nucleation at a crack tip and cleavage. Particularly they have shown how pronounced the geometrical hardening and softening in ideal plasticity analysis are. Moreover the nature of the localization of the plastic deformation changes with the crack tip orientation.

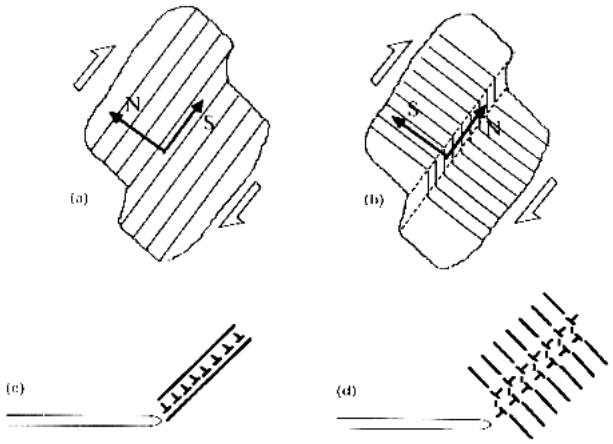

Figure 81: (a) Shear in band lying parallel to the active slip systems. (b) Shear by kinking mode in a band lying perpendicular to the slip direction. (c) Dislocations generated at the crack tip or from internal sources: **slip-plane-parallel shear band.** (d) Dislocations dipole loops nucleated from internal sources: **kinking shear band**. After [Rice et al., 1990].

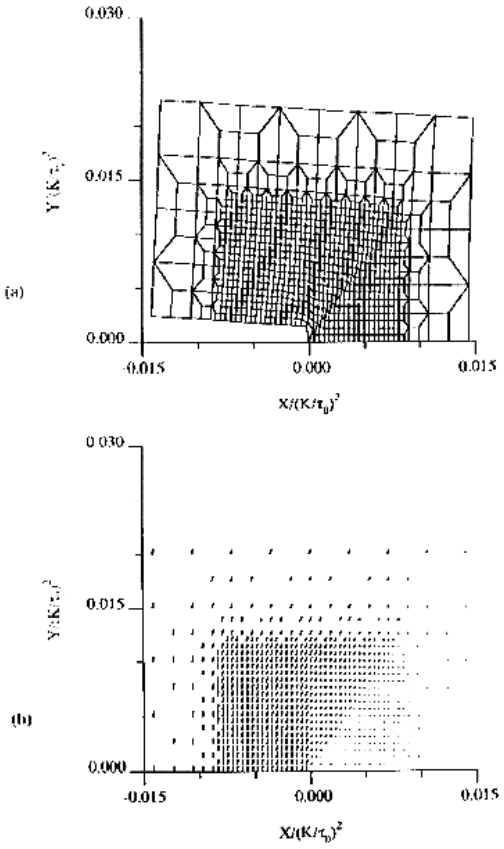

Figure 82: (a) Deformed mesh for stationary crack. (b) Line lengths proportional to accumulated displacements. From [Rice et al., 1990].

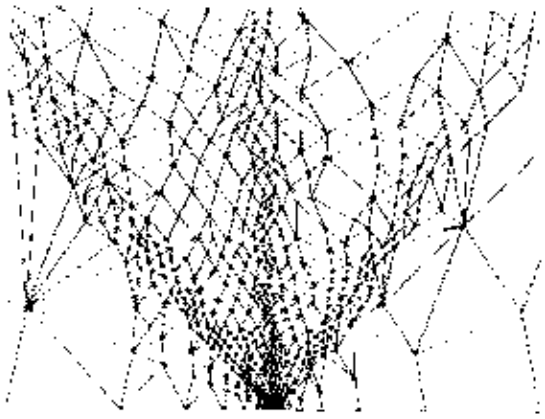

Figure 83: Final mesh of the near tip region of a crack on the (010) plane of a copper single crystal, with the crack front in the $[\bar{1}01]$ direction, and crack growth along [101]. From [Cuitino and Ortiz, 1993].

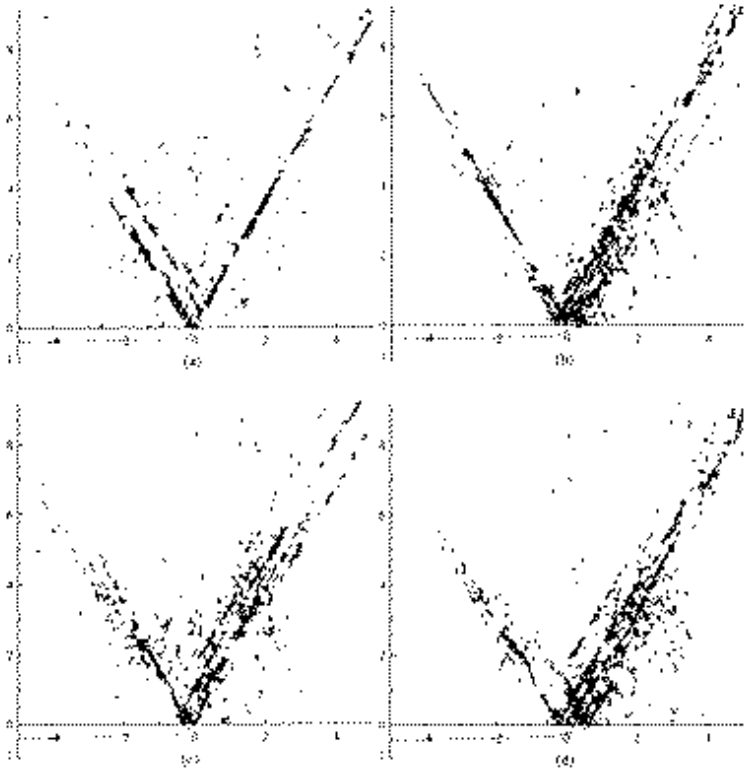

Figure 84: Edge dislocations interacting with a propagating mode I crack. Dislocation distributions for different obstacle densities and loading rates. From [Cleveringa et al., 1999].

3 Cosserat single crystal plasticity

3.1 Motivations

The fact that the strong strain gradients developing in the vicinity of the crack tip may affect the local mechanical response of a crystalline solid suggests that generalized continuum theories, including Cosserat, strain gradient and non local models, could be helpful for computing more realistic local stress-strain fields. The strain gradient model used in [Xia and Hutchinson, 1996], [Wei and Hutchinson, 1997] results in a substantial increase of the tractions ahead of the tip of a mode I crack within a domain of characteristic size described by a constitutive intrinsic length. This monitoring of the local strain field enables one to improve the prediction of subsequent crack growth.

The use of a generalized continuum model also strongly affects the localized deformation modes as demonstrated in [Forest, 1998] in the case of single crystals. In particular, as already seen above, classical crystal plasticity theory predicts two types of deformation bands in single crystals undergoing single slip: slip bands lying in the slip plane of the locally activated slip system, or kink bands lying in a plane normal to the slip direction of the slip system [Forest and Cailletaud, 1995]. The formation of a kink band is associated with the development of strong lattice rotation gradients at its boundary and may therefore be precluded if the model incorporates additional hardening related to lattice curvature [Forest, 1998].

One gives in this section a summary of the principal constitutive equations of a generalized crystal plasticity model for single crystals at finite deformation [Forest et al., 1997].

3.2 Kinematics of the Cosserat continuum

A material point M of body B at time t_0 is described by its position $\underline{\mathbf{X}}$ and its inner state, for an arbitrary initial placement, chosen as the reference configuration. At time t, its position is $\underline{\mathbf{x}}(\underline{\mathbf{X}},t)$ and its inner state $\underset{\sim}{\mathbf{R}}(\underline{\mathbf{X}},t)$, in a given reference frame E. If $(\underline{\mathbf{d}}_i)_{i=1,3}$ are three orthogonal lattice vectors in a released state at t and $(\underline{\mathbf{d}}_i^0)_{i=1,3}$ their initial placement in E, then the rotation $\underset{\sim}{\mathbf{R}}$ is defined through

$$\underline{\mathbf{d}}_i \;=\; \underset{\sim}{\mathbf{R}}\,\underline{\mathbf{d}}_i^0 \tag{21}$$

with

$$\underset{\sim}{\mathbf{R}}\underset{\sim}{\mathbf{R}}^T \;=\; \underset{\sim}{\mathbf{1}}, \quad \underset{\sim}{\mathbf{R}}(\underline{\mathbf{X}},t_0) \;=\; \underset{\sim}{\mathbf{1}} \text{ and } \operatorname{Det}\underset{\sim}{\mathbf{R}} \;=\; 1. \tag{22}$$

A rotating frame $E^\sharp(M)$ is attached to the lattice structure at each point $M \in$ B and each vector and tensor variable y considered with respect to $E^\sharp$ will be denoted ${}^\sharp y$. The link between the vector field $\underline{\phi}(\underline{\mathbf{X}},t)$ and the rotation field $\underset{\sim}{\mathbf{R}}(\underline{\mathbf{X}},t)$ is given by

$$\underset{\sim}{\mathbf{R}} \;=\; \exp(\underset{\sim}{\mathbf{1}} \times \underline{\phi}) \;=\; \exp(-\underset{\approx}{\varepsilon}\,\underline{\phi}) \tag{23}$$

The displacement field is defined by the difference

$$\underline{\mathbf{u}}(\underline{\mathbf{X}},t) \;=\; \underline{\mathbf{x}}(\underline{\mathbf{X}},t) \;-\; \underline{\mathbf{X}} \tag{24}$$

In the framework of the Cosserat medium $\underline{\mathbf{u}}$ and $\underline{\phi}$ are regarded as independent kinematic variables which can be connected on the balance or constitutive level by some constraint. The deformation gradient classically transforms the initial infinitesimal material segment $d\underline{\mathbf{X}}$ to its current position $d\underline{\mathbf{x}}$

$$d\underline{\mathbf{x}} \;=\; \underset{\sim}{\mathbf{F}}\; d\underline{\mathbf{X}} \tag{25}$$

so that

$$\underset{\sim}{\mathbf{F}} \;=\; \underline{\mathbf{u}} \otimes \underline{\nabla} \;=\; u_{i,j}\, \underline{\mathbf{e}}_i \otimes \underline{\mathbf{e}}_j \tag{26}$$

Partial derivatives are taken implicitly with respect to X_j.
In the same way, we compute the variation $d\underset{\sim}{\mathbf{R}}$ of microrotation along a material segment $d\underline{\mathbf{X}}$. Defining $\delta\underline{\phi}$ by

$$(d\underset{\sim}{\mathbf{R}})\; \underset{\sim}{\mathbf{R}}^T \;=\; \underset{\sim}{\mathbf{1}} \times \delta\underline{\phi} \;=\; \underset{\approx}{\varepsilon}\, \delta\underline{\phi} \tag{27}$$

We derive [Sievert, 1992]

$$\delta\underline{\phi} \;=\; -\frac{1}{2}\, \underset{\approx}{\varepsilon}(d\underset{\sim}{\mathbf{R}}\, \underline{\mathbf{R}}^T) \;= \underset{\sim}{\mathbf{K}}\, d\underline{\mathbf{X}} \tag{28}$$

With

$$\underset{\sim}{\mathbf{K}} \;=\; \frac{1}{2}\, \underset{\approx}{\varepsilon} : (\underset{\sim}{\mathbf{R}}\; (\underset{\sim}{\mathbf{R}}^T \otimes \underline{\nabla})). \tag{29}$$

From (28) one can see that $\delta\underline{\phi}$ is not a total differential. Contrary to $\underset{\sim}{\mathbf{F}}$, $\underset{\sim}{\mathbf{K}}$ generally is not always invertible. With respect to the local space frame $E^\sharp$,

$$^\sharp d\underline{\mathbf{x}} \;=\; {}^\sharp\underset{\sim}{\mathbf{F}}\; d\underline{\mathbf{X}} \quad \text{and} \quad {}^\sharp\delta\underline{\phi} \;=\; {}^\sharp\underset{\sim}{\mathbf{K}}\; d\underline{\mathbf{X}}, \tag{30}$$

Where $^\sharp d\underline{\mathbf{x}} \;=\; \underset{\sim}{\mathbf{R}}^T\; d\underline{\mathbf{x}}$ and $^\sharp\delta\underline{\phi} \;=\; \underset{\sim}{\mathbf{R}}^T\; \delta\underline{\phi}$, and

$$^\sharp\underset{\sim}{\mathbf{F}} \;=\; \underset{\sim}{\mathbf{R}}^T\; \underset{\sim}{\mathbf{F}}, \quad {}^\sharp\underset{\sim}{\mathbf{K}} \;=\; \underset{\sim}{\mathbf{R}}^T\; \underset{\sim}{\mathbf{K}} \tag{31}$$

The relative measures $^\sharp\underset{\sim}{\mathbf{F}}$ and $^\sharp\underset{\sim}{\mathbf{K}}$ can be considered as natural Cosserat strains for the development of constitutive equations due to their invariance under any Euclidean transformation [Kafadar and Eringen, 1971]. They are called respectively the Cosserat deformation tensor and the wryness (or bend-twist, or torsion-curvature) tensor. An alternative expression of the wryness tensor is then

$$^\sharp\underset{\sim}{\mathbf{K}} \;=\; -\frac{1}{2}\, \underset{\approx}{\varepsilon} : (\underset{\sim}{\mathbf{R}}^T\; (\underset{\sim}{\mathbf{R}} \otimes \underline{\nabla})) \tag{32}$$

In order to compute the time derivative of the Cosserat strains we define the velocity and the gyration tensor, $\underline{\mathbf{v}}$, by

$$\underline{\mathbf{v}} \;=\; \dot{\underline{\mathbf{u}}} \;=\; \dot{u}_i\, \underline{\mathbf{e}}_i \quad \text{and} \quad \underset{\sim}{\upsilon} \;=\; \dot{\underset{\sim}{\mathbf{R}}}\, \underset{\sim}{\mathbf{R}}^T \tag{33}$$

and which can be replaced, due to its skew-symmetric property, by the associated gyration vector

$$\overset{\times}{\underline{\upsilon}} \;=\; -\frac{1}{2}\, \underset{\approx}{\varepsilon}\, \underset{\sim}{\upsilon} \tag{34}$$

Thus the time derivative of the Cosserat strains can be related to the gradient of the latter quantities:

$$ {}^{\sharp}\dot{\underset{\sim}{\mathbf{F}}}\ {}^{\sharp}\underset{\sim}{\mathbf{F}}^{-1} \;=\; \underset{\sim}{\mathbf{R}}^{T}\ (\underline{\mathbf{v}}\otimes\underline{\nabla}^{c} \;-\; \underset{\sim}{\mathbf{1}}\times\overset{\times}{\underline{\upsilon}})\ \underset{\sim}{\mathbf{R}}, \tag{35} $$

$$ {}^{\sharp}\dot{\underset{\sim}{\mathbf{K}}}\ {}^{\sharp}\underset{\sim}{\mathbf{F}}^{-1} \;=\; \underset{\sim}{\mathbf{R}}^{T}\ \overset{\times}{\underline{\upsilon}}\otimes\underline{\nabla}^{c}\ \underset{\sim}{\mathbf{R}}, \tag{36} $$

where $\underline{\nabla}^{c} \;=\; \dfrac{\partial}{\partial x_i}\,\underline{\mathbf{e}}_i \;=\; \underset{\sim}{\mathbf{F}}^{-T}\,\underline{\nabla}$ (Euclidean representation, *c* stands for current).
$\underline{\mathbf{v}}\otimes\underline{\nabla}^{c} \;-\; \underset{\sim}{\upsilon}$ is the relative velocity gradient and describes the local motion of the material element with respect to the microstructure.

3.3 Forces and stresses

The introduction of forces and stresses and the associated equilibrium equations are deduced from the application of the method of virtual power developed in the case of micromorphic media [Germain, 1973]. In [Forest et al., 1997] one can find how this method is adapted to the case of a Cosserat continuum. The virtual power of the internal forces has been applied in the framework of a first gradient theory and is a linear form of the virtual motions and their gradients. The dual quantities involved in this form are denoted $\underset{\sim}{\sigma}$ and $\underset{\sim}{\mu}$ respectively and are assumed to be objective tensors. Thus one has obtained the local equilibrium equations

$$ \begin{cases} \underline{\mathrm{div}}\,\underset{\sim}{\sigma} \;+\; \underline{\mathbf{f}} \;=\; 0 \\ \underline{\mathrm{div}}\,\underset{\sim}{\mu} \;+\; 2\overset{\times}{\underline{\sigma}} \;+\; \underline{\mathbf{c}} \;=\; 0 \end{cases} \tag{37} $$

and the boundary conditions

$$ \begin{cases} \underset{\sim}{\sigma}\,\underline{\mathbf{n}} \;=\; \underline{\mathbf{t}} \\ \underset{\sim}{\mu}\,\underline{\mathbf{n}} \;=\; \underline{\mathbf{m}} \end{cases} \tag{38} $$

where the partial derivatives are taken with respect to the current configuration and $\underline{\mathbf{f}}, \underline{\mathbf{c}}, \underline{\mathbf{t}}$ and $\underline{\mathbf{m}}$ are the external forces. $\underset{\sim}{\sigma}$ is called the Cauchy force stress tensor and $\underset{\sim}{\mu}$ the couple-stress tensor. They are generally not symmetric.

3.4 Isotropic elasticity

From the equations obtained in the framework of a hyperelastic material and with the assumptions that the strain, torsion curvature and microrotations remain small

$$ \begin{cases} \underset{\sim}{\mathbf{R}} \;\simeq\; \underset{\sim}{\mathbf{1}} \;+\; \underset{\sim}{\mathbf{1}}\times\underline{\phi} \;=\; \underset{\sim}{\mathbf{1}} \;-\; \underset{\approx}{\varepsilon}\,\underline{\phi} \\ {}^{\sharp}\underset{\sim}{\mathbf{F}} \;\simeq\; \underset{\sim}{\mathbf{1}} \;+\; \underline{\mathbf{u}}\otimes\underline{\nabla} \;+\; \underset{\approx}{\varepsilon}\,\underline{\phi} \;=\; \underset{\sim}{\mathbf{1}} \;+\; \underset{\sim}{\mathbf{e}} \\ {}^{\sharp}\underset{\sim}{\mathbf{K}} \;\simeq\; \underline{\phi}\otimes\underline{\nabla} \;=\; \underset{\sim}{\kappa} \end{cases} \tag{39} $$

where $\underset{\sim}{\kappa}$ is the torsion curvature tensor. Furthermore, ${}^{\sharp}\underset{\sim}{\sigma} \simeq \underset{\sim}{\sigma}$ and ${}^{\sharp}\underset{\sim}{\mu} \simeq \underset{\sim}{\mu}$. Consequently, for linear elasticity, two four rank elasticity tensors are introduced

$$ \begin{cases} \underset{\sim}{\sigma} \;=\; \underset{\approx}{\mathbf{E}} \;:\; \underset{\sim}{\mathbf{e}} \\ \underset{\sim}{\mu} \;=\; \underset{\approx}{\mathbf{C}} \;:\; \underset{\sim}{\kappa} \end{cases} \tag{40} $$

These tensors have some symmetry properties due to the hyperlelasticity conditions and material symmetries. The form of the Cosserat elasticity tensors for all symmetry classes has been established by [Kessel, 1964]. In the isotropic case equation (40) gets the simple form

$$\begin{cases} \underset{\sim}{\sigma} = \lambda \underset{\sim}{\mathbf{1}} \operatorname{Tr}\underset{\sim}{\mathbf{e}} + 2\mu \{\underset{\sim}{\mathbf{e}}\} + 2\mu_c \{\underset{\sim}{\mathbf{e}}\} \\ \underset{\sim}{\mu} = \alpha \underset{\sim}{\mathbf{1}} \operatorname{Tr}\underset{\sim}{\kappa} + 2\beta \{\underset{\sim}{\kappa}\} + 2\gamma \{\underset{\sim}{\kappa}\} \end{cases} \tag{41}$$

and then depends on the two classical Lamé constants λ, μ complemented by four additional parameters [Wilmański and Woźniak, 1967].

3.5 Elastoplastic Cosserat single crystal

In the case of single crystals we use the main principal results in Cosserat theory at large strains [Sievert, 1992]. Elastic and plastic Cosserat deformations and curvatures are introduced due to the non-homogeneous permanent lattice rotations, which may be induced by non-homogeneous plastic deformations in single crystals. They are denoted by: ${}^\sharp\underset{\sim}{\mathbf{F}}^e$, ${}^\sharp\underset{\sim}{\mathbf{F}}^p$, ${}^\sharp\underset{\sim}{\mathbf{K}}^e$ and ${}^\sharp\underset{\sim}{\mathbf{K}}^p$.
We use, as proposed in [Mandel, 1971], the multiplicative decomposition for the Cosserat deformation:

$${}^\sharp\underset{\sim}{\mathbf{F}} = {}^\sharp\underset{\sim}{\mathbf{F}}^e \, {}^\sharp\underset{\sim}{\mathbf{F}}^p \tag{42}$$

Moreover a decomposition of the entire wryness tensor is [Sievert, 1992]:

$${}^\sharp\underset{\sim}{\mathbf{K}} = {}^\sharp\underset{\sim}{\mathbf{K}}^e \, {}^\sharp\underset{\sim}{\mathbf{F}}^p + {}^\sharp\underset{\sim}{\mathbf{K}}^p \tag{43}$$

The plastic deformation of single crystals is the result of slip processes on slip systems. For each slip system s, we define

$$\underline{\mathbf{m}}^s = \underline{\mathbf{b}}^s / \|\underline{\mathbf{b}}^s\| \tag{44}$$

Where $\underline{\mathbf{b}}^s$ is the Burgers vector. $\underline{\mathbf{z}}^s$ is the unit vector normal to the slip plane. In consequence the plastic strain rate takes the form

$${}^\sharp\dot{\underset{\sim}{\mathbf{F}}}^p \, {}^\sharp\underset{\sim}{\mathbf{F}}^{p-1} = \sum_{s\in S} \dot{\gamma}^s \, {}^\sharp\underset{\sim}{\mathbf{P}}^s. \tag{45}$$

$\dot{\gamma}^s$ is the slip rate for the system s. ${}^\sharp\underset{\sim}{\mathbf{P}}^s$ is given by the kinematics of slip

$${}^\sharp\underset{\sim}{\mathbf{P}}^s = {}^\sharp\underline{\mathbf{m}}^s \otimes {}^\sharp\underline{\mathbf{z}}^s \tag{46}$$

where ${}^\sharp\underline{\mathbf{z}}^s = \underset{\sim}{\mathbf{R}}^T \underline{\mathbf{z}}^s$.
[Forest et al., 1997] proposed the following kinematics for the plastic wryness

$${}^\sharp\dot{\underset{\sim}{\mathbf{K}}}^p \, {}^\sharp\underset{\sim}{\mathbf{F}}^{p-1} = \sum_{s\in S} \frac{\dot{\theta}^s}{l} \, {}^\sharp\underset{\sim}{\mathbf{Q}}^s \tag{47}$$

The θ^s are angles that measure the plastic curvature and torsion over a characteristic length l. At small strain we imply have

$$\begin{cases} \underset{\sim}{\mathbf{e}} = \underset{\sim}{\mathbf{e}}^e + \underset{\sim}{\mathbf{e}}^p \\ \underset{\sim}{\kappa} = \underset{\sim}{\kappa}^e + \underset{\sim}{\kappa}^p \end{cases} \tag{48}$$

3.6 Explicit integration of the constitutive equations

We give below explicit integrated forms of the previous constitutive equations.

3.6.1 Kinematic of plastic deformation and curvature

The expression of $\overset{\sharp}{\mathbf{Q}}{}^s$ is derived from the analysis of the dislocation density tensor [Forest et al., 1997]. This one can be decomposed into the contributions of edge and screw dislocations. In the following we use the index $(\perp)$ as the lattice curvature due to edge dislocations and the symbol $(\odot)$ as the lattice torsion due to screw dislocations. Thus the decomposition of the plastic torsion-curvature can be written with the help of two associated orientation tensors $\underset{\sim}{\mathbf{Q}}_{\perp}$ and $\underset{\sim}{\mathbf{Q}}_{\odot}$

$$\overset{\sharp}{\underset{\sim}{\dot{\mathbf{K}}}}{}^p \overset{\sharp}{\underset{\sim}{\mathbf{F}}}{}^{p-1} = \sum_{s=1}^{n} \left(\frac{\dot{\theta}^s_{\perp}}{l_{\perp}} \underset{\sim}{\mathbf{Q}}^s_{\perp} + \frac{\dot{\theta}^s_{\odot}}{l_{\odot}} \underset{\sim}{\mathbf{Q}}^s_{\odot} \right) \tag{49}$$

And

$$\underset{\sim}{\mathbf{Q}}^s_{\perp} = \underline{\xi}^s \otimes \underline{\mathbf{m}}^s, \quad \underset{\sim}{\mathbf{Q}}^s_{\odot} = \frac{1}{2}\underset{\sim}{\mathbf{1}} - \underline{\mathbf{m}}^s \otimes \underline{\mathbf{m}}^s, \tag{50}$$

where $\underline{\xi}^s = \underline{\mathbf{n}}^s \times \underline{\mathbf{m}}^s$ is the edge dislocation line vector.

3.6.2 Generalized Schmid law

The Peach and Koehler's formula given by [Kröner, 1956] allows the Schmid's criterion to have a physical meaning. This one is used to compute the slip rate on slip system s

$$\dot{\gamma}^s = \left(\frac{\mathrm{Max}(0, \mid \tau^s - x^s \mid - r^s)}{k^s} \right)^{n^s} \mathrm{sign}(\tau^s - x^s) \tag{51}$$

Where $\tau^s = \overset{\sharp}{\underset{\sim}{\sigma}} : \overset{\sharp}{\underset{\sim}{\mathbf{P}}}{}^s$. x^s and r^s are internal kinematic and isotropic hardening variables. They represent respectively the back-stress and the yield threshold, which are supposed to describe with sufficient accuracy the dislocation structure for a correct modelling of the hardening behaviour. The viscosity properties are characterized by the parameters k^s and n^s.

For the viscoplastic torsion-curvature variables [Forest, 1996] proposed a expression such as

$$\dot{\theta}^s = \left(\frac{\mathrm{Max}(0, \mid \overset{\sharp}{\underset{\sim}{\mu}} : \overset{\sharp}{\underset{\sim}{\mathbf{Q}}}{}^s \mid - l\, r^s_c)}{l k^s_c} \right)^{n^s_c} \mathrm{sign}(\overset{\sharp}{\underset{\sim}{\mu}} : \overset{\sharp}{\underset{\sim}{\mathbf{Q}}}{}^s) \tag{52}$$

where r^s_c denotes the threshold and k^s_c and n^s_c are viscosity parameters. The formula is to be applied successively for edge and screw dislocations belonging to the same system.

The evolution rules for the thresholds r^s and r^s_c used in this work are then

$$r^s = r_0 + q \sum_{r=1}^{n} h^{sr}(1 - \exp(-b v^r)) + H' \mid \theta^s \mid \quad \text{with} \quad \dot{v}^s = \mid \dot{\gamma}^s \mid \tag{53}$$

$$r_c^s = r_{c0}$$

The components h^{rs} of the interaction matrix account for self- and latent hardening. The threshold for plastic curvature is taken constant for simplicity. A simple linear coupling term H' is added to more conventional nonlinear contributions.

4 Numerical analysis of near tip fields for different orientations of the crystal

4.1 Conditions of the finite element calculations

We will present in this part some calculations with two models. The first one is a classical model of single crystals at large deformations based on the constitutive equations proposed by Mandel [Mandel, 1971]. The second is a Cosserat plasticity model which takes explicitly elastoplastic lattice torsion-curvature into account . Both are implemented in the finite element code ZéBuLoN [Forest, 1998].

4.1.1 General conditions

The finite element mesh of the considered single crystalline CT specimen to be computed under plane strain conditions is represented on Fig. 85.

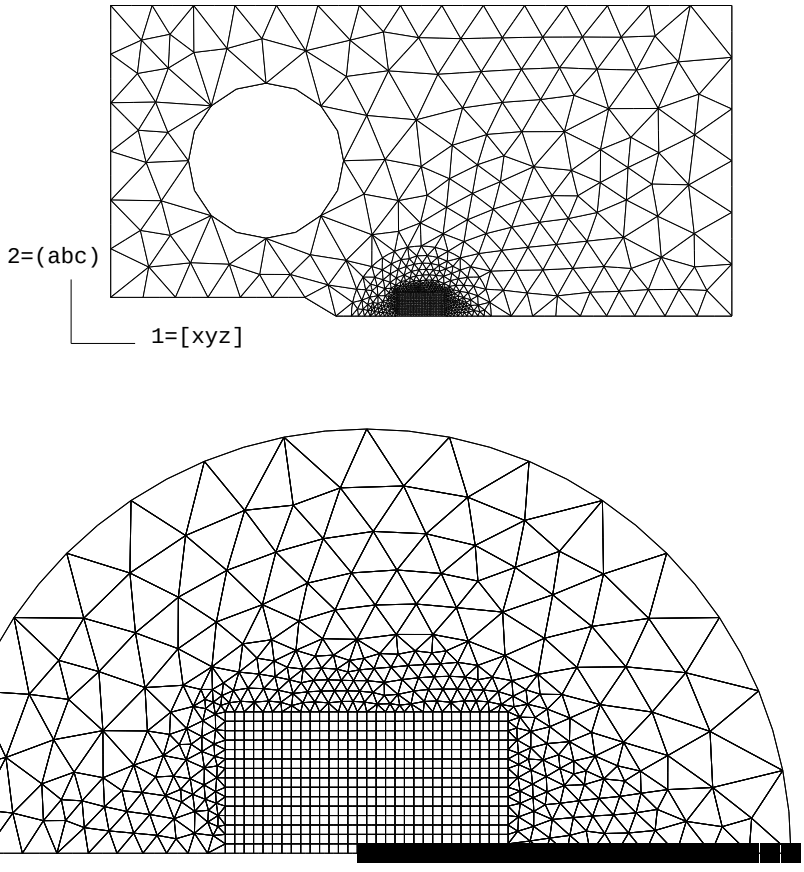

Figure 85: Finite element mesh of the CT specimen (above, the mesh of the pin is not represented); mesh of the crack tip zone, the nodes belonging to the ligament being represented by black squares (below).

A regular mesh with quadratic elements and reduced integration is used at the crack tip. Such a mesh has been shown in [Forest and Cailletaud, 1995] to be able to capture shear bands of any orientation and thus to minimize the mesh-dependence of the results associated with localization phenomena. It is important since the orientation of the localization bands must be a prediction of the model. Displacement in direction 2, see Fig. 85, is prescribed to the nodes of the ligament. An additional boundary condition needed for the generalized continuum is a vanishing lattice rotation at the ligament for symmetry reasons. The orientation of the specimen will be described by the crack plane ((abc) on Fig. 85) and the initial crack growth direction ([xyz] on Fig. 85).

4.1.2 Conditions of the analysis with classical crystal plasticity

We use the elastic constants of the single crystal nickel-base superalloy SC16 [Ziebs and Frenz, 1997] calibrated at 650°C with a classical procedure [Olschewski, 1997]. Octahedral slip only is taken into account for simplicity, involving 12 $\{111\}\langle 110\rangle$ slip systems. Parameter k (resp. n) are chosen low (resp. large) enough in order to get a rate-independent behavior. Moreover we introduce in some cases a softening in the isotropic hardening, which has an initial radius of 500 MPa, and a diagonal interaction matrix to amplify the localisation phenomena.

4.1.3 Conditions of the analysis with the Cosserat model

For simplicity we only consider the effects of the local curvature due to the accommodation of edge-type dislocations. The elastic moduli are such that the Cosserat elasticity strain $\underset{\sim}{\mathbf{e}}^e$ remains symmetric and the bending moduli of $\underset{\approx}{\mathbf{C}}$ are equal to 10^{-3} MPa m^2. We take a very small threshold for plastic curvature. The parameters are such that the same behaviour is obtained as the classical crystal plasticity for a vanishing H'. Parameter H' will vary from 0 to 10000 MPa to investigate the effect of lattice curvature on localization.

4.2 Results and interpretation of the localization bands

4.2.1 Results obtained with the classical model and the Cosserat model with vanishing H'

A summary of all investigated orientations is given in table 14. The structure of the localization band patterns found at the tip of $(011)[100]$ and $(001)[100]$ cracks is illustrated by the equivalent strain in Fig. 86 for a calculation with the classical model and Fig. 87 (below) for a computation with the model of Cosserat and vanishing H'. Both models give almost identical results. Moreover an analysis of the slip systems activated in each band for these crack orientations allows us to know, almost for certain bands, the motion of the edge dislocations on planes. Fig. 89 shows a schematic representation of such dislocation motions when the interpretation is possible. In the following we will use the band numbers given in Fig. 89. From these results a characterization of the bands is given in the next section.

4.2.2 Characteristic of the inelastic strain localization bands

Mainly three types of strain localization bands have been found.

Slip band:

In the band (2) of the $(011)[100]$ crack (see Fig. 89, above), two slip systems are activated simultaneously with the same amount of slip, the result being an effective macroscopic $(100)[011]$ slip band, see Fig. 86, above. Two symmetric slip bands are found for the $(001)[110]$ oriented crack too, see Fig. 91, note that the $(011)[100]$ oriented crack of the b.c.c. single crystal is a similar case. Moreover slip bands induce almost no lattice rotation at all, see Figs. 88 (above), 91 (below).

Kink band:

From Fig. 86, 89 the second band (1) of the $(011)[100]$ crack can be interpreted as a kink band for the effective slip system $(111)[\bar{2}11]$. Similarly the vertical band on Fig. 91 (above) is a kink band for the $(001)[110]$ oriented crack. In contrast with the previous case significant localized lattice rotation and therefore strong lattice curvature is observed, see Figs. 88 (above), 91 (below).

Multislip band:

The pattern observed at the $(001)[100]$ crack tip is much more complicated and four slip systems are activated simultaneously in each band, see Fig. 86 (below). In band (2) of Fig. 89 (below), the activated slip systems can be divided into two groups of two slip systems with different amount of slip for each group. According to the Fig. 88 (below) a high lattice rotation occurs in the multislip bands. Contrary to the two first types this one cannot be apparently identified as crystallographic localization plane. Similar non-crystallographic shear bands for double slip have been obtained in [Forest and Cailletaud, 1995].

A fourth situation is possible concerning the nature of the strain localization at the crack tip of single crystals but it is not another type of band. In band (1) of the $(001)[100]$ crack for instance, the amount of slip is the same for the four systems and the band can be interpreted as the superposition of an effective $(\bar{1}01)[101]$ slip band and of an effective $(101)[\bar{1}01]$ kink band, see Fig. 89 (below). As for the multislip bands the amount of lattice rotation is rather high.
After this review of the main types of bands of strain localization it is interesting to investigate their behaviour when the additional hardening due to the lattice curvature in the Cosserat model is taken into account.

4.2.3 Consequences of the introduction of hardening due to lattice curvature

If sufficiently strong additional hardening H' is introduced, the picture is drastically changed. Due to the small amount of the lattice rotation in slip bands, these one remain, as shown on Fig. 90 (above). The opposite result is obtained for the kink band.

For the $(011)[100]$ crack, see Fig. 90 (above), the two kink bands have disappeared, as it could have been expected from the bifurcation analysis of [Forest, 1998]. From Fig. 87 (above) we observe that the combination between the effective slip and the effective kink is no more present, because of the non negligible amount of lattice rotation. The same property exists for the crack which is oriented along $(001)[100]$, see Fig. 90 (below). For the crack configurations $(001)[100]$ and $(011)[0\bar{1}1]$ we observe that the multislip bands remain even if the amount of lattice rotation is high, see Figs. 87 (above) and 90 (below). Actually lattice curvature inside these bands leads to higher local stresses and therefore more limited localization.

It must be noted that contrary to the isotropic elastoplastic case, the localization patterns computed under plane stress conditions are not significantly different.
The introduction of moderate work-hardening leads to more diffuse deformation but does not significantly alter the structure of the crack tip stress-strain field.
For the $(011)[100]$ oriented crack, the global load-displacement curve of each models have been plotted on Fig. 92. The Cosserat model shows a stronger hardening as the classical model. Moreover the corresponding experimental curve can be used to identify the value of the additional hardening due to lattice curvature.

4.3 Discussion

The previous computations indicate that, if additional hardening due to lattice curvature is introduced in continuum modelling, (effective) kink bands are precluded at the crack tip in favour of (effective) slip bands. If all possible bands are associated with lattice curvature, some of them subsist. The physical relevance of the result is difficult to assess since only scarce precise observations of the crack tip in single crystals are available. In [Shield and Kim, 1994], a b.c.c. single crystal is carefully studied for crack orientation that is similar to our $(001)[110]$ crack for symmetry reasons. Indeed the vertical kink band expected in the classical analysis, see Fig. 91, does not seem to be present. However no special attention is paid to this point in [Shield and Kim, 1994]. If localization bands are regarded as preferential bifurcation paths for possible crack branching, the present work leads us to postulate that crack branching from a stable path to a localization band with strong lattice curvature is not possible. This can be supported by some experimental results provided in [Henderson and Martin, 1995] for a CT specimen and in [Ziebs and Frenz, 1997] for two sharply notched SC16 specimens under cyclic loading, described in the second part (see Section 5.2 below).
However, for nickel base superalloys one should introduce in the behaviour the cubic slip family. In order to assess the influence of such slip family on the strain localization pattern at the crack tip, the calculation in small deformation of the $(011)[100]$ configuration has been performed with the constants of the classical model calibrated for SC16 at 650°C.
From Fig. 93 one can observe the presence of three bands of inelastic strain localization. Two of them are due to the octahedral slip system and the other one is due to the cubic slip system. The orientation of these bands is the same as the one obtained in the same problem analysed only with the octahedral slip system family. A detailed analysis of the activated slip in each band shows that the two symmetric bands are identified as kink

bands and the vertical one is a slip band. Thus, even if the bands of localization do not belong to the same slip system family as in the simplified calculation of Section 4.1.3, the nature of the bands does not change at all.

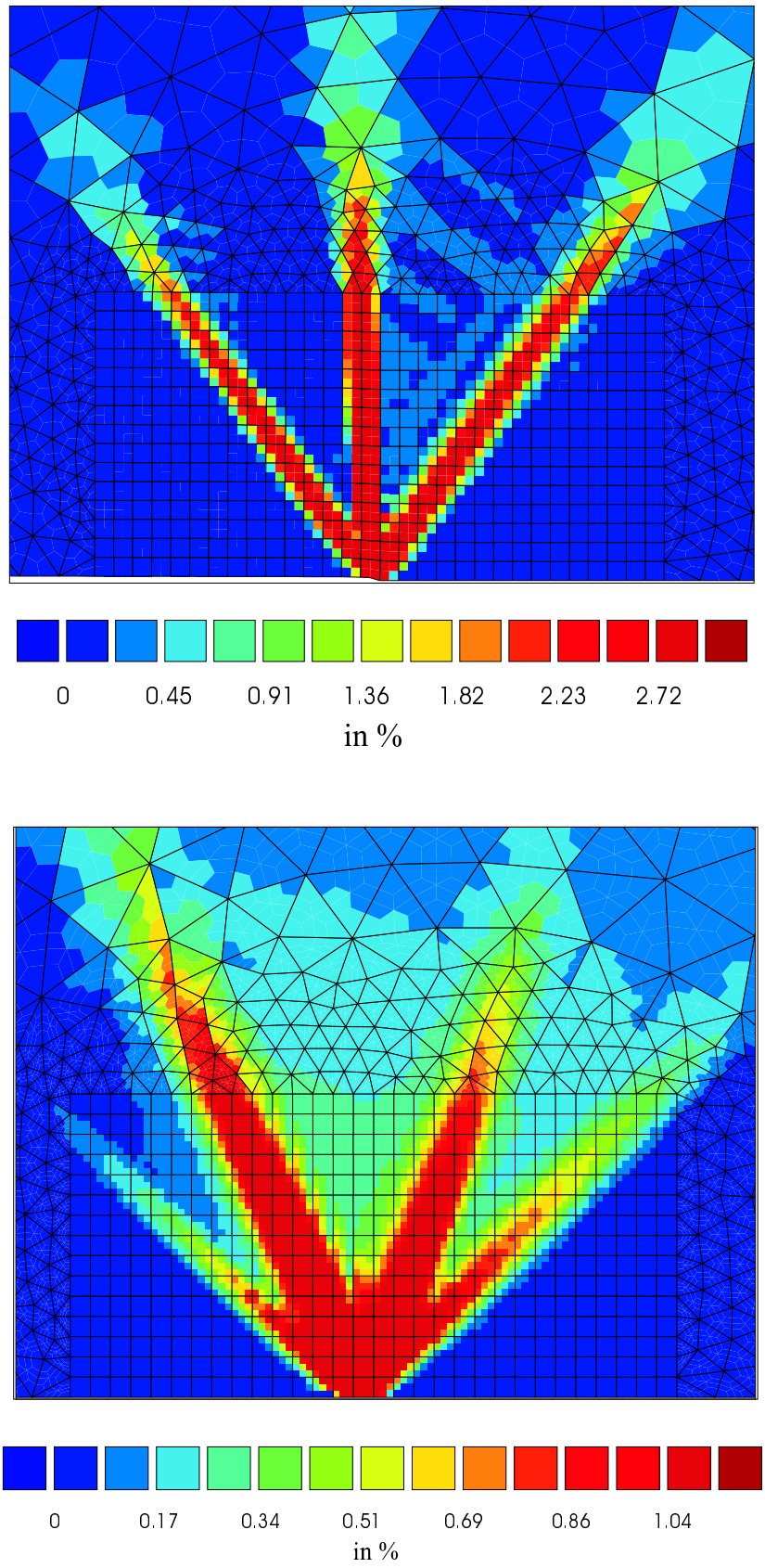

Figure 86: Strain localization pattern at the crack tip obtained with the Mandel model: $(011)[100]$ crack (above) and $(001)[100]$ crack (below), equivalent plastic strain.

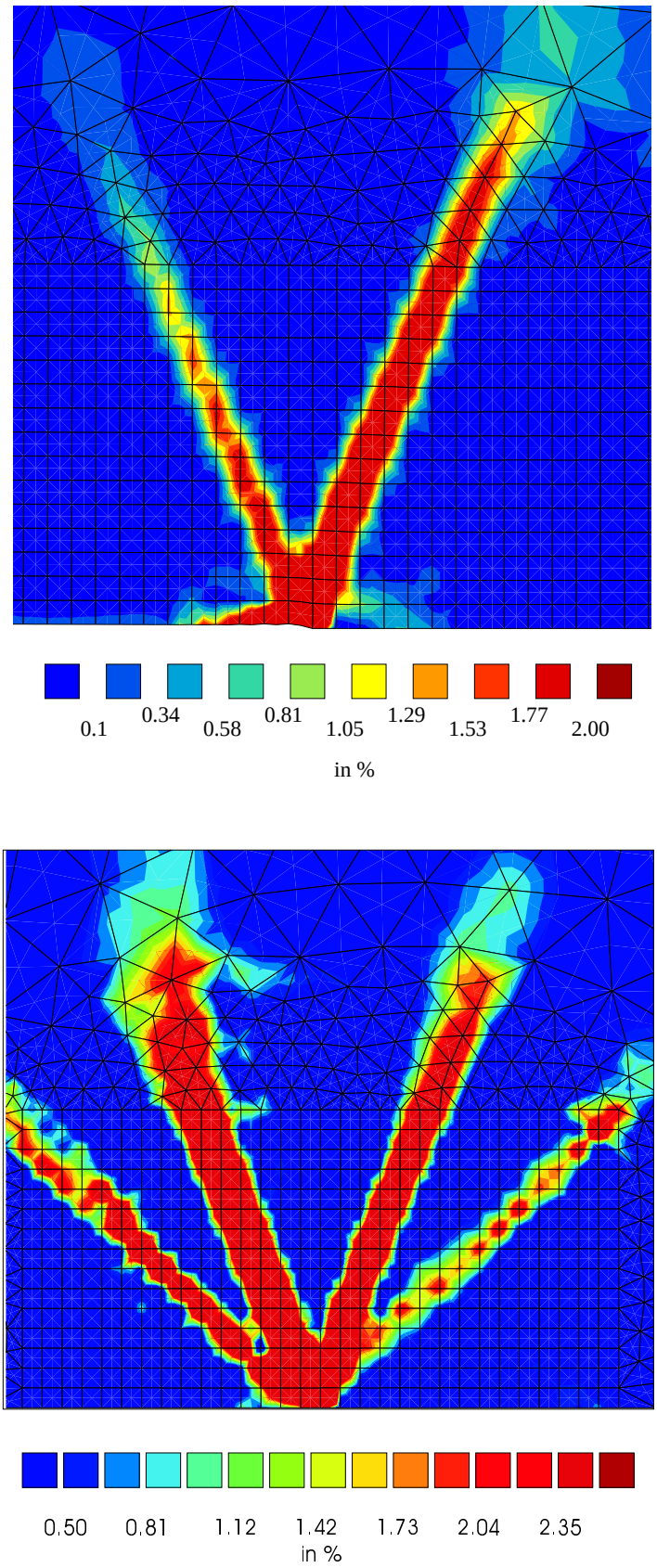

Figure 87: Strain localization pattern at the $(011)[0\bar{1}1]$ (above, $H' = 5000$) and $(001)[100]$ (below, $H' = 0$) oriented crack tip obtained with the Cosserat model: contour of equivalent plastic strain.

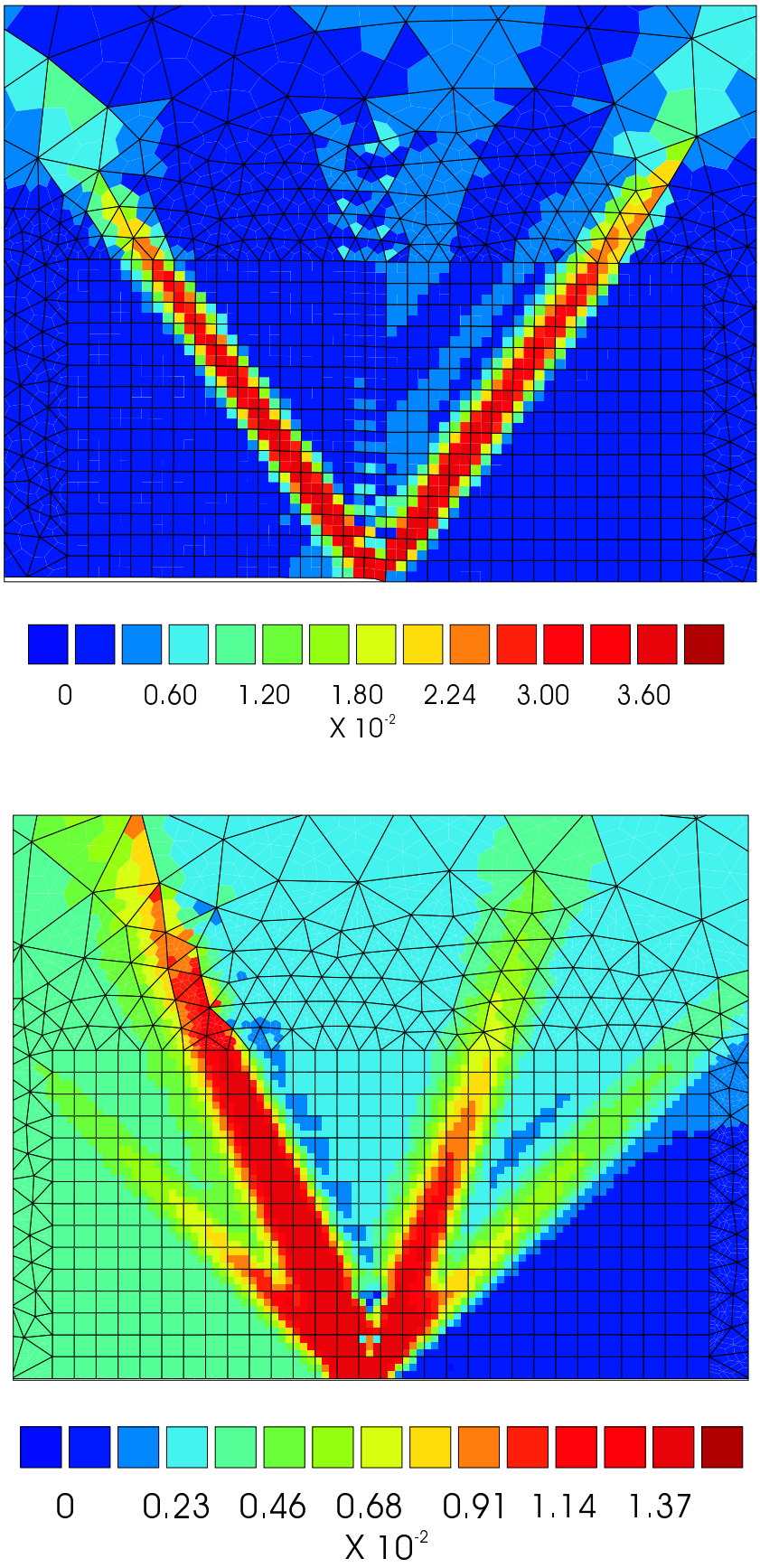

Figure 88: Amount of lattice rotation at the crack tip obtained with the Mandel model: $(011)[100]$ crack (above) and $(001)[100]$ crack (below).

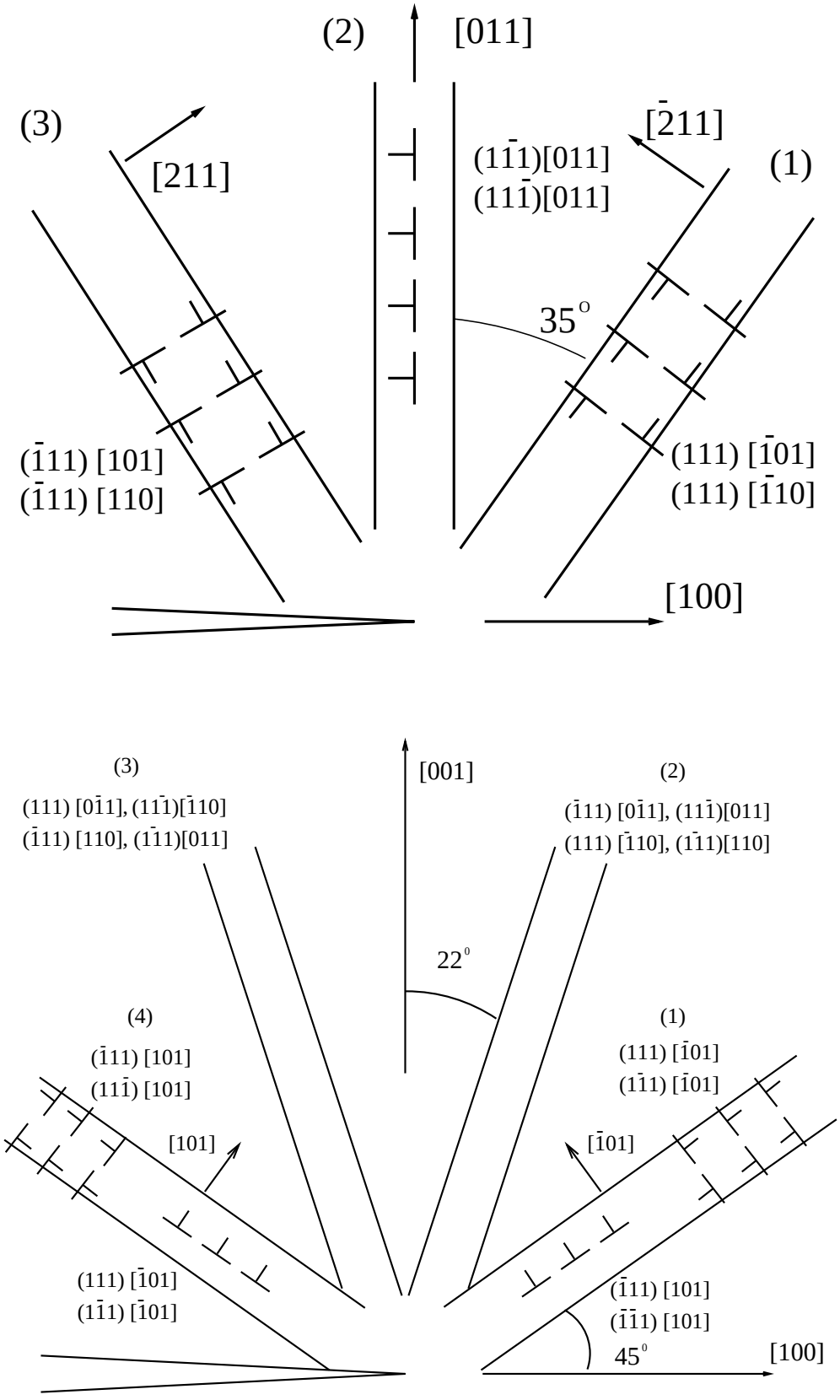

Figure 89: Localization band patterns: $(011)[100]$ crack (above) and $(001)[100]$ crack (below); the indicated slip sytems are significantly activated in the nearest band.

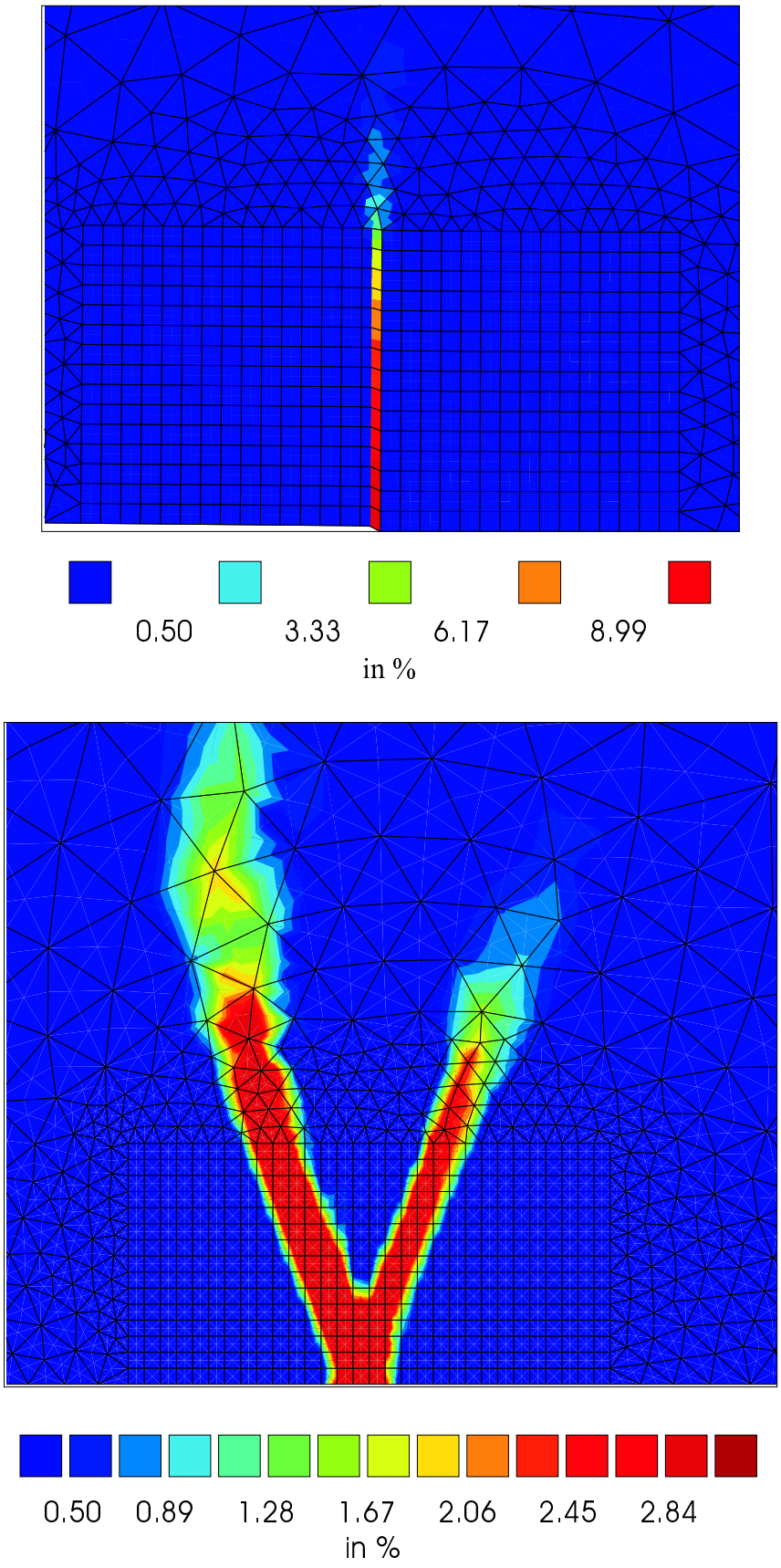

Figure 90: Strain localization patterns at the crack tip including lattice curvature effects: $(011)[100]$ crack (above) and $(001)[100]$ crack (below); contour of plastic strain.

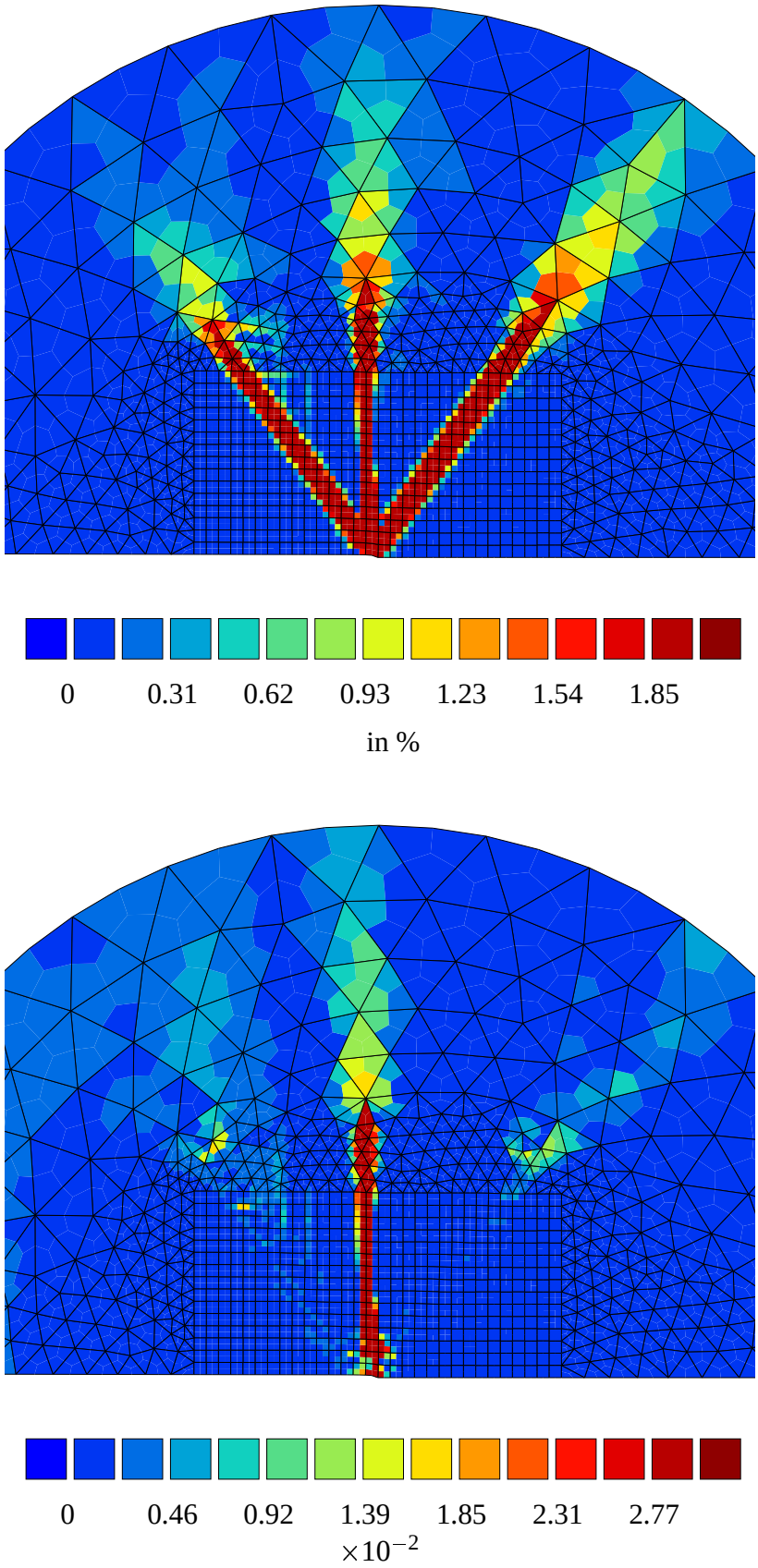

Figure 91: Strain localization pattern at a b.c.c. $(011)[100]$ oriented crack tip obtained with the Mandel model: contour of equivalent plastic strain (above) and amount of lattice rotation (below) (for comparison with [Shield and Kim, 1994]).

crack orientation	number of bands: classical (Cosserat) / band characteristics (orientation and type)
$(011)[100]$	3 (1) / (55° *kink*), 90° *slip*, (125° *kink*)
$(001)[110]$	3 (2) / 55° *slip*, (90° *kink*), 125° *slip*
$(001)[100]$	4 (2) / (45° *slip*+*kink*), 68° *multislip*, 112° *multislip*, (135° *kink*+*slip*)
$(011)[0\bar{1}1]$	3 (2) / 68° *multislip*, (90° *slip*+*kink*), 112° *multislip*

Table 14: List and structure of investigated localization bands for several crack configurations; for the cases illustrated in Fig. 89, the band orientations and types are listed in the order given by the numbers on Fig. 89, i.e. counterclockwise starting from the right; the bands in brackets do not appear for sufficiently high values of H.

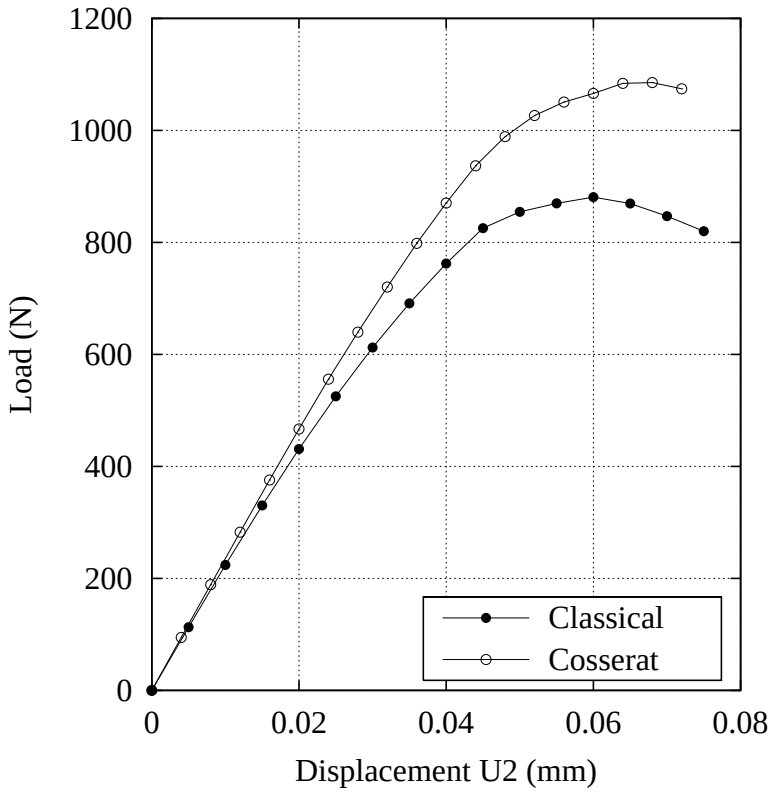

Figure 92: Comparison between the classical and the Cosserat model for single crystal for the $(011)[100]$ oriented crack tip; load-displacement curves.

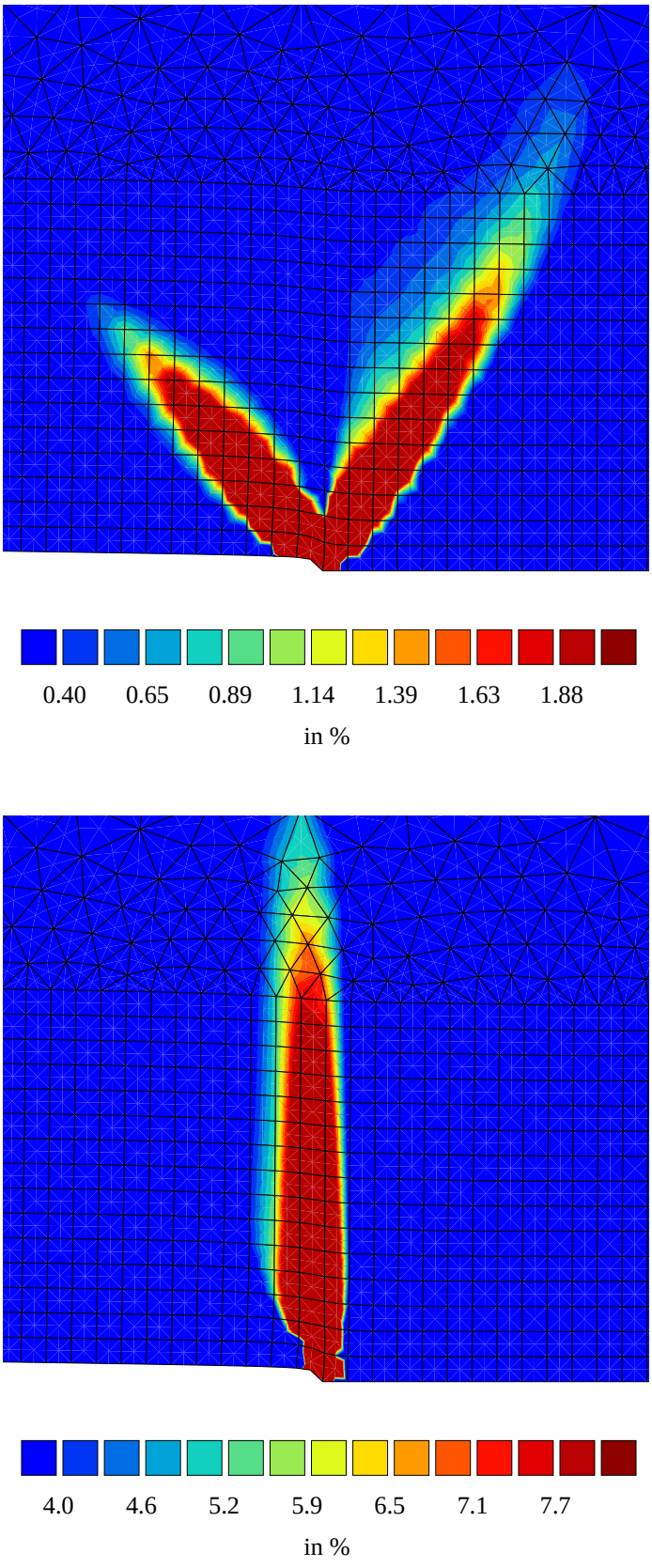

Figure 93: Strain localization pattern at the crack tip of the $(011)[100]$ SC16 oriented specimen with the classical viscoplastic model for small deformations: octahedral (above) and cubic (below) equivalent inelastic strain.

5 Application to tridimensional notched specimens

In oder to simulate these experimental results we try to model the crack configurations with, first, the equivalent two-dimensional problem, and then the 3D specimen. For both calculations the classical crystal plasticity model at small deformation has been used. The information resulting from numerical simulations and allow us to interpret some experimental observations concerning cracks bifurcations.

5.1 Analysis of the 2D equivalent problem

If we consider the previous initial crack configuration we can assume a plane strain deformation in the middle section normal to the crack plane. Thus, for a qualitative analysis of the strain localization at the crack tip, the mesh of the CT specimen already used in this work is sufficient.

The similar two-dimensional calculation previously presented in Section 4.1.1 has been performed. The cubic slip systems of the single crystal SC16 in addition of the octahedral slip system have been introduced. The initial crack front has been oriented along $(001)[110]$. A calculation in tension with the constants of the classical crystalline model previously identified at 650°C in small deformation has been carried out.

As for the case of the $(011)[100]$ oriented crack tip (Section 4.3) the cubic slip system is activated and one vertical band of inelastic strain can be observed. The other two symmetric bands of the octahedral slip system have the same orientation as in the previous calculation performed with only the octahedral slip system family (see table 14). Moreover if we investigate in detail which slip systems are activated for each slip system family we obtain the same interpretation concerning the nature of the strain localization bands. Along $[001]$ we have a kink band and the symmetric ones, which are the traces of the planes (111) on the crack plane, are two slip bands. As a consequence, we expect to obtain with the analysis of Cosserat and sufficiently strong additional hardening the same results summarized in table 14: only the two symmetric bands of inelastic strain localization remain.

5.2 Comparison with experimental results

Low-cycle fatigue tests on Nickel base single crystal superalloy SC16 have been performed on sharp notched specimens at the BAM. After a short presentation of their main characteristics we compare the results with those expected with the numerical approach. The diameter of the minimal cross section of the round cylindrical specimens is 9 mm.

A notch 0.4 mm in depth on one side of the circular section has been saw-cut. The initial sharp notches correspond to $(001)[100]$ and $(001)[110]$ oriented cracks. Uniaxial and symmetric low-cycles fatigue tests have been performed under stress controlled at 650°C in air. Some interruptions have been made in order to identify the crack growth

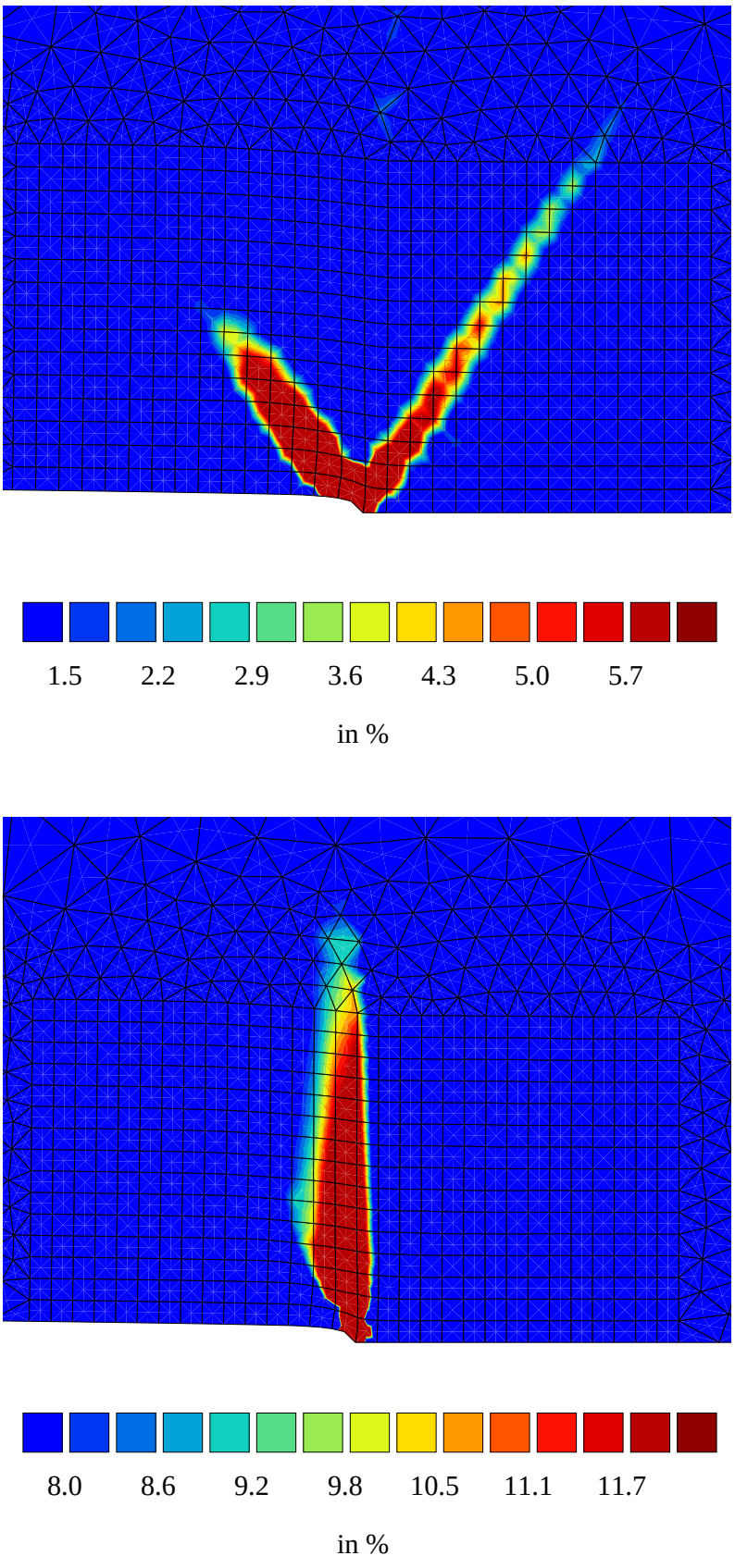

Figure 94: Strain localization pattern at the crack tip of the $(001)[110]$ SC16 oriented specimen with the classical viscoplastic model for small deformations: octahedral (above) and cubic (below) equivalent inelastic strain.

mechanism in single crystal and to determine the planes of the possible crack bifurcations.

The micrographs of the surface rupture of the two sharply notched specimens are given Fig. 95. After a certain number of cycles, crack growth becomes unstable. In the case of the $(001)[100]$ oriented crack, the fracture surface is complex but the crack remains globally in its initial plane. In the case of the $(001)[110]$ oriented crack, it deviates on a (111) plane, as expected from the previous finite element analysis. Indeed the $(001)[110]$-crack deviates on pure slip bands, compare Fig. 94 above, and the $(001)[100]$-crack does not branch out on kink bands or multislip bands with lattice curvature, compare Fig. 88 below. This observation supports the hypothesis that the crack branching on localisation bands with strong lattice curvature is difficult. The agreement between the experiment and the finite element calculation is satisfactory and encourages us to improve the model for tridimensional component.

5.3 Analysis of the whole component

The calculation of the $(001)[110]$ oriented initial crack, machined in a SC16 cylindrical round specimen have been performed. The cubic symmetry of the material and the geometry of the specimen allow us to mesh only one fourth of the structure, see Fig. 96. The mesh is composed of 2190 linear elements and the finite element problem has 8613 degrees of freedom. The structure has been computed in tension with the same model as for the equivalent 2D calculation.

The equivalent cumulative inelastic strain for each slip system family are given Fig. 97. Even for the octahedral slip family we obtain a vertical band of strain localization. Note that the mesh has very few elements in the vicinity of the crack front and along the axial loading. Moreover linear elements are not well-suited for localization analysis. For these reasons we assume that no conclusion can be drawn about the localization of the inelastic strain at the crack tip from this calculation. Furthermore we can not compare its results with those of the experiment.

6 Conclusion

According to the previous numerical analyses the Cosserat model precludes the kink bands at the crack tip of a nickel base single crystal superalloy if sufficient additional hardening due to lattice curvature is introduced. If such localization bands can be considered as privileged bifurcation paths, leading to possible crack branching, one has to promote a model which precludes strong lattice curvature. Furthermore a non linear additional hardening term should be introduced instead of the two simple H' terms.
A twodimensional calculation shows that the Cosserat model is in a good agreement with the experimental results for one particular crack configuration. A decisive experiment would be to consider a $(011)[100]$ specimen for which we expect no crack deviation in spite of the kink bands predicted by the classical crystal plasticity. Furthermore more realistic fully three-dimensional crack configurations must be investigated numerically.

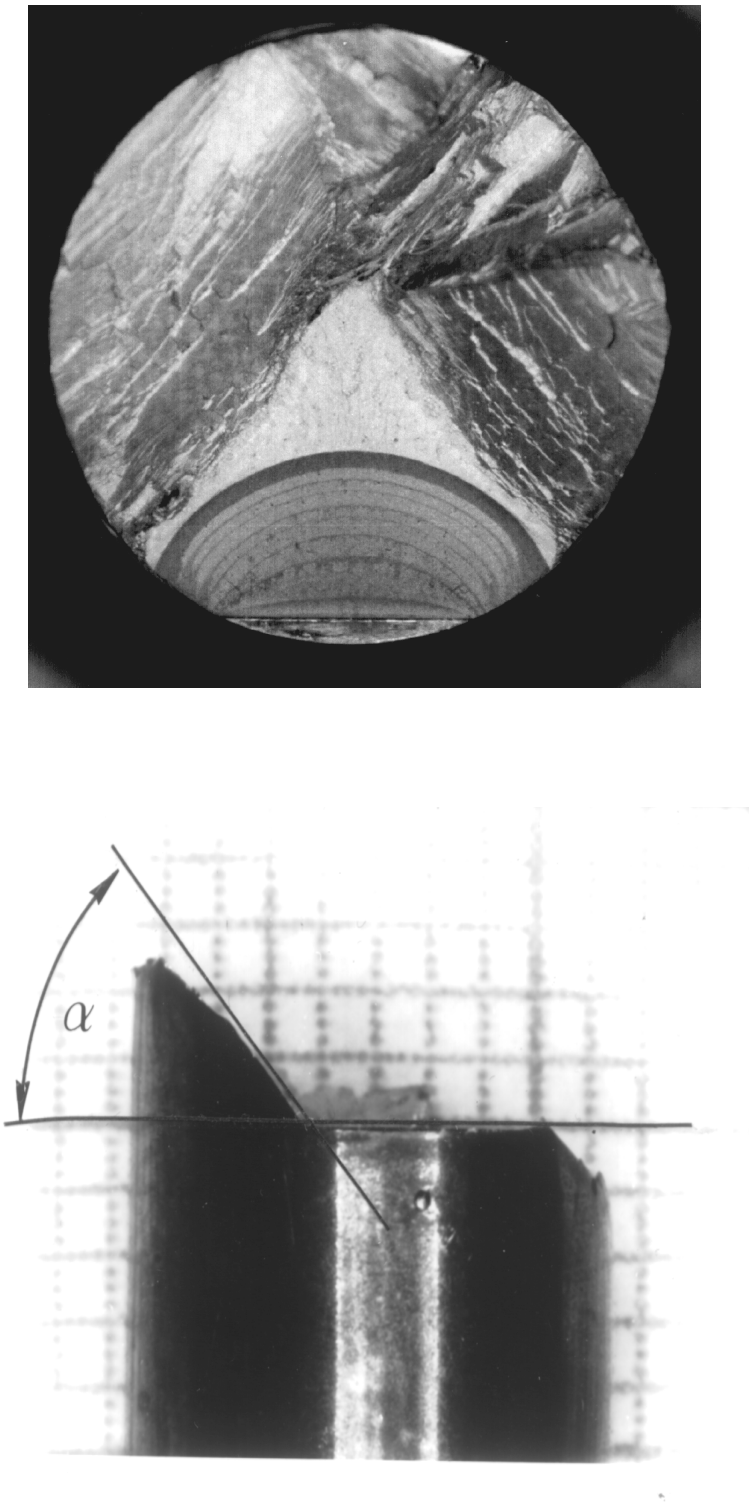

Figure 95: Final unstable crack path for two sharply notched $[001]$ SC16 specimens under cyclic loading (specimen diameter: 9mm): fracture surface for a $(001)[100]$ initial crack (left, the tensile direction $[001]$ is normal to the fracture surface) and side view of the fracture surface for a $(001)[110]$ initial crack showing the trace of the bifurcation plane (111) (right).

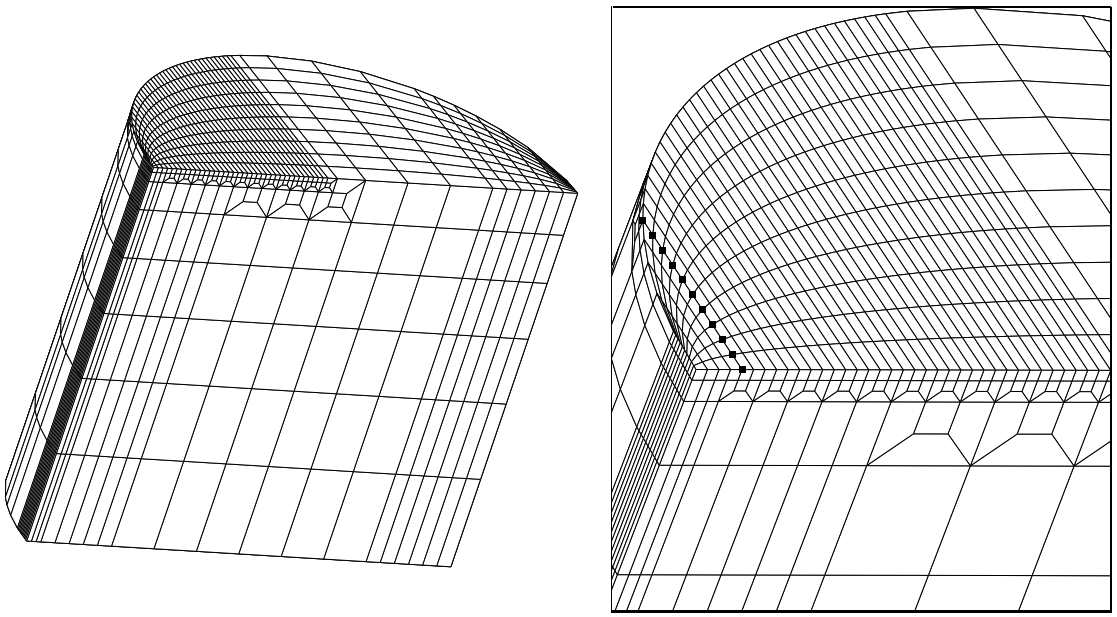

Figure 96: Finite element mesh of one fourth of the notched specimen. Right the nodes belonging to the crack front are represented by black squares.

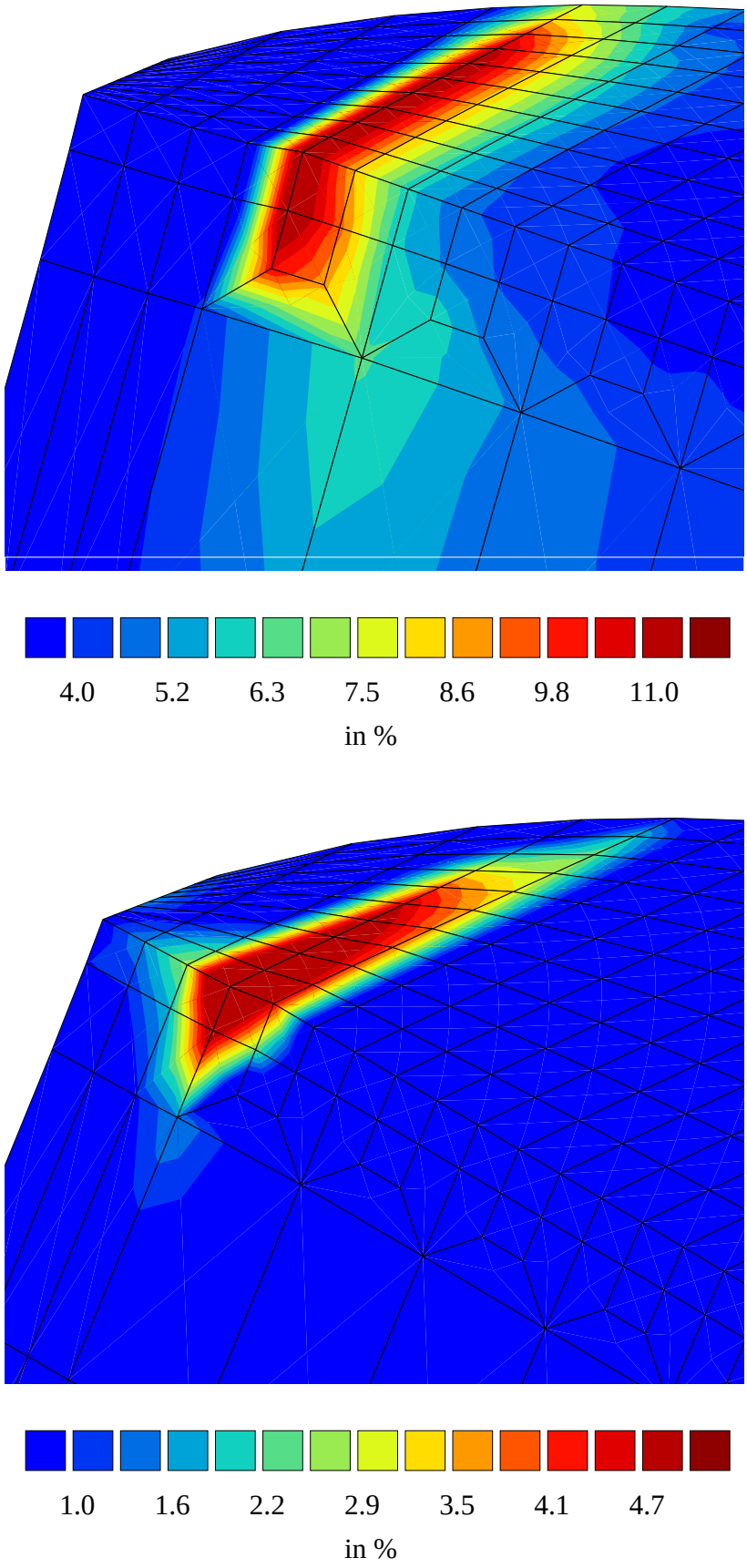

Figure 97: Strain localization pattern at the crack tip of the $(001)[110]$ SC16 oriented specimen with the classical viscoplastic model for small deformations: octahedral (above) and cubic (below) equivalent inelastic strain.

Part VI
Conclusion

The life prediction of single crystal components was studied in this work through an experimental approach and numerical modelling. It has been observed that a good evaluation of the life must include both a crack initiation model and a prediction of the crack propagation.

The main contribution of the thesis deals with crack initiation: a huge experimental data base on SC16 has been made, and two original approaches have been proposed for the simulation of the tests. Most of the tests performed in the study are unique in the literature, specially the section concerning the notched specimens with $\langle 001 \rangle$, $\langle 011 \rangle$ and $\langle 111 \rangle$ crystallographic orientations. Several notched radii and orientations of the material have been used. Metallurgical observations have been made to characterize crack location and the rupture mode. One main crack is present for the $\langle 011 \rangle$ and $\langle 111 \rangle$ oriented specimens, but *two* cracks can be seen for the $\langle 001 \rangle$ oriented specimen: they are symmetric with respect to the minimum section plane. As a matter of fact, the position of the main cracks corresponds to the specimen area presenting the maximum total cumulated slip for the cubic slip system family.

The simulation section includes first the identification of the material parameters for a crystallographic model valid for non isothermal cyclic loadings, in the complete temperature range, a special attention being payed to $950^{\circ}\mathrm{C}$. It has to be noted that the same set of coefficients is valid for monotonic loadings, including creep, and cyclic loadings with or without hold periods, for all the crystallographic orientations tested, with either single or multiple slip. Usually, this appears to be a difficult problem, which is not often successfully solved.

This model was used to simulate isothermal LCF tests on circumferentially notched specimen using a FE technique. Crack initiation models can then be applied in a post-processor to achieve the life prediction. A new definition of the critical variable is then proposed: at the point of maximum total cumulated slip on the surface, the value of the maximum resolved shear stress for the corresponding slip system family. Even if the resolved shear stresses represent the “physical components” of the full state stress for the single crystal, we cannot know with accuracy if its maximum value is “physically” responsible for the damage. On the other hand, it was observed from micrographs of the rupture surfaces that the cracks initiate from casting pores present near the surface. A second approach is then proposed to account for this defect distribution in the life prediction. This is a “multiscale probabilistic failure model” based on the real distribution and location of the defects in the specimen. This statistical failure model has been successfully applied too.

The methodology derived from the specimen observation is then validated on a “technological specimen” tested by KWU, simulating the most critical zone of a turbine blade.

The classical procedures used in industry for life prediction are more and more questionable, due to the increasing complexity of the thermal and mechanical loading histories. The FE model was taken from KWU, and the two previously defined assessment rules were successfully applied. Both lifetime and crack location given by the model were found in good agreement with experiment.

The last section of this work is a numerical study concerning the strain localisation patterns at the crack tip in f.c.c. single crystals under plane strain conditions at low temperature. This has to be seen as a first step for a better understanding of the crack propagation process, having in view the competition between strain localisation models and fracture mechanics approach. The theoretical results are well known in the literature for classical continuum mechanics. Our contribution concerns the modification of these results produced by the introduction of the generalized continuum theory. A Cosserat model for single crystal has then been used, for several orientations of the specimen. The analysis of the FE results shows three characteristic strain localization bands: slip, kink or multislip bands. The introduction of sufficient additional hardening due to lattice curvature in Cosserat modelling shows that effective kink bands are precluded in favour of effective slip bands. If one assumes that crack branching at the tip is on these slip bands, one has to choose a constitutive model which precludes the strong lattice curvature. Few experimental results are available to draw a decisive conclusion, but at least the approach is now available for future work.

Following this study, many points need more investigations. First, experimental studies would be welcome. Since most of the tests made here are original, it would be nice to confirm the results obtained, maybe on different loading conditions, like plane strain or plane stress specimens, seeking also to check the results for other temperatures. The experimental domain to cover includes non-isothermal tests under multiaxial loading, and, as pointed out previously, crack propagation tests. The results given by the models used in this work should be compared with these new experimental results. Since the problem in the blades is related to crack initiation from the cooling holes, one has to investigate short crack propagation, three-dimensional crack fronts, and mainly, the influence of the coating of the blade.

Moreover three-dimensional calculations involving a larger number of elements should be performed to correctly reproduce the geometries of the turbine blade (or any modern industrial component...). Parallel FE computations should be made simple enough to allow a routine usage in industry.

If compared with the classical mechanical approach, Cosserat model was shown to predict a qualitatively different answer to the problem of strain localisation at a crack tip. This study has to be extended, and confirmed with experimental observations. Anyway such an approach seems to be promising, since it is well known that a gradient effect may be helpful in rapidly varying stress fields. It may also provide interesting information to properly define the transition between crack initiation and crack propagation models.

References

[Bertram and Olschewski, 1991] Bertram, A. and Olschewski, J. (1991). Formulation of anisotropic linear viscoelastic constitutive laws by a projection method. In *High temperature constitutive modeling - theory and application*, Freed, A. D. and Walker, K. P., editors, volume 121, pages 129–137. ASME.

[Bertram and Olschewski, 1996] Bertram, A. and Olschewski, J. (1996). Anisotropic creep modelling of the single crystal superalloy SRR99. *Computational Materials Science*, 5, 12–16.

[Besson and Foerch, 1998] Besson, J. and Foerch, R. (1998). Object–Oriented Programming Applied to the Finite Element Method. Part I. General Concepts. *Revue Européenne des Éléments Finis*, 7(5), 535–566.

[Besson et al., 1998] Besson, J., Le Riche, R., Foerch, R., and Cailletaud, G. (1998). Object–Oriented Programming Applied to the Finite Element Method. Part II. Application to Material Behaviors. *Revue Européenne des Éléments Finis*, 7(5), 567–588.

[Bischoff-Beiermann, 2000] Bischoff-Beiermann, B. (2000). Advanced analysis tools to predict failure mechanisms in TBC coated and uncoated single crystal superalloys. Technical report, KWU. 6 Month progress report, Brussels.

[Bischoff-Beiermann B., 1999] Bischoff-Beiermann B. (1999). Private communication.

[Boubidi and Sievert, 2000] Boubidi, P. and Sievert, R. (2000). Analysis of low-cyclic fatigue at notches in a single crystal superalloy at high temperature. In Fuentes, M., Martín-Meizoso, A., and Martínez-Esnaola, editors, *The 13th European Conference on Fracture, Fracture Mechanics: Application and Challenges*, San Sebastiàn, Spain. ESIS, Elsevier.

[Boubidi et al., 1998] Boubidi, P., Sievert, R., Klingelhöffer, H., Noack, D., and Olschewski, J. (1998). Advanced analysis tools to predict failure mechanisms in TBC coated and uncoated single crystal superalloys, annual progress report, Brite-Euram project BRPR.CT.97.0428. Technical report, Brussels.

[Boubidi et al., 1999] Boubidi, P., Sievert, R., Klingelhöffer, Ell, M., Matzak, C., Mück, S., Schmidt, B., Österle, W., Engelhardt, M., and Olschewski, J. (1999). Advanced analysis tools to predict failure mechanisms in TBC coated and uncoated single crystal superalloys, annual progress report, Brite-Euram project BRPR.CT.97.0428. Technical report, Brussels.

[Bui, 1969] Bui, H. D. (1969). *Etude de l'évolution de la frontère du domaine du domaine élastique avec l'écrouissage et relation de comportement élastoplastique des métaux cubiques*. PhD thesis, Université Pierre et Marie Curie - Paris VI.

[Busso et al., 1998] Busso, E., Meissonier, F. T., O'Dowd, N. P., and Nouailhas, D. (1998). Length scale effects on the geometric softening of precipitated single crystals. *J. de Physique*, 8, 55–61.

[Cailletaud, 1987] Cailletaud, G. (1987). *Une approche micromécanique phénoménologique du comportement inélastique des métaux*. PhD thesis, Université Pierre et Marie Curie - Paris VI.

[Cailletaud and Pilvin, 1993] Cailletaud, G. and Pilvin, P. (1993). Identification and inverse problems: a modular approach. *ASME*.

[Cailletaud and Quilici, 2000] Cailletaud, G. and Quilici, S. (2000). Advanced ana-lysis tools to predict failure mechanisms in TBC coated and uncoated single crystal superalloys. Technical report, École Nationale Supérieure des Mines de Paris. Final report, Brussels.

[Chaudonneret, 1994] Chaudonneret, M. (1994). Fatigue life prediction of components: An analysis of the different working steps. In *Fourth international conference on biaxial/multiaxial fatigue*, SF2M, editor, volume 1, pages 479–488. ESIS.

[Chaudonneret and Chaboche, 1986] Chaudonneret, M. and Chaboche, J. L. (1986). Fatigue life prediction of notched specimen. *Int. Mech. Eng.*, C296/86, 503–510.

[Cleveringa et al., 1999] Cleveringa, H. H. M., Van der Giessen, E., and Needleman, A. (1999). Edge dislocations interacting with a propagating mode I crack. In *20th Riso International Symposium on Materials Science*, page 293.

[Cottrell and Hull, 1957] Cottrell, A. H. and Hull, D. (1957). *Proc. R. Soc.*, 242A, 211–213.

[Cuitino and Ortiz, 1993] Cuitino, A. M. and Ortiz, M. (1993). Computational modelling of single crystals. *Modelling and Simulation in Materials Science and Engineering*, 1, 225.

[Danzer, 1988] Danzer, R. (1988). Lebensdauerprognose hochfester metallischer Werkstoffe im Bereich hoher Temperaturen. Gebrüder Borntraeger, Berlin, Stuttgart.

[Defresne, 1989] Defresne, A. (1989). *Endommagement en fatigue oligocyclique à $650^{\circ}C$ de superalliages monocristallins à base de nickel: Influence de l'orientation cristallographique et d'une concentration de contrainte*. PhD thesis, École Nationale Supérieure des Mines de Paris.

[Defresne and Rémy, 1990] Defresne, A. and Rémy, L. (1990). Fatigue behaviour of CMSX2 superalloy [001] single crystal at high temperature, part 1: Low cycle fatigue of notched specimens. *Material Science Engineering*, A129, 45–53.

[Dennis, 2000] Dennis, R. J. (2000). *Mechanistic modelling of deformation and void growth behaviour in superalloy single crystals*. PhD thesis, Imperial College, University of London.

[Espié, 1996] Espié, L. (1996). *Etude expérimentale et modélisation numérique du comportement mécanique de monocristaux de superalliages*. PhD thesis, École Nationale Supérieure des Mines de Paris.

[Fedelich, 1999] Fedelich, B. (1999). A microstructural model for the monotonic and the cyclic behavior of single-crystals of superalloys at high temperatures. to appear in Int. J. of plasticity.

[Feng et al., 1996] Feng, H., Biermann, H., and Mughrabi, H. (1996). Microstructure-based 3D finite element modelling of lattice misfit and long-range internal stresses in creep-deformed nickel-base superalloy single-crystals. *Material Science Engineering*, A214, 1–16.

[Fleury, 1991] Fleury, E. (1991). *Endommagement du superalliage monocristallin AM1 en fatigue isotherme et anisotherme*. PhD thesis, École Nationale Supérieure des Mines de Paris.

[Forest, 1996] Forest, S. (1996). *Mechanical modelling of non-homogeneous deformation of single crystals*. PhD thesis, École Nationale Supérieure des Mines de Paris.

[Forest, 1998] Forest, S. (1998). Modeling slip, kink and shear banding in classical and generalized single crystal plasticity. *Acta Mater.*, 46, 3265.

[Forest et al., 2000] Forest, S., Boubidi, P., and Sievert, R. (2000). Strain Localization Patterns at a Crack Tip in Generalized Single Crystal Plasticity. To appear in *Scripta Met.*

[Forest and Cailletaud, 1995] Forest, S. and Cailletaud, G. (1995). Strain localization in single crystals: bifurcation analysis, effects of boundaries and interfaces. *Eur. J. Mech., A/Solids*, 14, 747.

[Forest et al., 1997] Forest, S., Cailletaud, G., and Sievert, R. (1997). A Cosserat theory for elastoviscoplastic single crystals at finite deformation. *Arch. Mech.*, 49, 705–736.

[Forest et al., 1996] Forest, S., Olschewski, J., Ziebs, J., Kühn, H.-J., Meersmann, J., and H., F. (1996). The elastic/plastic deformation behaviour of various oriented SC16 single crystals under combined tension/torsion fatigue loading. In *Sixth International Fatigue Congress*, Lütjering, G. and Nowack, H., editors, pages 1087–1092. Pergamon.

[Forest and Pilvin, 1996] Forest, S. and Pilvin, P. (1996). Modelling the cyclic behavior of two-phase single-crystal nickel-base superalloys. In *IUTAM Symposium on Micromechanics of Plasticity and Damage of Multiphase Materials*, Pineau, A. and Zaoui, A., editors, pages 51–58. Kluwer.

[Gallerneau, 1995] Gallerneau, F. (1995). *Etude et modelisation de l'endommagement d'un superalliage monocristallin revetu pour aube de turbine*. PhD thesis, École Nationale Supérieure des Mines de Paris.

[Germain, 1973] Germain, P. (1973). The method of virtual power in continuum mechanics, part 2: Microstructure. *J. Appl. Math.*, 25, 556–575.

[Guédou and Honnorat, 1993] Guédou, J. Y. and Honnorat, Y. (1993). Thermomechanical fatigue in turbo-engine blade superalloys. In *Thermomechanical fatigue behaviour of materials*, page 1186. ASTM-STP.

[Halford, 1991] Halford, G. R. (1991). Evolution of Creep-Fatigue Life Prediction Models. In *Creep-Fatigue Interaction at High Temperature*, volume AD-21. ASME.

[Han, 1995] Han, J. (1995). Identifikation der elastischen Kennwerte anisotroper Hochtemperaturlegierung mittels Resonanzmessungen und Finite-Elemente Simulation. Technical report, VDI, Dusseldorf.

[Hanriot, 1993] Hanriot, F. (1993). *Comportement du superalliage monocristallin AM1 sous sollicitations cycliques*. PhD thesis, École Nationale Supérieure des Mines de Paris.

[Hanriot et al., 1991] Hanriot, F., Cailletaud, G., and Rémy (1991). Mechanical behavior of a nickel-base superalloy single crystal. In *Conference on high temperature constitutive modelling*, pages 139–150. ASME.

[Henderson and Martin, 1995] Henderson, M. B. and Martin, J. W. (1995). The influence of crystal orientation on the high temperature fatigue crack growth of a Ni-based single crystal superalloy. *Acta Metall.*, 44(1), 111–126.

[J. Asaro, 1983] J. Asaro, R. (1983). Crystal plasticity. *J. Appl. Mech.*, 50, 921–934.

[Jiao et al., 1996] Jiao, F., Bettge, D., Österle, W., and Ziebs, J. (1996). Tension-compression asymmetry of the (001) single crystal nickel base superalloy SC16 under cyclic loading at elevated temperatures. *Acta Metall.*, 44, 3933–3942.

[Kafadar and Eringen, 1971] Kafadar, C. B. and Eringen, A. C. (1971). Micropolar media: I the classical theory. *Int. J. Engng Sci.*, 9, 271–305.

[Kessel, 1964] Kessel, S. (1964). *Lineare Elastizitätstheorie des anisotropen Cosserat-Kontinuums*, volume 16. Abhandlungen der Braunschweig. Wiss. Ges.

[Kröner, 1956] Kröner, E. (1956). Die Versetzung als elementare Eigenspannungsquelle. *Z. Naturforschg.*, 11a, 969–985.

[Lemaitre and Chaboche, 1985] Lemaitre, J. and Chaboche, J. (1985). *Mécanique des Matériaux Solides*. Dunod.

[Mandel, 1971] Mandel, J. (1971). *Plasticité classique et viscoplasticité*. cours CISM, Udine, Springer Verlag.

[Méric, 1991] Méric, L. (1991). *Une modélisation mécanique du comportement des monocristaux*. PhD thesis, École Nationale Supérieure des Mines de Paris.

[Méric et al., 1991a] Méric, L., Poubanne, P., and Cailletaud, G. (1991a). Single crystal modeling for structural calculations. part 1: Model presentation. *J. of Engng. Mat. Technol.*, 113, 162–170.

[Méric et al., 1991b] Méric, L., Poubanne, P., and Cailletaud, G. (1991b). Single crystal modeling for structural calculations. part 2: Finite element implementation. *J. of Engng. Mat. Technol.*, 113, 171–182.

[Mesarovic and Kysar, 1996] Mesarovic, S. D. and Kysar, J. W. (1996). Continuum aspects of directionally dependent cracking of an interface between copper and alumina crystals. *Mechanics of Materials*, 23, 271–286.

[Moftakhar and Glinka, 1992] Moftakhar, A. and Glinka, G. (1992). Elastic-plastic stress-strain analysis methods for notched bodies. In *Theoretical concepts and numerical analysis of fatigue*, Blom, A. J. and Beevers, C. J., editors, pages 327–342. EMAS.

[Mohan et al., 1992] Mohan, R., Ortiz, M., and Shih, C. F. (1992). An analysis of cracks in ductile single crystals - I. Anti-plane shear. *J. Mech. Phys. Sol.*, 40, 291–313.

[Mück, 1997] Mück, S. (1997). Schädigungsentwicklung in der Einkristallinen Nickelbasis-Superlegierung SC16 unter zyklischer Beanspruchung bei 950°C. Technical report, BAM.

[Neuber, 1961] Neuber, H. (1961). Theory of stress concentration for shear strained prismatical bodies with arbritary non linear stress-strain law. *Trans. of the ASME*, pages 540–550.

[Neumann, 1974] Neumann, P. (1974). New experiments concerning the slip processes at propagating fatigue cracks. *Acta Mater.*, 22, 1155–1165.

[Nissley et al., 1992] Nissley, D. M., Meyer, T. G., and Walker, K. P. (1992). Life prediction and constitutive models for engine hot section anisotropic materials program. Technical Report NAS3-23939, NASA.

[Nouailhas and Cailletaud, 1995] Nouailhas, D. and Cailletaud, G. (1995). Tension-torsion behavior of single-crystal superalloys: experiment and finite element analysis. *Int. J. of Plasticity*, 11(4), 451–470.

[Nouailhas et al., 1995] Nouailhas, D., Culié, J. P., Cailletaud, G., and Méric, L. (1995). Finite element analysis of the stress-strain behavior of single-crystal tubes. *Eur. J. Mech., A/Solids*, 14(1), 137–154.

[Nouailhas and Freed, 1992] Nouailhas, D. and Freed, A. D. (1992). A viscoplastic theory for anisotropic materials. *J. of Engng. Mat. Technol.*, 114, 97–104.

[Nouailhas and Lhuillier, 1997] Nouailhas, D. and Lhuillier, S. (1997). On the micro-macro modelling of γ/γ' single-crystal behavior. *Computational Materials Science*, 9, 177–187.

[Olschewski, 1997] Olschewski, J. (1997). Der kubisch-flächenzentrierte Einkristall in Theorie und Experiment Einige Untersuchungen zum Problemkreis - Orientierung-elastishe Konstanten-Gleitsysteme. Technical report, BAM - V.31.

[Olschewski, 1998] Olschewski, J. (1998). Determination of SC-elastic constants. Technical report, BAM - V.31.

[Ortiz and Quigley, 1991] Ortiz, M. and Quigley, J. J. (1991). Adaptive mesh refinement in strain localization problems. *Comput. Meth. Appl. Mech. Eng.*, 90, 1951.

[Pan et al., 1999] Pan, Y., Bischoff-Beiermann, B., and Schulenberg, T. (1999). Material testing for fatigue design of heavy-duty gas turbine blading with film cooling. In *Fatigue Design and Reliability*, Marquis, G. and Solin, J., editors, Amsterdam. ESIS23.

[Papadopoulos and Panoskaltsis, 1996] Papadopoulos, I. V. and Panoskaltsis, V. P. (1996). Invariant formulation of a gradient dependent multiaxial high-cycle fatigue criterion. *Engng. Fracture Mechanics*, 55, 513–528.

[Poubanne, 1989] Poubanne, P. (1989). *Etude et modélisation du comportement mécanique d'un superalliage monocristallin pour aube de turbine*. PhD thesis, Ecole Centrale Paris.

[Rémy, 1993] Rémy, L. (1993). Fatigue damage and lifetime prediction in alloys for gas turbine components submitted to thermal transients. In *Behavior of defects at high temperatures*. Ainsworth, R. A. and Skelton, R. P., editors, ESIS15.

[Rice, 1973] Rice, J. R. (1973). Plane strain slip line theory for anisotropic rigid-plastic materials. *J. Mech. Phys. Sol.*, 21, 63–74.

[Rice, 1984] Rice, J. R. (1984). On the theory of perfectly plastic anti-plane straining. *Mechanics of Materials*, 3, 55.

[Rice, 1987] Rice, J. R. (1987). Tensile crack tip fields in elastic-ideally plastic crystals. *Mechanics of Materials*, 6, 317–335.

[Rice et al., 1990] Rice, J. R., Hawk, D. E., and Asaro, R. J. (1990). Crack tip fields in ductile crystals. *Int. J. of Fracture*, 42, 301.

[Rice and Nicolic, 1985] Rice, J. R. and Nicolic, R. (1985). Anti-plane shear cracks in ideally plastic crystals. *J. Mech. Phys. Sol.*, 33, 595–622.

[Sato et al., 1985] Sato, T., Takeishi, K., and Sakan, T. (1985). Thermal fatigue life prediction of air-cooled gas turbine vanes. *J. Engng. Gas Turbines and Power*, pages 1–7.

[Shield and Kim, 1994] Shield, T. and Kim, K.-S. (1994). Experimental measurement on the near tip strain field in an iron-silicon single crystal. *J. Mech. Phys. Sol.*, 42, 845.

[Sievert, 1992] Sievert, R. (1992). *Eine Systematik für elastisch-plastische Stoffgleichungen*. PhD thesis, TU Berlin.

[Taylor, 1938] Taylor, G. (1938). Plastic strain in metals. *J Inst. Metals*, 62, 307–324.

[Telesman and Ghosn, 1995] Telesman, J. and Ghosn, L. J. (1995). Fatigue crack growth behaviour of pwa 1484 single crystal superalloy at elevated temperatures. *ASME*.

[Walker and Jordan, 1989] Walker, K. P. and Jordan, E. M. (1989). Biaxial constitutive modelling and testing of a single crystal superalloy at elevated temperatures. In *Biaxial and Multiaxial Fatigue*, Brown, M. W. and Miller, K. J., editors, pages 145–170.

[Wedell et al., 1996] Wedell, W., Chrzanowski, U., Frenz, H., Ziebs, J., and H., K. (1996). Low cycle fatigue behaviour of the single crystal superalloy SC16. In *Sixth International Fatigue Congress*, Lütjering, G. and Nowack, editors, volume 2, pages 807–812. Pergamon.

[Wei and Hutchinson, 1997] Wei, Y. and Hutchinson, J. (1997). Steady-state crack growth and work of fracture for solids characterized by strain gradient plasticity. *J. Mech. Phys. Sol.*, 45, 1253–1273.

[Wilmański and Woźniak, 1967] Wilmański, K. and Woźniak, C. (1967). On geometry of continuous medium with micro-structure. *Arch. Mech. Stos.*, 19(5), 715–723.

[Xia and Hutchinson, 1996] Xia, Z. and Hutchinson, J. (1996). Crack tip fields in strain gradient plasticity. *J. Mech. Phys. Sol.*, 44, 1621.

[Ziebs and Frenz, 1997] Ziebs, J. and Frenz, H. (1997). Schaufeln und Scheiben in Gasturbinen - Werkstoff und Bauteilverhalten, Sfb 339, pp. 01-IV-1. Technical report, TU Berlin.

A Orientation of the SC16 bulk smooth specimens used in the calibration of the crystallographic model

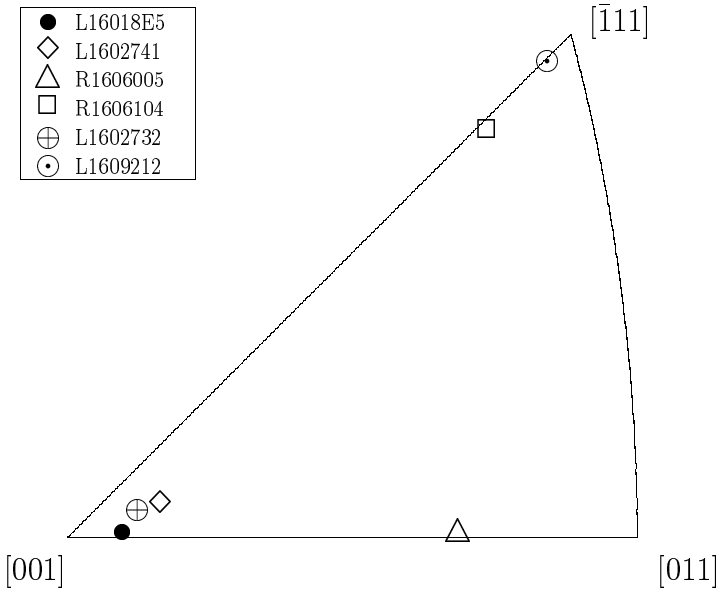

Figure 98: Orientation of the smooth specimens of the tests performed at 20 and 650°C.

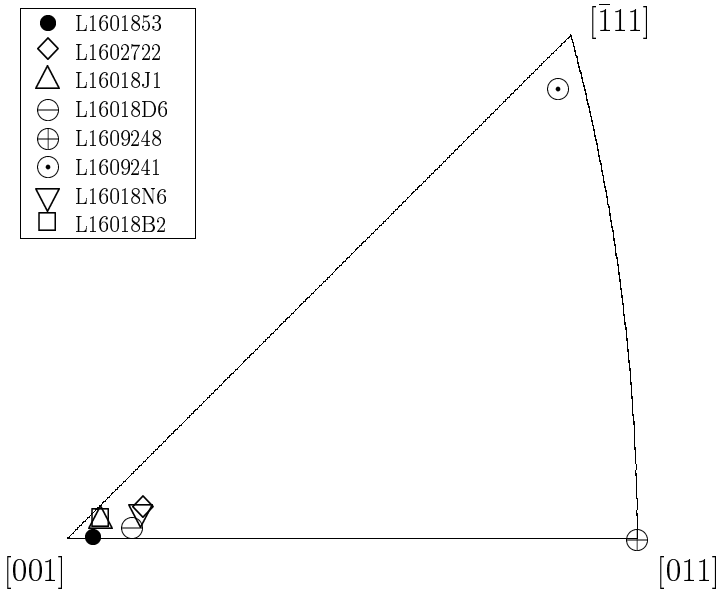

Figure 99: Orientation of the smooth specimens of the tests performed at 850°C.

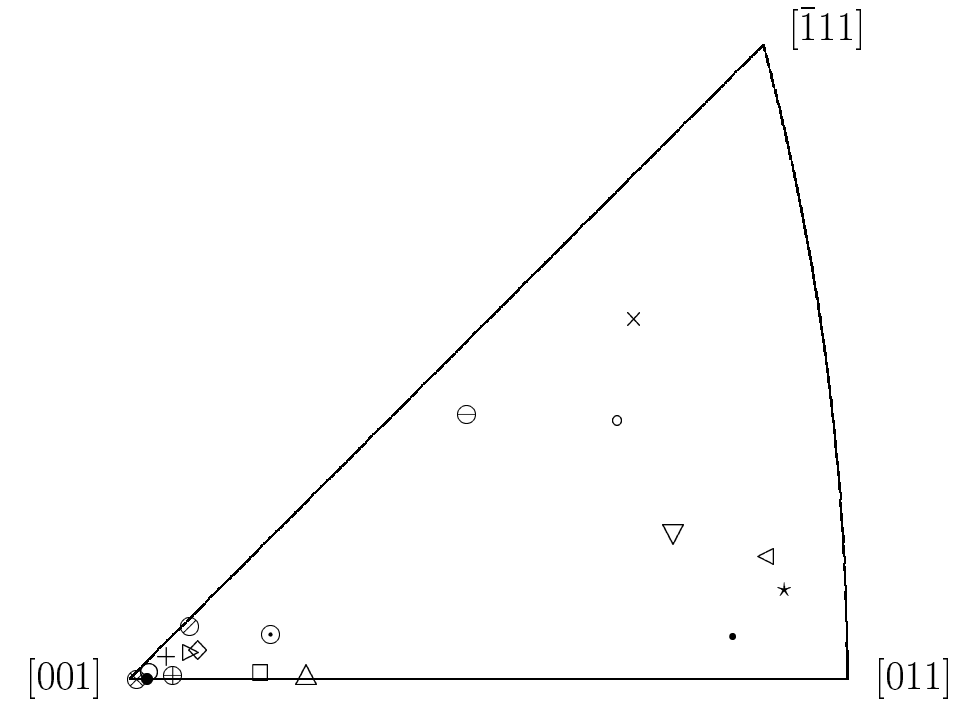

•	L16018C6	⊙	L1601831	⊘	K1602668
◇	L1602721	+	L1601816	▷	K1602675
△	L16018F1	×	R1606105	▽	R1604608
□	L16018F5	⋆	R1604013	•	R1604020
⊕	L16018N4	◁	R1604902	⊖	R1604113
○	L1602783	⊗	K1602662	∘	R1604125

Figure 100: Orientation of the smooth specimens of the tests performed at 950°C.
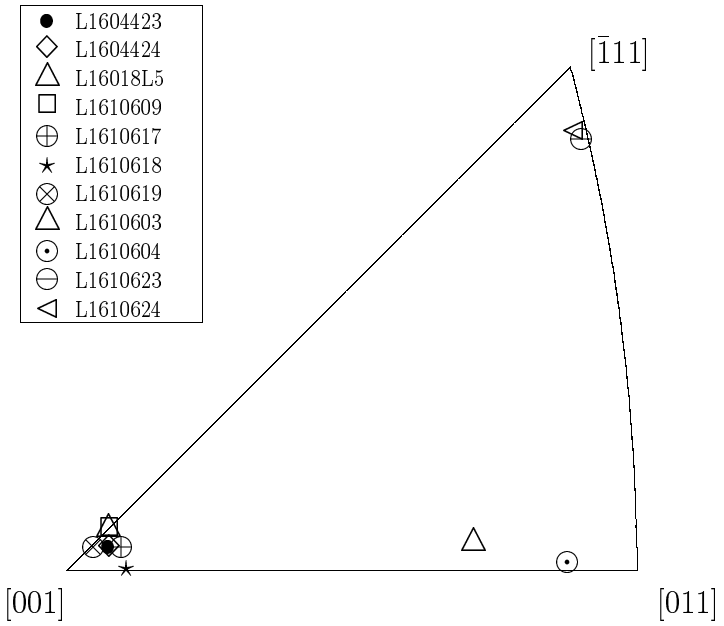
B Orientation of the SC16 notched specimens used in the LCF tests